KU LEUVEN

ARENBERG DOCTORAL SCHOOL
Faculty of Engineering Science

In situ testing of a building's overall heat loss coefficient

Embedding quasi-stationary and dynamic tests in a building physical and statistical framework

Geert Bauwens

Supervisor:
Prof. dr. ir. arch. Staf Roels

Dissertation presented in partial fulfillment of the requirements for the degree of Doctor in Engineering Science

November 2015

In situ testing of a building's overall heat loss coefficient

Embedding quasi-stationary and dynamic tests in a building physical and statistical framework

Geert BAUWENS

Examination committee:
Prof. dr. Adhemar Bultheel, chair
Prof. dr. ir. arch. Staf Roels, supervisor
Prof. dr. ir. Geert Lombaert
Prof. dr. ir. arch. Dirk Saelens
Prof. dr. ir. Henrik Madsen
(Technical University of Denmark)
Prof. dr. ir. Christopher Andrew Gorse
(Leeds Beckett University)
Dr. ir. Peter Wouters
(Belgian Building Research Institute)

Dissertation presented in partial fulfillment of the requirements for the degree of Doctor in Engineering Science

November 2015

© 2015 KU Leuven – Faculty of Engineering Science
Uitgegeven in eigen beheer, Geert Bauwens, Kasteelpark Arenberg 40, bus 2447, B-3001 Heverlee (Belgium)

Alle rechten voorbehouden. Niets uit deze uitgave mag worden vermenigvuldigd en/of openbaar gemaakt worden door middel van druk, fotokopie, microfilm, elektronisch of op welke andere wijze ook zonder voorafgaande schriftelijke toestemming van de uitgever.

All rights reserved. No part of the publication may be reproduced in any form by print, photoprint, microfilm, electronic or any other means without written permission from the publisher.

Preface

Nu dit boek, *bijna*, klaar is, neem ik graag de tijd om een aantal mensen te bedanken die me in dit onderzoek gesteund hebben, en die er mee voor gezorgd hebben dat dit boek, *straks*, af is.

I first want to extend my utmost gratitude to Knauf Insulation and its team, for making this project possible. Frédéric, to you I owe a flying start, and a number of interesting test cases that ended up in this book. It truly has been a pleasure working with you. Abby, Stephen, Barry, but also David and Bert, thank you for your open-mindedness, your continuous support and your critical voice throughout this project.

Ik dank graag mijn promotor, prof. Staf Roels. Staf, bedankt om me de kans te bieden dit onderzoek aan te vatten. Je ervaring en kennis, je belangstelling voor het onderwerp, en je ongelooflijke beschikbaarheid hebben we bijzonder gestimuleerd. Zonder jouw steun en input had ik dit werk niet in zijn huidige vorm kunnen presenteren. Bedankt ook om me secretaris te maken van het IEA EBC Annex 58 project. Zo zag ik de huidige stand van zaken onder mijn neus passeren, en kende ik gelijkgezinde onderzoekers al snel bij hun voornaam.

Ook dank ik mijn supervisors, prof. G. Lombaert en prof. H. Madsen. Geert, bedankt voor de kritische lezing van de uiteindelijke tekst, je input tijdens de tussentijdse overlegmomenten, en het vertrouwen dat je me daar steeds meegaf. Henrik, countless times we met during Annex 58 meetings, and countless times I ended up at your office door in Copenhagen. You and your team members, Peder, Philipp, Rune, were always prepared to lend a hand and share your great expertise. Peder, you have been extremely helpful in getting up and running with most of the analysis techniques that are used in this work.

I sincerely thank all members of the examination committee, for their careful reading of this work, and their valuable suggestions to improve it.

Ik dank het technisch personeel van het Departement Bouwkunde, voor hun ondersteuning in het opzetten van meetopstellingen en het betrouwbaar verzamelen van data. *Zonder hen had u in dit boek geen enkele grafiek gevonden.* Patricia en Wim, jullie hebben me leren kennen als het zoveelste

doctoraatskonijn, dat liefst dubbel zoveel co-heating testen had uitgevoerd, en liefst allemaal in de eerste winter. Ik heb sindsdien wel leren temporiseren, denk ik. Bedankt om me met jullie expertise bij te staan, in het opstellen van complexe experimenten, en het bouwen van leuke schaalmodellen om op te oefenen. Met jullie op stap was het steeds aangenaam werken.

Ook wil ik alle collega's van harte bedanken, voor de aangename momenten van ontspanning, tijdens de vele koffie- en lunchpauzes, op conferentie, en buiten in het zonnetje voor het kasteel. Jelle en Wout, bedankt voor jullie fijn gezelschap en zin voor ondernemen. Bedankt ook om regelmatig jullie kritische blik op kleine stukjes tekst te werpen, en hier en daar de overmaat aan *hipstertaal* eruit te filteren.

Dit project heeft de Afdelingen Bouwfysica en Bouwmechanica misschien net iets dichter bij mekaar gebracht. Graag dank ik prof. E. Reynders, voor alle hulp bij het toepassen van systeemidentificatie op onze data. Edwin, ook al heeft stochastic subspace identification uiteindelijk geen plaats gekregen in het boek, bedankt voor het delen van uw ongelooflijk inzicht in dit domein.

Het boek is bijna af, maar de goesting, *geef me nu wel even een week of twee*, is gebleven. Tot mijn groot plezier krijgt dit project een vervolg, onder de vorm van een IWT-innovatiemandaat. Graag dank ik Wim Fyen, Joke Willems, en veel van hun collega's bij LRD, voor hun ondersteuning bij het opstellen van de projectaanvraag. Wim, bedankt voor de vele verrijkende brainstormsessies. Mede dankzij jou kunnen we een mooi vervolg breien aan dit boek.

Heel graag bedank ik mijn ouders, om me alle kansen te geven die een mens zich maar kan wensen, en voor hun niet aflatende steun. Ik hoop dat ik jullie met dit boek toch een beetje fier kan maken. Kris en Tom, bedankt voor de regelmatige momenten van ontspanning onder de broers. Ik dank mijn schoonouders, Christine en Hannes, om ons te huisvesten, gedurende de tijd dat ons appartement, *heel even maar*, onbewoonbaar was gedurende de renovatie. En ik wil jullie allemaal bedanken om Romi altijd zo fantastisch op te vangen. Zonder jullie hadden Katharina en ik nooit de tijd gevonden onze onmogelijke doelen achterna te jagen.

Ten slotte, Katharina, aan jou wil ik me hier vooral verontschuldigen, voor alle verloren tijd. Nog voor dit doctoraat begon, verscheen je zo onverwacht in mijn leven. Zo ingrijpend heb je er sindsdien zin aan gegeven. Bedankt voor je oneindige geduld bij het schrijven van dit boek.

Als ik wijze Opajo mag citeren: *'T is klaar, als 't klaar is.*
Voilà, het is nu echt klaar. Ik wens u veel leesplezier.

9 november 2015

Abstract

The building sector accounts for about 40% of Europe's total final energy use. Buildings thus harbour enormous potential to save energy, and reduce carbon dioxide emissions. More than half of their energy use is attributable to space heating, which is dependent on the thermal performance of their envelopes, that separate the indoor environment from external influences, and their usage. In order to reduce the energy use of buildings, policy makers are increasingly demanding with regard to their energy performance and the thermal performance of their envelopes, and use mandatory energy labelling to enforce compliance. The building sector is transforming as a result.

Several studies, however, indicate a discrepancy, between the designed and the actual performance of buildings. With regard to building envelopes, such discrepancies may rise up to 400 % on the scale of building envelope parts, and up to 100 % on the scale of a whole building. Today, however, there is little transparency with regard to the actual performance of building envelopes. If we are to effectively advance the building stock's energy efficiency, we need reliable methods to verify this performance.

In this work, we investigate the thermal performance characterisation of whole building envelopes, by fitting simplified thermal models to data collected during dedicated heating experiments, performed on vacant houses. We thereby focus on the overall heat loss coefficient, H, in $\mathrm{W\,K^{-1}}$. We develop a building physical framework, that captures the physical phenomena that inform a building's dynamic thermal behaviour, during such heating experiments. From this framework, we derive simplified thermal models, that are apt to be fitted, using linear regression, input-output polynomial modelling (ARX), or grey-box modelling, to data collected from quasi-stationary and dynamic heating experiments. The link between the building physical framework and the simplified thermal models reveals physical phenomena that get lumped into the simplified models' parameters, and uncovers guidelines for organising high quality experiments. At the same time, the building physical framework provides the practitioner with an extended model library.

By deriving, from a first-order grey-box model, a black-box ARX model, we show that ARX models comprise parameters that remain physically relevant. We thus derive explicit ARX models, but their application to test cases shows that implicit ARX models are much better apt to deal with data from dynamic heating experiments.

We define four scenarios, that provide appropriate strategies to estimate H, based on the building typology, the heating experiment, and the analysis method. We illustrate that the analyses commonly found in literature, can only be applied in a limited number of cases. The developed methodology is applied to three quasi-stationary and three dynamic test cases. They are analysed adopting similar statistical techniques; but we show that the selection of an appropriate scenario underpins the reliability and physical relevance of the obtained estimates.

We show that scenarios where H is estimated as the stationary gain with regard to T_i yield reliable and robust results. The results also indicate that a dynamic test, analysed with ARX modelling, is not more robust than a co-heating test, analysed with either linear regression or ARX modelling, nor does it yield reliable results for a shorter duration. On the other hand, the combination of a dynamic test and grey-box modelling rewarded measurement durations of 4 to 5 days with reliable results. On the basis of the developed methodology, and its application on six test cases, we suggest an onset for a flowchart, to guide the practitioner in reliably characterising the overall heat loss coefficient of buildings.

Beknopte samenvatting

De bouwsector is verantwoordelijk voor ongeveer 40 % van Europa's totaal eindenergiegebruik. Gebouwen herbergen dan ook een enorm potentieel om energie te besparen, en de uitstoot van broeikasgassen te verminderen. Meer dan de helft van dit energiegebruik gaat naar het verwarmen van gebruiksruimtes in gebouwen, en wordt bepaald door de thermische prestatie van de gebouwschil en het gebouwgebruik. Om het energiegebruik van gebouwen te reduceren, stellen beleidsmakers steeds strengere eisen aan hun energieprestatie en de isolatiekwaliteit van hun schil. De verplichte certificatie gebruiken ze daarbij als tool om de conformiteit aan deze eisen na te gaan.

Meerdere studies tonen echter aan dat er een kloof bestaat, tussen de ontworpen en de werkelijke energieprestatie van gebouwen. Wat de gebouwschil betreft, kunnen deze verschillen oplopen tot 400 % op de schaal van een bouwdeel, en 100 % op de schaal van een volledige woning. Vandaag beschikt men echter zelden over kwantitatieve gegevens, met betrekking tot de thermische prestatie van een gebouwschil, eens opgeleverd. Als we het menen dat we de energieprestatie van de gebouwvoorraad willen verbeteren, zijn betrouwbare methodes om dit te verifiëren van groot belang.

In dit boek onderzoeken we de mogelijkheid tot het karakteriseren van de thermische prestatie van de volledige gebouwschil, door het identificeren van eenvoudige thermische modellen op basis van meetdata die verzameld wordt tijdens specifieke verwarmingsexperimenten, uitgevoerd op woningen die niet in gebruik zijn. We concentreren ons daarbij op de globale warmteverliescoëfficiënt, H, in $\mathrm{W\,K^{-1}}$. We ontwikkelen een uitgebreid bouwfysich kader, dat het thermisch gedrag van een gebouw gedurende een verwarmingsexperiment beschrijft. Aan de hand van dit kader leiden we vereenvoudigde thermische modellen af, die geschikt zijn om met behulp van lineaire regressie, meer complexe polynomische (ARX) modellen, of toestandsruimtemodellen geïdentificeerd te worden, aan de hand van meetdata verzameld tijdens quasi-stationaire en dynamische verwarmingsexperimenten. De link tussen het uitgebreid bouwfysisch kader, en de vereenvoudigde modellen

legt fysische fenomenen bloot die ingekapseld zitten in de geschatte parameters en legt richtlijnen bloot die toelaten experimenten van hoge kwaliteit te organiseren. Tezelfdertijd biedt het bouwfysisch kader een uitgebreide staalkaart van vereenvoudigde modellen.

Door van een eenvoudig toestandsruimtemodel een input-output polynomisch (ARX) model af te leiden, tonen we dat ARX modellen parameters bevatten die fysisch relevant blijven. Op theoretische basis leiden we expliciete ARX modellen af, maar hun toepassing op een testcase illustreert dat impliciete ARX modellen beter geschikt zijn om het gebouwgedrag tijdens een dynamisch verwarmingsexperiment te beschrijven.

We definiëren vier scenario's, die op basis van gebouwtypologie, verwarmingsexperiment en de weerhouden analysemethode, geschikte strategieën aanbieden, om H te schatten. We tonen aan dat de analyses, zoals we die vaak in de literatuur aantreffen, slechts toegepast kunnen worden in een beperkt aantal gevallen. In dit boek wordt de ontwikkelde methode toegepast op drie quasi-stationaire en drie dynamische testcases. Ze worden allen met gelijkaardige statistische technieken onderzocht, maar we tonen aan dat het categoriseren van de testcase onder een geschikt scenario van uitermate belang is, om H betrouwbaar en fysisch correct te schatten.

We tonen aan dat als we H kunnen schatten op basis van parameters die betrekking hebben op T_i, we zeer betrouwbare en robuuste resultaten bekomen. We tonen ook aan dat een dynamisch verwarmingsexperiment dat geanalyseerd wordt met ARX modellen, niet leidt tot robuustere schattingen van H, dan een quasi-stationair experiment dat geanalyseerd wordt m.b.v. linear regressie of ARX. De combinatie van een dynamisch experiment en het gebruik van toestandsruimtemodellen laten dan weer een betrouwbare schatting, op basis van een korte meetperiode van 4 à 5 dagen. Op basis van de ontwikkelde methode, en de toepassing hiervan op zes testcases, stellen we een stappenplan voor, dat aan te houden is bij het karakteriseren van de globale warmteverliescoëfficiënt van gebouwen.

List of Symbols

Greek Symbols

α	Solar radiation absorption factor	-
β	Angle of incidence	rad
Δ	Difference	-
ϵ	Residuals	-
λ	Lagrange weighting coefficient	-
λ	Thermal conductivity	$\mathrm{W\,m^{-1}\,K^{-1}}$
ω	Model parameter	-
Φ	Thermal power	W
ρ	Density	$\mathrm{kg\,m^{-3}}$
σ	Standard deviation	-
τ	Time constant	h

Roman Symbols

A	Surface area	$\mathrm{m^2}$
B,q	Backward shift operator	-
C	Heat capacity	$\mathrm{J\,K^{-1}}$
c	Specific heat capacity	$\mathrm{J\,kg^{-1}\,K^{-1}}$
d	Thickness	mm
F	Factor	-

f	Frequency	Hz
G	Mass flow rate	$\mathrm{kg\,s^{-1}}$
g	Total energy transmittance, or g-value	-
H	Heat loss coefficient	$\mathrm{W\,K^{-1}}$
h	Heat transfer coefficient	$\mathrm{W\,m^{-2}\,K^{-1}}$
h	Latent heat	$\mathrm{J\,kg^{-1}\,K^{-1}}$
I	Specific power	$\mathrm{W\,m^{-2}}$
j	Lag	-
k	Model order	-
N	Number of samples	-
n	Air change rate	$\mathrm{h^{-1}}$
P	Pressure	Pa
p	Permeability	$\mathrm{s\,m^{-1}}$
R	Thermal resistance	$\mathrm{K\,m^2\,W^{-1}}$
r	Specific thermal resistance	$\mathrm{K\,W^{-1}}$
T	Temperature	K or °C
t	Time	s
U	Heat transfer coefficient	$\mathrm{W\,m^{-2}\,K^{-1}}$
V	Volume	$\mathrm{m^3}$
w	Wind	$\mathrm{m\,s^{-1}}$

Subscripts

50	At 50 Pa air pressure difference
a	Air
az	Sun azimuth
$azel$	Sun vector angle; concoction of azimuth and elevation
c	Continuous, Constrained, Cellar

$conv$	Convection
d	Direction
dif	Diffuse
dir	Direct
e	Outdoor, ambient, external
el	Sun elevation
f	Fabric
g	Ground
h	Heating, heater
i	Indoor, interior, internal
l	Latent, Laboratory
lw	Long-wave
m	Capacitive medium
n	Neighbouring, adjacent
o	Opaque
rad	Radiation
s	Surface, Solid, Sampling, South
sa	Supply air
sol	Solar
sp	Set-point
sr	Sensor
sw	Short-wave
tr	Transmission
v	Ventilation; Velocity
w	Window

Contents

Abstract **iii**

Contents **xi**

1 Introduction **1**

1.1 Background and problem statement 1

1.2 Scope 5

1.3 Research questions 6

1.4 Outline 7

2 Building physical framework **9**

2.1 Buildings as dynamic thermal systems 10

2.2 Single zone building heat balance 11

2.2.1 Heating power 14

2.2.2 Solar gains 16

2.2.3 Latent heat 17

2.2.4 Transmission heat loss 18

2.2.5 Ventilation heat loss 22

2.2.6 Dissipation heat flow 23

2.2.7 Sensor measurement 23

2.2.8 Conclusions 23

3 Quasi steady-state tests **25**

3.1 The co-heating test legacy 25

3.2 A brief history 26

3.3 Heating experiments 32

3.4 Building physical framework 35

3.4.1 Heating power 36

3.4.2 Solar gains 37

3.4.3 Latent heat 37

3.4.4 Transmission heat loss 37

3.4.5 Ventilation heat loss 39

3.4.6 Dissipation heat flow 39

3.4.7 Sensor measurement 39

3.4.8 Single zone building heat balance 40

3.5 Solving heat balance using linear regression 44

3.5.1 Limited data 44

3.5.2 Correlations 47

3.6 Estimating H 49

3.6.1 Test case scenarios 50

3.6.2 Link with co-heating test literature 52

3.6.3 Visualising co-heating test analysis 53

3.7 Conclusions 55

4 Dynamic tests **57**

4.1 Literature review 59

4.2 Modelling building as reduced-order linear time-invariant (LTI) system 63

4.2.1 Continuous-time stochastic state space model . . . 64
4.2.2 Auto-Regressive models with eXogenous inputs (ARX) . 66
4.2.3 First-order model T_i . . . 69
4.2.4 Second-order model $T_i + T_1$ . . . 74
4.3 Estimating H . . . 77
4.3.1 Continuous-time stochastic state space model . . . 77
4.3.2 Discrete-time transfer function model . . . 79
4.4 Conclusions . . . 80

5 Test Cases **81**
5.1 Statistical tools to fit and evaluate simplified thermal models . 82
5.1.1 Preparing building performance data . . . 82
5.1.2 White noise residuals, please. . . . 83
5.1.3 Reliability plots . . . 87
5.1.4 Confidence intervals . . . 87
5.2 Test Case 1: Terraced house in Herstal, Belgium . . . 90
5.2.1 Description . . . 90
5.2.2 Co-heating test . . . 93
5.2.3 Estimating H using linear regression . . . 97
5.2.4 Estimating H_v . . . 99
5.2.5 Thermally charging building fabric . . . 101
5.2.6 Reliability plots . . . 104
5.2.7 Comparison with expected values . . . 104
5.2.8 Discussion . . . 107
5.3 Test Case 2: Detached house in Limelette, Belgium . . . 108
5.3.1 Description . . . 108

5.3.2 Co-heating test 110
5.3.3 Estimating H_{tr} using linear regression 114
5.3.4 Estimating H_{tr} using ARX models 118
5.3.5 Reliability plots 121
5.3.6 Comparison with expected values 121
5.3.7 Discussion 123
5.4 Test Case 3: Detached house in Verlaine 124
5.4.1 Description 124
5.4.2 Co-heating test 126
5.4.3 Estimating H using linear regression 128
5.4.4 Estimating H using ARX modeling 131
5.4.5 Estimating H_v 131
5.4.6 Reliability plots 133
5.4.7 Comparison with expected values 135
5.4.8 Discussion 135
5.5 Test Case 4: IEA EBC Annex 58 Round Robin Experiment . . 136
5.5.1 Description 137
5.5.2 Dynamic test using PRBS heating power 139
5.5.3 Estimating H using ARX models 141
5.5.4 Estimating H using CTSM-R 144
5.5.5 Reliability plots 147
5.5.6 Comparison with expected values 149
5.5.7 Discussion 149
5.5.8 Appendix: Expected value for H 150
5.5.9 Appendix: Reduced-order models 153
5.6 Test Case 5: Twin Test House 154
5.6.1 Description 154

5.6.2 Dynamic test using ROLBS heating power 156
5.6.3 Estimating H using ARX models 158
5.6.4 Reliability plots 162
5.6.5 Comparison with expected values 162
5.6.6 Discussion 162
5.7 Test Case 6: Detached house in Limelette, Belgium 164
5.7.1 Dynamic heating experiment 164
5.7.2 Estimating H_{tr} using ARX modelling 167
5.7.3 Estimating H_{tr} using CTSM-R 169
5.7.4 Reliability plots 170
5.7.5 Comparison with expected values 172
5.7.6 Discussion 172
5.7.7 Appendix: Reliability plots ARX model with $\mu \neq 0$ . . . 173
5.8 Conclusions 174

6 Conclusions **179**
6.1 Concluding remarks 179
6.2 Flowchart to estimate H 181
6.3 Further fine-tuning of methodology 184
6.4 Towards on-board monitoring 184
6.5 Applications 185

A T_i and T_e together apart **187**

Bibliography **189**

Curriculum **195**

Publications **197**

Chapter 1

Introduction

1.1 Background and problem statement

In Europe, the building sector accounts for about 40 % of total final energy use (Economidou, 2011; European Parliament, 2002). It thereby represents the largest sector, and it is expanding. Our building stock thus harbours enormous potential to save energy, and reduce carbon dioxide emissions, in a cost-effective way. Efforts to improve its energy efficiency lower our dependence on energy supply, and reduce investments needed to increase energy capacity. They might even help us actually meet the climate change deadline. Moreover, they improve comfort and avoid fuel poverty (Economidou, 2011). They advance technology, create employment and develop regions.

In order to reduce the energy use of buildings, policy makers are increasingly demanding with regard to the energy performance of new buildings and renovated buildings, and the use of energy from renewable resources. The Energy Performance of Buildings Directive (EPBD), with its first version published beginning of 2003, compels member states to improve energy performance of buildings. Figure 1.1 shows maximum levels of building element heat transfer coefficients, or U-values, that the Flemish government thus imposes for new and heavily renovated buildings. Clearly, demands are growing more strict at a significant rate. A revised version of the EPBD, published in 2010, even imposes that, by the end of 2020, all new buildings are nearly zero-energy buildings. The EU pledged to cut its energy use by 20 % compared to its projected level, and cut greenhouse gas emissions by 20 % by the year 2020, compared to 1990 levels. Moreover, they commit to further reduce these emissions by at least 80 % below 1990 levels by 2050 (European Commission, 2011). In that respect, they recognise that significant energy savings are needed, up to 41 % by 2050, compared to peak levels in 2005-2006.

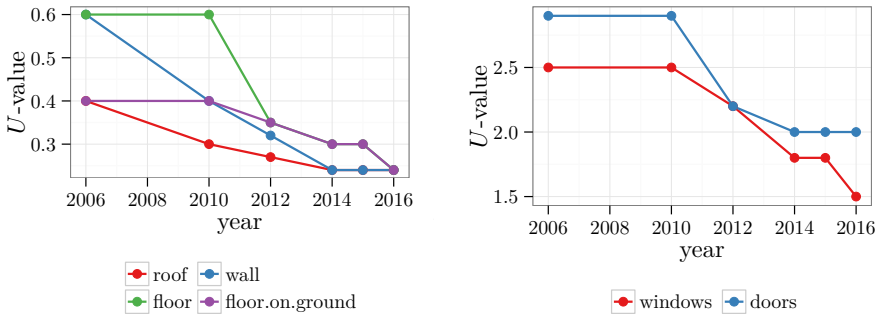

Figure 1.1: Evolution of demands, as imposed by the Flemish government, with regard to thermal transmittance, U, in $\mathrm{W\,m^{-2}\,K^{-1}}$, for different building elements.

A building's actual energy performance essentially depends on three factors: the thermal characteristics of its envelope, the efficiency of its services, and finally, its usage. Kemna (2014) estimates that the total building heat demand in Europe amounts to 2823 TW h. Among others, they assume an average building envelope heat transfer coefficient, or U-value, of $0.93\ \mathrm{W\,m^{-2}\,K^{-1}}$. Compared to the total final energy consumed by end users, 1.284×10^4 TW h (Eurostat, 2015), this represents 22 %, and compared to final energy use that is attributable to buildings, 56 %. The EU's aim to reduce its final energy use by 20 % by 2020 (European Parliament, 2012) thus requires that we also reduce building heat demand, by effectively insulating building envelopes, whilst improving public understanding, to avoid that the increased energy efficiency is not undone, due to excessive comfort take.

With little exception, the policy makers' demands relate to how buildings are rated in the design phase: a theoretical energy use, calculated on the basis of building plans and specifications, determines the performance category. Well-established simulation software and energy labels support this. Detailed simulation software grows increasingly powerful, and integrates increasingly well with the construction process. In Europe, the EPBD directive compelled member states to label energy performance of houses. The mandatory energy labelling has compelled many architects, engineers and builders to reconsider the construction process, and the building sector is transforming as a result.

But there are limitations to using simulation software and energy labels as a basis to enforce energy efficiency. A detailed building energy performance simulation is costly, as it takes significant expertise and time. A large number

of parameters can be assumed, but nonetheless simulation models idealise and simplify reality. Furthermore, the model accuracy is very difficult to assess (Madsen and Holst, 1995). Energy labels simplify reality even to a higher degree, and make crude assumptions with regard to, for instance, indoor temperatures. In any case, neither simulations, nor labels offer insight into how the building is actually constructed. Meanwhile, several studies show that the designed performance of buildings, that we simulate or certify, often differs substantially from its actual, as-built performance. Also the latter is determined by the three factors mentioned before. In the current study, we focus on the building envelope, as it represents the primary factor in a building's heat demand.

Several studies illustrate cases where the building envelope under-performs. Hens et al. (2007) and Houvenaghel and Hens (2003) show this for individual building elements, whereas Lowe et al. (2007) and Bell et al. (2010) show this on a whole building scale. Building envelopes might under-perform due to poor workmanship, inadequate building processes, and the use of materials or detail designs other than specified in the project brief. For instance, Hens et al. (2007) illustrate, in Figure 1.2a, the significant impact workmanship can have on a single building element's heat transfer coefficient: for an insulated cavity wall, they find discrepancies above 400 %. Houvenaghel and Hens (2003) mention, for pitched roofs, discrepancies that range from 10 %, for carefully drafted details, to 200-300 %, for cases where the quality of workmanship is questionable. Figure 1.2b compares measured and designed overall heat loss coefficients of 18 full-scale houses in the UK (Wingfield et al., 2011). None of them realise the designed performance. Moreover, in some cases, measured performance even rises up to twice that value. These studies seem to indicate that the actual performance hardly ever measures up to the designed performance.

To appreciate the potential economic and environmental impact of this discrepancy, we return to the total building heat demand in Europe. Part of Europe's buildings is heated by district heating and process waste heat, among others. A larger part, however, is heated by specific building-own heating systems, and thereby accounts for about 2025 TW h, or 71 % of the total (Kemna, 2014). Assuming that these heating systems are 100 % efficient, and assuming an average electricity and gas unit price of €0.12 per kW h (VREG, 2014), Europeans spend a combined €243 billion to cover that. Many of the houses, represented in Figure 1.2b, show discrepancies above 50 %. Let us assume that, over the whole EU housing stock, the average discrepancy amounts to 25 %. This results in a yearly recurring additional cost of €36 billion. Moreover, if we assume an average carbon dioxide emission of electricity and natural gas of 0.365 $\mathrm{kg\,kW^{-1}\,h^{-1}}$ (Carbon Independent, 2015), this results in an additional yearly emission of 108 million tons of CO_2.

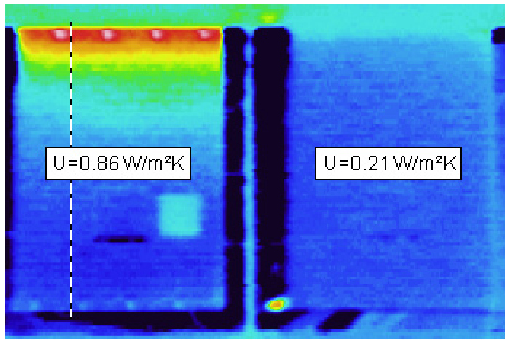

(a) Infrared pictures of two highly insulated cavity walls, both with a design U-value of 0.2 $\mathrm{W\,m^{-2}\,K^{-1}}$ (Hens et al., 2007). The wall on the left was insulated poorly, with air gaps around the insulation layer and at the joints, while the wall on the right was insulated rigorously. The temperature scale varies from warm (red) to cold (blue). At the time the picture was taken, these walls were mounted in the VLIET-test building, at KU Leuven premises. Poor workmanship clearly impacts their thermal performance. The left wall has a very high measured U-value, due to air looping around the insulation. On the other hand, the wall on the right, has a measured U-value that is close to its design value.

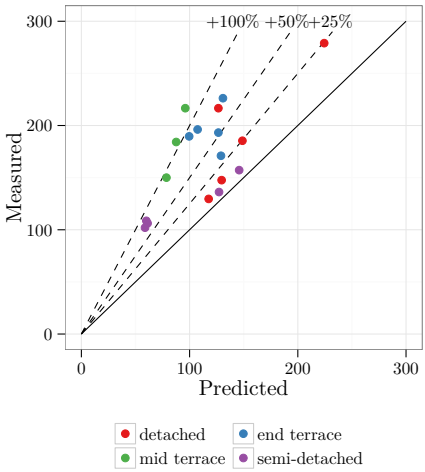

(b) Measured (y-axis) versus designed (x-axis) whole house heat losses, in $\mathrm{W\,K^{-1}}$, for 18 newly built houses in the UK (Wingfield et al., 2011). None of the houses reach their designed building envelope performance. Moreover, measured and designed performance deviate up to 100 %. On the basis of these results, together with forensic investigation on site, an important heat loss mechanism was revealed through the party wall.

Figure 1.2: Comparison between measured and design building envelope performance, on (a) the component scale, and (b) on the whole house scale.

Today, there is little transparency with regard to the actual building envelope performance of our building stock. If we want to effectively advance its energy efficiency, we need tools to verify its performance. Especially now that energy efficiency measures have become increasingly challenging to the building sector. A. Nielsen and B. Nielsen (1983) are among many to see value in assessing performance before and after an *energy conserving measure*. Strachan and Guy (1992) stress the value of being able to estimate physical properties of complex components in calibrating simulation models of whole buildings. Madsen, Bacher, and Delff (2010) recognise that, already today, an abundance of frequent energy consumption readings are available. Smart meters are proliferating. And given appropriate analysis, they can prove invaluable to characterise buildings, improve comfort, better integrate renewable energy, and control the energy supply. Madsen and Schultz (1993) also mention that regularly repeated measurements could reveal ageing effects. Once a building is delivered and in operation, it becomes relevant to know how its energy use compares with the design value, and whether retrofits indeed lead to savings (Rabl, 1988). If we can assess the building envelope thermal performance, energy performance can be split into parts that are related to the three main factors mentioned before, and we can provide feedback with regard to their individual influence.

1.2 Scope

In this work, we take a step towards bridging the gap between designed and as-built energy performance of buildings. Our major aim is to investigate the *thermal performance characterisation* of *whole building envelopes*, by fitting simplified quasi-stationary or dynamic thermal models, thus applying *parameter estimation*, to data acquired from dedicated quasi-stationary or dynamic *heating experiments* that use tailored, experiment-own heaters and equipment, to inject well-defined heating power sequences into real full-scale buildings that are *not in use*. We thereby focus on residential houses.

The building envelope constitutes the integrated building fabric elements that separate indoor and outdoor environment. We aim to estimate a stationary performance indicator that expresses the amount of heating power that is needed to sustain, over the integrated building envelope, a temperature difference of 1 K, i.e. the overall heat loss coefficient H, in $\mathrm{W\,K^{-1}}$. H cannot be measured directly. But we can infer it based on building performance and outdoor environmental data collected during dedicated heating experiments. Estimating H, and the related confidence interval, is our priority. Additional building performance characteristics that can be inferred in the process are welcome, but they are not our drive.

1.3 Research questions

This work builds on a vast amount of research, that dates back to the 1970s. Chapters 3 and 4 briefly outline previous research that focused on quasi-stationary and dynamic tests, with the aim of characterising stationary and dynamic thermal performances of buildings. This work will focus on five aspects that are often neglected or missing in the current state of the art.

First, in literature, the investigated building's actual thermal behaviour is approximated using *simplified thermal models*. Their parameters, limited in number, thus lump together different physical phenomena. What is the physical relevance of these parameters? Can we pinpoint the physical phenomena they lump? Can we follow specific guidelines, when performing quasi-stationary and dynamic heating experiments, or when analysing their data, to accurately distinguish thermal performance characteristics of interest? Are model assumptions in current literature correct? How can we improve them?

Second, researchers often make a trade-off between grey-box models, that are born in continuous-time and have lumped parameters that directly represent physics, and black-box models, that are born in discrete-time and merely explain a certain output on the basis of a set of inputs. The latter are very flexible with regard to model order, demand little computation time, and model fits are quickly generated. But are the parameters, embedded in these models, physically relevant? How do they relate to the actual physics, and to a simplified thermal model that has physically relevant parameters?

Third, in current literature, quasi-stationary tests, with the co-heating test as most popular exponent, are analysed by researchers that generally have less experience in statistical analysis. On the other hand, dynamic tests are generally analysed with more statistical rigour. Can we embed both in a consistent statistical framework? Can we facilitate the use of appropriate models, that are fitted to data, using for instance multiple linear regression? Can we, for both quasi-stationary and dynamic tests, assess the robustness of an estimate, obtained for a certain test, and based on a limited data set?

Fourth, there are currently no procedures available, that discern between different combinations of building typology and heating experiments. Moreover, there are currently no procedures available, that specify how to deal with inputs that, even though they do not influence the building in a dynamic way, nonetheless influence relevant model parameters. Can we suggest robust procedures, to guarantee that a practitioner, for different building typologies and heating experiments, correctly interprets the model parameters, and reliably estimates H? How do unaccounted for inputs influence this estimate?

Fifth, in literature, we have not found many benchmark exercises, where the estimated values for physically relevant parameters, are verified against their designed or expected values.

1.4 Outline

In Chapter 2, we define a building physical framework, that captures in detail the physical phenomena that inform a building's dynamic thermal behaviour, during typical dedicated heating experiments. This building physical framework serves to thread together all chapters in this dissertation.

Heating experiments, and the data that they generate, only reveal part of a building's behaviour. Hence, we are only able to identify simplified thermal models. We derive such models from the building physical framework. Although simplified, they thus accurately describe the building's apparent behaviour. In Chapter 3, we derive a quasi-stationary heat balance model that is suited to analyse quasi-stationary heating experiments. Such experiments create stationary conditions indoor, by thermostatically controlling the indoor air temperature T_i. Nonetheless, dynamic weather conditions, and the building fabric's inertia, tend to challenge a perfect equilibrium. Linear regression analysis is used to estimate the model's parameters. In Chapter 4, we derive, again from the building physical framework, a dynamic heat balance model, suited to analyse dynamic heating experiments. These experiments deliberately excite the building with a dynamic heating power, and we closely monitor how T_i responds. To estimate building performance characteristics, continuous-time lumped stochastic space space models, and discrete-time ARX models are fitted to collected measurement data.

At the end of Chapters 3 and 4, we suggest appropriate strategies, to estimate H on the basis of respective simplified thermal models. To collect these strategies, we define four scenarios. Each test case can be categorised in one of them. Chapter 5, where we apply the analysis methods developed in Chapters 3 and 4 on several test cases, illustrates and validates the methodology. For each test case, we compare the assessed value for H with its expected value. In a concluding chapter, we evaluate the developed methodology, among others on the basis of the results that it generates for the different test cases. We suggest an onset for a flowchart, to guide the practitioner in reliably characterising the overall heat loss coefficient of buildings.

Chapter 2

Building physical framework

We want to characterise the thermal performance of building envelopes, that separate the internal environment from external influences. To do so, we analyse high quality heating experiments, using methodologies that are informed by a solid *building physical framework*. A physical framework that describes the dynamic thermal behaviour of buildings and the relevant physical phenomena that drive it.

In this chapter, we derive a comprehensive *single zone dynamic heat balance* of a building that is exposed to a dedicated heating experiment. In general, buildings comprise multiple zones, that might be heated and used very differently. They might have very different orientations, glazing areas and thermal performance. With regard to the heating experiments considered in this dissertation, however, it is reasonable to assume that they behave as a single zone. Nonetheless, the developed framework can be extended to describe a building's behaviour when heating experiments deliberately cause it to behave as multiple zones.

During dedicated heating experiments, building performance data are collected. Inevitably, these data only reveal part of the building's actual behaviour. At best, they allow us to identify simplified thermal models that approximate this behaviour. The building physical framework developed in this chapter provides us with the necessary theoretical baggage to confidently suggest such models. Models that are appropriate to describe the behaviour of a building during a heating experiment, and that can be identified based on limited data. Moreover, this framework helps us to interpret the estimated model parameters and pinpoint physical phenomena that work behind the scenes.

2.1 Buildings as dynamic thermal systems

Buildings are dynamic thermal systems, that can be modelled as a distributed set of thermal nodes, with temperatures that vary in time, as a function of temperature and spatial distribution of surrounding thermal nodes. The building behaviour can thus effectively be described as a system of linear differential equations, that define how their *thermal nodes* are linked. Thermal nodes can represent an indoor air temperature, a temperature inside the building fabric, or the temperature attained by heaters, among many others. They have a certain capacity to charge or discharge heat, are linked together with thermal resistances and take input from external sources such as solar radiation. Often, they are referred to as system *states*.

If we want to exactly describe a building's dynamic thermal behaviour, we need to discern an infinite number of states. The building's heat balance can then be written as an infinite system of differential equations that apply the first law of thermodynamics, i.e. conservation of energy, which states that the divergence of a heat flow field changes the energy content of an object:

$$\text{for } j = 1, 2, ..., \infty : \sum \mathbf{\Phi_j} = C_j \frac{dT_j}{dt} \tag{2.1}$$

where $\sum \mathbf{\Phi_j}$ represents the sum of heat flow rates, in W, towards temperature state T_j; and C_j denotes the heat capacity of T_j, in $\mathrm{J\,K^{-1}}$.

During the heating experiments considered in this work, it is reasonable to consider the building as a homogeneous heated zone, that is separated from the external environment by the investigated building envelope. We thus lump the rooms, that together form the heated zone, into a *single zone*. As illustrated in Figure 2.1, we represent it with *thermal node* T_i. Neighbouring rooms, conditioned to a different set point temperature, T_n, are lumped into another zone. In many situations, T_n plays an important role. Consider, for instance, a semi-detached house that loses heat towards its neighbour. Finally, we represent the soil mass underneath the building as T_g.

Our aim is to assess the actual thermal performance of the building envelope, bounded by the red and light blue lines in Figure 2.1, that separates T_i from the external environment, defined by the external air temperature T_e, solar and sky radiation and precipitation, and the soil mass underneath the building, represented by ground temperature T_g. This part of the building fabric determines how the indoor air temperature T_i is affected by changes in these boundary conditions.

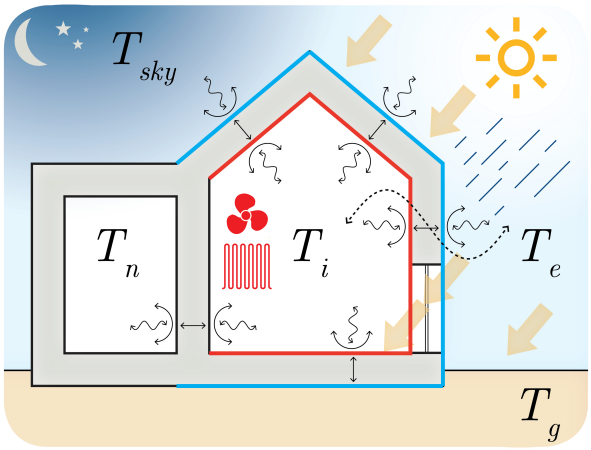

Figure 2.1: Scale model of a typical whole building heating experiment scenario. The red line depicts the indoor surface area, at temperature T_{si}, with which the room air T_i exchanges heat by means of *convection* and *radiation*. On its turn, T_{si} exchanges heat with T_i and the outdoor surface area of the building enclosure, at temperature T_{se}. T_{se} is shaped by conduction heat exchange with T_{si}, and convective and radiative heat exchange with the external air T_e, the environment, sun and sky. Finally, latent heat might impact both T_{si} and T_{se}, e.g. in case of driving rain uptake.

2.2 Single zone building heat balance

Eq. 2.2 describes a dynamic heat balance towards the indoor air temperature state T_i, that takes into account all physical phenomena that influence it. We illustrate it schematically in Figure 2.2.

$$C_i \frac{dT_i}{dt} = \Phi_h + \Phi_{sol} + \Phi_l + \Phi_{tr} + \Phi_v + \Phi_m + \Phi_{sr} \tag{2.2}$$

where Φ_h is the net heating power supplied to T_i by a heating system, and dissipated by ancillary equipment, e.g. electrical equipment or ventilators; Φ_{sol} are solar gains through transparant fabric parts; Φ_l is the latent heat, associated with hygroscopic loading and unloading of building fabric parts; Φ_{tr} is the equivalent transmission heat loss towards the external environment, ground and neighbouring zones, taking into account indirect heat gains attributable to short-wave solar irradiation of opaque fabric surfaces, heat gains or losses attributable to long-wave radiative heat exchange with sky and environment, and latent heat gains or losses due to moisture loading and unloading of building parts. The latter typically arises due to moisture, encapsulated in the building

fabric, that dries out; Φ_v represents ventilation heat loss towards T_e and T_n; As the heat capacity of indoor air, C_i, is limited, T_i appeals to additional thermal capacity: Φ_m represents the thermal power charged from T_i into the capacitive building fabric and indoor furniture; Finally, to monitor T_i, we use sensors. Although small, they also have a certain heat capacity, that influences how we observe T_i. Φ_{sr} reflects the heat exchange between T_i and a sensor temperature T_{sr}.

Figure 2.2 will help us rewrite Eq. 2.2 in terms of the corresponding *driving forces*. Examples of such driving forces are the external air temperature T_e, and temperature state T_i. Aside from T_i, Figure 2.2 introduces many new temperature states: T_{si}, T_{si}^n, and T_{si}^g refer to the indoor surfaces of the building fabric parts. Superscripts are used to distinguish between the external environment (-), neighbouring zones (n), and soil mass (g); T_{se}, T_{sn}, and T_{sg} refer to their outdoor surfaces; State T_m represents the capacitive fabric and furniture, T_{sr} the sensors, and T_h the heaters; Finally, in between T_{si} and T_{se}, T_{si}^n and T_{sn}, and T_{si}^g and T_{sg}, we discern k temperature states. For now, k is assumed to go to ∞.

Figure 2.2 also introduces the heat capacities, denoted C, associated with the temperature states, and the specific thermal resistances, denoted r, that link states with other states and external inputs.

As we develop the system from T_i outwards, we write down heat balance equations that correspond to each of the temperature states. The system of equations will thus grow more and more complex.

Modelling buildings as linear time-invariant (LTI) systems As the range of temperatures that are involved, during typical heating experiments, is generally limited, we assume all heat flows to be *linearly* dependent on their driving forces, thereby hiding eventual non-linear phenomena that take place in the actual system.

We also model buildings as time-invariant. A building responds to a certain excitation, e.g. heating, in a way that is independent of the absolute time this excitation takes place.

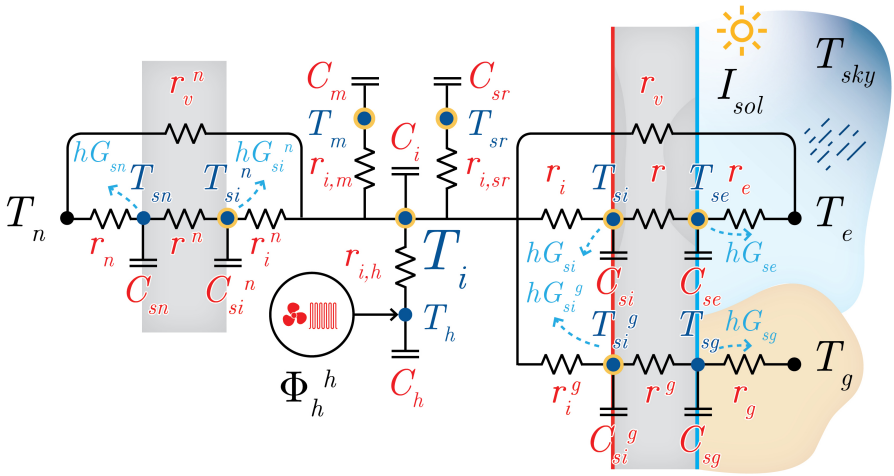

(a) Single zone dynamic heat balance.

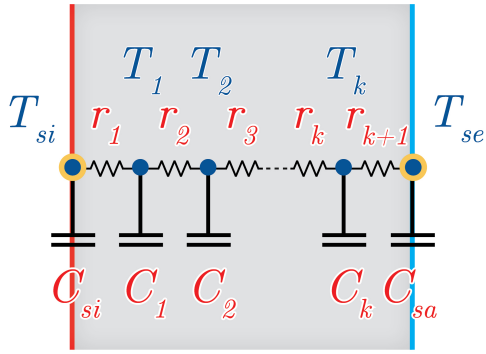

(b) Building envelope parts are divided into a infinite series of capacitive thermal nodes.

Figure 2.2: (a) Single zone heat balance, and (b) detail of building envelope part. Inputs and outputs are shown in black. They include the internal air temperature T_i, external air temperature T_e, ground temperature T_g, sky temperature T_{sky}, solar radiation I_{sol}, neighbouring zone air temperature T_n, and finally, heating power Φ_h^h. Thermal nodes, or *states*, are shown in blue. Although indicated in blue, T_i can serve both as input and state. Parameters, that inform the system's behaviour, are depicted in red. The figure shows a small subset of the parameters that are involved in reality. Yellow circles, around some of the blue points, indicate that those thermal nodes might be affected, either directly or indirectly, by solar radiation. Finally, dashed blue lines represent latent heat gains or losses, e.g. hG_{si}.

2.2.1 Heating power

During a heating experiment, a dedicated heating system injects a well-controlled heating power into the investigated house. This heating power, Φ_h^h, is monitored throughout the heating experiment. In most cases, we can assume it heats T_i directly. But in some cases, the heating system is associated with a significant heat capacity, that we need to account for explicitly. For instance, an electric resistance heater takes time and consumes power to heat up its coil, before it actually delivers heat. Likewise, after it is toggled off, it only gradually decreases in temperature, thereby continuing to deliver heat for some time. To model this, we introduce a temperature state T_h, with heat capacity C_h, and distinguish between the controlled and monitored heating power of the heating system, Φ_h^h, and the heating power that is actually delivered to building zone T_i, Φ_h. Heating power Φ_h^h then serves to heat T_h, which, in its turn, exchanges heat not only with T_i, but also with surrounding surface areas:

$$C_h \frac{dT_h}{dt} = \Phi_h^h + \frac{1}{r_{i,h}}(T_i - T_h) + \frac{1}{r_{si,h}}(T_{si} - T_h) + \frac{1}{r_{si,h}^n}(T_{si}^n - T_h) + \frac{1}{r_{si,h}^g}(T_{si}^g - T_h) \tag{2.3}$$

where C_h is the heating system's heat capacity, in $\mathrm{J\,K^{-1}}$, and $r_{i,h}$, $r_{si,h}$, $r_{si,h}^n$ and $r_{si,h}^g$ are specific resistances, in $\mathrm{K\,W^{-1}}$, between heater temperature T_h and indoor air temperature T_i, and between T_h and indoor surface temperatures T_{si}, T_{si}^n and T_{si}^g, respectively.

The heating power that injects heat into T_i, is noted Φ_h:

$$\Phi_h = \frac{1}{r_{i,h}}(T_h - T_i) \tag{2.4}$$

The specific thermal resistance $r_{i,h}$, in Eqs. 2.3 and 2.4 represents a resistance against *convection*, whereas $r_{si,h}$, $r_{si,h}^n$ and $r_{si,h}^g$ (not indicated in Figure 2.2) represent resistances against *radiation*. We elaborate on these heat exchange modes in the inset on page 15.

Convection depends on the bulk movement of a fluid. Convective heat transfer combines heat conduction and mass transfer. When a fluid is adjacent to a solid material, heat is transferred between them. The heat flow by convection at a solid wall-fluid interface is described by Newton's law:

$$\Phi_{conv} = h_{conv} A (T_s - T_\infty) = \frac{1}{r_{conv}} (T_s - T_\infty) \tag{2.5}$$

where h_{conv} is the surface heat transfer coefficient for convection, A is the area of the shared surface, T_s is the temperature of the solid and T_∞ is the temperature of the fluid far from the solid.

The definition of h_{conv} encapsulates the non-linear combined effect of heat transfer and mass flow (Hens, 2008). For natural convection, it is primarily dependent on $T_s - T_\infty$, whereas for forced convection its value is primarily determined by the air speed. Typical values for h_{conv} range between 2 and 25 $\mathrm{W\,m^{-2}\,K^{-1}}$. Values can vary significantly based on local surface conditions.

Heat exchange by radiation occurs between all objects that have different temperatures and are in optical contact. It is emitted in the form of electromagnetic waves and therefore does not need a medium to propagate in. For instance, radiation is the mode by which heat is transferred from the sun to the earth.

There will be net radiative heat exchange between two bodies if they are at different temperatures:

$$\Phi_{rad} = h_{rad} A (T_s - T) = \frac{1}{r_{rad}} (T_s - T) \tag{2.6}$$

Where T_s and T represent temperature of radiation exchanging bodies, in this case the building surfaces, the sun and the sky. h_{rad} is the radiative surface heat transfer coefficient. Again, it encapsulates actual non-linearities associated with this heat exchange mode. It is dependent on the emissivity of the surface, the temperatures of both bodies raised to the fourth power, the view factor between the bodies and the cloudiness of the sky. Typical values range from 0 to 5 $\mathrm{W\,m^{-2}\,K^{-1}}$.

2.2.2 Solar gains

Throughout the day, the sun travels a certain path along the celestial sphere, thereby viewing the investigated building from a different angle along the way. The intensity with which it irradiates the investigated building depends on factors that include the sun angle $azel$, cloudiness of the sky, shading, e.g. by surrounding trees, and the reflectivity of the earth's surface. Solar radiation can impact a building's temperature household significantly, as part of it enters the building, either directly or indirectly, through transparent building envelope parts. This heating energy is referred to as *solar gains*. They can be described as follows:

$$\Phi_{sol} = (\sum_{j=1}^{k} g_j(\beta_j) A_j(azel)) I_{sol}^{dir} + (\sum_{j=1}^{k} g_j A_j(azel)) I_{sol}^{dif} \tag{2.7}$$

where $azel$ represents the sun vector angle, i.e. the angle between a vector that is aligned with the sun beams and a vector on an on-site horizontal plane. It can be split into its *elevation* angle, el, with respect to the local tangent plane, and its *azimuth* angle, az, around the horizon, increasing eastward from a 0 ° north. Using readily available algorithms, we can accurately calculate el and az. We thus consider $azel$ as known; The *angle-of-incidence* β_j is the angle between the sun vector and the normal vector to transparant component j; $g(\beta_j)$ represents the *total energy transmittance*, or *g-value*. This unitless factor expresses the portion of solar radiation that passes through the window surface, either directly or indirectly. It is dependent on the transparant component *composition* and *angle-of-incidence* β_j; The surface areas $A_j(azel)$ seen by the sun are dependent on its position in the celestial sphere, the orientation of the transparant component j and shading provided by surrounding buildings and trees, among others; I_{sol}^{dif} denotes diffuse solar radiation, and I_{sol}^{dir} denotes direct solar radiation, measured along the sun vector. For our purpose, we assume they include solar radiation that is reflected of the earth's surface.

Since solar radiation is often measured on site, we do not account for the sky's cloudiness explicitly. In total, we distinguish k groups of transparant components, with different values for g_j, β_j and $A_j(azel)$. In practice, they can likely be grouped per facade orientation.

As indicated in Eq. 2.7, solar radiation comprises both direct, I_{sol}^{dir}, and diffuse, I_{sol}^{dir}, parts, both in $\mathrm{W\,m^{-2}}$. Their proportion depends in large on the position of the sun and the cloudiness of the sky. Given limited resources, separate measurements for I_{sol}^{dir} and I_{sol}^{dif}, are often unavailable. Mostly, only global solar radiation I_{sol} is available. Moreover, it is often not measured along the sun vector, but perpendicular to a fixed plane, e.g. a horizontal plane.

Rewriting Eq. 2.7 as a function of I_{sol}, we obtain:

$$\Phi_{sol} = \frac{(\sum_{j=1}^{k} g_j(\beta_j)A_j(azel))I_{sol}^{dir} + (\sum_{j=1}^{k} g_j A_j(azel))I_{sol}^{dif}}{I_{sol}} I_{sol}$$

$$\Phi_{sol} = A_{sol}(azel)I_{sol} \tag{2.8}$$

where $A_{sol}(azel)$ is typically referred to as a *global solar aperture* with respect to T_i, in m^2. It can be understood as the virtual window area through which measured solar radiation passes perpendicularly and unimpededly. It is dependent on the sun vector angle $azel$, the g-values of the transparant components, their surface area and orientation. Equation 2.8 also reveals that $A_{sol}(azel)$ depends on the ratios between direct and global, and diffuse and global solar radiation, and on the angle along which I_{sol} is measured. Let it be clear that, in practice, the link between $A_{sol}(azel)$ and the actual physics is heavily blurred.

We focused here on solar gains through transparant building envelope parts. Aside from this, I_{sol} initiates other thermal dynamics as well. For instance, outdoor surface temperatures of opaque envelope parts rise when irradiated by the sun. As a result, local transmission heat losses through the envelope are reduced, or even turned into heat gains. We will discuss this in more detail in Section 2.2.4.

2.2.3 Latent heat

Latent heat flows, Φ_l, arise due to *hygroscopic loading and unloading of building parts*. Consider, for instance, encapsulated building moisture that evaporates towards the indoor environment. This evaporation demands latent heat, that can be described as:

$$\Phi_l = h(G_{si} + G_{si}^n + G_{si}^g) \tag{2.9}$$

with h the latent heat of evaporation, in $J\,kg^{-1}\,K^{-1}$, and G_{si}, G_{si}^n and G_{si}^g the moisture exchange rates, in $kg\,s^{-1}$, between room air and the indoor surfaces of the building fabric parts between T_i and T_e, T_i and T_n, and T_i and T_g, respectively.

2.2.4 Transmission heat loss

Let us now take a closer look at the equivalent transmission heat loss term Φ_{tr}. As illustrated in Figs. 2.1 and 2.2, such heat flows take place at *three interfaces*: from T_i towards the ambient, Φ^e_{tr}, from T_i towards neighbouring properties and adjacent conditioned rooms that are not part of the heated volume, Φ^n_{tr}, and from T_i towards ground, Φ^g_{tr}. We develop them one by one.

Conductive heat flows through building fabric parts directly relate to the *surface temperature gradient* across them. In what follows, we link T_i with indoor surface temperatures T_{si}, T^n_{si} and T^g_{si}. From there, we consider appropriate intermediate states until we reach T_{se}, T_{sg} and T_{sn}. Finally, we link these surface temperatures with the external conditions that inform them. The aim is to fully capture the thermal link between T_i and boundary conditions T_e, T_g and T_n. Only then can we extract the characteristics of the building envelope, bounded by the red and light blue lines in Figures 2.1 and 2.2, that links T_i with both T_e and T_g.

As illustrated in Figure 2.3, the outdoor surface temperature of opaque and transparant fabric parts, T_{se}, can differ significantly from the outdoor air temperature T_e. Surface temperatures of opaque fabric parts rise when struck by short-wave solar radiation. Similarly, surface temperatures of opaque and transparant parts typically drop at night due to long-wave radiative exchange with sky and surroundings. They are also influenced by latent heat gains due to condensing water vapour or rain water uptake, or latent heat losses due to evaporating moisture, or again, water uptake. For instance, when moisture evaporates at the external fabric surface, it locally lowers surface temperature T_{se}. Similarly, indoor surface temperatures are also influenced by inputs other than T_i, be it solar gains, long-wave radiative heat exchange to other interior surfaces, or latent heat.

We start by interpreting the transmission heat loss from T_i as the thermal energy that it exchanges with indoor surface temperature states T_{si}, T^n_{si} and T^g_{si}. These heat exchanges indirectly relate to heat losses towards T_e, T_n and T_g, respectively. T_{si}, T^n_{si} and T^g_{si} (Figure 2.2) represent small local areas of the indoor surface. Although this means we can distinguish many different T_{si}'s, we group them in these generic quantities.

$$\Phi_{tr} = \frac{1}{r_i}(T_{si} - T_i) + \frac{1}{r^n_i}(T^n_{si} - T_i) + \frac{1}{r^g_i}(T^g_{si} - T_i) \tag{2.10}$$

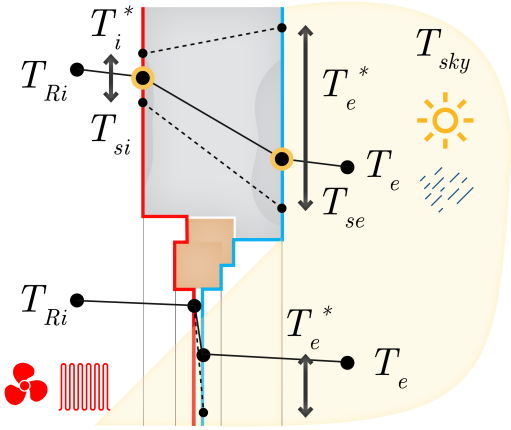

Figure 2.3: Solar radiation and long-wave radiative heat exchange with sky pushes outdoor, and to a lesser degree indoor, surface temperatures of opaque and transparant building fabric parts above or below respective air temperatures.

Now we focus on each of the right-hand side terms of Eq. 2.10. The first term introduces the temperature state T_{si}. Given Figure 2.2, the corresponding heat balance reads:

$$C_{si}\frac{dT_{si}}{dt} = \frac{1}{r_i}(T_{Ri} - T_{si}) + A_{sol,si(azel)}I_{sol} + hG_{si} + \frac{1}{r_1}(T_1 - T_{si}) + \frac{1}{r_{si,h}}(T_h - T_{si}) \tag{2.11}$$

where T_{Ri} represents a weighted average of the central room air temperature, T_i, and the temperatures of the surrounding surfaces, e.g. T^g_{si}, with which T_{si} exchanges radiation. The weighting factors correspond to the ratio of convective and radiative heat transfer coefficients, resp., to $\frac{1}{r_i}$ (Hens, 2008). T_{Ri} is used here for convenience. The last term of above equation still considers radiative heat exchange with the heating system separately. The specific thermal resistance r_i, in $\mathrm{K\,W^{-1}}$, reflects the resistance to convective and radiative heat exchange, whereas r_1 reflects the thermal resistance to conduction through the envelope part between T_{si} and T_1. $A_{sol,si}(azel)$ reflects that part of the solar gains that is absorbed at the indoor surface. It depends on the angle of incidence, the sun angle and the surface's short-wave absorption factor. Finally, hG_{si} describes the effect of moisture loading and unloading of the fabric at the indoor surface.

Regrouping some terms in above equation allows us to introduce the *equivalent indoor temperature* T_i^*:

$$C_{si}\frac{dT_{si}}{dt} = \frac{1}{r_i}(T_i^* - T_{si}) + \frac{1}{r_1}(T_1 - T_{si}) + \frac{1}{r_{si,h}}(T_h - T_{si}) \tag{2.12}$$

with $T_i^* = T_{Ri} + r_i(A_{sol,si}(azel)I_{sol} + hG_{si})$. Although unconventional, by defining an equivalent indoor temperature T_i^*, we simplify notation significantly, and we can more easily discern those driving forces that are relevant for analysis in Chapters 3 and 4.

We continue to describe new temperature states in the building fabric that emerge, e.g. T_1 in Eq. 2.12, using differential equations, until we reach the outdoor surface temperature T_{se}. In so doing, the building envelope parts that separate T_i from the external environment are chopped into k small bits (Fig. 2.2b):

$$C_1\frac{dT_1}{dt} = \frac{1}{r_1}(T_{si} - T_1) + \frac{1}{r_2}(T_2 - T_1) \tag{2.13a}$$

$$C_2\frac{dT_2}{dt} = \frac{1}{r_2}(T_1 - T_2) + \frac{1}{r_3}(T_3 - T_2) \tag{2.13b}$$

$$\dots$$

$$C_k\frac{dT_k}{dt} = \frac{1}{r_k}(T_{k-1} - T_k) + \frac{1}{r_{k+1}}(T_{se} - T_k) \tag{2.13c}$$

$$C_{se}\frac{dT_{se}}{dt} = \frac{1}{r_e}(T_e^* - T_{se}) + \frac{1}{r_{k+1}}(T_k - T_{se}) \tag{2.14}$$

with $T_e^* = T_e + r_e(A_{sol,se}(azel)I_{sol} + \frac{1}{r_{sky}}(T_{sky} - T_{se}) + hG_{se})$ the equivalent outdoor temperature T_e^* (Sonderegger, 1978; Hens, 2008). As the ground and surrounding buildings likely exhibit similar surface temperatures to the investigated building's fabric, Eq. 2.14 ignores the associated radiative heat exchange. On the other hand, we explicitly model long-wave radiative heat exchange with the sky. During a clear night, the sky temperature, T_{sky}, lies around 21 °C below the outdoor air temperature T_e (Hens, 2008).

A second term in Eq. 2.10 introduces state T_{si}^n, that indirectly relates to transmission heat loss towards *neighbouring or adjacent zones that are conditioned differently*:

$$C_{si}^n\frac{dT_{si}^n}{dt} = \frac{1}{r_i^n}(T_i^{*,n} - T_{si}^n) + \frac{1}{r_1^n}(T_1^n - T_{si}^n) + \frac{1}{r_{si,h}^n}(T_h - T_{si}^n) \tag{2.15}$$

With $T_i^{*,n} = T_{Ri} + r_i^n(A_{sol,si}^n(azel)I_{sol} + hG_{si}^n)$. Again, we discern k capacitive thermal nodes between T_{si}^n and T_{sn}. But we immediately skip to the latter's dynamic heat balance:

$$C_{sn}\frac{dT_{sn}}{dt} = \frac{1}{r_n}(T_{Rn} - T_{sn}) + A_{sol,sn}(azel)I_{sol} + hG_{sn} + \frac{1}{r_{k+1}^n}(T_k^n - T_{sn}) \tag{2.16}$$

where T_{Rn} represents a weighted average of the central neighbouring zone air temperature, T_n, and the temperatures of the surfaces that surround it. As illustrated in Eq. 2.16, also the surface temperature at the neighbouring side can be expected to be influenced by, among others, solar gains of its own. Again, we simplify notation by introducing an equivalent temperature, $T_n^* = T_{Rn} + r_n(A_{sol,sn}(azel)I_{sol} + hG_{sn})$, to represent the neighbouring zone temperature:

$$C_{sn}\frac{dT_{sn}}{dt} = \frac{1}{r_n}(T_n^* - T_{sn}) + \frac{1}{r_{k+1}^n}(T_k^n - T_{sn}) \tag{2.17}$$

The last term in Eq. 2.10 quantifies *ground floor transmission heat loss* Φ_{tr}^g:

$$C_{si}^g\frac{dT_{si}^g}{dt} = \frac{1}{r_i^g}(T_i^{*,g} - T_{si}^g) + \frac{1}{r_1^g}(T_1^g - T_{si}^g) + \frac{1}{r_{si,h}^g}(T_h - T_{si}^g) \tag{2.18}$$

With $T_i^{*,g} = T_{Ri} + r_i^g(A_{sol,si}^g(azel)I_{sol} + hG_{si}^g)$. And at the floor-ground interface, we have, with $T_g^* = T_g + r_g hG_{sg}$:

$$C_{sg}\frac{dT_{sg}}{dt} = \frac{1}{r_g}(T_g^* - T_{sg}) + \frac{1}{r_{k+1}^g}(T_k^g - T_{sg}) \tag{2.19}$$

Above equations describe the dynamic heat balance at the indoor and outdoor surfaces of building fabric *parts* that interface with the outside world. As already mentioned, they are generic. They describe building fabric parts that are *composed* differently. Consider, for instance, insulated and uninsulated parts. They describe parts that are *situated and oriented* differently: different parts of a building component can be either *irradiated or shaded*, and this differently at *inside or outside* surfaces. For instance, outdoor surfaces are shaded depending on their position with regards to surrounding buildings and trees. Indoor surfaces are irradiated depending on their position with regards to windows. Multiple phenomena take place simultaneously. Multiple building enclosure parts individually exchange radiation with sun and sky. Different materials absorb and emit short-wave and long-wave radiation differently and depending on the angle. And finally, moisture content of components near outside and inside surfaces might vary locally, due to precipitation and built-in moisture.

Without generic equations, the multitude of cases sketched above would elicit our system of equations to expand dramatically. As the underlying concepts remain similar, we chose not to indulge on page-filling symbol crunching. The presented equations provide sufficient theoretical baggage to sensibly interpret scenarios seen in practice.

2.2.5 Ventilation heat loss

In general, during specific heating experiments, ventilation systems and air-conditioners are turned off and inlets and outlets are sealed. Hence, we disregard heat losses associated with mechanical ventilation, and intended natural ventilation.

When motivated by a pressure difference ΔP_a, an airflow G_a arises along air leakage paths in the building envelope, thereby providing a direct connection between T_i and T_e, or, although less likely, between T_i and T_n. This is commonly referred to as *infiltration* or *exfiltration*, depending on the direction of flow.

Two driving forces are responsible for significant ΔP_a's to arise. On one hand, a significant ΔT, e.g. $T_i - T_e$, causes a *thermal stack effect*. On the other hand, wind gives rise to *overpressures* at the windward and *underpressures* at the leeward side. They depend on the wind velocity and its direction, and the situation and geometry of the investigated building. Moreover, they vary significantly over the facade surface.

We approximate ventilation heat losses by following linear equation:

$$\Phi_v = c_a \rho_a n_{actual} V_i \Delta T = c_a G_a \Delta T \tag{2.20}$$

with c_a the specific heat capacity of air, in $\mathrm{J\,kg^{-1}\,K^{-1}}$, and ρ_a its density, in $\mathrm{kg\,m^{-3}}$. n_{actual} represents the *actual* air changes per hour, that occur under heating experiment conditions. Finally, V_i represents the net air volume enclosed by the building envelope.

To harmonise the expression for Φ_v with above Equations, we rewrite the ventilation heat loss coefficient $c_a G_a$, in $\mathrm{W\,K^{-1}}$, as $\frac{1}{r_v}$. The ventilation heat loss term Φ_v in Eq. 2.2 then becomes:

$$\Phi_v = \frac{1}{r_v}(T_e - T_i) + \frac{1}{r_v^n}(T_n - T_i) \tag{2.21}$$

2.2.6 Dissipation heat flow

The one but last term in Eq. 2.2 is the dissipation heat flow Φ_m. The temperature state T_m represents a charging and discharging thermal tank that comprises available thermal capacity of indoor walls, floors, and large furniture, among others. The indoor air, T_i, has limited capacity of its own, but as described by Eq. 2.22, it can appeal to T_m. Eq. 2.23 describes the corresponding differential equation.

$$\Phi_m = \frac{1}{r_{i,m}}(T_m - T_i) \quad (2.22) \qquad C_m \frac{dT_m}{dt} = \frac{1}{r_{i,m}}(T_i - T_m) \quad (2.23)$$

2.2.7 Sensor measurement

Finally, a heating experiment involves measurements of, among others, the indoor air temperature T_i. To that end, specific sensors are used, with thermodynamic characteristics of their own. Most important, as described in Eq. 2.25, due to their heat capacity, C_{sr}, they can introduce minor lags between measured values and the actual quantity being measured. Eq. 2.24 describes the corresponding heat exchange between T_i and T_{sr}.

$$\Phi_{sr} = \frac{1}{r_{i,sr}}(T_{sr} - T_i) \quad (2.24) \qquad C_{sr} \frac{dT_{sr}}{dt} = \frac{1}{r_{i,sr}}(T_i - T_{sr}) \quad (2.25)$$

2.2.8 Conclusions

In this chapter, we developed a general *building physical framework*. We described an extended dynamic heat balance of a building, that behaves as a *single zone*, while it is exposed to a dedicated *heating experiment*. The external environment, ground and neighbouring zones acts as its primary boundary conditions. We wrote the heat balance as an infinite system of *differential equations*, and we linearised the involved physical phenomena. Non-linearities are thereby captured in the model parameters.

In the next chapters, we use this framework as a blueprint, and distill from it simplified thermal models, that are suitable to describe a building's behaviour during specific heating experiments. In Chapter 3, we derive models for *quasi-stationary heating experiments*, and in Chapter 4, for *dynamic heating experiments*. As these heating experiments only reveal part of the actual building's behaviour, we only realise part of our blueprint.

Chapter 3

Quasi steady-state tests

3.1 The co-heating test legacy

At the time of writing, a method commonly used to evaluate the thermal performance of buildings is the *co-heating test*. This test applies a straightforward *linear regression analysis on averaged building performance data*, acquired during *quasi-stationary heating experiments*. During a co-heating test, a vacant building is homogeneously heated to an elevated steady-state indoor air temperature T_i, e.g. 25 °C, using electric heaters and ventilator fans that are dispersed throughout it. The electrical energy use, indoor and outdoor air temperatures and relative humidities, wind speed and direction, and solar radiation are monitored during the experiment. Transient effects, induced by charging and discharging of the building's thermal mass are limited, by keeping T_i constant, by sensibly choosing the experiment period, and by averaging the collected measurement data over a large time span. Monitored indoor and outdoor climate conditions are related to delivered heating power using *regression analysis*. The linear regression coefficients then represent building thermal performance characteristics of interest: the *overall heat loss coefficient*, H, in $\mathrm{W\,K^{-1}}$, and one or more characteristics relating heating power to e.g. solar radiation. In its turn, H comprises both transmission and ventilation heat loss. To decouple both, a co-heating test is generally combined with a pressurisation or tracer gas test.

Researchers first developed the co-heating test in the late 1970s, where Sonderegger and Modera (1979) and Sonderegger (1980) applied it to determine the on site efficiency of duct heating and cooling systems, under actual boundary conditions. They heated real full-scale houses with, alternately, the

building's own heating system and electric heaters with known efficiency. Hence the name *co-heating*. Ever since it's conception, the co-heating test method has also been applied to estimate thermal characteristics of the building envelope (Lowe et al., 2007; Bell et al., 2010; Bauwens, Standaert, et al., 2012), and to localise heating loads (Sonderegger and Modera, 1979).

This chapter crystallises the current state of the art, with regard to the co-heating test. In Section 3.2, we briefly unfold its history, from which we drew considerable inspiration. A typical co-heating test is presented in Section 3.3. We then start from the single zone heat balance defined in Chapter 2, but simplify it in two stages. First, in Section 3.4, we take into account the distinct characteristics of this test, to distill a simplified quasi-stationary heat balance. It will move us to propose a more fine-grained way to deal with co-heating test data. Second, in Section 3.5, we discuss additional simplifications that are typically applied, when using linear regression to estimate the heat balance parameters. Section 3.6 offers strategies, tailored to the investigated building, to estimate H.

3.2 A brief history

Sonderegger and Modera (1979) and Sonderegger (1980) are among the first to present building performance assessments on the basis of dedicated heating experiments. They chose to organise these experiments at night, and in stages: in the initial and final stages of the experiment, the building's heating demand is covered solely by electric heaters; in an intermediate stage, the building's own heating system covers part of this demand. They labelled this as *co-heating*. The co-heating test thus allows to assess a whole range of quantities. First, when the heating system takes over part of the building's heat demand, the electric heaters need to deliver less power; the difference between this reduced power level and the level they would attain when satisfying 100% of the building's heat demand, gives us the net power delivered by the heating system; taking the ratio between net and monitored gross power then yields an estimate of heating system efficiency. Similarly, cooling system efficiencies can be determined. Second, as evident from Eq. 3.1, when dividing averages of the electric heating energy Φ_h delivered to the building, by averages of the indoor-outdoor air temperature difference ΔT, we can characterise the *overall heat loss coefficient* H:

$$\Phi_h = H\Delta T \tag{3.1}$$

Third, by controlling and monitoring energy used by the heaters individually, heat loss contributions from individual building zones can be separated. An application that Sonderegger and Modera (1979) refer to as *load localisation*.

H was identified to comprise two heat loss mechanisms: transmission heat loss, H_{tr}, and ventilation heat loss, H_v, both in $\mathrm{W\,K^{-1}}$ (Eq. 3.2). To disaggregate H into its parts, co-heating experiments are generally accompanied by pressurisation tests or tracer gas tests to assess the actual air change during the experiment. The air change rate is then often assumed constant over the test period.

$$\Phi_h = (H_{tr} + H_v)\Delta T \tag{3.2}$$

In all of the cases discussed in (Sonderegger and Modera, 1979), the electric heaters are scattered throughout the buildings such that the indoor air temperatures are uniform. Ventilation fans serve to mix indoor air and avoid stratification. In most of the research work discussed here, very similar experimental setups are seen.

Sonderegger and Modera (1979) propose to analyse 40-min averaged data points. They assume a stationary heat balance, with the inside-outside temperature difference, ΔT, as a sole driver for heat loss. An assumption, however, that they only consider accurate under certain conditions: they briefly mention that it might be disturbed by solar gains and ground floor heat losses. As the measurements were performed from late evening into nighttime, they neglect solar gains. Moreover, they neglect the slow dynamics associated with ground floor heat losses.
Sonderegger (1980) reports that estimates for H, that result from tests performed in different periods, vary considerably. Over the course of one single test, however, they vary little. He attributes this to the light-weight nature of his test cases. He thus argues that the co-heating test remains valid to assess heating system efficiency.

In their effort to define low-cost performance evaluation procedures for passive solar buildings, Palmiter et al. (1979) distinguish between *one-time measurements* and *continuous measurements*. Both lead to thermal performance factors, including H. To estimate the latter, they propose to apply linear regression, assuming following equation:

$$\Phi_h = \omega_e T_e - A_{sol} I_{sol} + \mu \tag{3.3}$$

with $H = -\omega_e$; A_{sol} represents a *solar aperture value* that relates I_{sol} to actual solar gains; and μ is a regression constant.
In Eq. 3.3, the indoor air temperature T_i is assumed constant, and $\omega_i T_i$ is lumped into μ. To facilitate comparison, we rewrite this Equation to obtain ΔT as a driving force. Hence, we remove $\omega_i T_i$ from μ again. Nonetheless, we retain μ, as there might be other phenomena that cause Φ_h to drift from 0, when all predictors are 0.

$$\Phi_h = H\Delta T - A_{sol} I_{sol} + \mu \tag{3.4}$$

Palmiter et al. (1979) investigate in-use houses. They collected measurement data every 1 hour, and as a basis for analysis, average it over 5 to 10 days. They recommend to estimate an *overall furnace efficiency* by dividing the heat delivered to the indoor air by the consumed fuel energy. Moreover, they propose infiltration and capacitance measurements to validate assumed simplifications.

Whereas Sonderegger and Modera (1979) and Sonderegger (1980) limited their analysis to a simple linear regression with Φ_h as dependent variable and ΔT as independent variable, Palmiter et al. (1979), and later Siviour (1981) and Everett (1985), suggest the use of multiple, e.g. triaxial, linear regression. In the early 1980's, Siviour (1981) proposes two options to include the influence of solar gains: either calculate them separately, based on geometry and physical characteristics of the investigated building and its surrounding environment, or deduce them empirically, by applying multiple linear regression. He suggests both options are best served by experiments performed during the heating season. The former is argued to endure a shorter measurement period of for instance 1 week in winter, whereas the latter might require a longer measurement period, including days with sufficient solar radiation. Both Palmiter et al. (1979) and Siviour (1981) also suggest to mathematically transform Eq. 3.4: by dividing all terms by ΔT, they obtain Eq. 3.5:

$$\frac{\Phi_h}{\Delta T} = H - A_{sol}\frac{I_{sol}}{\Delta T} \tag{3.5}$$

Assuming the heat balance in Equation 3.4 to hold, the parameters of interest, H, A_{sol} and μ, are generally determined by applying simple or multiple linear regression techniques on co-heating measurement data. Essentially, three options can be discerned here. First, Φ_h can, for instance on a daily averaged basis, be corrected for solar gains, and plotted as a function of ΔT. This implies that we assume a calculated value for the solar aperture parameter A_{sol}, or that we simply set $A_{sol} = 0$, thereby neglecting the solar gains $A_{sol}I_{sol}$ altogether. As illustrated in Fig. 3.1a, *the slope of the regression line*, that results from applying a simple linear regression on the corrected measurement data set, indicates H (Bell et al., 2010). Second, I_{sol} can be considered as an *additional independent variable*, aside from ΔT, that explains the variability of Φ_h. Multiple linear regression then allows to determine both H and A_{sol} in Eq. 3.4 (Lowe et al., 2007; Everett et al., 1985). The disadvantage of this method is that we can not easily visualise it. Third, all terms in Eq. 3.4 can be divided by ΔT, thus obtaining Eq. 3.5. As illustrated in Figure 3.1b, an estimate of H is then given by the intercept. And A_{sol} represents the downward slope. This option thus allows to read both characteristics from a two-dimensional graph (Rabl, 1988).

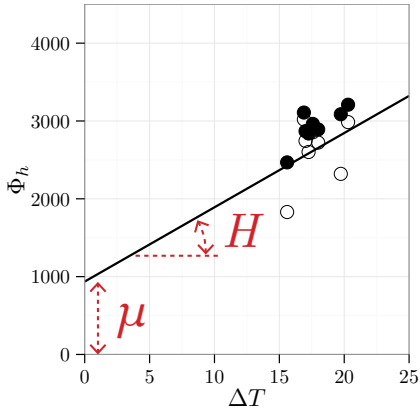

(a) (Filled points): Φ_h^h; (Hollow points): Φ_h^h, corrected for solar gains ($\Phi_h^h + A_{sol} I_{sol}$).

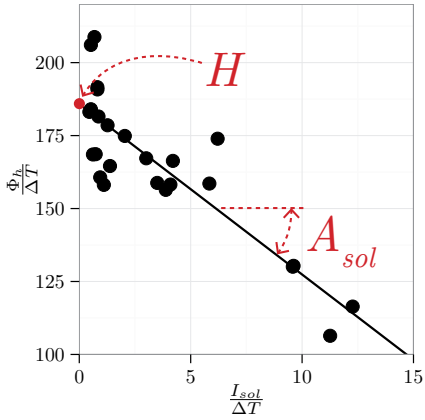

(b)

Figure 3.1: Estimating H and A_{sol}, by applying simple linear regression. The curved arrows indicate the *slope* of the regression line.

The mathematical transformation applied in the third option implicitly forces μ, in Eq. 3.4, to be 0. In the first and second option, a non-zero intercept μ is possible due to discrepancies between the assumed stationary model and the measurement data to which it is fitted.

Ortega et al. (1981) refer to the co-heating test as a well-established experimental method to determine H. Nonetheless, they stress that the heating energy part that is charging or discharging the buildings thermal mass needs to be limited. To best approach stationary fabric conditions, they suggest to keep the indoor air temperature constant during a period in which outdoor air temperatures are stable. They argue that these requirements can be loosened in the case of lightweight constructions, but that they are indeed critical in heavyweight constructions. To resolve the latter, Ortega et al. (1981) suggest to pre-heat the investigated building for several days, whilst eliminating solar gains.

Everett et al. (1985) build upon the work of Siviour (1981), and looked to increase the accuracy of estimates for H and A_{sol}. The Linford project included experimental work on a number of occupied houses and one vacant test house. They opt to assess heat loss through the ground floor, Φ_{tr}^g, separately, using heat flux sensors spread over its surface. They then solve the building's heat balance as a *triaxial regression*, with Φ_{tr}^g assumed constant during the test:

$$\Phi_h + A_{sol} I_{sol} = H \Delta T + \Phi_{tr}^g \tag{3.6}$$

They also decouple ventilation heat loss, H_v, from H in Eq. 3.6, by estimating it on the basis of pressurisation tests and tracer gas tests with constant concentration.

Everett et al. (1985) base their analysis on daily and weekly averaged measurement data. Global solar radiation I_{sol} was measured on a *vertical and south oriented* surface. Inspired by Palmiter et al. (1979) and Siviour (1981), they transform Eq. 3.6 into a form that allows for simple linear regression, or *biaxial regression*:

$$\frac{\Phi_h - \Phi_{tr}^g}{\Delta T} = H - A_{sol}\frac{I_{sol}}{\Delta T} \tag{3.7}$$

In this particular case, H does not include ground floor heat loss. We again find it as the intercept of the regression curve, while A_{sol} represents its negative slope. To obtain accurate estimates of both H and A_{sol}, they propose to select measurement campaigns that have a large spread of $\frac{I_{sol}}{\Delta T}$ data points, with a significant number of them showing low values. The study shows that when considering daily averaged data, thermal lag effects need to be taken into account. To allow maximum time for solar gains, charged during the day, to be discharged overnight, they average measurement data from dawn to dawn. As the air infiltration can vary significantly during experiments, they advise to measure this separately.

Everett (1985) wrote a seminal work on the co-heating test, for *"those fool enough to want to test the thermal performance of a house"*. In his report, he builds on a vast array of earlier project work, including the Linford project mentioned earlier. Also here, as a basis for analysis, he uses daily and weekly averaged data. He reports solar gains, air infiltration, ground floor losses and party wall heat losses as factors that make the analysis more complex. To have ΔT much larger than associated measurement errors, to avoid solar gains from overheating the indoor air during the day and to limit the influence of wind speed on air infiltration, he proposes to elevate T_i as high as practically feasible. He does not, however, consider increased air infiltration due to stack effects that might result from increased T_i's. To diminish the effect of charging and discharging of the building's thermal mass, he advises to precede the experiment by 2 to 3 days of heating. With regard to data analysis, he argues that it is difficult to obtain a large spread on ΔT over a measurement period. In most cases, however, H and A_{sol} can be estimated separately, as the covariance of I_{sol} and ΔT is generally low. To better model thermal lag effects, he suggests to relate Φ_h with a Y-response weighted average of T_e and T_i.

Boogaerts (1987) mentions that following factors increase the quality of a co-heating test: better interior climate control, moderately constant weather conditions over an extended period and, finally, a well-insulated fabric that

exhibits low thermal mass. On the other hand, following factors might decrease its quality: the uncertainty related to the actual air change rate and actual solar gains, influence of wind, and heat losses through ground floor and to unheated adjacent spaces.

Howard and Saunders (1989) report of several studies that reveal shortcomings in the building fabric as primary reasons for the actual building energy performance to turn out poor. They see the combination of an electric co-heating test and air leakage test as an easy to apply and low-cost method, leading to accurate estimates of a building's heat loss coefficient and air permeability.

In order to increase the accuracy of the heating system efficiency assessment, Andrews (1995) suggests to repeat the co-heating test twice, in two consecutive nights, to form a so-called *"flip-flop-protocol"*: each night the building is heated alternately with the heating system and electric heaters, but the order in which they alternate is reversed from one night to the other. The authors warn that in case of high thermal mass, one night might influence the next. In such cases, they advise to plan sufficient time in between consecutive test nights.

More recently, the co-heating test has been applied in (Masy, 2004; Francisco et al., 2006; Lowe et al., 2007; Bell et al., 2010; Palmer et al., 2011; Stamp, 2011; Bauwens, Standaert, et al., 2012; Deconinck and Leunis, 2012; Bauwens and Roels, 2014). Often, co-heating tests are combined with empirical investigations into possible heat loss mechanisms, that would otherwise not be as apparent. For instance, infrared images, taken during a combined co-heating and pressurisation test, can reveal local infiltration losses and cold bridges. A striking result of such forensic work is the identification of the *party wall thermal bypass*, specific to building typologies and detailing in UK (Lowe et al., 2007).

Since its conception, many short-term and dynamic assessment methodologies have been developed from and as possible alternatives to the co-heating test: Short Term Energy Monitoring (STEM), using the Primary and Secondary Terms Analysis and Renormalisation (PSTAR) (Subbarao et al., 1988; Palmer et al., 2011); Measured Performance Rating (MPR) (Howard and Saunders, 1989; Andrews, 1995); Princeton Scorekeeping Method (PRISM) (Fels, 1986; Kissock et al., 2003); and, more recently, Quick measurements of energy efficiency of building (QUB) (Mangematin et al., 2012). This is a non-limitative list and includes methods that incorporate system efficiency and user behaviour with various degree of detail. Although they are not discussed here, they take considerable input from the co-heating test. For instance, a STEM/PSTAR test includes a co-heating test at nighttime, to evaluate envelope heat loss, and one at daytime, to quantify the effect of solar gains.

3.3 Heating experiments

The co-heating test procedure comprises a quasi-stationary heating experiment performed on a vacant building. Over a period of several days to weeks, the building's indoor air is heated to an elevated steady-state temperature T_i, e.g. 25 °C, using electric heaters and ventilators. To obtain homogeneous temperatures in the different zones, interior doors are opened. The building thus behaves as a single zone, at temperature T_i. As T_i is thermostatically controlled to a constant level, the effect of charging and discharging the thermal mass of the building is diminished. Nonetheless, some transient effects still take place due to dynamic weather conditions. For instance, indoor and outdoor wall and floor surfaces absorb solar radiation, and later partly discharge this energy to T_i.

The electrical energy use, the indoor and outdoor air temperatures, indoor and outdoor relative humidities, wind speed and direction, precipitation and solar radiation are monitored throughout the test. From the measurements taken in the different rooms, a representative indoor air temperature signal, T_i, is deduced using e.g. principal component analysis or plain averaging. Data are sampled at a high rate, e.g. every 5 minutes. This allows to capture in detail the building dynamics that persist during the experiment and to correctly interpret the *aggregated data points*. As a basis for analysis, the measurement data is aggregated over a sufficient time span, e.g. 1 day or 1 week, thereby assuming suitable start times, e.g. at midnight or at dawn, in the case of 1 day time spans. We can aggregate data by averaging or decimating. Combined with the effort, made during the experiment, to diminish thermal charging and discharging of the building's thermal mass, such pre-processing supports the quasi-stationary nature of the co-heating test.

In order to undertake a successful co-heating measurement campaign, a researcher needs tailored equipment. Figures 3.2a and 3.2b illustrates a typical co-heating test set up inside a house. Figure 3.2c shows the pressurisation test, and Figure 3.2d the tracer gas test equipment. Figures 3.2e and 3.2f depict the weather station. A more elaborate description of co-heating test equipment is provided in (Johnston et al., 2013).

As already indicated in the previous section, H comprises both transmission and ventilation heat loss. Ventilation, on its turn, can comprise both *natural* and *forced* parts. During a co-heating test, however, the latter is diminished, as ducts and other purposefully placed channels are taped. Nonetheless, significant heat losses can still occur due to *air infiltration and exfiltration*. To decompose H into its transmission, H_{tr}, and ventilation, H_v, parts, we need to estimate the actual *natural* background air change rate n_{actual}, that occurs during the experiment. After all, given n_{actual}, Eq. 2.20 allows to calculate $c_a G_a = H_v$.

To estimate the actual air change, n_{actual}, two tests are generally applied: tracer gas tests and pressurisation tests. The former can take place whilst the co-heating test is running, whereas the latter can only be performed before and after. During a *tracer gas test*, we inject a certain gas into the investigated building. We then either monitor the gas flow needed to sustain a constant gas pressure, or monitor the gas pressure decay. This test thus delivers a *continuous estimate* of n_{actual}. It has a high measurement accuracy, but comes at considerable cost and complexity.

A pressurisation test, or blowerdoor test, imposes a range of pressure differences over the investigated building fabric, i.e. 10 to 100 Pa, in steps of 10 Pa. It can be performed just before and right after the test. It results in an estimate of the n_{50}-value, or the air change rate occurring at a pressure difference inside-outside, ΔP_a, of 50 Pa. Evidently, such high levels for ΔP_a are not representative for real scenarios. Moreover, since the test is performed only momentarily, only discrete air change rate estimates are within reach. It can be performed at low cost, but comes with low accuracy and no insight into the evolution in time of the actual air change rate. Nonetheless, (Kronvall, 1978) propose a rule of thumb, to calculate n_{actual} as the n_{50}-value, divided by a value that depends on the building typology, and ranges from 10 to 30. They distilled this rule by comparing pressurisation test data with actual air change rate data. Assuming $n_{actual} \approx \frac{n_{50}}{20}$, and $c_a \rho_a \frac{1}{3600} \approx \frac{1}{3}$, we can rewrite the right-hand side of Eq. 2.20:

$$c_a G_a \Delta T = \frac{n_{50}}{60} V_i \Delta T \tag{3.8}$$



(a)



(b)



(c)



(d)



(e)



(f)

Figure 3.2: Co-heating test equipment: (a-b): heat sources (red) controlled by thermostats, ventilators (black), temperature sensor and pulse meters spread throughout the different zones of the investigated dwelling; (c-d): Pressurisation and tracer gas test performed to estimate air change rates; (e-f): Monitoring outside weather conditions with a mobile weather station.

3.4 Building physical framework

By performing a successful co-heating experiment, we take an important first step towards our end goal. But in order to estimate reliable thermal performance characteristics of the building envelope, we now need to appropriately analyse the collected measurement data. In any case, given the nature of the co-heating test, we can only estimate a limited number of parameters. Therefore, in this section, departing from the building physical framework presented in Chapter 2, we distill simplified quasi-stationary models. This allows us to uncover physical phenomena that effectively work behind the scenes. Phenomena that are often overlooked in related research work.

Given a thermostatically controlled indoor air temperature T_i, and given appropriately aggregated performance data, we can neglect $\frac{dT_i}{dt}$, in Eq. 2.2. The single zone building heat balance thus simplifies to a stationary form:

$$\Phi_h + \Phi_{sol} + \Phi_l + \Phi_{tr} + \Phi_v + \Phi_m + \Phi_{sr} = 0 \tag{3.9}$$

Furthermore, in this chapter, we assume that significant efforts are made during the experiment to diminish thermal charging and discharging of the building's thermal mass. Figure 3.3 illustrates the resulting crude model of the actual building response. It assumes that the building's thermal mass and the heating experiment equipment are in equilibrium. In practice, we never truly attain this. We are unable to perfectly control the indoor environment, and the equipment has its own dynamics. But most importantly, also weather conditions, e.g. solar gains, impose their dynamics.

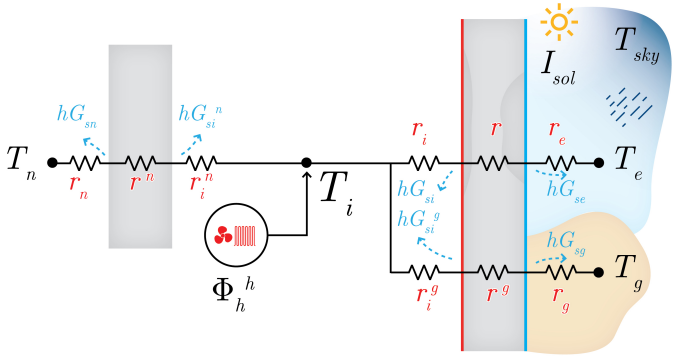

Figure 3.3: Heat balance of a co-heating experiment. Inputs and outputs are shown in black. Parameters in red. The figure only shows a small subset of the parameters that are involved in reality. Dashed blue lines represent latent heat gains or losses.

In the remainder of this section, similar to Chapter 2, we write heat loss and heat gain terms in Eq. 3.9 as a function of the corresponding driving forces. Contrary to Section 2.1, we take into account the specific conditions that are attained during a properly performed co-heating experiment, i.e. a stationary experiment, with constant indoor conditions and a quasi-static building fabric. Along the way, we collect guidelines on how to organise a qualitative co-heating test.

3.4.1 Heating power

The first term in Eq. 3.9 is the thermostatically controlled heating power Φ_h. Throughout the heating experiment, we monitor the actually delivered heating power, Φ_h^h, in Eq. 2.3. Our aim is to bring Φ_h^h as close as possible to Φ_h, such that it can be considered to directly heat T_i. To keep T_i constant, Φ_h^h varies in time, between a very low baseline level that includes power delivered by continuously running ventilators, and a higher level, up to several kW, when electric heaters are active. For instance, given a temperature set point $T_{i,sp}$, a dead-band of 0.5 °C, and sensor temperature T_{sr}, heaters might be toggled on when $T_{i,sp} - T_{sr} > 0.5$, and toggled off when $T_{sr} - T_{i,sp} > 0.5$. As a result, the temperature attained by the heaters, T_h, is bound to vary significantly: $\frac{dT_h}{dt}$. Hence, to simplify Eq. 2.3, *heaters should have a very low heat capacity*: $C_h \approx 0$. In any case, C_h is negligible in comparison with the building fabric's heat capacity, and the associated time constant is smaller than sampling times typically assumed in co-heating test analysis. With $C_h \approx 0$, we can rewrite Eq. 2.3 as follows:

$$0 = \Phi_h^h + \frac{1}{r_{i,h}}(T_i - T_h) + \frac{1}{r_{si,h}}(T_{si} - T_h) + \frac{1}{r_{si,h}^n}(T_{si}^n - T_h) + \frac{1}{r_{si,h}^g}(T_{si}^g - T_h) \tag{3.10}$$

To further simplify Eq. 3.10, we need to limit radiative heat exchange, between heaters, at temperature T_h, and fabric surface temperature states T_{si}, T_{si}^g and T_{si}^n. *Heaters should thus primarily exchange heat by air convection*:

$$\Phi_h^h = \frac{1}{r_{i,h}}(T_h - T_i) \tag{3.11}$$

We find that Φ_h^h is equal to the right-hand side of Eq. 2.4, and thus to Φ_h. Hence, if heaters have a limited heat capacity, and they primarily exchange heat by convection, the measured heating power Φ_h^h can be considered to directly feed into T_i.

3.4.2 Solar gains

Already in Chapter 2, the link between the global solar aperture $A_{sol}(azel)$ and the actual physics became blurred. As we average measurement data over larger sampling times, the dynamics of solar radiation, driven by, among others, the sun vector angle, $azel$, become even more blurred. Eq. 2.8 reduces to:

$$\Phi_{sol} = A_{sol} I_{sol} \tag{3.12}$$

On a sunny day, we will, on average, measure high values for global solar radiation, regardless of orientation. For instance, daily average values for global solar radiation, measured perpendicular to a horizontal plane, will be significantly correlated with values measured perpendicular to an upright, south oriented plane. One quantity can be converted to the other. A_{sol} now merely represents an *average global solar aperture*, that relates averaged values of I_{sol} to apparent averaged solar gains Φ_{sol}. Its value depends on the orientation along which I_{sol} is measured. On the other hand, the estimate of H is invariable to the direction along which I_{sol} is measured.

3.4.3 Latent heat

In case the building fabric contains moisture in its inner layers, the co-heating test likely causes part of it to evaporate towards the indoor environment. Part of Φ_h^h then delivers the associated latent heat. We can copy Eq. 2.9 unaltered:

$$\Phi_l = h(G_{si} + G_{si}^n + G_{si}^g) \tag{3.13}$$

3.4.4 Transmission heat loss

Now we take a closer look at the equivalent transmission heat loss term Φ_{tr}. First, we look at transmission heat losses from T_i towards the ambient T_e. Not only do we assume that T_i is constant during a co-heating test, we also neglect any heat dynamics related to the building fabric. A proper co-heating test thus *minimises the amount of heating energy, that is charged or discharged by the fabric, during the period that is considered for analysis.*

Assuming $\frac{dT_{si}}{dt} = \frac{dT_1}{dt} = \frac{dT_2}{dt} = ... = \frac{dT_k}{dt} = 0$ in Eqs. 2.12 to 2.13 and reformulating yields:

$$\frac{1}{r}(T_{se} - T_{si}) = \frac{1}{r_i}(T_{si} - T_i^*) \tag{3.14}$$

Similarly, assuming $\frac{dT_{se}}{dt} = \frac{dT_k}{dt} = ... = \frac{dT_2}{dt} = \frac{dT_1}{dt} = 0$ in Eqs. 2.13 to 2.14 and reformulating yields:

$$\frac{1}{r}(T_{se} - T_{si}) = \frac{1}{r_e}(T_e^* - T_{se}) \tag{3.15}$$

As introduced in Chapter 2, T_i^* and T_e^* constitute equivalent indoor and outdoor temperatures, respectively. Equations 3.14 and 3.15 now allow us to relate these temperatures to the heating power Φ_{tr} that, in stationary conditions, sustains $T_{si} - T_{se}$ across the envelope:

$$\begin{aligned} \Phi_{tr} r_i &= T_{si} - T_i^* \\ \Phi_{tr} r &= T_{se} - T_{si} \\ \Phi_{tr} r_e &= T_e^* - T_{se} \end{aligned} \tag{3.16}$$

Summing above equations, we obtain:

$$\Phi_{tr} = \frac{1}{r_i + r + r_e}(T_e^* - T_i^*) = H_{tr}(T_e^* - T_i^*) \tag{3.17}$$

The transmission heat loss coefficient, H_{tr}, related to the building envelope part that separates T_i^* from T_e^* can thus be found as $(r_i + r + r_e)^{-1}$. It closely relates to the envelope's heat transfer coefficient, or U-value, multiplied by its surface A. The U-value, however, assumes norm values for r_i and r_e, whereas H_{tr} incorporates average surface resistances r_i and r_e, that occur under actual experiment conditions.

Transmission heat loss towards neighbouring properties or rooms can be derived in much the same way. Also here, we assume that the fabric between T_i and T_n is in equilibrium. Assuming $\frac{dT_{si}^n}{dt} = \frac{dT_1^n}{dt} = \frac{dT_2^n}{dt} = ... = \frac{dT_k^n}{dt} = 0$ and rewriting Eq. 2.15 accordingly yields:

$$\frac{1}{r_n}(T_{sn} - T_{si}^n) = \frac{1}{r_i^n}(T_{si}^n - T_i^{*,n}) \tag{3.18}$$

And assuming $\frac{dT_{sn}}{dt} = \frac{dT_k^n}{dt} = ... = \frac{dT_2^n}{dt} = \frac{dT_1^n}{dt} = 0$ in Eq. 2.16, we obtain:

$$\frac{1}{r^n}(T_{sn} - T_{si}^n) = \frac{1}{r_n}(T_n^* - T_{sn}) \tag{3.19}$$

Combining Eqs. 3.18 and 3.19, we can express stationary transmission heat losses towards T_n:

$$\Phi_{tr}^n = \frac{1}{r_i^n + r^n + r_n}(T_n^* - T_i^{*,n}) = H_{tr}^n(T_n^* - T_i^{*,n}) \tag{3.20}$$

A last transmission term describes heat loss towards the ground. Here, quasi-stationary fabric conditions are straightforward to obtain. Any heat input to T_g will only induce a very small $\frac{dT_g}{dt}$, since a large soil mass underneath the building is excited along with it. By setting $\frac{dT_g}{dt} = 0$ in Eq. 2.18, we find:

$$\frac{1}{r^g}(T_{sg} - T_{si}^g) = \frac{1}{r_i^g}(T_{si}^g - T_i^{*,g}) \tag{3.21}$$

And from Eq. 2.19:

$$\frac{1}{r^g}(T_{sg} - T_{si}^g) = \frac{1}{r_g}(T_g^* - T_{sg}) \tag{3.22}$$

Combining Equations 3.21 and 3.22, we obtain:

$$\Phi_{tr}^g = \frac{1}{r_i^g + r^g + r_g}(T_g^* - T_i^{*,g}) = H_{tr}^g(T_g^* - T_i^*) \tag{3.23}$$

The transmission heat loss coefficient with respect to the ground floor fabric components, H_{tr}^g, can then be written as $(r_i^g + r^g + r_g)^{-1}$.

3.4.5 Ventilation heat loss

Ventilation heat loss directly connects T_i with T_e, and T_i with T_n; we can copy Eq. 2.21 unaltered. As we ignore building dynamics, we are unable to distinguish between transmission and ventilation heat loss on the basis of co-heating test data alone. To extract ventilation heat loss from H, we need additional data, generated by, for instance, a pressurisation test.

3.4.6 Dissipation heat flow

Indoor walls and floors, and furniture, are assumed to be in equilibrium with T_i during the co-heating test. The dissipation heat flow, Φ_m, is thus ignored.

3.4.7 Sensor measurement

The time constants related to typical sensors are negligible in comparison with the building fabric, and the typical sampling times assumed in co-heating test data analysis. Their dynamics are thus likely filtered out completely.

3.4.8 Single zone building heat balance

We are now ready to collect all heat flows discussed above in an overarching heat balance that approaches the behaviour of the investigated building, when exposed to a quasi-stationary co-heating test. Bear in mind that these expressions only relate to small parts of the building envelope at a time. For instance, $A_{sol,si}(azel)$, in Eq. 2.11, relates to a part with a specific composition, orientation and position. Hence, for each part, we can envisage a different equivalent indoor temperature T_i^*. To cope with this, we consider these coefficients to be generic, meaning that they can relate to the specifics of a whole array of building envelope parts. We then suffice by taking the sum over all of them. Starting from Eq. 3.9, we thus obtain following heat balance:

$$\begin{aligned}
&\Phi_h^h + \sum_{j=1}^{w} A_{sol} I_{sol} + h(G_{si} + G_{si}^n + G_{si}^g) \\
&+ \sum_{j=1}^{w} \overset{w}{H}_{tr}(T_e^* - T_{Ri}) + \sum_{j=1}^{w} \overset{w\ \ n}{H}_{tr}(T_{Rn} - T_{Ri}) \\
&+ \sum_{j=1}^{o} \overset{o}{H}_{tr}(T_e^* - T_i^*) + \sum_{j=1}^{o} \overset{o\ \ n}{H}_{tr}(T_n^* - T_i^{*,n}) \\
&+ \sum_{j=1}^{o} \overset{o\ \ g}{H}_{tr}(T_g^* - T_i^{*,g}) + H_v(T_e - T_i) + H_v^n(T_n - T_i) = 0
\end{aligned} \tag{3.24}$$

In constructing Eq. 3.24, we distinguished between transparent fabric parts, abbreviated w for windows, and opaque fabric parts, abbreviated o. For transparent fabric parts, both direct and indirect solar gains are already included in Φ_{sol}. Nonetheless, long-wave radiation still influences their outdoor surface temperatures and thus, indirectly, transmission heat losses through them. To keep Eq. 3.24 general, in a fourth term, we also consider transmission heat loss through transparent fabric parts towards neighbouring zones, in which case T_n^* reduces to T_{Rn}.

Until this point, we considered Φ_{tr} a constant heat loss term between steady-state temperature nodes at either side of the different building envelope components. The fact that T_e^*, and also T_i^*, vary dynamically, is tackled by averaging measurement data over a large number of successive time steps. However, high sampling times are unlikely to fully cancel out transient effects, and as a result, the stationary heat balance in Eq. 3.24 becomes invalid. To explicitly model remaining transient effects, we consider the building envelope, with regard to T_e^*, as a *low-pass filter*. As illustrated in Figure 3.4, at the indoor surface, we observe a *dampened* and *phase-shifted* version of T_e^* (Sonderegger,

1978). The heating power, Φ_h, necessary to sustain a constant, elevated temperature inside is thus phase-shifted with regard to the dynamic weather conditions outside: Φ_h at time step t will depend largely on T_e^* at time step $t - k\Delta t$, with $k\Delta t$ the phase-shift induced by the fabric.

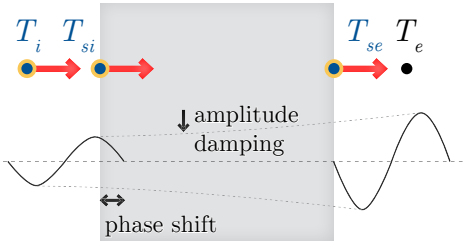

Figure 3.4: A capacitive envelope component acts as a low-pass filter. It dampens the amplitude of the incoming signals and imposes a phase-shift.

A low-pass filter in discrete-time essentially boils down to an exponential moving average (*EMA*). The *EMA*, S_t, of, for instance, T_e^*, can be calculated recursively:

$$S_t = \alpha T_{e,t}^* + (1 - \alpha) S_{t-1} \tag{3.25a}$$

As we now describe how some dynamics unfold in time, we consider time t, and without loss of generality, we set Δt, between successive time steps, equal to 1. Assume $\alpha = 1 - \phi$, and rewrite:

$$S_t = \frac{1 - \phi}{1 - \phi B} T_{e,t}^* \tag{3.25b}$$

with B the backward shift operator.

Figure 3.5 shows a response of a low-pass filtered signal to a unit step.

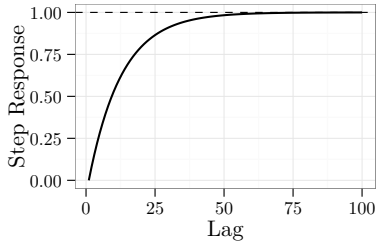

Figure 3.5: Estimated step response, with ϕ in Eq. 3.25b set to 0.92.

Given Eq. 3.25b, we can rewrite Eq. 3.24:

$$\Phi_h^h + \sum_{j=1}^{w} A_{sol} I_{sol} + h(G_{si} + G_{si}^n + G_{si}^g)$$
$$+ \sum_{j=1}^{w} \overset{w}{H}_{tr}(T_e^* - T_{Ri}) + \sum_{j=1}^{w} \overset{w}{H}_{tr}^{\ n}(T_{Rn} - T_{Ri})$$
$$+ \sum_{j=1}^{o} \overset{o}{H}_{tr}(\frac{1-\phi_e}{1-\phi_e B} T_e^* - T_i^*) + \sum_{j=1}^{o} \overset{o}{H}_{tr}^{\ n}(\frac{1-\phi_n}{1-\phi_n B} T_n^* - T_i^{*,n})$$
$$+ \sum_{j=1}^{o} \overset{o}{H}_{tr}^{\ g}(\frac{1-\phi_g}{1-\phi_g B} T_g^* - T_i^{*,g}) + H_v(T_e - T_i) + H_v^n(T_n - T_i) = 0 \quad (3.26)$$

In Eq. 3.26, we only low-pass filtered T_e^* and T_n^* in case of opaque components. Thermal lags do not affect low-capacitive transmission heat loss through windows, nor do they affect ventilation heat loss. We need not apply low-pass filtering with regards to I_{sol} that leads to solar gains through windows. But solar gains do tend to thermally charge and discharge the interior layers of the fabric, which introduces another time constant; the thermally charged indoor surfaces will discharge towards T_i, only after some time. To model this, we low-pass filter I_{sol} in respective T_i^*'s, by multiplying with $\frac{1-\phi_i}{1-\phi_i B}$.

We now expand T_i^*'s and T_e^*'s in Equation 3.26, according to their definitions in Chapter 2, and taking into account the specifics of transparent and opaque fabric parts, and the above described dynamics. We place Φ_h^h on the left-hand side, and on the right-hand side we order the inputs, to highlight how they individually affect Φ_h^h. To simplify notation, we assign parameters ω to each of them. They are written in full in Eq. 3.28 (inset on page 43).

$$\Phi_h^h = \omega_{Ri} T_{Ri} + \omega_i^i T_i + \omega_e T_e + \omega_e^{B_e} \frac{1-\phi_e}{1-\phi_e B} T_e$$
$$+ \omega_{sol} I_{sol} + \omega_{sol}^{B_i} \frac{1-\phi_i}{1-\phi_i B} I_{sol} + \omega_{sol}^{B_e} \frac{1-\phi_e}{1-\phi_e B} I_{sol}$$
$$+ \omega_{sky}(T_{sky} - T_{se}) + \omega_{sky}^{B_e} \frac{1-\phi_e}{1-\phi_e B}(T_{sky} - T_{se})$$
$$+ \omega_{Rn} T_{Rn} + \omega_{Rn}^{B_n} \frac{1-\phi_n}{1-\phi_n B} T_{Rn} + \omega_n T_n + \omega_g^{B_g} \frac{1-\phi_g}{1-\phi_g B} T_g$$
$$+ \omega_G G_{si} + \omega_G^n G_{si}^n + \omega_G^g G_{si}^g$$
$$+ \omega_G^{e^{B_e}} \frac{1-\phi_e}{1-\phi_e B} G_{se} + \omega_G^{n^{B_n}} \frac{1-\phi_n}{1-\phi_n B} G_{sn} + \omega_G^{g^{B_g}} \frac{1-\phi_g}{1-\phi_g B} G_{sg} \quad (3.27)$$

$$
\begin{aligned}
\omega_{Ri} &= \sum_{j=1}^{w} \overset{w}{H}_{tr} + \sum_{j=1}^{w} \overset{w}{H}_{tr}{}^{n} + \sum_{j=1}^{o} \overset{o}{H}_{tr} + \sum_{j=1}^{o} \overset{o}{H}_{tr}{}^{n} + \sum_{j=1}^{o} \overset{o}{H}_{tr}{}^{g} \\
\omega_i^i &= H_v + H_v^n \\
\omega_e &= -(\sum_{j=1}^{w} \overset{w}{H}_{tr} + H_v) \qquad\qquad \omega_e^{B_e} = -\sum_{j=1}^{o} \overset{o}{H}_{tr} \\
\omega_{sol} &= -\sum_{j=1}^{w} A_{sol} \\
\omega_{sol}^{B_i} &= \sum_{j=1}^{o} \overset{o}{H}_{tr} r_i A_{sol,si} + \sum_{j=1}^{o} \overset{o}{H}_{tr}{}^{n} r_i^n A_{sol,si}^n + \sum_{j=1}^{o} \overset{o}{H}_{tr}{}^{g} r_i^g A_{sol,si}^g \\
\omega_{sol}^{B_e} &= -\sum_{j=1}^{o} \overset{o}{H}_{tr} r_e A_{sol,se} \\
\omega_{sol}^{B_n} &= -\sum_{j=1}^{o} \overset{o}{H}_{tr}{}^{n} r_n A_{sol,sn} \\
\omega_{sky} &= -\sum_{j=1}^{w} \overset{w}{H}_{tr} r_e \frac{1}{r_{sky}} \qquad\qquad \omega_{sky}^{B_e} = -\sum_{j=1}^{o} \overset{o}{H}_{tr} r_e \frac{1}{r_{sky}} \\
\omega_{Rn} &= -\sum_{j=1}^{w} \overset{w}{H}_{tr}{}^{n} \qquad\qquad \omega_{Rn}^{B_n} = -\sum_{j=1}^{o} \overset{o}{H}_{tr}{}^{n} \\
\omega_n &= -H_v^n \\
\omega_g^{B_g} &= -\sum_{j=1}^{o} \overset{o}{H}_{tr}{}^{g} \\
\omega_G &= h - \sum_{j=1}^{o} \overset{o}{H}_{tr} r_i h \qquad\qquad \omega_G^{e^{B_e}} = \sum_{j=1}^{o} \overset{o}{H}_{tr} r_e h \\
\omega_G^n &= h - \sum_{j=1}^{o} \overset{o}{H}_{tr}{}^{n} r_i^n h \qquad\qquad \omega_G^{n^{B_n}} = \sum_{j=1}^{o} \overset{o}{H}_{tr}{}^{n} r_n h \\
\omega_G^g &= h - \sum_{j=1}^{o} \overset{o}{H}_{tr}{}^{g} r_i^g h \qquad\qquad \omega_G^{g^{B_g}} = \sum_{j=1}^{o} \overset{o}{H}_{tr}{}^{g} r_g h
\end{aligned}
\tag{3.28}
$$

3.5 Solving heat balance using linear regression

The co-heating test methodology distills stationary thermal performance characteristics of the investigated building, by fitting a simple stationary heat balance model to aggregated performance data, using *linear regression*. The advantage of linear regression over plain averaging is that possible outliers can be taken into account in a more sensible way, and solar gains can be quantified separately.

In a previous section, based on co-heating test specifics, we introduced a number of simplifications to the building physical framework developed in Chapter 2. Nonetheless, Eqs. 3.27 and 3.28 remain highly complex. At the same time, we monitor only a limited number of variables, we have a building fabric that behaves quasi-static, and we filter out most of the remaining dynamics by aggregating data. Given these constraints, in this section, we investigate which of the parameters, collected in Eq. 3.28, we can estimate, using linear regression. We thus relate the building physical framework, and its reduced version developed in this chapter, to the parameters that we generally find in literature.

3.5.1 Limited data

We often only have a limited number of measurements available. As output $\mathbf{Y}_t$, we have heating power Φ_h^h, and inputs, $\mathbf{U}_t$, commonly include T_i, T_e, and I_{sol}. Given such a restricted data set, we are forced to shrink Eq. 3.27 dramatically:

$$\Phi_h^h = \omega_i T_i + \omega_e T_e + \omega_e^{B_e} \frac{1-\phi_e}{1-\phi_e B} T_e + \omega_{sol} I_{sol} + \omega_{sol}^{B_i} \frac{1-\phi_i}{1-\phi_i B} I_{sol} + \omega_{sol}^{B_e} \frac{1-\phi_e}{1-\phi_e B} I_{sol} + \mu + \epsilon \quad (3.29)$$

Equation 3.29 represents a linear regression model, with a constant term, μ, and residuals ϵ. The latter represents the difference between model output, $\hat{\Phi}_h^h$, and measured values for Φ_h^h.

By casting the terms that describe the influence on Φ_h^h, of $T_{sky} - T_{se}$, T_n, T_g and all G's, as described in Eqs. 3.27 and 3.28, in the constant term μ, we lose some of our ability to describe Φ_h^h's variability. The following paragraphs discuss the error that we thereby might introduce. But in a first paragraph, we discuss the impact of replacing $\omega_{Ri} T_{Ri} + \omega_i^i T_i$, in Eq. 3.27, with $\omega_i T_i$, in Eq. 3.29.

Weighted average temperature of room air and surrounding surfaces As introduced in Chapter 2, T_{Ri} represents a weighted average of T_i, and the fabric surface temperatures that surround it. In Eq. 3.29, we replaced $\omega_{Ri}T_{Ri} + \omega_i^i T_i$ with $\omega_i T_i$. ω_i can thus be written as:

$$\omega_i = \omega_{Ri}\frac{T_{Ri}}{T_i} + \omega_i^i \tag{3.30}$$

For well-insulated building envelopes, $T_{Ri} \approx T_i$. For poorly insulated buildings T_{Ri} and T_i might diverge more. The surface temperature plots of Test Case 1 (Section 5.2, page 101) clearly illustrate this. Now assume $T_{Ri} \neq T_i$. On one hand, T_{Ri} might be lower than T_i. Eq. 3.30 then shows that ω_i decreases. As a result, we might underestimate H. Consider, for instance, Test Case 1 (Section 5.2, page 101), which discusses a co-heating test performed on a terraced brick cavity wall house from the beginning of the 70's. At the beginning of the first test stage, its fabric only slowly heats up. Based on indoor surface temperature measurements, we calculate a T_{Ri} of 23.75 °C. Given that for this test case, $\omega_{Ri} \gg \omega_i^i$, we underestimate ω_i by about 5 %. On the other hand, T_{Ri} might be higher than T_i. Eq. 3.30 then shows that ω_i increases. As a result, we might overestimate H. Imagine, for instance, T_i is heated primarily by radiation, e.g. by a floor heating system. In the case of most dedicated heating experiments, however, we can assume that the impact remains small.

Radiative heat exchange with sky In contrast to solar irradiation, radiative heat exchange with the sky depends on the outdoor surface temperature T_{se}. To illustrate its potential impact, we estimate values that $\omega_{sky}^{B^e}$, in Eq. 3.27, might attain. As a first example, we consider the well-insulated and very compact building, discussed in Test Case 5 (Section 5.6). We can approximate $1/r_{sky}$ as $\epsilon_{lw}C_bF_TF_a(1-F_c)A$, with ϵ_{lw} the long-wave emissivity of the outdoor fabric surfaces, C_b the black-body radiation constant, 5.67 $\mathrm{W\,m^{-2}\,K^{-4}}$, F_T the temperature factor for radiation, F_a the angle factor, F_c a cloud factor, and A the opaque envelope surface area, in $\mathrm{m^2}$. Assuming $\epsilon_{lw} = 0.9$, $F_T = 0.85$, $F_a = 0.5$, $F_c = 0.4$, and $A = 45.9$ $\mathrm{m^2}$, we find that $1/r_{sky} \approx 59.7$ $\mathrm{W\,K^{-1}}$. On the other hand, r_e is a small number. Assuming $r_e = h_e^{-1}A^{-1}$, we obtain 9.5×10^{-4} $\mathrm{K\,W^{-1}}$. $\omega_{sky}^{B^e}$ then amounts to -0.4 $\mathrm{W\,K^{-1}}$. If we now assume that $T_{sky} - T_e = -21$ K, the influence of radiative heat exchange of the opaque envelope parts could amount to 7.4 W, or less than 1 % of the average heating power (940 W) delivered to T_i, during the heating experiment performed in Test Case 5. Hence, in this case we can safely ignore its influence. For poorly insulated building, radiative heat exchange between T_{se} and T_{sky} has more impact. Consider again Test Case 1 (Section 5.2). Based on the assumptions above, we estimate the influence of radiative heat exchange to rise to 8.5 % of the average heating power, delivered during

the heating experiment. As illustrated in Fig. 3.4, however, the larger part of its influence is *dampened* by the opaque envelope parts. Poorly insulated low-capacitive parts, i.e. windows, possibly have a more pronounced and direct impact. For instance, a poorly insulated glazed facade, that stretches over large surfaces, could impact Φ_h^h significantly.

Neighbouring zone air temperature The direct term, $\omega_{Rn}T_{Rn}$, in Eq. 3.27, only matters when we have low-capacitive fabric components between a building and neighbouring zones. We rarely find this in party walls between individual houses. Also ventilation heat exchange between T_i and T_n can generally be ignored.

That leaves us with the low-pass filtered term, $\omega_{Rn}^{B_n}\frac{1-\phi_n}{1-\phi_n B}T_{Rn}$. If T_n is thermostatically controlled, we can assume this term as constant, and part of μ. Moreover, if the party wall is insulated, we suggest to ignore it. Consider again Test Case 1 (Section 5.2). After insulation, the party wall has a U-value of 0.48 $\mathrm{W\,K^{-1}}$. If we assume the neighbour controls his house to 18 °C, the constant heat loss through this party wall amounts to 132.9 W. As we assume T_i and T_n to be constant, we ignore the fabric's dampening effect. Compared to a mean value for Φ_h^h of 2.5 kW, delivered to the house, the party wall heat loss for this Test Case is low, representing 5 % of the delivered heating power.

Soil mass temperature The soil mass underneath the building exhibits a slowly varying temperature T_g, depending on ground material, boundary conditions, and in some cases, ground water flows. It varies harmonically with a small amplitude and a period that far outlasts the experiment period. T_g is likely to remain unimpressed by a heating experiment, especially when the ground floor is insulated. Moreover, Φ_h^h will only see a low-pass filtered version of T_g. Hence, throughout the experiment duration, $\omega_g^{B_g}\frac{1-\phi_g}{1-\phi_g B}T_g$, in Eq. 3.27, can safely be assumed a constant. If the ground floor is insulated, we might even propose to ignore this term. Consider, for instance, Test Case 3, a detached house built according to the current insulation standards, discussed in Chapter 5, Section 5.4. The ground floor of the investigated house has a calculated U-value of 0.2 $\mathrm{W\,m^{-2}\,K^{-1}}$. With an associated surface area of 84 $\mathrm{m^2}$, the transmission heat loss coefficient through the ground floor, H_{tr}^g, amounts 16.5 $\mathrm{W\,K^{-1}}$. Compared to a total expected transmission heat loss, H_{tr}, including the influence of thermal bridges, of 207.2 $\mathrm{W\,K^{-1}}$, this amounts to 7.9 %. Taking into account that T_g is likely to attain a stable level between 10 and 15 °C, the associated heating power, Φ_{tr}^g, between T_i and T_g, varies around 205.8 W, 4.9 % of Φ_h^h's mean value during the experiment.

Latent heat With regard to the latent heat terms in Eqs. 3.27 and 3.28, we again consider Test Case 3 (Chapter 5, Section 5.4), and calculate the part of Φ_h^h that dries out the building fabric. On the basis of a stationary moisture balance, we estimate that, during the experiment, the fabric dries out at a rate, G_{si}, of approximately 9.6×10^{-5} kg s^{-1}. And given Eq. 3.28, we estimate $\omega_{G_{si}}$. The latent heat of evaporation, h, approximately equals $2.26e{+}6$ J kg^{-1}. The transmission heat loss of opaque parts is expected to lie around 119.8 W K^{-1}. The specific indoor surface resistance, r_i, in K W^{-1}, can be calculated as $h_i^{-1}A_{T,o}^{-1}$, with h_i the indoor surface heat transfer coefficient and $A_{T,o}$ the heat loss surface of opaque components. We assume $h_i = 8$ W m^{-2} K^{-1}, and measured $A_{T,o}$ to be 330.8 m^2. r_i thus approximately equals 3.8×10^{-4} K W^{-1}, a very small number. Taken together, $\omega_G G_{si}$ amounts to 206.3 W, or 5 % of Φ_h^h.

Test Case 3 has been tested just after its completion. Hence, the wet plaster and structural elements still contain a significant amount of moisture. If building encapsulated moisture should ever influence a co-heating test, Test Case 3 should uncover that. In practice, we can thus often ignore the influence of latent heat.

3.5.2 Correlations

To ensure our steady-state assumptions hold, we average measurement data over a larger time span of, for instance, 1 day. As a result, lagged values of the inputs are mutually correlated. Respective ω's, e.g. ω_e and $\omega_e^{B_e}$, collapse into a single stationary gain. This does not entail that we completely discard the effect of thermal lags; by averaging input values over current and previous time steps, we often obtain more accurate and consistent estimates for H. Eq. 3.29 thus becomes:

$$\Phi_h^h = \omega_i T_{i,avg} + \omega_e T_{e,avg} + \omega_{sol} I_{sol,avg} + \mu + \epsilon \tag{3.31}$$

Where ω_e now groups ω_e and $\omega_e^{B_e}$ (Eq. 3.28), and ω_{sol} groups ω_{sol}, $\omega_{sol}^{B_i}$ and $\omega_{sol}^{B_e}$ (Eq. 3.28). Here, it also makes sense to take into account averaged values of $T_{i,avg}$. For instance, if yesterday's solar gains caused T_i to surpass the set-point temperature $T_{i,sp}$, today's heating power might still depend on that.

In fact, (Bacher and Delff, 2013a) point out that, when T_i surpasses $T_{i,sp}$, e.g. due to excessive solar gains, $\Phi_h^h \approx 0$, our model is no longer suitable to describe the building's behaviour. However, they recognise that, as we re-sample data to a higher sampling time t_s, this effect is averaged out and the model remains valid.

During a co-heating test, T_i is thermostatically controlled. Within T_i's operation range, i.e. a narrow dead-band around a temperature set-point, T_i is approximately constant and Φ_h^h is independent of T_i (Madsen, Bacher, Bauwens, et al., 2015). We could thus incorporate term $\omega_i T_{i,avg}$, in Eq. 3.31, in μ.

$$\Phi_h^h = \omega_e T_{e,avg} + \omega_{sol} I_{sol,avg} + \mu + \epsilon \tag{3.32}$$

In a next section, however, we illustrate that, in some cases, ω_i provides a suitable estimate for H. We thus hold onto Eq. 3.31. Figure 3.6 collects typical co-heating test data, averaged over 12 h. Consider $T_{i,avg}$. Most of the scatter points are clustered around 25.1 °C. During some days, solar gains cause T_i to surpass the control dead-band. Although $T_{i,avg}$'s range is limited, it clearly is negatively correlated with Φ_h^h. In some cases, this proves significant and a negative value is estimated for ω_i. Physically, however, ω_i is positive. In other cases, linear regression analysis yields a zero intercept, i.e. $\mu = 0$, and thus a positive ω_i. But we can also lend a hand, and force ω_i to be positive, either by adding a linear constraint to Eq. 3.31, or by simply assuming that $\mu = 0$. The latter leads to Equation 3.33, with again both ω_i and ω_e as separate predictors:

$$\Phi_h^h = \omega_i T_{i,avg} + \omega_e T_{e,avg} + \omega_{sol} I_{sol,avg} + \epsilon \tag{3.33}$$

Before forcing $\mu = 0$, we need to verify that those physical phenomena, discussed in Section 3.5.1, that influence Φ_h^h significantly, are properly accounted for.

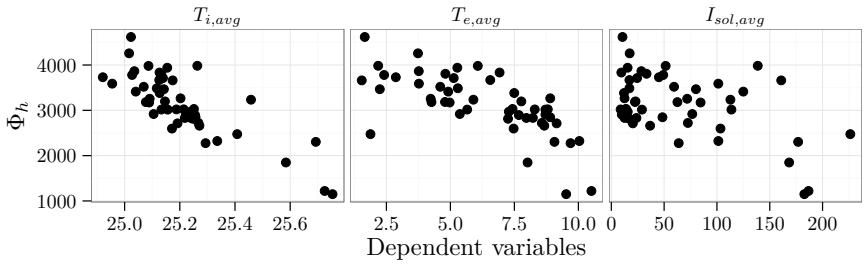

Figure 3.6: Measurement data from Test Case 2 (Section 5.3), averaged over 12h.

Solving quasi-stationary heat balance using ARX modeling As introduced on page 40, and written down in Eqs. 3.27 and 3.28, Φ_h^h is dependent on low-pass filtered versions of predictors T_i, T_e and I_{sol}. When considering smaller sampling times, we can explicitly model these low-pass filters, by fitting ARX models, as in Eq. 3.34, to more fine-grained co-heating test data.
Because we can assume smaller sampling times t_s, we retain more informative data points. Moreover, these models more easily generate white-noise residuals. As such, they support the use of commonly applied statistical hypothesis tests. Among others, we can more accurately estimate the uncertainty associated with the estimated parameters. We discuss parameter estimation on the basis of ARX models in more detail in Chapter 4, where we use it to analyse dynamic heating experiments.

$$\begin{aligned}
\omega_h(B)\Phi_{h,t} &= \omega_i(B)B^{-1}T_{i,t} + \omega_e(B)B^{-1}T_{e,t} + \omega_{sol}(B)B^{-1}I_{sol,t} + \epsilon_t \\
\omega_h(B) &= 1 - \omega_{h,1}B + \omega_{h,2}B^2 - ... - \omega_{h,k}B^k \\
\omega_i(B) &= \omega_{i,1}B + \omega_{i,2}B^2 + ... + \omega_{i,k}B^k \\
\omega_e(B) &= \omega_{e,1}B + \omega_{e,2}B^2 + ... + \omega_{e,k}B^k \\
\omega_{sol}(B) &= \omega_{sol,1}B + \omega_{sol,2}B^2 + ... + \omega_{sol,k}B^k
\end{aligned} \tag{3.34}$$

3.6 Estimating H

We aim to estimate the overall heat loss coefficient, H, that relates to the building envelope. The building envelope is bounded by red and blue lines in Figure 3.7, and represents the building fabric part that separates T_i from the external environment, and, if relevant, the soil mass, or an equivalent zone, underneath. If possible, we disentangle it into a transmission heat loss, H_{tr}, and a ventilation heat loss, H_v. Eq. 3.35 collects the different heat loss parts that are grouped in H.

$$H = H_{tr} + H_v = \sum_{j=1}^{w} \overset{w}{H}_{tr} + \sum_{j=1}^{o} \overset{o}{H}_{tr} + \sum_{j=1}^{o} \overset{o}{H}_{tr}^{\ g} + H_v \tag{3.35}$$

As evidenced by Eq. 3.28, we find these parts embedded in ω_{Ri}, ω_i^i, and ω_e. As discussed in Section 3.5.1, ω_{Ri} and ω_i^i generally collapse into ω_i. We can estimate ω_i and ω_e, by fitting the linear regression model in Eq. 3.31 to co-heating test data.

Linear regression analysis only allows to uncover as many parameters as there are independent variables, for instance T_e, that significantly influence the

dependent variable, in this case Φ_h^h. From Eqs. 3.28 and 3.31, we can thus conclude that, to disaggregate H into H_{tr} and H_v, we need additional tests. As natural ventilation heat exchanges with neighbouring zones, H_v^n, are often limited, we can mostly ignore it. Knowledge of H_v, e.g. from a pressurisation test result, then allows to separate H_{tr} and H_v.

We can also conclude that, on the basis of a co-heating test, we are unable to distinguish transmission heat losses through transparent parts from transmission heat losses through opaque parts, even if we provide additional measurements of window surface areas.

3.6.1 Test case scenarios

To sensibly estimate H on the basis of ω_i and ω_e, we consider four scenarios. They are illustrated schematically in Figure 3.7. As each of them calls for a different strategy, we go through them one by one.

Scenario 1: Floor on ground and neighbouring zones We begin with the most complicated scenario. To understand what happens to the estimated linear regression coefficients, we reinsert T_n as independent variable in Eq. 3.31, whilst $\omega_g T_g$ remains in μ:

$$\Phi_h^h = \omega_i T_{i,avg} + \omega_e T_{e,avg} + \omega_n T_{n,avg} + \omega_{sol} I_{sol,avg} + \mu + \epsilon \qquad (3.36)$$

Φ_h^h is unlikely to be significantly correlated with T_n. But in case it is, we can estimate ω_n. Applying Eq. 3.28, H then can be estimated as $\omega_i + \omega_n$. At the same time, however, T_n might be correlated with T_e. As a result, we cannot accurately estimate ω_n. Moreover, ω_e is now influenced by heat losses between T_i and T_n. In the more likely case that Φ_h^h is not correlated with T_n, $\omega_n T_n$ resides in μ, and Eq. 3.36 again simplifies to Eq. 3.31. Nonetheless, ω_i still embeds the influence of transmission and ventilation heat loss towards T_n. Meanwhile, ω_e excludes heat losses towards T_g. Hence, neither ω_i, nor ω_e represent reasonable estimates for H.

To correctly estimate H, in case we cannot accurately estimate ω_n, we need to measure or estimate the transmission heat loss towards the neighbouring zone, Φ_{tr}^n, and assume $\Phi_h^h - \Phi_{tr}^n$ as model output:

$$\Phi_h^h - \Phi_{tr}^n = \omega_i T_{i,avg} + \omega_e T_{e,avg} + \omega_{sol} I_{sol,avg} + \mu + \epsilon \qquad (3.37)$$

ω_i, and, in case T_n is correlated with T_e, also ω_e, are thus stripped of terms that relate to heat losses between T_i and T_n.

H can now be estimated as ω_i. To do so, we neglect μ, in Eq. 3.37. Hence, as elaborated in Section 3.5.1, this strategy can only be applied in case we can

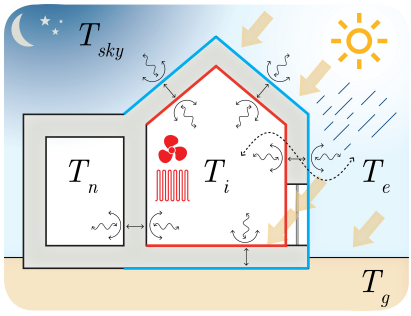

(a) Scenario 1: Floor on ground and neighbouring zones

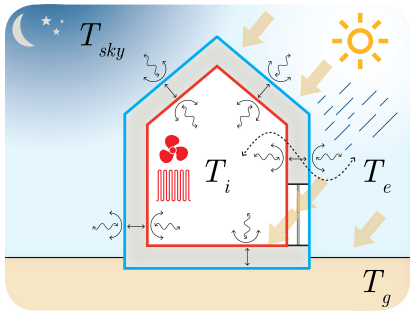

(b) Scenario 2: Floor on ground

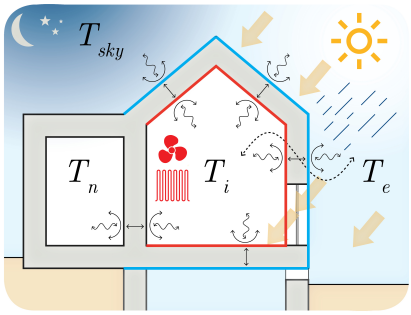

(c) Scenario 3: Neighbouring zones

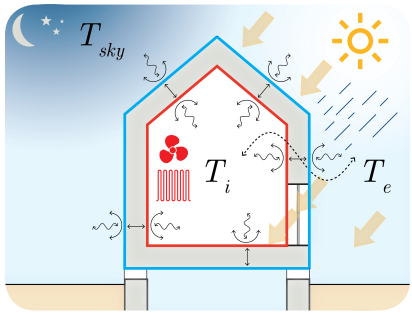

(d) Scenario 4: Neither floor on ground, nor neighbouring zones

Figure 3.7: Four test case scenarios

ignore the influence of radiative heat exchange with the sky, ground floor heat losses, and latent heat. Alternatively, H can be estimated departing from ω_e, as $-\omega_e + \frac{\Phi^g_{tr}}{\Delta T_g}$, although this demands many additional measurements. If T_n is correlated with T_e, we assume Eq. 3.37. If not, we can assume Eq. 3.31.

Scenario 2: Floor on ground Here, Φ^h_h remains model output, and H can be estimated as ω_i, or alternatively, as $-\omega_e + \frac{\Phi^g_{tr}}{\Delta T_g}$. We apply this Scenario in Test Case 2 (Section 5.3) and Test Case 3 (Section 5.4).

Scenario 3: Neighbouring zones Assuming T_n and T_e are not correlated, this a straightforward scenario: H can be estimated as $-\omega_e$. On the other hand, if T_n and T_e are correlated, ω_e is corrupted. Test Case 1 (Section 5.2) exemplifies this. To resolve it, we need to additionally measure Φ^n_{tr}, and assume $\Phi^h_h - \Phi^n_{tr}$ as output of the linear regression model. Since we do not have ground

floor heat losses, ω_i and ω_e then represent similar physical phenomena. If we can safely ignore μ, and thus estimate ω_i, we can either estimate H as ω_i, or as a minimum variance weighting of ω_i and ω_e, as elaborated in Appendix A. In any case, H is likely to lean more closely to ω_i, as ω_e is generally associated with a larger uncertainty. Additionally measuring Φ_{tr}^n might thus also prove beneficial, in case T_n and T_e are not correlated.

Scenario 4: Neither floor on ground, nor neighbouring zones Again, we distinguish two cases here. If we are unable to estimate ω_i, we calculate H as $-\omega_e$. On the other hand, if ω_i proves to be significant and positive, ω_i and $-\omega_e$ are equally valid estimates for H, and by following the procedure elaborated in Appendix A, we combine them into one minimum variance estimate for H.

In case we apply **ARX modeling**, we can proceed in a very similar way. We now estimate H as a combination of the stationary gains, with regard to T_i, $\frac{\omega_i(1)}{\omega_h(1)}$, and T_e, $-\frac{\omega_e(1)}{\omega_h(1)}$. Again, above guidelines indicate, for each of the four Scenarios, how to combine them appropriately.

3.6.2 Link with co-heating test literature

In literature, often ΔT, or $T_i - T_e$, is considered as an independent variable, instead of T_i and T_e separately. This essentially implies that $\omega_i = \omega_e$. As shown in the previous Section, however, in many practical cases, coefficients ω_i and ω_e accommodate different physical phenomena. Only in Scenario 3, if Φ_{tr}^n is measured and $\mu = 0$, and in Scenario 4, can we rightfully assume ΔT as a predictor. Rewriting Eq. 3.31 accordingly yields:

$$\Phi_h^h = \omega_{ie}\Delta T_{avg} + \omega_{sol} I_{sol,avg} + \mu + \epsilon \tag{3.38}$$

With $\omega_{ie} = \sum_{j=1}^{w} \overset{w}{H}_{tr} + \sum_{j=1}^{o} \overset{o}{H}_{tr} + H_v$.

The constraint that, in these Scenarios, $\omega_i = \omega_e$, can actually be formulated as a linear constraint, added to the linear regression equation with T_i and T_e as separate predictors. This is illustrated in Appendix A. We thus advise to retain Eq. 3.31 as a basis, and evaluate each test case against the four scenarios discussed in Section 3.6, to sensibly estimate H from ω_i and ω_e.

3.6.3 Visualising co-heating test analysis

In this section, we discuss possible ways to visualise co-heating test analyses. Adequate visuals help us compare and evaluate, at a glance, different test cases and different analyses. First, we visualise analyses based on Eq. 3.38, with ΔT and I_{sol} as independent variables. Second, we visualise analyses based on Eq. 3.31, where we have both T_i and T_e, and again I_{sol} as independent variables.

ΔT as independent variable As discussed in Section 3.2, (Palmiter et al., 1979) and (Siviour, 1981) proposed to mathematically transform the co-heating test heat balance equation in Eq. 3.38, such that $\Phi_h^h/\Delta T$ serves as dependent variable, and $I_{sol}/\Delta T$ serves as independent variable. We thus only need to perform a single linear regression, and we can easily visualise it on a two-dimensional plot. But we need to be cautious. The estimated linear regression coefficients become unstable when ΔT hovers around 0, as $I_{sol}/\Delta T$ and $\Phi_h^h/\Delta T$ then take on very large negative and positive values. Therefore, we advise to apply multiple linear regression.

Researchers regularly avoid considering both ΔT and I_{sol} as independent variables, mainly because the multiple linear regression needed to solve Eq. 3.38 does not allow for a very intuitive visualisation, as illustrated in Figure 3.8a. To counter this, we propose to look at the three-dimensional regression *surface* as if we are the $(\Phi_h^h, \Delta T)$ plane. Figure 3.8b illustrates this. The thick line with positive slope depicts where the regression surface intersects with the $(\Phi_h^h, \Delta T)$ plane. Its slope reflects the estimate for $\omega_{ie} = H$. From this line, a flag hangs downwards, bordered by dashed contour lines. Its bottom edge also has slope H and corresponds to a value for I_{sol}, of 100 $\mathrm{W\,m^{-2}}$. At the same time, the width of the flag illustrates the spread of measured values for ΔT. By measuring the distance between the thick regression line and the dashed bottom edge of this flag, we can visually determine the solar aperture coefficient, A_{sol}, in $\mathrm{m^2}$, as the traversed heating power, $\Delta\Phi_h^h$, in W, divided by 100 $\mathrm{W\,m^{-2}}$. Evidently, in case I_{sol} proves not to be significant, the same graph can be used to visualise single linear regression. It thus also visualises whether single or multiple linear regression is applied. Different co-heating test results can be compared, regardless of the independent variables that prove significant.

T_i and T_e as independent variables Figure 3.9 adheres to the concepts that we introduced in the previous Section. But instead of ΔT, we now have T_i and T_e as independent variables (Eq. 3.33). Hence, to retain a similar two-dimensional visualisation as in Figure 3.8b, we plot two graphs side-by-side. On one, we plot $\Phi_h^h - \omega_i T_i$ as a function of $-T_e$, and on the other, we plot $\Phi_h^h - \omega_e T_e$ as a function of T_i. Figure 3.9 again illustrates that, to obtain a positive, and thus physically relevant ω_i, the corresponding linear regression line needs to pass through the origin ($\mu = 0$).

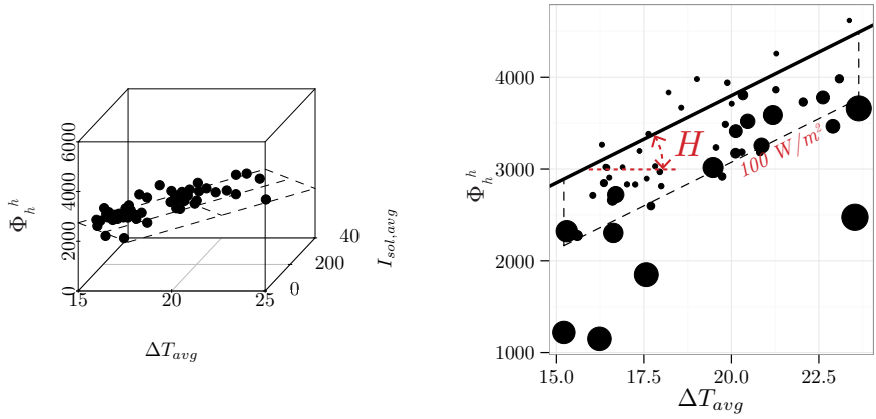

(a) (b)

Figure 3.8: Three-dimensional (a) and alternative two-dimensional (b) representation of multiple linear regression analysis of co-heating measurement data, with ΔT as independent variable (Eq. 3.33).

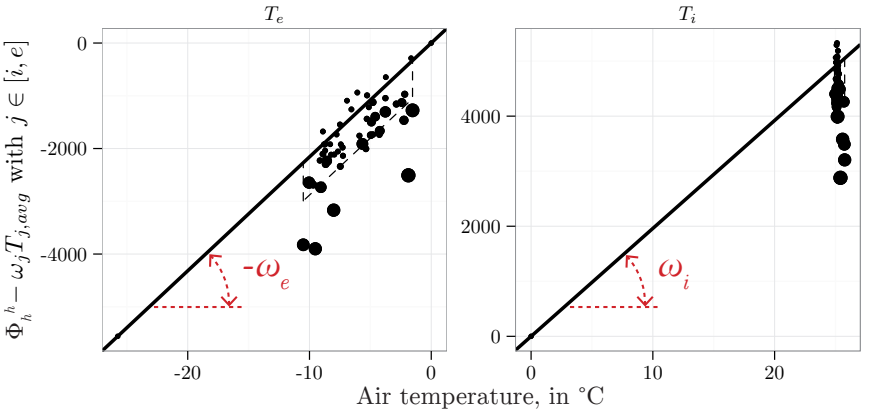

Figure 3.9: Linear regression analysis of co-heating test data plotted in Figure 3.6, assuming Eq. 3.33. On the y-axis, we plot the heating power Φ_h^h, corrected with respective $\omega_j T_{j,avg}$'s.

3.7 Conclusions

This chapter focused on the quasi-stationary co-heating test, today widely recognised as a viable procedure to characterise thermal performance of buildings. Starting from the building physical framework, introduced in Chapter 2, we derived simplified quasi-stationary heat balance models, that take into account the specific conditions that are attained during a properly performed co-heating test.

The link between the extended models of Chapter 2, and the simplified models that we derived here, reveals that, in order to organise a proper co-heating test, the electric heaters should have limited heat capacity, and exchange heat with T_i primarily by convection. A proper co-heating test should also minimise the heat that is charged or discharged by the fabric, during the period that is considered for analysis.

This chapter uncovered that, although the co-heating test seems very straightforward, to obtain reliable estimates for H, it requires insight into the investigated building, the performed heating experiment, and the combined action of a range of physical phenomena. Moreover, the potential impact of physical phenomena that are not accounted for explicitly, need to be verified for each test case. We also confirmed that ventilation heat loss cannot be discerned on the basis of a co-heating test alone.

This chapter considered quasi-stationary heat balance models, with Φ_h^h as output. Conversely, the next chapter will consider dynamic heat balance models, with T_i as the sole output. Instead of thermostatically controlling T_i, we throw a dynamic heating power signal at the building, and track how T_i responds.

Chapter 4

Dynamic tests

Dynamic tests combine dynamic heating experiments with well-known parameter estimation techniques. Whereas in Chapter 3, we assumed that quasi-stationary conditions are obtained during the heating experiments, we now model the building's dynamic behaviour explicitly, and assume data that is averaged over smaller sampling times. Dynamic tests thus hold the promise of yielding more accurate and fine-grained results, on the basis of shorter measurement campaigns.

When we refer to dynamic experiments in the framework of this work, we limit ourselves to heating experiments where the imposed heating power, Φ_h^h, follows a sequence that switches between two discrete levels: a high level, with heaters switched *on*, and a low level, with heaters switched *off*. Power consumed by continuously running ventilators and sensor equipment is assumed to be exhausted to the indoor air as heat. The indoor air temperature, T_i, now acts as output to our models. It responds to outdoor weather conditions, but most actively to the imposed heating power. The heating power sequence concatenates several step inputs, and has an auto-correlation that approximates that of white noise (Godfrey, 1980). Given sufficient amplitude, it *persistently excites* the building. Moreover, it is uncorrelated with outdoor weather conditions. Hence, we can unravel how weather conditions and heating power individually affect T_i.

We begin with a literature review on building performance characterisation on the basis of dynamic heating experiments. We then look into parameter estimation techniques that assume lumped state space models and transfer function models. In comparison with the extended model defined in Chapter 2, these models are simplified, and have a reduced order. By departing from the extended model, however, we uncover physical phenomena that are embedded in the simplified model parameters.

The periods in between heating power switches are commonly determined by a Pseudo-Random Binary Sequence (PRBS), or a Randomly Ordered Logarithmic Binary Sequence (ROLBS).

A PRBS is uncorrelated with typical weather conditions and has an auto-correlation that approximates that of white noise (Godfrey, 1980; Madsen and Holst, 1995). Madsen and Schultz (1993) suggest to relate the shortest time period, t_{PRBS}, at which it is maintained at one power level, to the building's smallest expected time constant. Moreover, they suggest to select a signal order, k, such that $(2^k-1)t_{PRBS}$ closely relates to the largest time constant of the building. The resulting signal spends time periods between t_{PRBS} and kt_{PRBS} at one level.

A ROLBS signal also consists of several step inputs. A ROLBS signal, however, does not focus on particular time constants. Instead, it aims to cover the whole frequency spectrum with equal weight (Baker and H. van Dijk, 2008). This makes it universally applicable to any building, even when no prior physical knowledge about its dynamics are available.

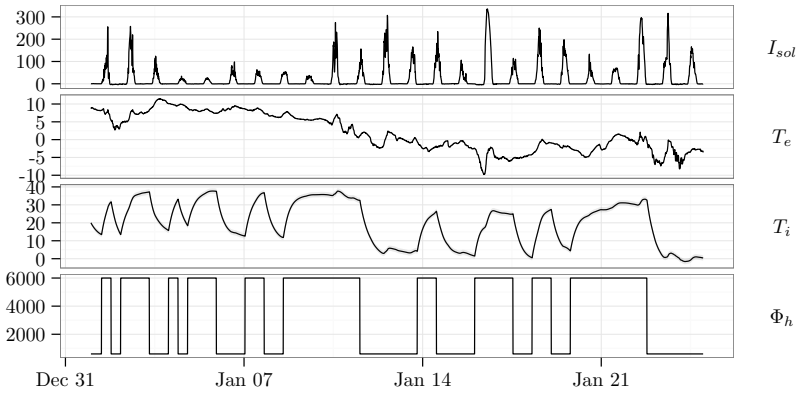

Figure 4.1: Time series plot of a typical heating experiment. Weather data, T_e, in °C, and I_{sol}, in $\mathrm{W\,m^{-2}}$, are collected from a weather station, situated at the KU Leuven test site. The heating power signal strings together two consecutive PRBSs: a first part, until January 6, 7am, with $\lambda = 3$h and order $k = 3$, designed to excite the building around time constants of 3h and 21h; and a second part, with $\lambda = 6$h and order $k = 4$, to excite it around time constants of 6h and 90h. The indoor air temperature, T_i, is *simulated*, using CTSM-R (CTSM-R, 2015) and assuming the first-order model presented in Section 4.2.3.

4.1 Literature review

In this section, a brief overview is given of the body of research work that advanced the thermal performance characterisation of buildings, on the basis of dynamic heating experiments.

Based on limited data collected during heating experiments, the dynamic thermal models that we can identify are of limited complexity. Nonetheless, Sonderegger (1978) shows that such simplified models, within a limited frequency spectrum, are able to accurately describe the actual building response. He was one of the first to exploit the analogy between the actual building, as a distributed system, and simplified thermal models, which he refers to as *analogs*. They are straightforward Resistor-Capacitor (RC) models, and consist of a limited number of *equivalent resistors and capacitors*. Their limited complexity allows them to be fitted to measurement data with relative computational ease.

Fraisse et al. (2002) compare lumped state space model matrices, that describe simplified thermal models, with the exact solution of the diffusion equation, that describes how temperatures of a continuous medium change over time, and as a function of their spatial distribution. Using frequency analysis, they show that such models are valid when internal inputs exhibit periods longer than 3 hours. Naveros and Ghiaus (2015) recognise that the frequency spectrum within which reduced-order models need to be valid, depends on a number of factors. First, the nature of the system imposes an upper limit to the frequency spectrum of the inputs that potentially makes the output vary. As also discussed in (Sonderegger, 1978) and (Fraisse et al., 2002), the building fabric tends to attenuate, i.e. damp and phase-shift temperature variations. Amplitude-damping increases with frequency of the imposed signal. Above a certain frequency, the amplitude reduces such that it can no longer be observed. Second, the duration of a measurement campaign sets a lower limit to the system's frequency spectrum that the data can reveal. Third, the sampling time sets its upper limit.

A. Nielsen and B. Nielsen (1983) set out to model a low-energy test house as an RC-circuit. To characterise its effective heat capacity, they performed dynamic heating experiments, using electric heaters that obeyed a PRBS. They fit a first-order state space model to the collected data, but are unable to estimate a second-order one. The first-order model parameters slightly underestimate the actual building envelope's thermal resistance. They suggest that an improved model should consider two time constants. Madsen and Holst (1995) confirm that the proposed first-order model insufficiently describes the building's short-term dynamics.

In 1988, Rabl (1988) reviewed a large collection of commonly applied parameter estimation methods. He recognises that there is no limit to the complexity of a thermal RC-network, when used to simulate buildings. On the other hand, for inverse problems, where we estimate their parameters by fitting them to data, the RC-network should be simple, and the number of adjustable parameters small. Rabl (1988), and later also Baker and H. van Dijk (2008), highlight the danger of over-fitting, where errors induced by several wrong parameters might compensate each other. Even though a model describes the building response very accurately, it is not guaranteed to have parameters that are physically correct. Arguing for input-output polynomial models as external models describing building behaviour, Rabl (1988) states: "In view of the narrow range of temperatures involved, one can suppose a linear approximation for all heat transfer equations." Moreover, models should be causal, in that the behaviour of the building at the current time step is the result of the output and inputs at previous time steps.

As a result of the PASSYS collaboration, several software packages were developed to analyse dynamic heating experiments (Baker and H. van Dijk, 2008). MRQT, which formed the basis for LORD (Gutschker, 2008), implements a deterministic output-error (OE) method, thereby neglecting both model and observation noise. Also Kramer and van Schijndel (2012) fit state space models to actual measurement data, by minimising the sum of squared simulation errors. Although computing times are limited, the OE method likely generates auto-correlated residuals. Moreover, Kristensen et al. (2004) show that a missing noise description might lead to biased estimates for dynamic models. Later versions of LORD, and also CTLSM, implement a prediction-error (PE) method. Hence, they account for both model and observation errors. CTLSM evolved into CTSM, and later into the R-package CTSM-R (CTSM-R, 2015). CTSM-R allows to analyse both non-linear and non-stationary systems. Melgaard (1994) describes CTSM as a *"tool for maximum likelihood estimation of multivariate stochastic differential equations with a linear or non-linear state space formulation"*. Given discrete-time measurements of building performance, it estimates parameters and states using a *maximum likelihood method*, calculating the likelihood function using a Kalman filter (Madsen and Holst, 1995; Kristensen et al., 2004).

Melgaard and Madsen (1992) find that CTSM, with a 1-step ahead prediction, yields reasonable parameter and uncertainty estimates. When the prediction horizon is increased , one likely obtains auto-correlated residuals. Nonetheless, parameter estimates might remain consistent. Melgaard (1994) compares a *k-step prediction criterion* with a low-pass filter that favours the building's low frequency dynamics. When residuals are auto-correlated, however, a number of model validation tests are no longer valid and uncertainties are underestimated.

Melgaard (1994) suggests to overcome this obstacle by applying a suitable anti-aliasing filter. After that, we can again apply a one-step prediction criterion, and thereby avoid auto-correlated residuals.

To estimate the U-value of an attic ceiling, Norlen (1993) uses black-box ARX models to relate the indoor surface heat flux to indoor and outdoor surface temperatures. He combines the stationary gains related to both inputs, to obtain one minimum variance estimate for U, in $\mathrm{W\,m^{-2}\,K^{-1}}$, by adding the constraint that, in stationary conditions, they are indeed equal. This procedure is also elaborated in Appendix A. Norlen (1993) thus obtains consistent U-value estimates. Estimates for the related time constants, however, turn out to be more challenging.

Madsen and Schultz (1993) describe the analysis of heating experiments carried out in the Danish PASSYS test cells. The heat input is controlled by a PRBS, designed to excite the test cell around its expected time constants: a short time constant, that relates to its indoor air heat capacity, and a long time constant, that relates to its capacitive *fabric*. They suggest principal component analysis, or PCA, to build a single representative air temperature from several measurements, performed at different positions. The first principal component was found to weigh each sensor more or less equally, indicating that all sensors were functioning and positioned appropriately. The second principal component reveals that temperature stratification increases when heating power is switched on. Finally, the third principal component reflects transient behaviour of the temperatures just after the heating system is turned on and off. The authors use CTLSM to fit a second-order linear stochastic state space model to the measurement data. The model describes the indoor air temperature very well, except in the periods just after the heating power is switched on or off. An effect that the third principal component already signaled. To improve this, the authors suggest to explicitly model the heat capacity of the heaters.

Madsen and Holst (1995) use CTSM to analyse the heating experiment that A. Nielsen and B. Nielsen (1983) already considered. To facilitate the direct interpretation of physical parameters, they advise to keep the parametrisation in continuous-time from the very onset. A second-order model is described, with a *capacitive* medium, T_m, and a *lighter* interior state, T_i, that comprises both room air and inner parts of the walls.

Jimenez and Madsen (2008) and Jimenez, Madsen, and Andersen (2008) investigate two components: a light-weight opaque component, with plywood at either side of a thick insulation layer; and a double-glazed window. Heating experiments follow the PASLINK test procedure. Linear and non-linear continuous-time stochastic state space models and transfer function models are

assumed. The authors conclude that non-linear models are most appropriate. Jimenez, Madsen, and Andersen (2008) focus on multiple output ARMAX-models. They report very low identification errors for the overall heat loss coefficient, H, and the solar aperture, A_{sol}.

Both Delff et al. (2013) and Bacher and Delff (2013b) apply continuous-time stochastic state space models. They assume varying levels of system noise, to avoid that an inadequate modelling of one physical phenomenon, for instance solar radiation, cripples estimates of particular interest, in this case H.

Rabl (1988) raises some issues that might disturb the physical interpretation of the estimated parameters. First, ventilation heat loss, H_v, is directly dependent on the air change rate; the rate at which the building's air volume is replaced with fresh air. This rate might vary considerably, also during a heating experiment. Second, solar gain modelling poses a major challenge. Often, solar aperture values are defined with regard to the global solar radiation measured on a horizontal surface. This topic is also addressed in this work, in Sections 2.2.2, 3.4.2 and 4.2.3. Third, the building fabric's actual heat capacity is very challenging to determine, and demands specifically designed heating experiments. Instead, we generally estimate an *effective heat capacity*, which Rabl (1988) describes as the quantity of heat that is charged under the applied excitation. Slower excitation causes it to increase. And faster excitation causes it to decrease. After all, a periodic signal is damped more as its frequency rises.

D. van Dijk et al. (1992) mention that, to identify steady-state characteristics, T_i needs to vary with a period that is much longer than the largest time constant of the investigated system. Moreover, its amplitude should greatly surpass the measurement errors associated with inputs and the amplitude of model residuals. To ensure parameters are easily disentangled, correlation between different inputs, e.g. T_e and I_{sol}, needs to be minimal.

As we can think of a whole range of candidate simplified thermal models to approximate the actual building response, we need a strategy to uncover models that are most suited. Bacher and Madsen (2011) suggest a *forward selection strategy*, to select the most suitable model out of a library of candidate grey-box models. The parameters of these continuous-time lumped state space models are fitted to discrete-time measurement data using a *maximum likelihood method*. The modeller starts with the most simple model and builds his way up to increasingly complex models. At each stage, a *likelihood ratio test* is used to compare the current model with an extended version. This test takes into account the respective model complexities, i.e. degrees of freedom, and how likely they are to observe the data. The procedure stops when none of the candidate model extensions yield a better fit.

Bacher and Delff (2013b) suggest a model selection procedure to select suitable ARX models. All polynomials in the back-shift operator are assumed to be of equal order; this order is increased until white noise residuals are obtained and higher model orders do not significantly improve their white noise characteristics. In Bacher and Delff (2013a), the authors suggest an additional criterion: the time constants, related to the auto-regressive part of the model, need to be well-separated. If this is not the case, the authors propose either to stop at the last model that did have well-separated time constants, or to increase sampling time, such that smaller model orders suffice to remove significant residual auto-correlation. Nonetheless, a shorter sample period remains beneficial, as we retain more informative data points. Finally, Madsen, Bacher, Bauwens, et al. (2015) advise to retain the highest-order model for which all auto-regressive coefficients are significant. Bacher and Delff (2013b) acknowledge that increasing the order of all polynomials simultaneously easily leads to over-fitting. Although this has a limited influence on the mean estimates of stationary performance indicators, the associated uncertainty might be suboptimal. They suggest to counter this by varying the order of the different polynomials.

4.2 Modelling building as reduced-order linear time-invariant (LTI) system

In this Section, we depart from the infinite dimensional distributed model, that we defined in Section 2.2, but we reduce its order, to fit the data's reach. As put forward by Sonderegger (1978) and, more recently Naveros and Ghiaus (2015), we can appropriately describe a buildings thermal behaviour with models that have only a limited number of thermal nodes. Such reduced-order models should consistently reflect the actual building's behaviour, in the frequency spectrum that is relevant given the nature of the building, weather conditions, measurement campaign duration and sampling time.

We start with continuous-time state space models. They bear closest resemblance to the distributed model. We then add a layer of stochastics, such that we appropriately deal with data that are laden with noise, and models that simplify the actual system. We show how continuous-time stochastic state space models relate to their discrete-time equivalents. We discuss the typical trade-off between grey-box and black-box models, after which we go from grey-box state space models to black-box transfer function models. ARX models are defined as a special case of latter. Based on a first-order model, we illustrate how they all relate, and which physical phenomena are embedded in their parameters. Also a second-order model is developed, to support the final section of this chapter, where we discuss how to estimate H, from the estimated model parameters.

In what follows, we adopt the notation $\mathbf{T}(t)$ for continuous-time models. For discrete-time models, we write $\mathbf{T}_t$. In both case, t denotes time.

4.2.1 Continuous-time stochastic state space model

As described in Chapter 2, Section 2.2, writing a heat balance towards the indoor air of a single zone building leads us to define a *distributed continuous-time state space model*: an infinite dimensional system of differential equations (DEs), that describes the system's temperature states and the physical phenomena that take place between them. To simplify matters and support further discussion, we pour this system of DEs in a convenient matrix notation:

$$d\mathbf{T}(t) = \mathbf{A_c}\mathbf{T}(t)dt + \mathbf{B_c}\mathbf{U}(t)dt \tag{4.1}$$

where $\mathbf{T}$ represents the temperature state vector, and $\mathbf{U}$ the input vector. Matrix $\mathbf{A_c}$ describes our physical system's dynamic behaviour, i.e. how its states interact, and $\mathbf{B_c}$ describes how inputs affect them.

Given initial values for the state vector, $\mathbf{T}(0)$, we can in principle solve Eq. 4.1 analytically to describe the temperature states $\mathbf{T}(t)$ as a deterministic function of time (Reynders, 2012):

$$\mathbf{T}(t) = e^{\mathbf{A_c}t}\mathbf{T}(0) + \int_0^t e^{\mathbf{A_c}(t-\tau)}\mathbf{B_c}\mathbf{U}(\tau)d\tau \tag{4.2}$$

In practice, however, we approximate the infinitesimal system of differential equations in Eq. 4.1, using only a *finite set of differential equations*. As such, we obtain a reduced order model, or *lumped state space model*. Essentially, we lump the distributed states into a finite set of states (Melgaard, 1994).

We now consider observations of the investigated building's behaviour, $\mathbf{Y}_t$. They can be written as a linear combination of states $\mathbf{T}$, and inputs $\mathbf{U}$:

$$\mathbf{Y}_t = \mathbf{C}\mathbf{T}_t + \mathbf{D}\mathbf{U}_t + \mathbf{e}_t \tag{4.3}$$

with $\mathbf{Y}_t$ a measurement vector, and $\mathbf{e}_t$ the observation noise, which we assume a Gaussian white-noise process, i.e. a sequence of serially uncorrelated random variables with zero mean and finite variance; $\mathbf{C}$ and $\mathbf{D}$ describe how the system states and the inputs affect measured quantities.

Contrary to what Eq. 4.2 seems to promise, we are unable to *exactly* predict future values of our temperature states. Our model might inadequately describe

some of the system's dynamics or ignore inputs that are of significant influence. Moreover, from Eq. 4.3, we already know that inputs are noisy. To deal with these uncertainties, we can add, to Eq. 4.1, a *diffusion term* $\mathbf{W}(t)$. We thus obtain following system of Stochastic Differential Equations, or SDEs:

$$d\mathbf{T}(t) = \mathbf{A_c}\mathbf{T}(t)dt + \mathbf{B_c}\mathbf{U}(t)dt + \mathbf{W}(t) \tag{4.4}$$

with $\mathbf{W}(t)$ continuous-time stochastic processes with independent and normal distributed increments, commonly referred to as Wiener processes.

The measurement equation remains unaltered. Together, Equations 4.4 and 4.3 represent a *continuous-time stochastic linear state space model.*

4.2.1.1 Parameter estimation

Kristensen et al. (2004) propose to estimate the unknown parameters and initial state values by finding the parameter and initial state set θ that maximises the likelihood function, $L(\theta; \mathbf{Y}_t \mid \theta)$, of a given sequence of measurements. The maximum likelihood (ML) estimates of the parameters and initial states can then be determined by solving the non-linear optimisation problem:

$$\hat{\theta} = \underset{\theta}{argmin}\{-ln\big(L(\theta; \mathbf{Y}_t \mid \theta)\big)\} \tag{4.5}$$

In case of LTI models, the initial probability density, $p(\mathbf{Y}_0 \mid \theta)$, and all subsequent conditional densities needed to determine the likelihood function can be calculated using Kalman filters. Kristensen et al. (2004) provide a detailed view into the underlying mathematics.

4.2.1.2 Pros and cons

The lumped state space models are 'born' in continuous-time, and their parameters relate to physics directly (Madsen and Schultz, 1993). Aside from stationary building envelope characteristics, we can estimate time constants and effective heat capacities associated with the model states.

The continuous-time stochastic model allows to describe explicitly how measurement and model errors enter into the model (Madsen and Holst, 1995). One-step ahead predictions allow the state space model to readily adapt to observations and yield residuals that are not auto-correlated (Madsen, Bacher, and Delff, 2010). Statistical tests thus remain valid and uncertainties are correctly estimated. Maximum likelihood estimation also allows to estimate non-linear and non-stationary model parameters. It might, however, be excessive for the purpose at hand: depending on data length, sampling time and model complexity, solving Eq. 4.5 iteratively takes time.

Trade-off between data and prior knowledge Parameter estimation techniques estimate reduced-order model parameters based on noisy observations. We need to choose whether we merely rely on data or whether we assume prior knowledge about the system that generates it. Figure 4.2 illustrates the typical trade-off that is made when analysing building performance data.

On one end of the spectrum, we have black-box models that completely discard prior knowledge, and solely aim to describe an output as a function of certain inputs. On the other end, we have white-box models that exploit prior information up to the hilt. No measurement data is involved. Instead, they consider detailed building design specifications to simulate the building's behaviour for certain weather data and building usage. In between both extremes, we have grey-box models (Melgaard, 1994). They are simplified physical models, that embed prior knowledge into a stochastic framework. Known physical characteristics of the investigated building are thus combined with information from performance data.

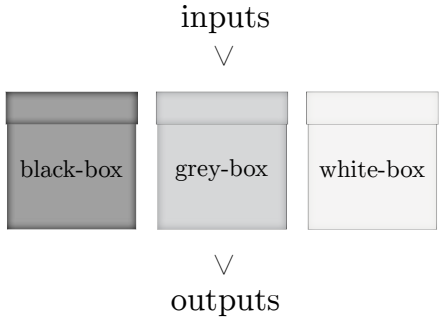

Figure 4.2: Different approaches towards identifying models that relate available inputs and outputs. Depending on the degree we count on data or prior knowledge of the identified system, we distinguish black-box, grey-box and white-box models.

4.2.2 Auto-Regressive models with eXogenous inputs (ARX)

In Section 4.2.1, we introduced a continuous-time stochastic state space model. To obtain the corresponding *discrete-time* one, we need to integrate Eq. 4.4 over the sample interval $[t, t + \Delta t]$ (Madsen and Holst, 1995). If we assume a

constant sampling time, i.e. Δt is constant, we obtain:

$$\mathbf{T}_{t+1} = \mathbf{A}\mathbf{T}_t + \mathbf{B}\mathbf{U}_t + \mathbf{W}_t \tag{4.6}$$

Calculations in the continuous-time domain equally apply to the discrete-time domain, when data are sampled properly, i.e. appropriate sampling times and anti-aliasing filters are applied to minimise loss of information (Melgaard, 1994).

Applying the z-transform on both Eqs. 4.3 and 4.6, yields:

$$z\mathbf{T}(z) = \mathbf{A}\mathbf{T}(z) + \mathbf{B}\mathbf{U}(z) + \mathbf{v}(z) \tag{4.7}$$

$$\mathbf{Y}(z) = \mathbf{C}\mathbf{T}(z) + \mathbf{D}\mathbf{U}(z) + \mathbf{e}(z) \tag{4.8}$$

We now eliminate the state vector $\mathbf{T}(z)$ from Eqs. 4.7 and 4.8. At the same time, we assume $\{\mathbf{Y_t}\}$ to be a stationary process and group noise terms $\mathbf{v}(z)$ and $\mathbf{e}(z)$ (Madsen and Holst, 1995). As such, a *discrete-time transfer function model* is obtained:

$$\begin{aligned}\mathbf{Y}(z) &= \mathbf{C}(z\mathbf{I} - \mathbf{A})^{-1}\mathbf{B}\mathbf{U}(z) + \big(\mathbf{C}(z\mathbf{I} - \mathbf{A})^{-1}\mathbf{K} + \mathbf{I}\big)\epsilon(z) \\ \mathbf{Y}(z) &= \mathbf{H}_1(z)\mathbf{U}(z) + \mathbf{H}_2(z)\epsilon(z)\end{aligned} \tag{4.9}$$

With $\mathbf{H}_1(z)$ and $\mathbf{H}_2(z)$ rational polynomials in z. The output $\mathbf{Y}(z)$ is now written as the sum of one *transfer function component*, $\mathbf{H}_1(z)$, that acts on the inputs $\mathbf{U}(z)$, and another one, $\mathbf{H}_2(z)$, that describes how disturbances $\epsilon(z)$ influence it.

Above relationship between grey-box and black-box models supports the use of the latter to characterise thermal performance of buildings.

We now rewrite above transfer function model to explicitly show the rational polynomial transfer function components:

$$\mathbf{Y}_t = \frac{\mathbf{B}(q)}{\mathbf{A_1}(q)}\mathbf{U}_t + \frac{\mathbf{C}(q)}{\mathbf{A_2}(q)}\epsilon_t \tag{4.10}$$

To model dynamic systems, often special cases of this general model are considered. First, the ARMAX model, or Auto-Regressive-Moving Average model with exogenous inputs, is obtained by assuming $\mathbf{A_1}(q) = \mathbf{A_2}(q) = \mathbf{A}(q)$.

$$\mathbf{A}(q)\mathbf{Y}_t = \mathbf{B}(q)\mathbf{U}_t + \mathbf{C}(q)\epsilon_t \tag{4.11}$$

Second, the *ARX model*, or *Auto-Regressive model with exogenous inputs*, is obtained when $\mathbf{C}(q) = 1$:

$$\mathbf{A}(q)\mathbf{Y}_t = \mathbf{B}(q)\mathbf{U}_t + \epsilon_t \tag{4.12}$$

In this work, we focus on ARX models that have the *indoor air temperature, T_i, as sole output*. All that is left for us to do is select variables that influence it. We find inspiration in Figure 2.2: $\mathbf{U}_t = [T_e, \Phi_h^h, I_{sol}, T_{sky}, T_n, T_g]$. The leftmost variables are most likely to impact T_i significantly, whilst relatively easy to generate. We can also imagine T_i to be dependent on previous values of itself, e.g. T_i is high when it was already high in previous time steps. This *auto-regressive* feature is built into Eqs. 4.11 and 4.12. It is described by the polynomial $\mathbf{A}(q)$, in the denominator of the rational transfer function components.

4.2.2.1 Parameter estimation

ARX models can be used to *simulate* the system's output $\hat{T}_{i,t}$. Given the simulation error, ϵ_t, that represents the difference between $\hat{T}_{i,t}$ and the actual measured output, $T_{i,t}$, the model parameters, $\hat{\theta}$, can be estimated by minimising the sum of squared simulation errors:

$$\hat{\theta} = \underset{\theta}{argmin} \sum_{t=1}^{N} (T_{i,t} - \hat{T}_{i,t})^2 = \underset{\theta}{argmin} \sum_{t=1}^{N} \epsilon_t^2(\theta) \tag{4.13}$$

With N the number of samples.

4.2.2.2 Pros and cons

To go from continuous-time stochastic state space models to discrete-time transfer function models, we had to make a number of concessions. First, to go from Eq. 4.4 to Eq. 4.6, we assumed a constant sampling time. We can thus no longer consider time-varying sampling times (Madsen, Bacher, and Delff, 2010). Second, to take the step from Eqs. 4.7 and 4.8 to Eq. 4.9, we grouped system and observation noise. Third, when we simplified the transfer function model in Eq. 4.10, to define ARMAX (Eq. 4.11) and ARX (Eq. 4.12) models, we further reduced the description of the noise process. Finally, by eliminating the state vector, the direct link with the physics is lost.

Discrete-time state space models, and thus also the transfer functions that we derive from them, contain more parameters than their continuous-time equivalents (Madsen, Bacher, and Delff, 2010). We illustrate this in Eq. 4.19, page 73.

Aside from stationary building performance characteristics, we can estimate time constants of the investigated building. Moreover, the order of the transfer function models can easily be varied (Jimenez, Madsen, and Andersen, 2008).

Minimising the sum of squared residuals demands little computation time, and model fits are quickly generated. However, going from state space to transfer function model representation is a one-way street. Where a unique transfer function can easily be derived from a state space model, infinitely many state space models can be made to correspond to one transfer function model.

4.2.3 First-order model T_i

In this section, we construct a straightforward first-order lumped state space model (Figure 4.3). We base it on the building physical framework, that was defined in Chapter 2. We illustrate the theoretical link between continuous-time stochastic state space models and discrete-time transfer functions models. And we show that the stationary gains, derived from ARX model parameters, remain physically relevant.

4.2.3.1 Continuous-time stochastic state space model

To appropriately describe the dynamic heat balance towards T_i, we run through the different terms of Eq. 2.2 (page 11), and see how they apply here. First, we consider *heating power* Φ_h. Similar to the co-heating test, we assume that the heat capacity associated with dedicated heating equipment is negligible, and that the heat exchange between T_h and T_i is primarily convective. We thus obtain that $\Phi_h = \Phi_h^h$: the measured heating power directly feeds into T_i.

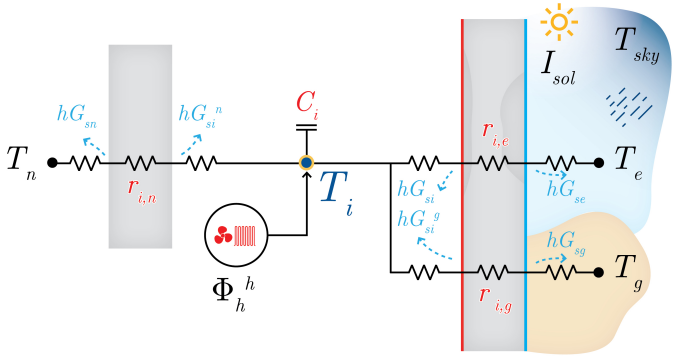

Figure 4.3: First-order lumped state space model. T_i is, at the same time, sole *system state* and *measured output*. T_e, Φ_h^h, I_{sol}, T_g, T_n, $(T_{sky} - T_{se})$, and latent heat terms serve as inputs.

Solar gains are easy to describe, we can simply copy Eq. 2.8, but challenging to interpret. As already indicated in Section 2.2.2, measuring I_{sol} along the sun vector remains costly. On site, we are often limited to measure global solar irradiation in just one direction, e.g. perpendicular to a south oriented upright plane. This term thus relates a particular global solar radiation projection to the actual dynamic solar gains that are discerned in T_i. Ideally, $A_{sol}(azel)$ would be a time-varying solar aperture that accounts for the varying sun position, and for the fact that the input is actually just a single projection of the solar radiation. In practice, however, most often an average value for A_{sol} is estimated, which we will also adopt here. We thus write solar gains as $A_{sol}I_{sol}$.

If present, building encapsulated moisture evaporates towards the indoor environment during the heating experiment. We assume Eq. 2.9.

As we neglect C_{si}, C_1 to C_k and C_{se} in Eqs. 2.12 to 2.14, this model is only adequate to describe light-weight building envelope structures. We simply do not discern any capacitive thermal node between T_i and T_e. The *transmission heat loss* towards T_e, Φ^e_{tr}, then simplifies to:

$$\Phi^e_{tr} = \frac{1}{r_{i,e}}(T^*_e - T^*_i) \tag{4.14a}$$

$$\Phi^e_{tr} = \frac{1}{r_{i,e}}\Big(T_e + r_e(A_{sol,se}I_{sol} + \frac{1}{r_{sky}}(T_{sky} - T_{se}) + hG_{se}) - \big(T_{Ri} + r_i(A_{sol,si}I_{sol} + hG_{si})\big)\Big) \tag{4.14b}$$

where the specific thermal resistance, $r_{i,e}$, is equivalent to $r_i+r_1+r_2+...+r_k+r_e$, in Figure 2.2.

As discussed in Section 3.5.1, we assume that we introduce only a minor error, by replacing T_{Ri} with T_i.

Similarly, given Eqs. 2.15 to 2.17, we can express transmission heat flows to the neighbouring zones:

$$\Phi^n_{tr} = \frac{1}{r_{i,n}}(T^*_n - T^*_i) \tag{4.15a}$$

$$\Phi^n_{tr} = \frac{1}{r_{i,n}}\Big(T_n + r_n(A_{sol,sn}I_{sol} + hG_{sn}) - \big(T_i + r^n_i(A^n_{sol,si}I_{sol} + hG^n_{si})\big)\Big) \tag{4.15b}$$

with $r_{i,n} = r^n_i + r^n_1 + r^n_2 + ... + r^n_k + r_n$ in Figure 2.2. Also here, we assume $T_{Rn} = T_n$ and $T_{Ri} = T_i$.

With regard to the floor on ground, Eqs. 2.18 and 2.19 yield:

$$\Phi^g_{tr} = \frac{1}{r_{i,g}}(T^*_g - T^*_i) \tag{4.16a}$$

$$\Phi^g_{tr} = \frac{1}{r_{i,g}}\Big((T_g + r_g h G_{sg}) - \big(T_i + r^g_i(A^g_{sol,si} I_{sol} + h G^g_{si})\big)\Big) \tag{4.16b}$$

with $r_{i,g} = r^g_i + r^g_1 + r^g_2 + ... + r^g_k + r_g$ in Figure 2.2.

As we do not discern any capacitive thermal node in the fabric, ventilation heat loss and transmission heat loss, between T_i and T_e, collapse into $r_{i,e}$. Similarly, $r_{i,n}$ captures both transmission and ventilation heat loss between T_i and T_n.

As illustrated in Figure 4.3, we assume that all the building's effective thermal mass is concentrated in the indoor air temperature state T_i. The buffer effect of building fabric, furniture, heating equipment, and sensors, is not modelled explicitly. Instead, their effective heat capacities are lumped into C_i.

We are now ready to write our first-order model in a system and measurement equation matrix form.

$$d\left[T_i\right] = \Big(\mathbf{A_c}\left[T_i\right] + \mathbf{B_c}\mathbf{U}(t)\Big)dt + dW(t) \tag{4.17a}$$

$$\left[T_i\right] = \left[1\right]\left[T_i\right] + \left[0\right]\mathbf{U}(t) + e_t \tag{4.17b}$$

with $\left[T_i\right]$ our sole system state. $\mathbf{A_c}$ describes how the system behaves dynamically, and $\mathbf{B_c}$ describes how inputs, $\mathbf{U}(t)$, feed into the system. The state T_i is also measured, as expressed in Eq. 4.18.

$$\mathbf{A_c} = \frac{1}{C_i}\left[\omega_i\right] \tag{4.17c}$$

$$\mathbf{B_c} = \frac{1}{C_i}[\omega_h \quad \omega_e \quad \omega_{sol} \quad \omega_{sky} \quad \omega_g \quad \omega_n \quad \omega_{G_{si}} \quad \omega_{G_{se}} \quad \omega_{G^n_{si}} \quad \omega_{G_{sn}} \quad \omega_{G^g_{si}} \quad \omega_{G_{sg}}] \tag{4.17d}$$

$$\mathbf{U}(t)^T = [T_e \quad \Phi_h \quad I_{sol} \quad (T_{sky} - T_{se}) \quad T_g \quad T_n \quad G_{si} \quad G_{se} \quad G^n_{si} \quad G_{sn} \quad G^g_{si} \quad G_{sg}] \tag{4.17e}$$

The elements of matrices $\mathbf{A_c}$ and $\mathbf{B_c}$ are found by assembling the coefficients for respective driving forces. They are collected in Eq. 4.18.

First-order model parameters

$$\omega_i = -(\frac{1}{r_{i,e}} + \frac{1}{r_{i,g}} + \frac{1}{r_{i,n}}) \quad \omega_h = 1 \quad \omega_e = \frac{1}{r_{i,e}}$$
$$\omega_{sol} = A_{sol}(azel) + \frac{1}{r_{i,e}} r_e A_{sol,se} - \frac{1}{r_{i,e}} r_i A_{sol,si}$$
$$+ \frac{1}{r_{i,n}} r_n A_{sol,sn} - \frac{1}{r_{i,n}} r_i^n A_{sol,si}^n - \frac{1}{r_{i,g}} r_i^g A_{sol,si}^g \tag{4.18}$$
$$\omega_{sky} = \frac{1}{r_{i,e}} r_e \frac{1}{r_{sky}} \quad \omega_g = \frac{1}{r_{i,g}} \quad \omega_n = \frac{1}{r_{i,n}}$$
$$\omega_{G_{si}} = h - \frac{1}{r_{i,e}} r_i h \quad \omega_{G_{si}^g} = h - \frac{1}{r_{i,g}} r_i^g h \quad \omega_{G_{si}^n} = h - \frac{1}{r_{i,n}} r_i^n h$$
$$\omega_{G_{se}} = \frac{1}{r_{i,e}} r_e h \quad \omega_{G_{sn}} = \frac{1}{r_{i,n}} r_n h \quad \omega_{G_{sg}} = \frac{1}{r_{i,g}} r_g h$$

The obtained parameters, ω, directly relate to the parameters that we derived in Section 3.4. Again, coefficients ω_i and ω_e differ: ω_i incorporates the influence of heat loss towards neighbouring zones and ground floor. And again, we find ourselves unable to distinguish between transmission and ventilation heat loss coefficients. We need to take additional measures if we want to disentangle both. Alternative to performing additional tests, however, we can now choose to *increase the model order*, by adding a state in the building envelope (Section 4.2.4). We can then discern between a *capacitive* heat flow, that passes through the new envelope state, and a heat flow that bypasses it, thereby connecting T_i and T_e directly. At the same time, this added envelope state allows to more adequately model the behaviour of heavy-weight building envelopes. Aside from ventilation heat exchange, however, $r_{i,e}$ might also reflect the influence of low-capacitive building envelope parts, as e.g. windows.

4.2.3.2 Discrete-time transfer function model

In this section, we relate above continuous-time stochastic state space model to a discrete-time transfer function model. When inputs $\mathbf{U}(t)$ are approximately constant throughout the sample interval, we can safely assume a Zero-Order Hold (ZOH), and map the continuous-time model matrices, $\mathbf{A_c}$ and $\mathbf{B_c}$ in Eqs. 4.17, to their discrete-time equivalents (Juang, 1994; Reynders, 2012):

$$\mathbf{A} = \exp(\mathbf{A_c}T) \tag{4.19a}$$

$$\mathbf{B} = (\mathbf{A} - \mathbf{I})\mathbf{A_c}^{-1}\mathbf{B_c} \tag{4.19b}$$

$$\mathbf{C} = \mathbf{C_c} \tag{4.19c}$$

$$\mathbf{D} = \mathbf{D_c} \tag{4.19d}$$

From the discrete-time state space model that results, following the procedure elaborated in Section 4.2.2, we eliminate the state vector, $\begin{bmatrix} T_i \end{bmatrix}$, to distill a discrete-time transfer function model. To simplify notation, we only consider inputs T_e, Φ_h and I_{sol}. After rearranging, the input transfer function component $\mathbf{H}_1(z)$ reads:

$$\mathbf{H}_1(z) = \begin{bmatrix} \frac{\omega_e(e^{\frac{-T\omega_i}{C_i}}-1)}{\omega_i(z-e^{\frac{-T\omega_i}{C_i}})} & \frac{\omega_h(e^{\frac{-T\omega_i}{C_i}}-1)}{\omega_i(z-e^{\frac{-T\omega_i}{C_i}})} & \frac{\omega_{sol}(e^{\frac{-T\omega_i}{C_i}}-1)}{\omega_i(z-e^{\frac{-T\omega_i}{C_i}})} \end{bmatrix} \tag{4.20}$$

We now derive the difference equation that corresponds to Eq. 4.20.

$$\omega_i(z - e^{\frac{-T\omega_i}{C_i}})T_i(z) = \tag{4.21a}$$
$$\omega_e(e^{\frac{-T\omega_i}{C_i}} - 1)T_e(z) + \omega_h(e^{\frac{-T\omega_i}{C_i}} - 1)\Phi_h^h(z) + \omega_{sol}(e^{\frac{-T\omega_i}{C_i}} - 1)I_{sol}(z)$$

Applying backward shift operator z^{-1}, shifting the equation such that $t+1$ becomes t and solving for $T_{i,t}$ gives:

$$T_{i,t} = -\frac{\omega_e}{\omega_i}\frac{1 - e^{\frac{-T\omega_i}{C_i}}}{1 - e^{\frac{-T\omega_i}{C_i}}B}BT_{e,t} - \frac{\omega_h}{\omega_i}\frac{1 - e^{\frac{-T\omega_i}{C_i}}}{1 - e^{\frac{-T\omega_i}{C_i}}B}B\Phi_{h,t}^h - \frac{\omega_{sol}}{\omega_i}\frac{1 - e^{\frac{-T\omega_i}{C_i}}}{1 - e^{\frac{-T\omega_i}{C_i}}B}BI_{sol,t} \tag{4.21b}$$

With B the backward shift operator. The low-pass filter we so pragmatically introduced at the end of Chapter 3, now appears explicitly. The associated time constant, τ, is $\frac{\omega_i}{C_i}$.

Assuming we suffice without a separate noise model, we can derive, from Eq. 4.21b, an ARX model that is equivalent to the state space model described in Eqs. 4.17:

$$\omega_i(B)T_{i,t} = \omega_e(B)BT_{e,t} + \omega_h(B)B\Phi_{h,t}^h + \omega_{sol}(B)BI_{sol,t} + \mu + \epsilon_t \tag{4.22}$$

With $\frac{\omega_e(B)}{\omega_i(B)}$, $\frac{\omega_h(B)}{\omega_i(B)}$ and $\frac{\omega_{sol}(B)}{\omega_i(B)}$ rational polynomial functions of the back-shift operator B that describe how inputs $T_{e,t}$, $\Phi_{h,t}^h$ and $I_{sol,t}$ dynamically influence output $T_{i,t}$.

Higher-order ARX models Building on Eq. 4.22, we can write down a general ARX model, with output T_i and model order k.

$$\omega_i(B)T_{i,t} = \omega_e(B)T_{e,t} + \omega_h(B)\Phi^h_{h,t} + \omega_{sol}(B)I_{sol,t} + \mu + \epsilon_t \tag{4.23a}$$

With

$$\begin{aligned}
\omega_i(B) &= 1 - \omega_{i,1}B - \omega_{i,2}B^2 - ... - \omega_{i,k}B^k \\
\omega_e(B) &= \omega_{e,1}B + \omega_{e,2}B^2 + ... + \omega_{e,k}B^k \\
\omega_h(B) &= \omega_{h,1}B + \omega_{h,2}B^2 + ... + \omega_{h,k}B^k \\
\omega_{sol}(B) &= \omega_{sol,1}B + \omega_{sol,2}B^2 + ... + \omega_{sol,k}B^k
\end{aligned} \tag{4.23b}$$

4.2.4 Second-order model $T_i + T_1$

Apart from the indoor air temperature state T_i, we now consider a second thermal node in the fabric, in between T_i and T_e. Hence, the actual distributed wall states are assumed to collapse into one wall state, T_1, with heat capacity C_1. Specific thermal resistances $r_{i,1}$ and $r_{1,e}$ represent the indoor and outdoor layers of the building fabric, that separate T_i from T_1 and T_1 from T_e, respectively.

4.2.4.1 Continuous-time stochastic state space model

Both T_i and T_1 are candidates to receive a fraction of I_{sol}. Depending on how capacities and resistances are distributed in the actual fabric, T_1 receives either a fraction of I_{sol} or a fraction of the solar gains or a fraction of both. As we are not certain, we assign separate parameters to them: ω^i_{sol} and ω^1_{sol}.

We chose T_1 as a sole state to represent the dynamic behaviour of the building fabric. Depending on how thermal resistances and capacities are distributed throughout the fabric, and depending how we excite the fabric, this sole state can shuffle through the distributed wall states in Figure 2.2b, and collect thermal capacity to make for fitting apparent time constants. Even though we select T_1, to make our point we could have selected any other of these distributed wall states.

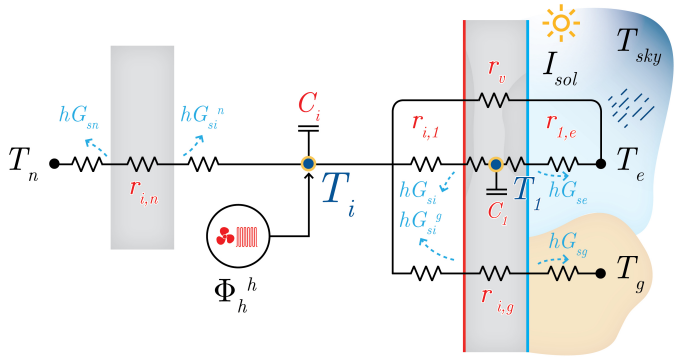

Figure 4.4: Second-order lumped state space model $T_i + T_1$. T_i is at the same time *system state* and *measured output*.

In comparison with above first-order model, we need to expand the DE, that describes T_i, to include heat losses between T_i and T_1, and a direct ventilation heat flow between T_i and T_e. We thereby ignore C_{si} in Eq. 2.12, and assume that Φ_h^h directly feeds into T_i:

$$\begin{aligned} C_i \frac{dT_i}{dt} &= \Phi_h^h + A_{sol} I_{sol} + \frac{1}{r_{i,1}} \Big(T_1 - \big(T_i + r_i (A_{sol,si} I_{sol} + hG_{si}) \big) \Big) \\ &+ \frac{1}{r_{i,n}} \Big(T_n + r_n (A_{sol,sn} I_{sol} + hG_{sn}) - \big(T_i + r_i^n (A_{sol,si}^n I_{sol} + hG_{si}^n) \big) \Big) \\ &+ \frac{1}{r_{i,g}} \Big(T_g + r_g hG_{sg} - \big(T_i + r_i^g (A_{sol,si}^g I_{sol} + hG_{si}^g) \big) \Big) \\ &+ \frac{1}{r_v} (T_e - T_i) \end{aligned} \tag{4.24}$$

We also need to write down an additional DE, to represent T_1. Given that we ignore C_2 to C_k and C_{se}, Eq. 2.13 becomes:

$$C_1 \frac{dT_1}{dt} = \frac{1}{r_{i,1}} (T_i^* - T_1) + \frac{1}{r_{1,e}} (T_e^* - T_1) \tag{4.25}$$

$$\begin{aligned} C_1 \frac{dT_1}{dt} &= \frac{1}{r_{i,1}} (T_i + r_i (A_{sol,si} I_{sol} + hG_{si}) - T_1) \\ &+ \frac{1}{r_{1,e}} (T_e + r_e (A_{sol,se} I_{sol} + \frac{1}{r_{sky}} (T_{sky} - T_{se}) + hG_{se}) - T_1) \end{aligned}$$

We write the second-order candidate model, described by Eqs. 4.24 and 4.26, in a matrix form.

$$d\mathbf{T}(t) = \Big(\mathbf{A_c}\mathbf{T}(t) + \mathbf{B_c}\mathbf{U}(t)\Big)dt + dW(t) \tag{4.26a}$$

$$\begin{bmatrix} T_i \end{bmatrix} = \begin{bmatrix} 1 & 0 \end{bmatrix} \mathbf{T}(t) + \mathbf{0}\mathbf{U}(t) + e_t \tag{4.26b}$$

with $\mathbf{T}(t)$ the system states, $\mathbf{A_c}$ the system matrix, $\mathbf{B_c}$ a matrix that describes the influence of the input vector, $\mathbf{U}(t)$, on the system. To simplify notation, we ignore the influence of sky radiative heat exchange and latent heat.

$$\mathbf{A_c} = \begin{bmatrix} \frac{\omega_i^i}{C_i} & \frac{\omega_1^i}{C_i} \\ \frac{\omega_i^1}{C_1} & \frac{\omega_1^1}{C_1} \end{bmatrix} \tag{4.26c}$$

$$\mathbf{B_c} = \begin{bmatrix} \frac{\omega_h^i}{C_i} & \frac{\omega_e^i}{C_i} & \frac{\omega_{sol}^i}{C_i} & \frac{\omega_g^i}{C_i} & \frac{\omega_n^i}{C_i} \\ \frac{\omega_h^1}{C_1} & \frac{\omega_e^1}{C_1} & \frac{\omega_{sol}^1}{C_1} & \frac{\omega_g^1}{C_1} & \frac{\omega_n^1}{C_1} \end{bmatrix} \tag{4.26d}$$

$$\mathbf{U}(t)^T = \begin{bmatrix} T_e & \Phi_h & I_{sol} & T_g & T_n \end{bmatrix} \tag{4.26e}$$

Second-order model parameters

$$\begin{aligned}
\omega_i^i &= -\left(\frac{1}{r_{i,1}} + \frac{1}{r_{i,n}} + \frac{1}{r_{i,g}} + \frac{1}{r_v}\right) & \omega_1^i &= \frac{1}{r_{i,1}} \\
\omega_i^1 &= \frac{1}{r_{i,1}} & \omega_1^1 &= -\left(\frac{1}{r_{i,1}} + \frac{1}{r_{1,e}}\right) \\
\omega_h^i &= 1 & \omega_e^i &= \frac{1}{r_v} \\
\omega_{sol}^i &= A_{sol} - \frac{1}{r_{i,1}} r_i A_{sol,si} \\
&\quad + \frac{1}{r_{i,n}} r_n A_{sol,sn} - \frac{1}{r_{i,n}} r_i^n A_{sol,si}^n + \frac{1}{r_{i,g}} r_i^g A_{sol,si}^g \\
\omega_g^i &= \frac{1}{r_{i,g}} & \omega_n^i &= \frac{1}{r_{i,n}} \\
\omega_h^1 &= 0 & \omega_e^1 &= \frac{1}{r_{1,e}} \\
\omega_{sol}^1 &= \frac{1}{r_{i,1}} r_i A_{sol,si} + \frac{1}{r_{1,e}} r_e A_{sol,se} \\
\omega_g^1 &= 0 & \omega_n^1 &= 0
\end{aligned} \tag{4.27}$$

4.3 Estimating H

Estimating H remains our primary aim. In this section, we discuss strategies that we can adopt, to distill H from the multitude of parameters that we find embedded in the continuous-time stochastic state space and discrete-time transfer function models, described above. More specifically, we return to the four test case scenarios, that we introduced in Section 3.6 of Chapter 3, and for each of them, we lay out an appropriate strategy to estimate H.

4.3.1 Continuous-time stochastic state space model

Regardless of the model order k, we calculate H directly from the estimated parameters:

$$H = \frac{1}{r_{i,e}} + \frac{1}{r_v} + \frac{1}{r_{i,g}} \tag{4.28}$$

Depending on the model parametrisation, the denominators $r_{i,e}$ and $r_{i,g}$ comprise one or more estimated parameters. For instance, for the second-order model discussed in the previous section, $r_{i,e}$ comprises the specific resistance between T_i and T_1, $r_{i,1}$, and the specific resistance between T_1 and T_e, $r_{1,e}$. As a matter of fact, the remainder of this section will focus on this second-order model. The strategies that we distill here equally apply to models of higher order k, that have, in addition to T_i, $k-1$ states in between T_i and T_e.

As elaborated in Section 4.2.4, and schematically illustrated in Figure 4.5, ω_i^i in the system matrix $\mathbf{A_c}$ (Eq. 4.26c) is informed by a number of physical phenomena:

$$\omega_i^i = -(\frac{1}{r_{i,1}} + \frac{1}{r_{i,n}} + \frac{1}{r_{i,g}} + \frac{1}{r_v}) \tag{4.29}$$

If T_n and T_g are not modelled explicitly, or if ventilation heat loss is not estimated separately, the terms in ω_i^i collapse into a reduced number of terms, that aggregate these phenomena. Depending on the Scenario at hand, we distinguish appropriate strategies to deal with this. In any case, if there is significant ventilation heat loss, and model order $k > 1$, we assume r_v can be estimated. If not, we ignore it.

Scenario 1: Floor on ground and neighbouring zones If T_g is significantly correlated with T_i, we can explicitly model the associated heat losses, and separately assess $r_{i,e}$, r_v, and $r_{i,g}$. H then follows from Eq. 4.28.

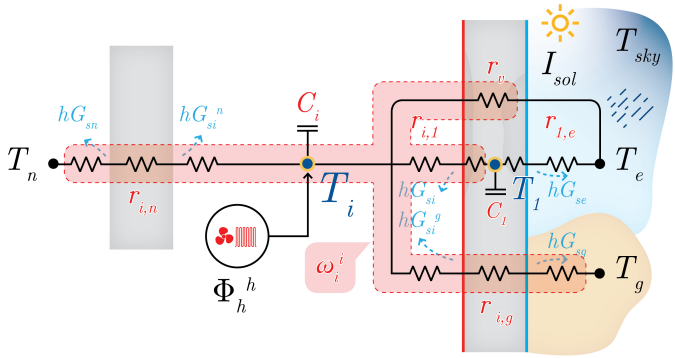

Figure 4.5: Second-order lumped state space model $[T_i, T_1]$. T_i is at the same time *system state* and *measured output*. The circuit part marked in red highlights the physical phenomena that influence ω_i^i.

In the more likely case that T_g and T_i are not correlated, and if T_g is not measured, $1/r_{i,1}$ and $1/r_{i,g}$, in ω_i^i, collapse into one term: $1/r_{i,1}^i$. To resolve this, we separately measure the transmission heat losses towards the neighbouring zones, Φ_{tr}^n, and assume $\Phi_h - \Phi_{tr}^n$ as heating power input. We can thus skip the term $1/r_{i,n}$, in 4.29, and ω_i^i simplifies to Eq. 4.30.

$$\omega_i^i = -(\frac{1}{r_{i,1}^i} + \frac{1}{r_v}) \qquad (4.30) \qquad\qquad \frac{1}{r_{i,g}} = \frac{1}{r_{i,1}^i} - \frac{1}{r_{i,1}} \qquad (4.31)$$

We can now calculate $1/r_{i,g}$, from Eq. 4.31. With $r_{i,1}^i$ estimated as part of ω_i^i, and $r_{i,1}$ estimated on the basis of matrix elements other than ω_i^i, in Eq. 4.27. In any case, we can estimate $r_{i,e}$, in Eq. 4.28, as the sum of $r_{i,1}$ and $r_{1,k}$. For model order $k = 1$ (Eq. 4.18), $r_{i,e}$ is estimated directly, and $H = -\omega_i$.

Scenario 2: Floor on ground Similar to Scenario 1, only now we retain Φ_h^h as heating power input. Test Case 6 (Section 5.7) illustrates this Scenario.

Scenario 3: Neighbouring zones ω_i^i is influenced by heat losses towards the neighbouring zones. Hence, $1/r_{i,1}$, and $1/r_{i,n}$, in ω_i^i, collapse into one term. We thus need to estimate $r_{i,e}$ on the basis of matrix elements other than ω_i^i, in Eq. 4.27.

Scenario 4: Neither floor on ground, nor neighbouring zones As there are no physical phenomena to be sidelined, this is the most straightforward scenario. H can be estimated directly from model parameters. Test Case 4 (5.5) offers an ideal example of this Scenario.

4.3.2 Discrete-time transfer function model

To estimate H, we set the backward shift operator B, in Eqs. 4.23, to 1. And we compare this model with the stationary model written down in Eq. 3.31 (Chapter 3, page 47). We find that $\omega_i = \frac{\omega_i(1)}{\omega_h(1)}$, $\omega_e = -\frac{\omega_e(1)}{\omega_h(1)}$, and $\omega_{sol} = -\frac{\omega_{sol}(1)}{\omega_h(1)}$.

Scenario 1: Floor on ground and neighbouring zones In the unlikely case that T_i and T_n are significantly correlated, we can separately estimate the stationary gain of the transfer function element, with regard to T_n: $\frac{\omega_n(1)}{\omega_h(1)}$. H can then be calculated as $\frac{\omega_i(1)}{\omega_h(1)} - \frac{\omega_n(1)}{\omega_h(1)}$. In the more likely case that T_i and T_n are not correlated, estimate Φ^n_{tr} separately, subtract it from Φ_h and consider $\Phi^h_h - \Phi^n_{tr}$ as heating power input. H can now be calculated as $\frac{\omega_i(1)}{\omega_h(1)}$.

Scenario 2: Floor on ground Also here, H can be estimated as $\frac{\omega_i(1)}{\omega_h(1)}$. Again, Test Case 6 (Section 5.7) illustrates this Scenario.

Scenario 3: Neighbouring zones Again the most straightforward scenario: $H = \frac{\omega_e(1)}{\omega_h(1)}$. But if T_n is correlated with T_e, $\frac{\omega_e(1)}{\omega_h(1)}$ is corrupted. We can resolve this by measuring Φ^n_{tr}, and assuming $\Phi^h_h - \Phi^n_{tr}$ as heating power input. H can then be found as the minimum variance weighting, elaborated in Appendix A, of $\frac{\omega_i(1)}{\omega_h(1)}$ and $\frac{\omega_e(1)}{\omega_h(1)}$. Test Case 5 (Section 5.6) exemplifies this Scenario.

Scenario 4: Neither floor on ground, nor neighbouring zones Both $\frac{\omega_i(1)}{\omega_h(1)}$ and $\frac{\omega_e(1)}{\omega_h(1)}$ are equally valid estimates for H, and by following the procedure elaborated in Appendix A, we combine them into one minimum variance estimate for H. An ideal example of this Scenario is found in Test Case 4 (Section 5.5).

4.4 Conclusions

This chapter discussed the analysis of data generated by dynamic heating experiments, with a heating power that switches between two discrete levels. The indoor air temperature T_i now serves as the logical system output. We assumed both continuous-time stochastic state space models, and discrete-time transfer function models, and derived the link between these two types of models, on a theoretical basis. The typical trade-off between grey-box and black-box models is discussed.

From the building physical framework in Chapter 2, we derived first-order and second-order lumped state space models. We showed that the parameters, when embedded in black-box transfer function models, remain physically relevant. Finally, we discussed strategies to estimate H on the basis of the multitude of parameters that grey-box and black-box models generate.

Together with the linear regression and ARX models, with output Φ_h^h, that we developed in Chapter 3, we are now fully equipped to appropriately analyse both quasi-stationary and dynamic tests. They await us, in Chapter 5.

Chapter 5

Test Cases

In this Chapter, we apply the methodology, laid out in Chapters 2, 3 and 4, to six *test cases*: three quasi-stationary co-heating tests, and three dynamic tests. For each Test Case, we estimate H using an appropriate strategy, dictated by one of the four scenarios that we introduced in Section 3.6, for quasi-stationary tests, and in Section 4.3, for dynamic tests. For each Test Case, we compare the estimated value for H with its expected value. In case these expected values are not already available from earlier reports, and if not specified otherwise, we calculate them, on the basis of standards (NBN B62-301, 1989), (ISO 13370, 2007) and (ISO 10456, 2007). We report the estimated values for H with 1 decimal number, and include a confidence interval (CI) of 95 %, calculated as $H \pm 2\sigma_H$, with σ_H the standard deviation.

The four Scenarios serve to focus the mind. Essentially, they *categorise* a test case's boundary conditions. Consider, for instance, Test Case 2, that discusses a co-heating test performed on a detached insulated brick house with a cellar. Although it has a ventilated cellar, we will categorise it in *Scenario 2: Floor on ground*. The slowly varying air temperature of its cellar is uncorrelated with both Φ_h^h and T_e, while heat losses from T_i towards the cellar, T_c, are part of H. It thus effectively behaves as the soil mass in Scenario 2.

Complementary to the four Scenarios, we need to account for phenomena that are very specific to the investigated Test Case. One example is Test Case 1, that discusses a co-heating test performed on a terraced house. Although we categorise it in *Scenario 3: Neighbouring zones*, its two neighbours behave very differently, leading us to fine-tune our strategy accordingly. Another example is Test Case 3, that discusses a co-heating test performed on a detached insulated brick house with a floor on ground. The test took place just after the house was constructed. Latent heat, due to drying out of wet plaster, thus gains importance.

Before we start, we briefly discuss a range of statistical tools that we will use throughout this chapter, to prepare building performance data, and to evaluate how appropriate our simplified thermal models are, with regard to the investigated building and the heating experiment. We conclude this introductory section with a view on the confidence intervals, with regard to the estimated and the expected values for H.

5.1 Statistical tools to fit and evaluate simplified thermal models

5.1.1 Preparing building performance data

The models that we assume in this dissertation describe the investigated building as a single zone. From the measured indoor air temperatures, we thus need to construct one signal that effectively represents all zones. Instead of merely averaging, we propose to use *principal component analysis*, as suggested by Madsen and Schultz (1993).

Principal component analysis, or *PCA*, is a multivariate analysis method that describes a larger set of possibly correlated measured times series with a smaller number of linearly uncorrelated time series, i.e. *principal components* (*PC*s). The first principal component, *PC*, collects the larger share of variability in the data. The variance of succeeding principal components is again maximised, but with the constraint that they need to be uncorrelated with preceding ones.

Often, the first principal component closely relates to the mean of indoor air temperatures. Nonetheless, PCA is sensitive to signals that show greater variance. As PCA tries to minimise the squared errors, it gives more weight to such outlier signals. One option is to remove them, before calculating the PCs. Another option is to assign weights, inspired by the relevancy the practitioner assigns to each of the signals.

For most test cases, we apply unweighted PCA, and select the first PC. In Test Case 2, however, we apply a volume-weighted average. Here, one of the heated rooms showed outlier temperature values. By assuming a volume-weighted average instead of the first PC, we assign more weight to the well-controlled temperature signals in the larger rooms, and we are less likely to get intimate with outlier signals.

5.1.2 White noise residuals, please.

Each model simplifies the actual building's behaviour. The difference between the response that it generates and the actual building response is reflected by its residuals. For instance, for a quasi-stationary test, as discussed in Chapter 3, residuals, ϵ_t, are calculated as $\Phi_h^h - \hat{\Phi}_h^h$. For the dynamic tests, discussed in Chapter 4, $\epsilon_t = T_{i,t} - \hat{T_{i,t}}$. Some models are better suited than others. To argue which model performs best, we investigate their residuals.

A model that *completely* describes a building's response, as a function of relevant inputs, essentially leaves none of its variability undescribed and shares its mean value. The corresponding residuals then constitute a completely random time series, or *white noise*.

White noise represents a sequence of mutually uncorrelated, identically distributed random variables with zero mean and constant variance (Madsen, 2008). We can test for white noise by verifying (1) that the residuals do not show unusual outlier values, (2) that the *autocorrelation function* is not significantly different from zero for all lags, and *cross-correlation functions* between the residuals and model inputs, or between residuals and unaccounted for inputs are not significantly different from zero for all lags, and (3) that the *periodogram* shows a variance uniformly distributed over all frequencies (Delff et al., 2013).

The next three sections discuss above mentioned statistical tools. We will not go into depth on the theory behind them. Instead, based on some examples that we pick from the test cases, we illustrate how we apply them to converge to the most appropriate thermal model. Furthermore, in Section 5.1.3, we introduce *reliability plots* as an invaluable tool to compare estimates for H, that result when assuming data subsets of varying duration.

5.1.2.1 Residual plots

The top row of Figure 5.1 shows the residuals generated by an explicit ARX model (left), and an implicit ARX model (right), as they are fitted to data from Test Case 5 (Section 5.6). These ARX models are discussed in more detail in Section 4.2.2 of Chapter 4, and Section 5.6 of this Chapter. Figure 5.1 clearly indicates that, for this Test Case, the *explicit* ARX model (left column in Fig. 5.1) generates residuals with large peaks, at time steps where the indoor air, $T_{i,t}$ (marked as system output $\mathbf{Y_t}$ in Figure 5.1), either starts to cool down or starts to heat up; $\hat{T_{i,t}}$ overshoots $T_{i,t}$'s heating curve each time. As a result, the estimate of H is corrupted.

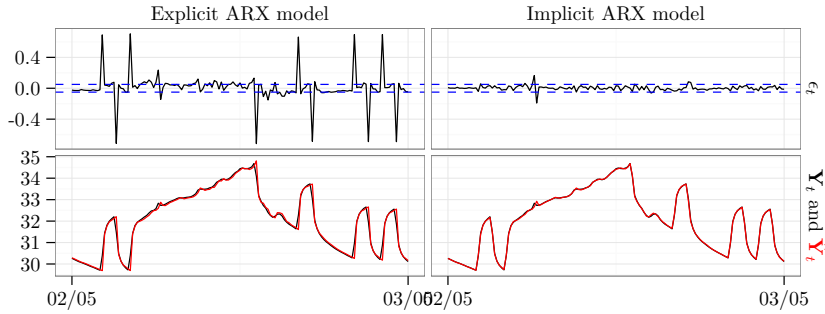

Figure 5.1: (First row): Model residuals, $\epsilon_t = T_{i,t} - \hat{T_{i,t}}$, in °C. (Second row): Time series plots of measured output, $\mathbf{Y}_t = T_{i,t}$, and model output, $\hat{\mathbf{Y}}_t = \hat{T_{i,t}}$ (in red), both in °C. (Left): Explicit ARX model; (Right): Implicit ARX model.

In case the time steps where $T_{i,t}$ heats up or cools down is determined by a PRBS or ROLBS signal, the inaccurate modelling of the explicit ARX model (Figure 5.1, left) might not be revealed, neither by the autocorrelation functions, nor by the periodograms. We should thus, complementary to these tools, investigate the residuals themselves.

5.1.2.2 Autocorrelation and cross-correlation functions

Autocorrelation functions, abbreviated ACFs, plot the values for a certain signal's autocorrelation, as a function of the number of lags. A signal's autocorrelation, for lag j, indicates how similar the signal is with a version of itself, lagged j time steps. Figure 5.2a depicts a typical example of Φ_h^h's autocorrelation, in the case of a co-heating test (Test Case 3, Section 5.4), and Figure 5.2b depicts the $ACF(T_i)$, in the case of a dynamic test, during which the indoor environment is excited with a heating power that follows a PRBS (Test Case 4, Section 5.5). The horizontal blue dashed lines depict the 95 % confidence bounds for statistical significance. In both cases, as the model outputs are significantly autocorrelated, they are exceeded often.

Cross-correlation functions, or CCF, plot the values for a certain signal's cross-correlation with another signal, as a function of the number of lags. They indicate how similar the signal is with the other, lagged j time steps. For our purpose, we consider the model output, Y_t, as one signal, and investigate the CCFs with inputs, $\mathbf{X_t}$, that might significantly influence it.

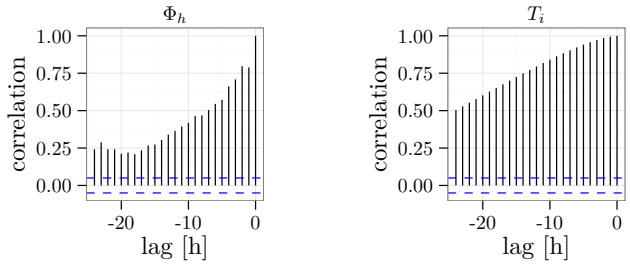

(a) $ACF(\Phi_h^h)$, with Φ_h^h taken from co-heating test in Test Case 3 (Section 5.4). Sampling time, t_s, is 60 min.

(b) $ACF(T_i)$, with T_i taken from dynamic test in Test Case 4 (Section 5.5). Sampling time, t_s, is 60 min.

Figure 5.2: Auto-correlation function (ACF).

Cross-correlations might be affected by the autocorrelation of the involved signals, or any shared trends that they may have. To cope with this, before calculating them, we pre-whiten both signals. First, we determine an ARIMA(1,1,0) model for Y_t (STAT 510, 2015): $(1 - \phi B)(1 - B)Y_t = \epsilon_t$, and then, we pre-whiten, or *filter*, both Y_t and X_t, using this model.

Figure 5.3 shows an example of Φ_h^h's cross-correlation with the indoor air temperature T_i, the outdoor air temperature T_e, solar radiation I_{sol}, attic air temperature T_{attic}, and cellar air temperature T_c, during a co-heating test (Test Case 2, Section 5.3). Consider, for instance, $CCF(\Phi_h^h, T_e)$. The negative values at the first lags, indicate that when T_e shows below average values in these lags, Φ_h^h will likely respond with above average values.

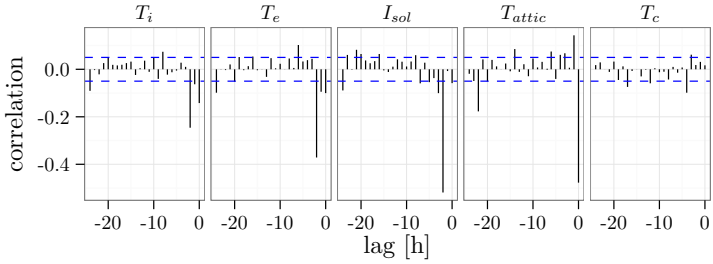

Figure 5.3: Φ_h^h's cross-correlation function (CCF), with T_i, T_e, I_{sol}, T_{attic}, and T_c. Sampling time, t_s, is 60 min.

5.1.2.3 Periodogram and cumulative periodogram

Each time series can be approximated as a combination of cosine or sine waves with different frequencies and amplitudes. The signal energy can thus be decomposed into contributions relating to different frequencies. A *periodogram* reveals those frequencies of a time series that are most dominant. A *cumulative periodogram* plots the cumulative values of the periodogram. Figure 5.4 shows the periodogram and the cumulative periodogram, related to residuals that are generated by ARX models fitted to co-heating test data, as discussed in Test Case 3 (Section 5.4).

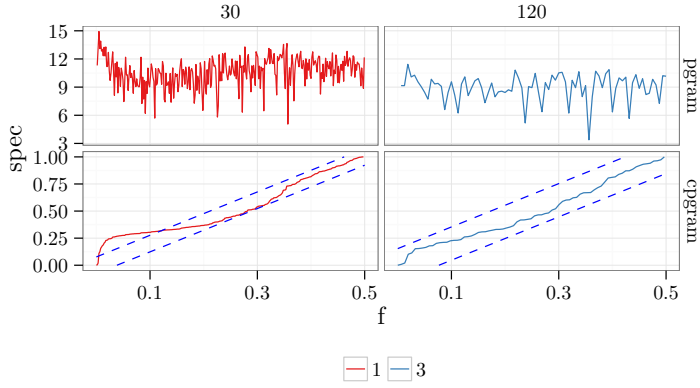

Figure 5.4: Log-periodogram, denoted *pgram* (top row), and cumulative periodogram, denoted *cpgram* (bottom row), of residuals ϵ_t, generated by implicit ARX models with output Φ_h^h, fitted to data from Test Case 3 (Section 5.4). Columns represent different sampling times t_s, in min. Colours reflects the ARX model order. The normalised frequency values, f (x-axis), express the number of cycles per unit of sampling time t_s. For instance, a f of 0.5, for a t_s of 720 min, corresponds to a period of *one day*. Higher signal frequencies are aliased.

As white noise varies uniformly across all frequencies, the associated periodogram varies around a constant, and the cumulative periodogram describes a diagonal between strict confidence bounds. These bounds depend on the sampling rate, and the number of samples. The cumulative periodogram of residuals, generated by a certain model, thus highlights those frequency ranges where the model does not properly capture the actual thermal system's dynamic response. We use these periodograms to select a sampling time, t_s, that is sensible to the test case, the performed heating experiment, and the applied analysis.

5.1.3 Reliability plots

Our aim is to estimate H, and its standard deviation, σ_H, on the basis of well-controlled heating experiments that have a limited *duration*, and are associated with weather conditions that we do not control. Both will impact H's reliability.

Aside from experiment duration and weather conditions, the reliability of H is also influenced by the characteristics of the investigated building, the performed heating experiment, and the analysis method used. To visualise the influence of these factors, we use *reliability plots*. Figure 5.5b shows an example, generated on the basis of Test Case 2 (Section 5.3), where we investigate a co-heating test performed on a detached house with a ventilated attic and cellar.

Figure 5.5a illustrates the principles behind a reliability plot. For Test Case 2, we have 20 days of measurements at our disposal. We can estimate H, on the basis of these 20 days of data, but we can also consider *data subsets*, that have a shorter *duration*. For instance, in (Figure 5.5a) data subsets A consider 7 days of measurements, and data subset B considers 16 days of measurements. To avoid correlated estimates, we avoid that data subsets overlap. For instance, data subsets A can start at day 0 (A1), and at day 7 (A2). The remaining data is skipped. Figure 5.5b indeed shows that, for a duration of 7 days, we have two estimates for H. Similarly, for data subset B, we only have one estimate.

We can perform the same exercise for different sampling times t_s. For instance, Figure 5.5c collects estimates for ω_i and $-\omega_e$, and assumes sampling times of 240 min to 1440 min. They are grouped as a function of data subset duration (x-axis), but are distinguished by their colour, and the fact that they are drawn apart horizontally.

5.1.4 Confidence intervals

Evidently, there are uncertainties associated with both the expected value of H, and the estimated value of H. The expected value of H, that we calculate on the basis of material characteristics of the building envelope, building geometry, construction details, and standard boundary conditions, unlikely captures all in situ eventualities. The *actual value* that H attains depends on a multitude of factors: building site planning, quality of workmanship and actually applied materials; the actual λ-values, in $\mathrm{W\,m^{-1}\,K^{-1}}$, of these materials, that depend on their temperature and moisture content; and surface heat transfer coefficients, h_i and h_e, in $\mathrm{W\,m^{-2}\,K^{-1}}$, that depend on the actual conditions for radiative and convective heat exchange at the surfaces of building envelope parts. We do not have all the information at hand, and as a result, H's

expected value might be biased. Section 5.5.9 discusses the potential impact, for the KI Test Box (Test Case 4), of a varying λ-value of the insulation layer, of additional material layers, and of varying h_i and h_e, on H's actual value. This test case, however, is very specific. It has a very low compactness, or volume to heat loss surface ratio, V_o/A_T, in m. Hence, even though it is well-insulated, varying these parameters significantly influences H. For well-insulated houses that exhibit a high compactness, the influence is limited. On the other hand, for poorly insulated houses with low compactness, the influence rises.

The confidence interval (CI), around the assessed value of H, is estimated as part of the statistical methods that we apply here. If, however, model residuals differ from white noise, the uncertainty of H is incorrectly assessed. For instance, when we analyse co-heating test data using linear regression, thereby assuming large sampling times, we unlikely obtain white noise residuals, and as a result, the confidence interval of H is likely underestimated.

Measurement errors and bias are an additional source of uncertainty, with regard to the assessed value of H. Measurement errors, given they have white noise characteristics, should not bias the estimates. Measurement bias, however, should be avoided. Consider for instance Test Case 2: if $T_{i,avg}$ has a 1 °C bias, we estimate a value of 140.2 $\mathrm{W\,K^{-1}}$ for H, whereas without bias, we estimate a value of 145.9 $\mathrm{W\,K^{-1}}$, a difference of 4%, which in this case corresponds to the bias to signal ratio of $T_{i,avg}$.

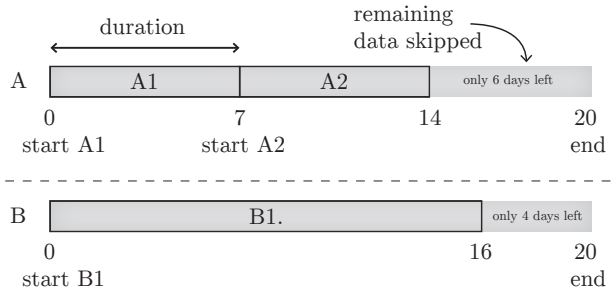

(a) Reliability plot principles.

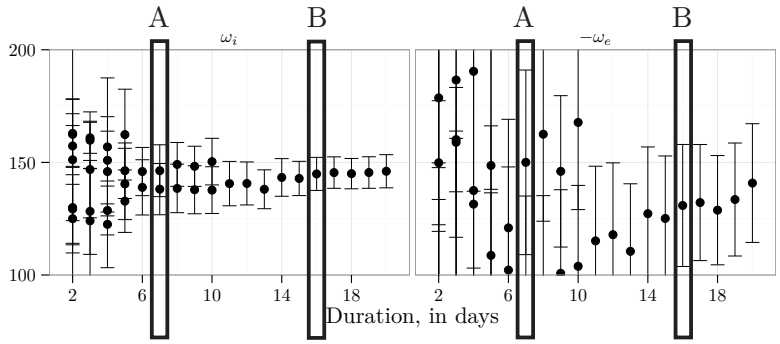

(b) Estimates of ω_i (left) and $-\omega_e$ (right), both in $\mathrm{W\,K^{-1}}$, that result from the linear regression analysis, applied in Test Case 2 (Section 5.3). Data subsets with varying duration (x-axis) are considered.

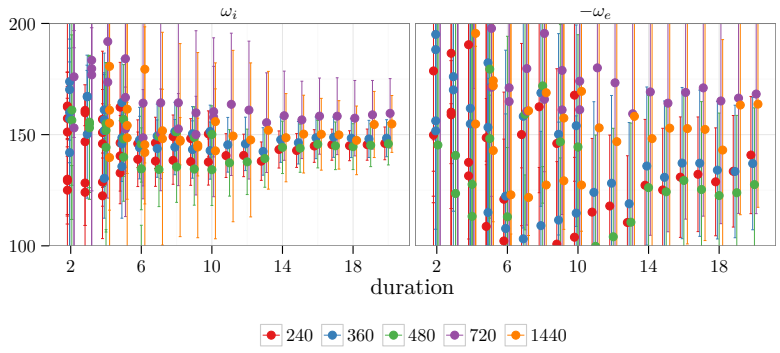

(c) Extension to middle plot: colours now mark five different sampling times, t_s. Moreover, the corresponding scatter points, and the associated confidence intervals, that relate to different t_s, are drawn apart horizontally.

Figure 5.5: Reliability plots.

5.2 Test Case 1: Terraced house in Herstal, Belgium

From February 16 to beginning of May 2012, we performed an extensive co-heating measurement campaign, on a terraced house in Herstal, just north of Liège in Belgium. Figure 5.8 shows its street and garden facade. We estimate its overall heat heat loss coefficient, H, by adopting the strategy elaborated as part of *Scenario 3* (Section 3.6). Particularly interesting about this test case is that, in between successive co-heating test runs, the investigated house was renovated. We can thus estimate H, before and after renovation. Moreover, by comparing these estimates, we can assess the actual renovation induced performance improvement.

5.2.1 Description

The terraced house comprises two floors, an attic and a cellar. Its garden facade is oriented southwest, 15° from the south direction. Table 5.1 collects its main geometric characteristics. It is a heavyweight building, with its facade walls constructed as cavity walls, with two layers of brickwork on either side of a 6 cm wide air cavity. The party walls have a similar design, with a cavity of about 5 cm wide. Floors are constructed in concrete. Both cellar and attic are ventilated. The heated zone comprises floor level 0 (rooms numbered *1* to *5* in Figure 5.7b), and floor level 1 (rooms numbered *6* to *10* in Figure 5.7c).

Table 5.1: Main geometric characteristics

Building volume (outer)	V_o	272.9 m^3
Building volume (inner)	V_i	213.7 m^3
Heat loss surface	A_T	193.1 m^2
Total window area	$A_{w,T}$	18.5 m^2

The timeline in Figure 5.6 collects important dates with regard to the complete measurement campaign. Two renovation steps, *Renovation step 1* and *renovation step 2*, divide the measurement campaign in three co-heating test periods: period *Before*, period *After 1*, and period *After 2*. On March 2, 2012, as part of *renovation step 1*, a contractor insulated the facade and party wall cavities, and the attic floor. Figures 5.9a and 5.9b shows him blowing in insulation in both facade and party wall cavities. That same day, as shown in Figures 5.9c and 5.9d, he also insulated the attic floor slab. On April 16, as part of *renovation step 2*, the basement floor was insulated from underneath.

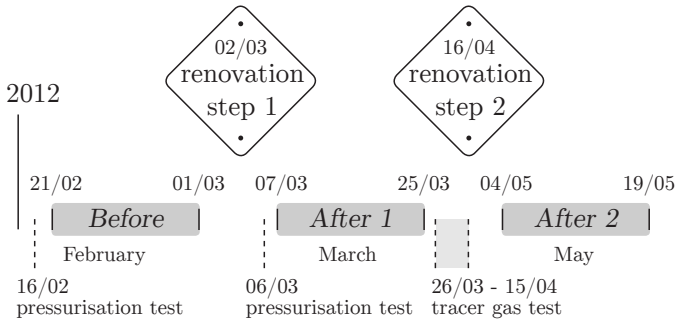

Figure 5.6: Measurement campaign timeline.

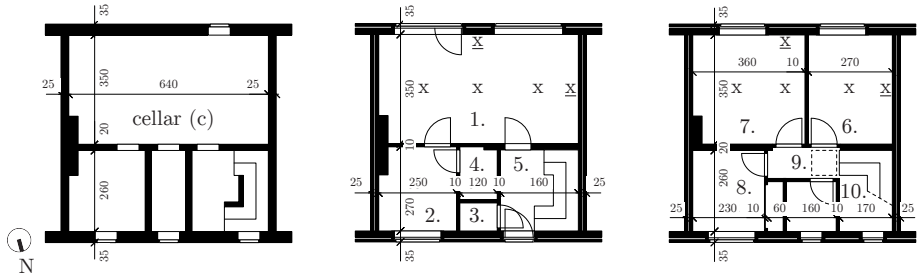

(a) Cellar plan. (b) Ground floor plan. (c) First floor plan.

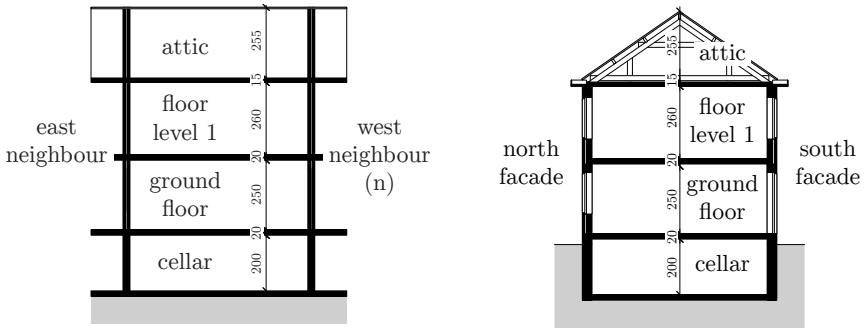

(d) Transverse Section. (e) Longitudinal Section.

Figure 5.7: Schematic plans and sections of the investigated house. The x's locate heat flux and surface temperature sensors. Where underlined, x, they are mounted on the wall.



(a)



(b) Ground floor plan.

Figure 5.8: View of street and garden facade. (Right): A weather station was mounted on a mast in the garden.



(a)



(b)



(c)



(d)

Figure 5.9: (a-b): Blowing in of insulation in the facade (a) and party wall (b) cavities; (c-d): Blowing insulation on the attic floor.

5.2.2 Co-heating test

Figure 5.10 depicts the fully deployed co-heating test equipment. Indoor air temperatures, $T_{i,k}$, are monitored throughout the heated zone. An additional air temperature measurement, T_c, is made in the cellar. Heating powers $\Phi^h_{h,k}$ are monitored in rooms *1*, *2*, *5*, and *6* to *8*. Electric heaters deliver a thermostatically controlled power, with a temperature set-point, $T_{i,sp}$, of 25°C. Outdoor weather conditions are monitored by a weather station that is mounted in the garden, as shown in Figure 5.8b. It measures outdoor air temperature, global horizontal solar radiation, wind speed and wind direction, and precipitation.

Two pressurisation tests were performed: at the start of the measurement campaign, on February 16, and after *renovation step 1*, on March 6. Additionally, tracer gas tests, with indoor gas pressure kept constant, were performed from March 26 to April 15, to collect more detailed information on building envelope airtightness and air infiltration rates. We use their results in a second phase, to distill transmission heat loss, H_{tr}, from H, by correcting for ventilation heat loss, H_v.



(a) Room 2.



(b) Room 1.

Figure 5.10: Co-heating test setup.

Figure 5.11 collects the acquired co-heating measurement data. In period *Before*, the thermostatic control works reasonably well. After renovation, and primarily during period *After 1*, however, T_i regularly overheats, or exceeds $T_{i,sp}$. In period *After 1*, as revealed by the many smooth daily curves in the time series of I_{sol}, a large fraction of the solar radiation I_{sol} is *direct*. In other words, we had many sunny days during this period. Moreover, in March, the sun elevation during mid day is still low, and the south oriented garden facade windows yield high solar gains. In combination with an increasing T_e, T_i tends to overheat. When it does, Φ^h_h reduces to a baseline level, delivered by the

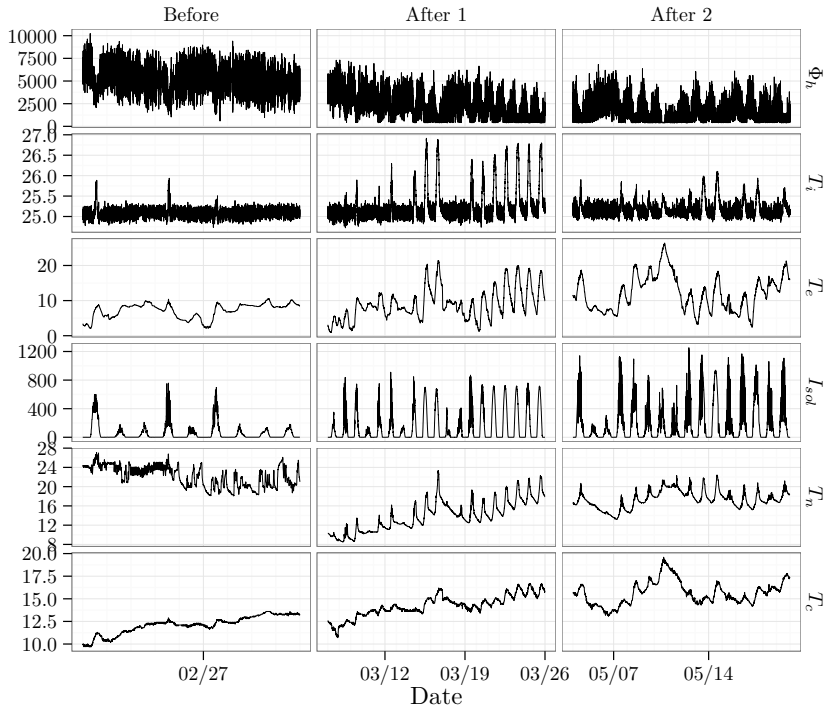

Figure 5.11: Measurement data collected during co-heating test ($t_s = 5$ min). The columns represent periods *Before*, *After 1* and *After 2*. The rows present, from top to bottom: heating power Φ_h^h, in W; first principal component of measured indoor air temperatures T_i, in °C; outdoor air temperature T_e, in °C; global solar radiation, measured perpendicular to a horizontal surface, I_{sol}, in $\mathrm{W\,m^{-2}}$; indoor air temperature of neighbour to the west, T_n, in °C; cellar air temperature T_c, in °C.

ventilators. They run continuously and deliver approximately 370 W. Also in period *After 2*, we see that T_i overheats on some days. T_e has continued to rise, and during this period, we record even higher peak values for I_{sol}. But its rapidly fluctuating values reveal that a large fraction of it is diffuse. Moreover, for this Test Case, I_{sol} is measured perpendicular to a horizontal surface. As the sun now elevates much higher during mid day, higher values for I_{sol} do not necessarily yield higher solar gains through upright windows.

The neighbours to the west allowed us to install one indoor air temperature sensor in their house, T_n in Figure 5.11, and three surface temperature sensors at different heights on their side of the party wall. T_n shows two distinct

dynamics, before and after renovation step 1. In period *After 1*, the inhabitants have moved out. Figure 5.11 clearly illustrates that, as a result, T_n drops out of the comfort zone: in periods *After 1* and *After 2*, T_n is no longer thermostatically controlled by a separate heating system. This is confirmed by the cross-correlation function, $CCF(T_e, T_n)$, in Figure 5.14: in periods *After 1* and *After 2*, T_n varies together with T_e. In period *Before*, it varies independently of T_e. Figure 5.13 plots the autocorrelation (ACF) of Φ_h^h, and the cross-correlation between Φ_h^h and different candidate predictors. Φ_h^h is clearly autocorrelated. Furthermore, it is strongly correlated with I_{sol}, especially in periods *After 1* and *After 2*. Hence, solar gains need to be included as a separate term in the assumed building's heat balance model. It is also moderately correlated with T_i, T_e and T_c. Finally, we discuss its correlation with T_n in more detail in a next Section.

Figure 5.12 shows that, in case of overheating, the first principal component (PC) more closely reflects the overheating that takes place in the heated zone, during mid day, in the south oriented rooms. For this test case, we select it to best represent T_i.

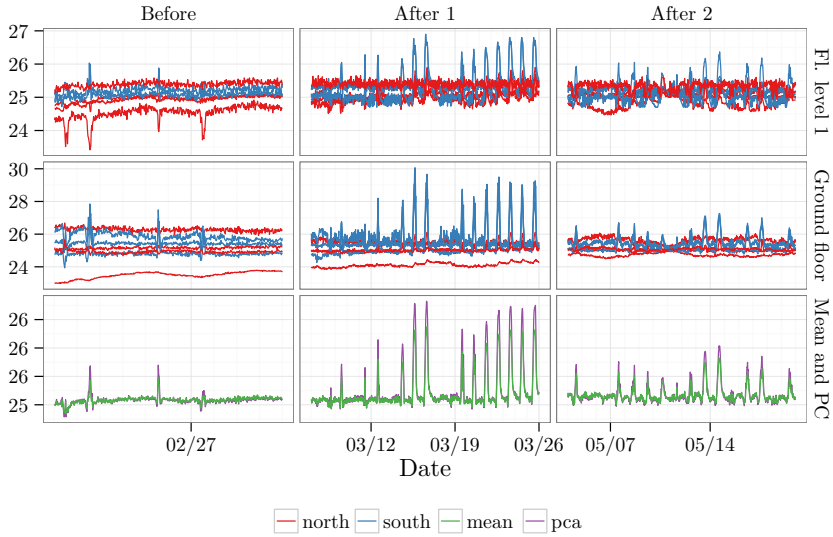

Figure 5.12: Time series of the indoor air temperatures of the different rooms of the heated zone, measured on floor level 1 (top row) and ground floor (middle row); and their mean and first PC (bottom row). Colours distinguish between north and south oriented rooms, and between mean and PC.

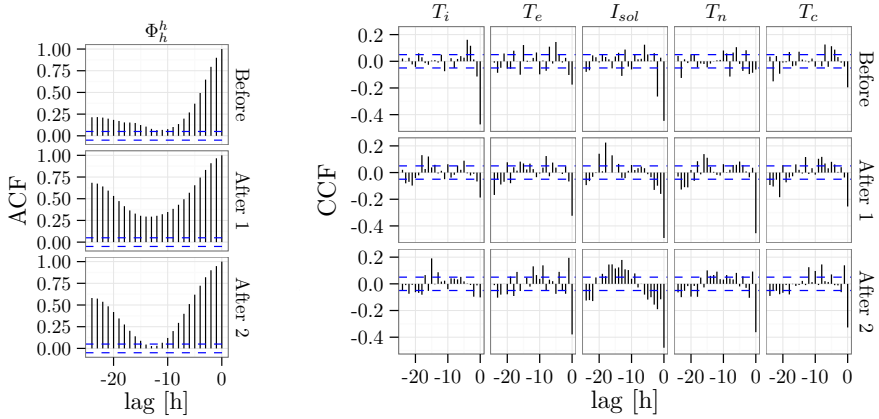

(a) (b)

Figure 5.13: (a): ACF of Φ_h^h. (b): CCFs of Φ_h^h and external variables that might influence the building's heat balance during the co-heating test. We consider data with sampling time, t_s, of 60 min.

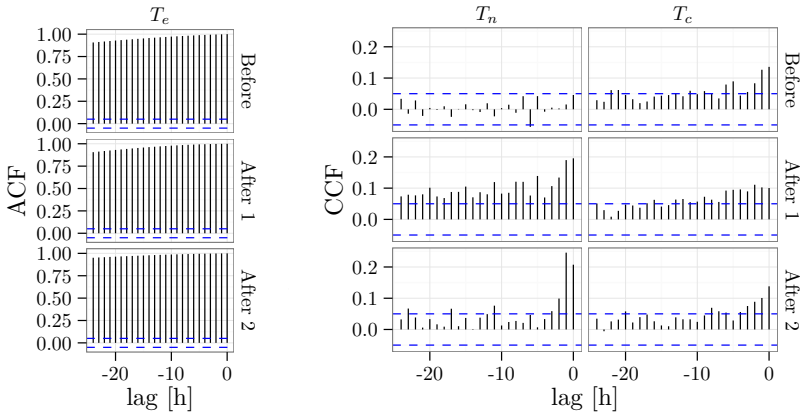

(a) (b)

Figure 5.14: (a): Autocorrelation of T_e. (Middle and right): Cross-correlations between T_e and T_n, and between T_e and T_c. We consider data with sampling time, t_s, of 60 min.

5.2.3 Estimating H using linear regression

The air temperature in the attic has not been monitored during the test. It is, however, a ventilated attic. Figure 5.9d shows how only roof tiles separate it from the external environment. We can thus safely ignore it; T_{attic}'s variation will be significantly informed by T_e and I_{sol}.

As illustrated in Figure 5.14, also the cellar air temperature T_c is significantly correlated with T_e, for all periods. As the house is terraced, it is surrounded by two neighbouring zones. We can thus categorise this test case as a *Scenario 3*, which we introduced in Section 3.6.

In one of the neighbouring houses, the *west neighbour's house*, we measured the indoor air temperature T_n. As illustrated in Figure 5.14, in period *Before*, T_e and T_n are not correlated. We assume the neighbours to the east to similarly control their house to comfort conditions. Hence, in period *Before*, ω_e is likely to remain undisturbed by heat losses towards neighbouring zones, and we can estimate H as $-\omega_e$. On the other hand, in periods *After 1* and *After 2*, T_e and T_n are correlated. As a result, ω_e is disturbed, at least by heat that is lost towards the west neighbour. To resolve this, we subtract the transmission heat loss towards this west neighbour, Φ^n_{tr}, from Φ^h_h. We estimate Φ^n_{tr} as the mean measured heat flux through the involved party wall, multiplied by its area. We then estimate ω_i, ω_e, and ω_{sol} on the basis of Eq. 3.37, on page 50, hence with $\Phi^h_h - \Phi^n_{tr}$ as output. With regard to heat losses towards the other neighbour, we assume that conditions similar to period *Before* persist. After all, only the west neighbour has moved out. The east neighbour is likely to continue a similar control of their indoors, and ω_i will still be disturbed by heat losses towards them. Hence, we do not estimate H as a minimum variance weighting of ω_i and $-\omega_e$. Instead, we rely solely on $-\omega_e$.

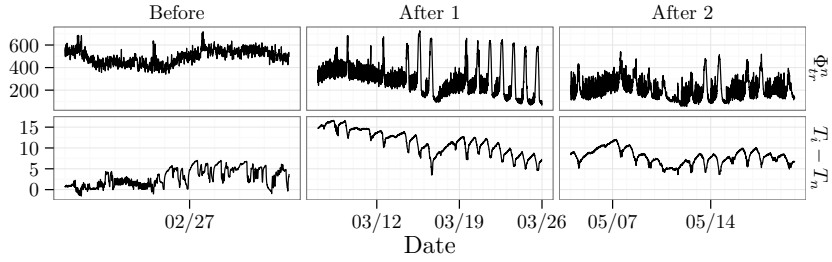

Figure 5.15: (Top): Measured values of heat losses Φ^n_{tr}, in W, towards west neighbour's house. After renovation step 1, this house is vacant. (Bottom): Temperature difference $T_i - T_n$, in °C, between both houses.

To select an appropriate sampling time t_s, we vary it from 240 to 1440 min, and investigate the linear regression model residuals on the basis of cumulative periodograms (Figure 5.16). We opt to assume a similar t_s for each period. We thus select a t_s of 1440 min, as this yields residuals that pass the criteria for white noise, at least based on the cumulative periodogram, for all three periods.

Table 5.2 collects the resulting estimates for H, and Figure 5.17 zooms in on the model residuals, for periods *Before*, *After 1*, *After 2*. Assuming Eq. 3.37, autocorrelated residuals are generated for each period, with significant values for $ACF(\epsilon_t)$ for lower lags. Hence, we should not trust the estimated parameters' confidence intervals (CIs). Nonetheless, they drop from one period to the next (σ_H in Table 5.2). In Section 5.2.5, we zoom in on a potential reason for this: as the building fabric is still thermally charging during period *Before* and *After 1*, estimates for H run the risk of being corrupted.

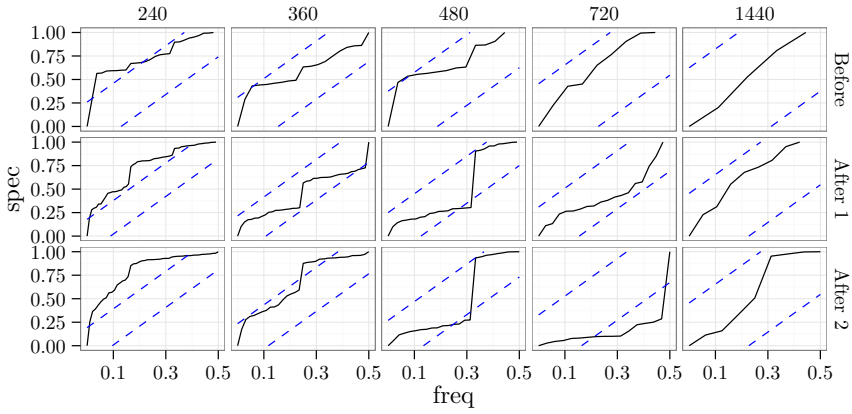

Figure 5.16: Cumulative periodogram, generated by model residuals, for different sampling times t_s.

Table 5.2: Estimates of H, for periods *Before*, *After 1* and *After 2*, using linear regression (Eq. 3.37).

	H	σ_H
Before	246.8	58.7
After 1	144.4	22.7
After 2	132.1	8.7

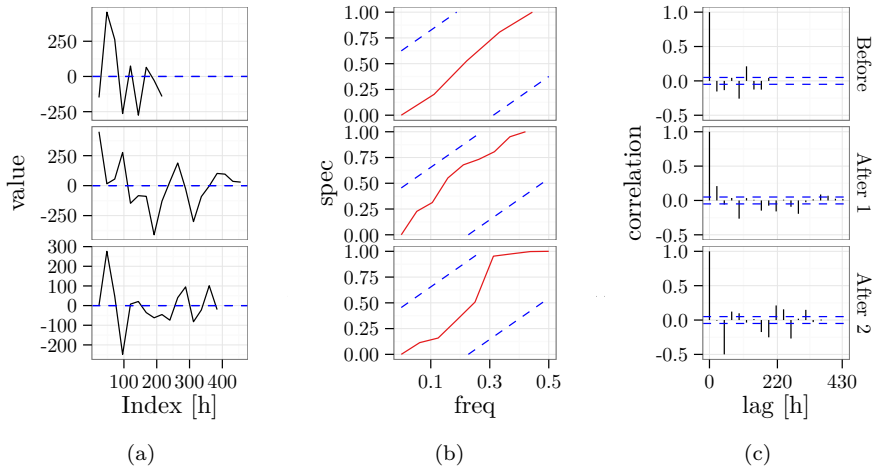

Figure 5.17: Model residuals.

5.2.4 Estimating H_v

As mentioned in Section 3.6, the overall heat loss coefficient H comprises both transmission heat losses, H_{tr}, and ventilation heat losses, H_v. To decouple both, we need to estimate the actual air change rate, n_{actual}, that takes place during the measurement campaign. As indicated in Figure 5.6, two pressurisation tests were performed, before and after renovation step 1. Moreover, a tracer gas test was applied between periods *After 1* and *After 2*.

Pressurisation tests estimate the n_{50}-value. From this value, we deduce a stationary estimate for the actual air change rate n_{actual}, using the rule of thumb introduced in Section 3.3: $n_{actual} = \frac{n_{50}}{20}$. On the other hand, tracer gas tests lead to direct estimates of n_{actual}. They are plotted in Figure 5.18.

Estimates based on pressurisation tests yield values of 0.18 h^{-1}, before renovation step 1, and 0.2 h^{-1}, after renovation step 1. They are indicated with red horizontal lines in Figure 5.18. They both seem to underestimate the actual air change rate. Seldom we see tracer gas test values drop below these numbers. Their mean, median, and mode values amount to 0.44 h^{-1}, 0.34 h^{-1}, and 0.29 h^{-1}, respectively.

Figure 5.19 shows that the values for ΔT, wind speed, w_v, and wind direction, w_d, that are measured during the period in which n_{actual} is available, do not differ significantly from their values in periods *Before*, *After 1* and *After 2*.

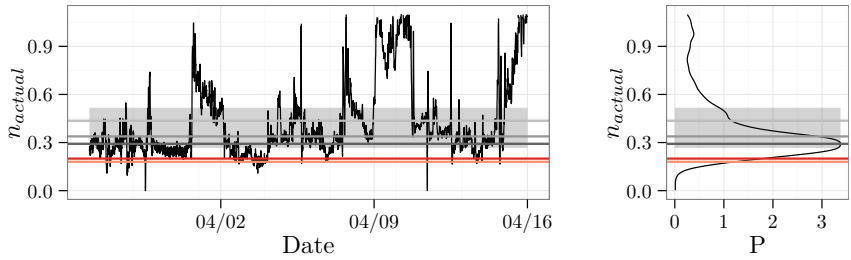

Figure 5.18: Estimated actual air change rates, in h^{-1}, using tracer gas testing. The probability distribution unveils skewness of the data. The grey horizontal lines depict, from top to bottom, mean, median and mode values of n_{actual}. An asymmetric ribbon around the median value spans from first to third quantile. The red lines denote estimates for n_{actual}, that are derived from pressurisation tests before (0.18 h^{-1}, light red) and after (0.2 h^{-1}, dark red) renovation step 1.

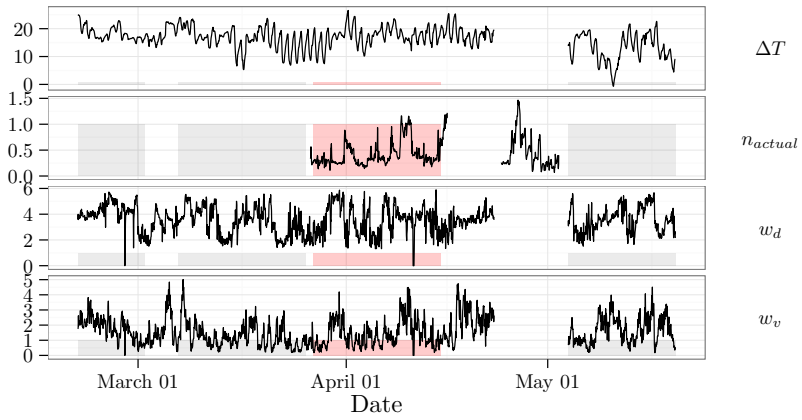

Figure 5.19: Measured values for $\Delta T = T_i - T_e$, in °C; Actual air change rate, n_{actual}, in h^{-1}; Wind velocity, w_v, in $m\,s^{-1}$; Wind direction, w_d, in rad, increasing eastward from north. Grey bands mark, from left to right, test periods *Before*, *After 1*, and *After 2*. Red bands mark the tracer gas test period (Figure 5.18).

Hence, instead of relying on pressurisation test results, we could argue for relying on these tracer gas test results. We thus propose to assume the corresponding mean value for n_{actual}, to calculate H_v, on the basis of Eq. 2.20 (Chapter 2, page 22). With $c_a = 1012\ J\,kg^{-1}\,K^{-1}$, $\rho_a = 1.25\ kg\,m^{-3}$, and a net volume, including interior walls and floor, of 213.7 m^3, H_v amounts to 25.4 $W\,K^{-1}$. We assume this value as a 'constant', for periods *Before*, *After 1* and *After 2*.

5.2.5 Thermally charging building fabric

In addition to the co-heating test, heat flux and surface temperature sensors were mounted on the indoor surfaces of different building fabric components (Figure 5.20). They allow us to evaluate their performance in detail. And they help us to assess the quality of the co-heating test.



(a) Ground floor above cellar.



(b) Facade wall.

Figure 5.20: Heat flux sensors and surface temperature sensors, mounted at the indoor surfaces of different fabric components.

The heat flux and surface temperature measurements are collected in Figures 5.22a and 5.22b, respectively. They reveal that the building fabric is only slowly heating up, and that it continuous to *thermally charge* until well into our measurement campaign. As shown in Figure 5.21, the house was pre-heated for a number of days. But the indoor air temperature, and the building fabric, had dropped to very low levels, due to inoccupancy and winter conditions. Moreover, with concrete floors and brickwork, this is a heavy-weight building, that demands significant heating energy to lift its fabric's temperature.

A considerable part of Φ_h^h thus ends up heating the fabric, instead of directly sustaining a thermostatically controlled T_i. As we overestimate Φ_h^h, that is needed to sustain T_i, we run the risk of overestimating H. To assess how important this risk is, we consider the measured heat fluxes at the ceiling, plotted in Figure 5.22a (top right). During period *Before*, average values lie around 40 $\mathrm{W\,m^{-2}}$, which, when integrated over the whole ceiling surface, corresponds to a power of 1.9 kW. Although the larger part of this is associated with heat exchange between T_i and T_e, a considerable part of that serves to heat up T_{si}. For instance, Figure 5.22b shows that, in period *Before*, the ceiling surface temperature increases by about 2 °C. Let us assume that we manage to heat up a capacity of 3.65×10^7 $\mathrm{J\,K^{-1}}$ (7 cm of this concrete ceiling, with a capacity of 6.09×10^6 $\mathrm{J\,K^{-1}}$, multiplied by 10 to safely account for other

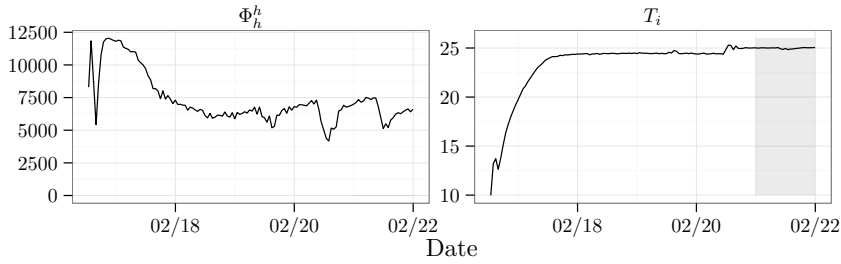

Figure 5.21: Pre-heating of house to attain stable co-heating test conditions. The start of the co-heating test period is indicated with a grey band. (Left): Heating power Φ_h^h, in W. (Right): Indoor air temperature T_i, in °C.

fabric parts), with 2 °C. If we want to accomplish this over the span of 8 days in period *Before*, this amounts to a heating power of 106 W. Compared to the mean value of Φ_h^h, during period *Before*, a mere 2.0 %. The influence of a thermally charging fabric thus remains small, especially in case H is high, as in this Test Case, before renovation step 1.

High heat flux values are measured in period *Before*, especially at the ceiling, but also in period *After 1*, at the floor above cellar. Only in period *After 2*, the fabric seems to have settled down. Before renovation step 1, the ceiling has not been insulated yet, hence it discharges heat towards the attic. As a result, during period *Before*, it only slowly heats up. After renovation step 1, however, measured heat flux values rapidly drop and the ceiling indoor surface temperature (top right plot in Figure 5.22b) rapidly attains stable levels. The same phenomenon can be seen at the floor above cellar, which in renovation step 2 is insulated from underneath. Hence, a building, be it heavy-weight or light-weight, is more easily pre-heated to quasi-stationary conditions, suitable for a co-heating test, when it is well-insulated.

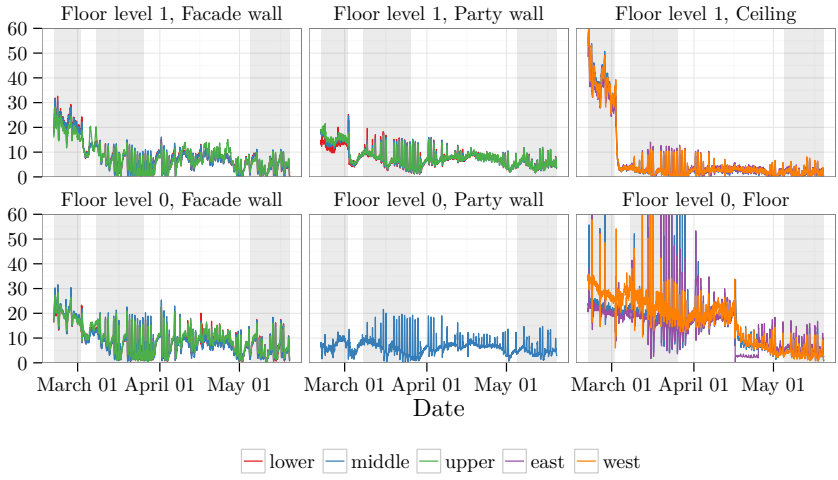

(a) Heat flux measurements, in $\mathrm{W\,m^{-2}}$.

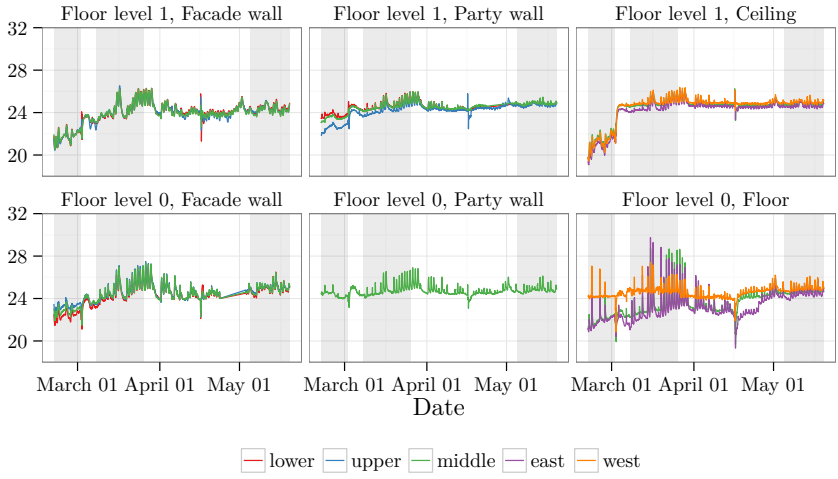

(b) Surface temperature measurements, in °C.

Figure 5.22: Values measured by (a) heat flux and (b) surface temperature sensors, mounted on different locations on the south facade wall, west party wall, ceiling and floor above cellar. Except for the sensors mounted on the floor above cellar (bottom right), they are not irradiated directly. The regular peaks are due to T_i that overheats. Grey bands mark, from left to right, test periods *Before*, *After 1*, and *After 2*.

5.2.6 Reliability plots

Although μ, in Eq. 3.37, is not forced to 0, in some cases, it is neglected as a result of the linear regression analysis. A positive ω_i can then be estimated. The estimates for ω_i appear to be stable, and are associated with small confidence intervals (CIs). On the other hand, ω_e is associated with larger CIs, although for larger durations they attain reasonable levels. In general, we have small CIs, but they should not be trusted, as Figure 5.17 showed that residuals are autocorrelated.

In period *Before*, $-\omega_e$ seems less stable, than in periods *After 1* and *After 2*, when the house is insulated. For a duration of 9 days, estimates for different t_s deviate up to 51.4 % from their mean. As discussed in Section 5.2.5, it is unlikely that this is due to the thermally charging building fabric. In any case, we have less measurement days, and estimates for H generally show a larger spread for shorter durations. When we compare period *Before*, with the results for periods *After 1* and *After 2*, the fact that we do not obtain consistent results in period *Before* is likely due to its limited duration. In period *After 1*, as of 11 days, consistent results for $-\omega_e$ seem to be obtained. However, they are not very robust. Depending on the chosen sampling time t_s, the estimates deviate up to 30 % from the mean. Similarly, in period *After 2*, as of 9 days, estimates still deviate up to 32 %.

5.2.7 Comparison with expected values

In Table 5.3, we compare H_{tr}, estimated as $H - H_v$, with its design value. Remarkably, the estimated values are much lower than the design values. As we know little about the actual performance characteristics of the building's materials and its construction, we were unable to pinpoint the exact reasons for this discrepancy. Nevertheless, the expected reductions of H_{tr}, induced by renovation step 1 and 2, can be calculated on the basis of the thickness of applied insulation and their λ-values. Table 5.4, on page 106, collects the expected values for H_{tr}, together with the contributions from the different building envelope parts, in the three measurement periods.

We focus on renovation step 1. From Table 5.3, we find that H_{tr} reduces by 102.4 $\mathrm{W\,K^{-1}}$. But we expected that, by insulating facade and party walls, and insulating the attic floor, H_{tr} would reduce by 167.7 $\mathrm{W\,K^{-1}}$. A likely reason for this discrepancy lies in the way the building was originally constructed. At the time of construction, it was common practice to close the cavity around the windows to reduce the difficulty of installing and stabilising window frames. As no insulation can be blown in where there is no cavity, locally, thermal

performance is not improved. This is clearly illustrated in the IR-images in Figure 5.24. The expected value for H_{tr} already assumes that 20 % of the cavity is not filled with insulation. But in reality, this fraction might be higher. Aside from structural elements, other impurities, e.g. connections of both masonry wall, or leafs and rubble in the cavity, might further reduce the actual reduction of H_{tr}.

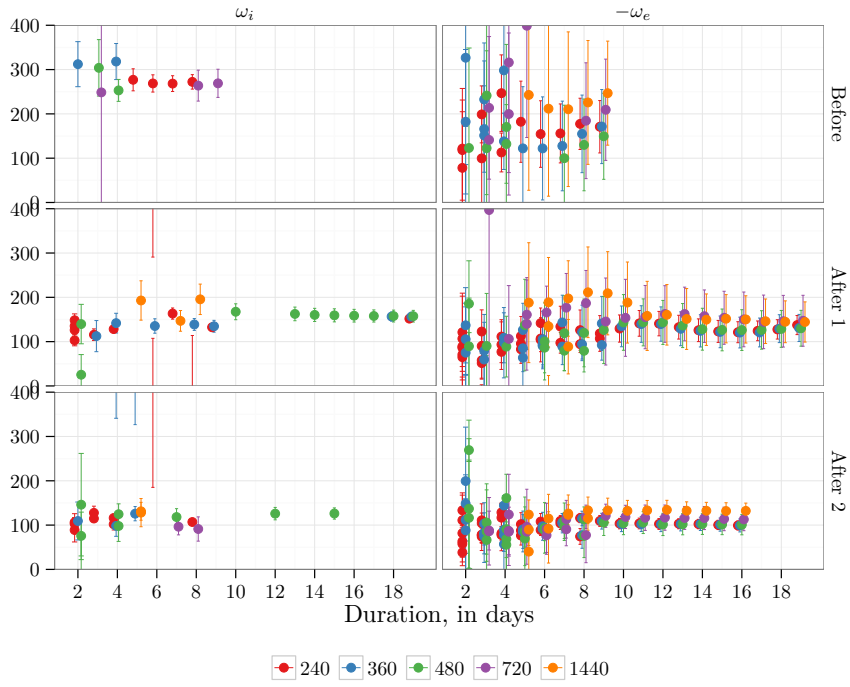

Figure 5.23: Estimates of ω_i (left column) and $-\omega_e$ (right column), in $\mathrm{W\,K^{-1}}$, that result from a linear regression analysis, assuming model $\Phi_h^h = \omega_i T_{i,avg} + \omega_e T_{e,avg} + \omega_{sol} I_{sol,avg} + \mu + \epsilon$ in period *Before*. In periods *After 1* and *After 2*, the model output is changed to $\Phi_h^h - \Phi_{tr}^n$, with Φ_{tr}^n the transmission heat loss towards the west neighbour. For each period, H is estimated as $-\omega_e$. The rows refer to co-heating test periods *Before*, *After 1*, and *After 2*. For each period, different sampling times t_s (dodged position and colour of points), and data subsets with varying duration (x-axis), are considered.

Table 5.3: Estimates of overall transmission heat loss coefficient H_{tr}, in $\mathrm{W\,K^{-1}}$. $\sigma_{H_{tr}}$ ignores the uncertainty, associated with H_v.

	Expected	Estimated using LR	$\sigma_{H_{tr}}$
Before	374.1	221.4	58.7
After 1	206.4	119	22.7
After 2	145.4	106.7	8.7

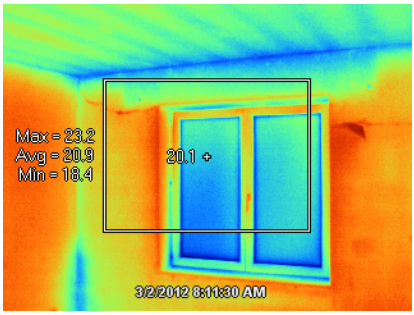

(a)

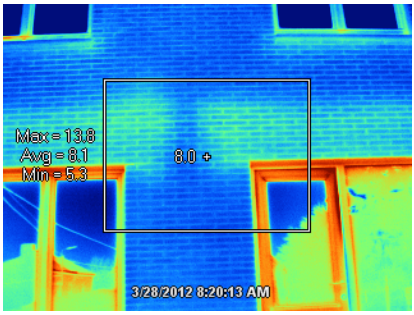

(b)

Figure 5.24: Infrared images clearly showing the cavity being closed at the lintel and sill.

Table 5.4: Expected thermal performance characteristics of different envelope parts and corresponding expected values for H_{tr}. Surface area A, in $\mathrm{m^2}$; heat transfer coefficient U, in $\mathrm{W\,m^{-2}\,K^{-1}}$; Transmission heat loss coefficient H_{tr}, in $\mathrm{W\,K^{-1}}$. (i) refers to that part of the facade wall that is insulated in renovation step 1.

Period		**Before**		**After 1**		**After 2**	
Component	A	U	H_{tr}	U	H_{tr}	U	H_{tr}
Roof	48.3	2.9	139.1	0.2	8.2	0.2	8.2
Facade wall (i)	62.4	1	61.8	0.4	25	0.4	25
Facade wall	15.6	2.7	42.1	2.7	42.1	2.7	42.1
Party wall	79.1	0.9	-	0.4	-	0.4	-
Floor	48.3	1.6	79.4	1.6	79.4	0.4	18.4
Windows	18.5	2.8	51.7	2.8	51.7	2.8	51.7
Total			**374.1**		**206.4**		**145.4**

5.2.8 Discussion

The house is terraced, with two neighbouring houses. Hence, we categorised it as Scenario 3. However, the west and east neighbours exhibit very different behaviour. To properly analyse this, we assembled the two strategies that are suggested in Section 3.6. As soon as T_n, the air temperature of the west neighbour started to show significant correlations with T_e, we assumed $\Phi_h^h - \Phi_{tr}^n$ as model output, thereby filtering out heat losses towards this neighbour. Φ_{tr}^n only captures transmission heat losses towards the west neighbour. Hence, we should not rely on ω_i, but on $-\omega_e$, to estimate H.

For this Test Case, we did not force μ, in Eq. 3.37, to zero. Especially in period *Before*, we have a thermally charging fabric, and important heat losses towards neighbouring zones. On the other hand, during periods *After 1* and especially *After 2*, we could argue that $\mu \approx 0$. Most of the building fabric has reached stable temperature levels, and insulating the party walls as part of renovation step 1, reduces heat losses towards neighbouring zones to 6 % of the total heating power (calculations in Section 3.5.1).

Table 5.2 showed that the confidence interval around the estimate for H decreases significantly, from period *Before*, over period *After 1*, to period *After 2*. Reasons for this include: the duration of the experiment, 9 days (*Before*), 19 days (*After 1*) and 16 days (*After 2*); the thermally charging building fabric, especially in period *Before*, and less significantly in period *After 1*; incomplete modelling of long-wave radiative heat exchange between indoor surfaces, and between sky and outdoor surfaces; and solar gains that overheat T_i, especially in period *After 1*. The latter causes σ_H, for period *After 1*, to be higher than σ_H, for *After 2*, even though in period *After 1* we have more measurement days.

5.3 Test Case 2: Detached house in Limelette, Belgium

In this Test Case, we investigate a co-heating test, performed on a detached test house, located on the premises of the Belgian Building Research Institute (BBRI) in Limelette, Belgium. Whereas in Test Case 1, we only applied linear regression analysis on measurement data sampled over larger sampling times t_s, we now additionally feed data to the ARX models, that we introduced on page 49 of Chapter 3. As these models explicitly model Φ_h^h's autocorrelation, they tolerate much smaller t_s. Moreover, they more easily generate white noise residuals, and thus more accurately estimate H's confidence interval.

5.3.1 Description

The test house is detached, and comprises a heated ground floor level, a cellar and an attic. Both cellar and attic are naturally ventilated. The longer side of the house is oriented parallel to the east-west axis. The main room has a large glazed facade part that faces south. Figure 5.25 collects plans and pictures of the investigated house. Table 5.5 collects its main geometric characteristics.

The ceiling floor, between ground floor and attic, is a light-weight wooden structure, insulated with 18 cm of mineral wool (MW). The floor above the cellar comprises a heavy-weight concrete structure, with on top a 6 cm thick layer of screed, that rests on 5 cm of expanded polystyrene (EPS). With regard to the thickness of the latter, the building plans and detailed drawings contradict themselves: one detail mentions 2.5 cm of insulation, and another mentions 5 cm; A typical example of uncertainties, that creep into the building process. We assume 5 cm of insulation, as this also returns in thermal performance calculations, performed by researchers at BBRI. Anyhow, this floor, and the stair case connecting the attic with the ground floor level, are additionally insulated from underneath, with 5 cm of expanded polystyrene (EPS). The facades are cavity walls, with concrete block walls at either side of 10 cm of mineral wool insulation. Windows are double glazed, with an associated U-value of 1.3 $\mathrm{W\,m^{-2}\,K^{-1}}$, and are built into wooden frames.

Table 5.5: Main geometric characteristics

Building volume (outer)	V_o	332.4 $\mathrm{m^3}$
Building volume (inner)	V_i	239.6 $\mathrm{m^3}$
Heat loss surface	A_T	346.9 $\mathrm{m^2}$
Total window area	$A_{w,T}$	27.8 $\mathrm{m^2}$

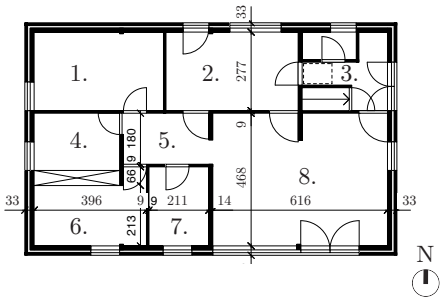

(a) Ground floor plan.

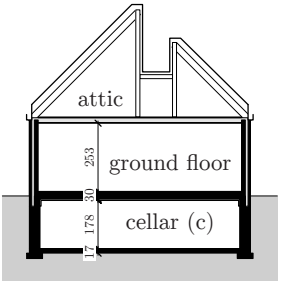

(b) Section along north-south axis.



(c) View of south and east facades.



(d) View of north and west facades.

Figure 5.25: Building plans and pictures of the detached test house at BBRI's premises in Limelette, Belgium.



(a) Co-heating test setup in hallway.



(b) Co-heating test setup in living room.

Figure 5.26: Co-heating test set up in the test house.

5.3.2 Co-heating test

Figure 5.26 depicts the experiment, set up inside the house. And Figure 5.27 shows the co-heating measurement data set, collected from February 21 to March 12, 2012. The actual heating experiment started earlier, but we tuned it to obtain more homogeneous temperatures. Among others, low powered IR-lamps were added in rooms *5* and *7*, to provide more localised heating power. Moreover, as we illustrated in Test Case 1, the building's thermal mass takes some days to charge to an equilibrium level. By February 15, homogeneous stationary conditions had been reached throughout the building. On February 20, however, we miss a series of data points for T_e. We thus consider the data as of February 21.

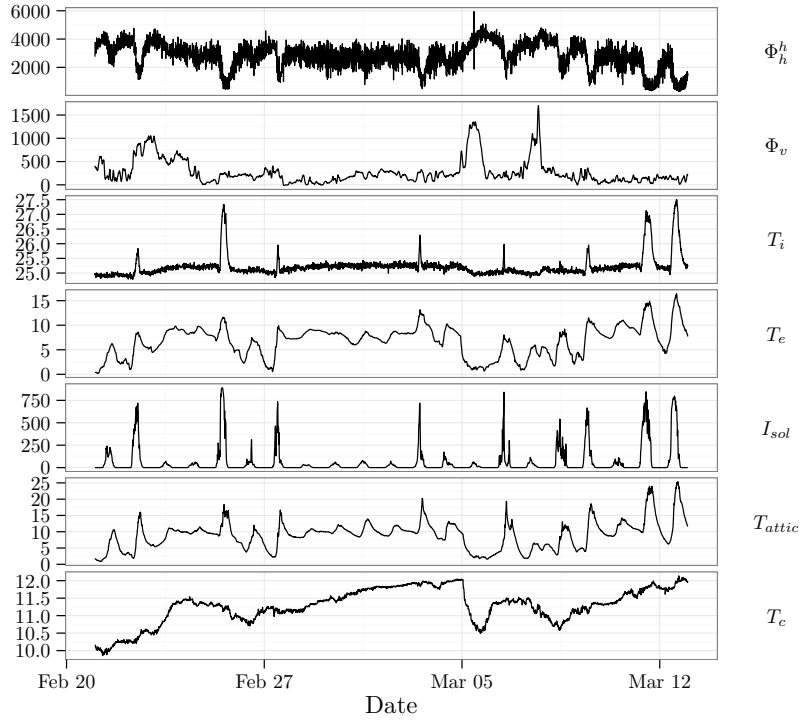

Figure 5.27: Co-heating measurement data ($t_s = 5$ min): heating power Φ_h^h, in W; volume-weighted indoor air temperature T_i, in °C; outdoor air temperature T_e, in °C; vertical south global solar radiation I_{sol}, in $\mathrm{W\,m^{-2}}$; first principal component of attic air temperatures T_{attic}, in °C; first principal component of cellar air temperatures T_c, in °C.

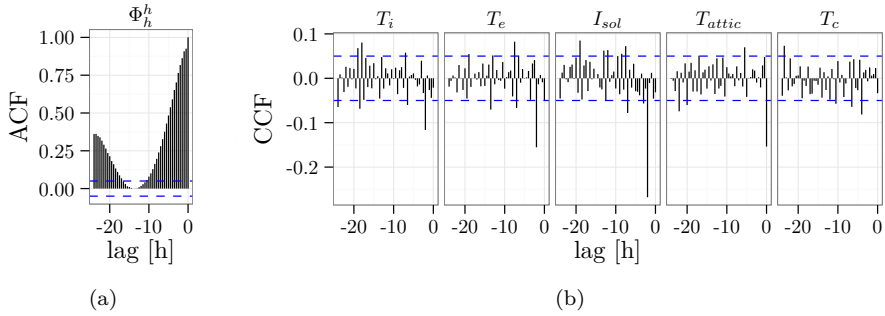

Figure 5.28: (a): $ACF(\Phi_h^h)$; (b): CCFs between Φ_h^h and candidate predictors T_i, T_e, I_{sol}, T_{attic} and T_c. 60-min averaged values are assumed.

Throughout the co-heating test, the heating power Φ_h^h is monitored. Complementary to the standard co-heating test, researchers at BBRI measured the actual air change rate, n_{actual}, of the ground floor level, using tracer gas tests with constant gas concentration. The results are plotted in Figure 5.29. From the measured values of n_{actual}, by applying Eq. 2.20, on page 22 in Chapter 2, we deduce the actual ventilation heat loss Φ_v, that takes place during the experiment.

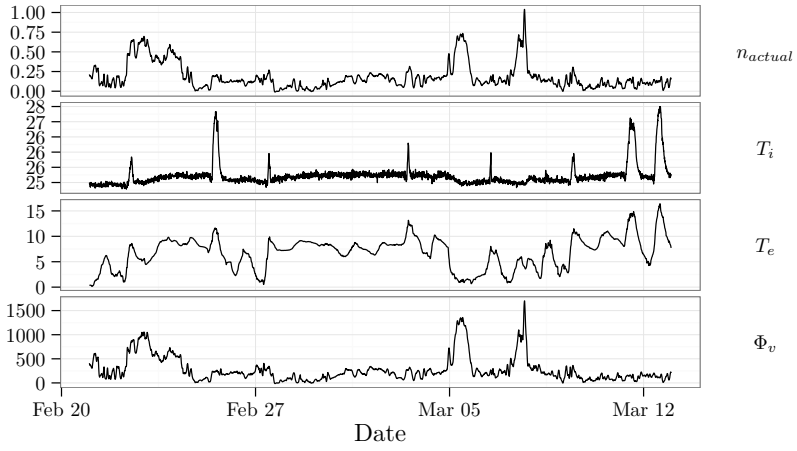

Figure 5.29: Ventilation heat loss, Φ_v, in W, calculated assuming the measured air change rate, n_{actual}, in h^{-1}, the volume-weighted indoor air temperature T_i, in °C, and outdoor air temperature T_e, in °C.

Given an interior air volume of 239.6 m^2, and a mean measured value for n_{actual} of 0.2 h^{-1}, H_v averages 14.7 $W K^{-1}$. Not always do we have such detailed information available to us. As an alternative, and similar to Test Case 1, we can estimate n_{actual} based on pressurisation test results and apply the rule of thumb (Section 3.3): $n_{actual} = \frac{n_{50}}{20}$. Martin et al. (1997) report an n_{50}-value of 1.5 h^{-1}, measured just after a range of measures were taken to improve the house's airtightness. Lethe et al. (2014) report a value of 4.3 h^{-1}. On October 11, we measured a n_{50}-value of 1.9 h^{-1} at both underpressure and overpressure. Assuming the latter, we obtain that $n_{actual} \approx 0.1$ h^{-1}, and $H_v =$ 7.6 $W K^{-1}$. In this case, we seem to obtain better results when we, as part of the rule of thumb, divide n_{50} by 10. We then obtain a H_v of 15.2 $W K^{-1}$. In any case, H_v is small, and only about 10 %, compared to H_{tr} (Section 5.3.6).

The indoor air temperature is elevated to a temperature set point $T_{i,sp}$ of 25 °C. During sunny days, solar gains tend to cover more than the actual heat load. Φ_h^h then drops to minimal values, and T_i rises above $T_{i,sp}$. Figure 5.30 shows air temperatures, that we measured in three zones: the conditioned rooms 1 to 8, the cellar and attic. For each of these zones, we calculate the principal component (PC), to represent the array of available temperature measurements. For cellar and attic, this yields reasonable results. But for rooms 1 to 8, the PC is drawn towards the indoor air temperature measured in room 3, $T_{i,3}$. We did not provide a separate heater for this room, and as a result, its temperature is lower and more responsive to external influences. It is, however, a small room, and it should only have a limited influence on T_i. In Figure 5.30, we plot two alternatives. First, we simply average the T_i's measured in each room. We thus obtain a signal that is also drawn towards $T_{i,3}$. Moreover, it minimises the effect of overheating. Second, we consider a volume-weighted average. This signal is more sensitive to overheating, that occurs mostly in the large room 8, and attributes only limited weight to $T_{i,3}$. Hence, as a basis for analysis, we select the volume-weighted average T_i. For T_{attic} and T_c, we retain their PCs.

The air temperature sensor in room 6 failed to monitor the indoor air temperature during most of the heating experiment. Therefore, we did not consider it when constructing a representative indoor air temperature signal. Before and after this sensor failed, however, it showed very stable and consistent values around 25 °C.

The outdoor air temperature, T_e, varies over a range of about 15 °C. Sunny days alternate with cloudy days. Solar radiation input, I_{sol}, represents the global solar radiation measured perpendicular to an upright and south oriented surface. As shown in Figure 5.27, and confirmed by the CCF in Figure 5.31, T_{attic} varies together with T_e. On the other hand, the cellar air temperature, T_c, varies only little during the experiment, and independently from T_e and T_i. Nonetheless, the heating experiment causes it to gradually heat up, by 2 °C.

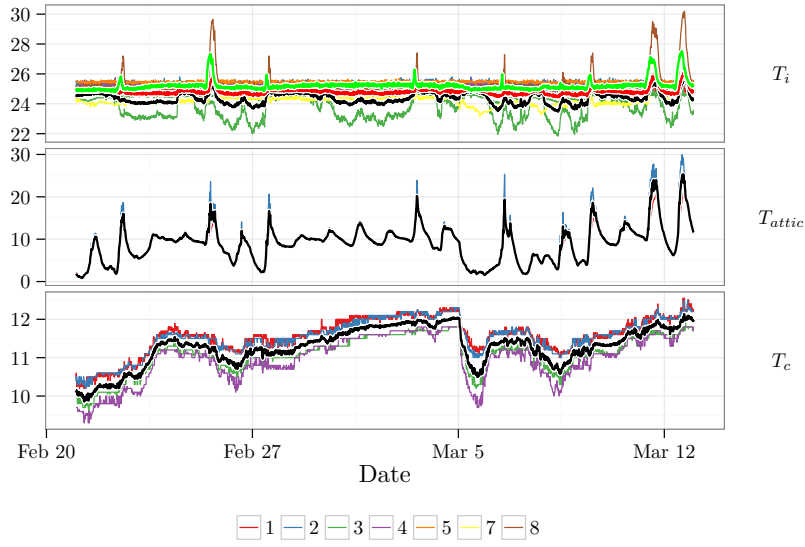

Figure 5.30: Principal component (PC) analysis to construct air temperature signals T_i, T_{attic} and T_c, that represent the range of air temperatures sensed in these zones: different rooms, and at different locations in larger rooms. For the heated volume, T_i, numbers 1 to 8 refer to the room numbers defined in Figure 5.25. The PCs are indicated by thick black lines. For T_i, as an alternative to its first PC, a plain average (thick red line) and a volume-weighted average (thick green line) are plotted.

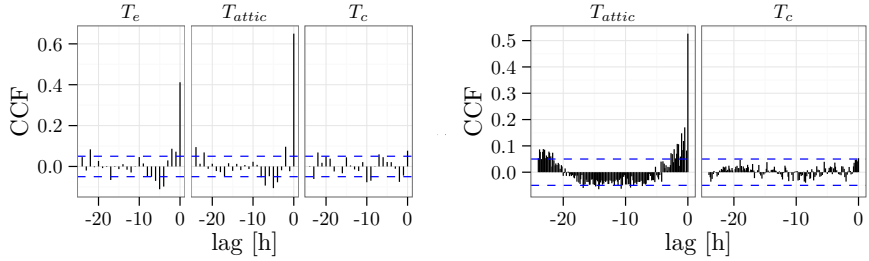

Figure 5.31: (a): Cross-correlations of T_i with T_e, T_{attic} and T_c. (b): Cross-correlations of T_e with T_{attic} and T_c. 60-min averaged values are assumed.

5.3.3 Estimating H_{tr} using linear regression

For this test case, we have detailed knowledge of the actual ventilation heat loss, Φ_v, that occurs during the test (Figure 5.29). Hence, in this section and the next, we focus on the transmission heat loss, H_{tr}. We estimate it based on Eq. 3.33 on page 48, but with $\Phi_h^h - \Phi_v$ as the model output:

$$\Phi_h^h - \Phi_v = \omega_i T_{i,avg} + \omega_e T_{e,avg} + \omega_{sol} I_{sol,avg} + \epsilon \tag{5.1}$$

Figure 5.31 showed that T_{attic} is correlated with T_e. This does not hold, however, for the cellar air temperature, T_c. T_c represents a slowly varying temperature, that is uncorrelated with both T_i and T_e. We can thus compare this test case with *Scenario 2*, introduced in Section 3.6 of Chapter 3: T_c effectively behaves as a soil mass, and a correct assessment of H includes heat losses from T_i to T_c. As T_c is not correlated with T_e, ω_e will fail to capture this. Instead, we estimate H as ω_i.

We consider $T_{i,avg}$, $T_{e,avg}$ and $I_{sol,avg}$ as candidate predictors. They represent averages of two successive values of the original time series. Predictors that prove insignificant are skipped. To estimate physically relevant values for ω_i, we ignore μ. We thereby ignore the physical phenomena that are lumped into this constant. For this specific case, the primary factor that might cause μ to drift away from 0, are heat exchanges between T_i and T_c. The associated transmission heat loss coefficient, H_{tr}^c, amounts to 33.2 $\mathrm{W\,K^{-1}}$. Multiplied by the average value $T_i - T_c$ during the experiment, this demands a heating power of about 461.6 W, or 18.5 % of the mean value of $\Phi_h^h - \Phi_v$. Not a small number. Imagine we add, to Eq. 5.1, $T_{c,avg}$ as an additional predictor:

$$\Phi_h^h - \Phi_v = \omega_i T_{i,avg} + \omega_e T_{e,avg} + \omega_{sol} I_{sol,avg} + \omega_c T_{c,avg} + \epsilon \tag{5.2}$$

Similar to the other predictors, we average it over current and previous values. We now compare the order of magnitude of the term $\omega_c T_{c,avg}$ to the other terms in Eq. 5.2. Multiplying the expected value H_{tr}^c with T_c's mean value, it represents a power of about 380 W. Compared to the term $\omega_i T_{i,avg}$, that we expect to lie around 3630 W, this amounts to 10.5 %. Still relatively important.

When we retain $\omega_c T_{c,avg}$ in Eq. 5.2, however, we obtain values for ω_i that are not within expected ranges. Adding this term makes the model overly complex with respect to the data, and clearly corrupts the resulting parameter estimates. We therefore decide to ignore it, and stick to Eq. 5.1. As a side-note, from Figure 5.31b, we learn that T_c is minimally correlated with T_e. Hence, ω_e, and perhaps also ω_{sol}, might take on some of T_c's influence on our model output.

To select an appropriate sampling time t_s, we vary t_s from 240 to 1440 min, and investigate the linear regression (LR) model residuals on the basis of periodograms and cumulative periodograms.

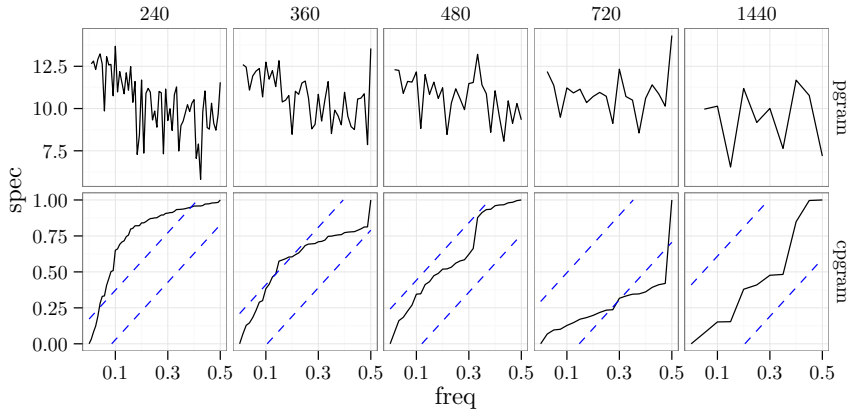

Figure 5.32: Cumulative periodogram of residuals.

From Figure 5.32, we conclude that the model performs well, when sampling times t_s are either 8 h (480 min), or 24 h (1440 min). To retain a maximum amount of informative data points, we select a t_s of 8 h. Figure 5.33 plots the input and output time series, and in red, the model output, $\hat{\Phi}_h^h$. Figure 5.34 plots the residual autocorrelation, $ACF(\epsilon_t)$, and its cross-correlation with model output Φ_h^h, and model inputs. Similar to Test Case 1, we find that the LR method generates autocorrelated residuals; the values for $ACF(\epsilon_t)$ regularly exceed the confidence bounds. Hence, we do not obtain white noise. The resulting estimate for H might thus be biased, and its confidence interval is underestimated. Table 5.6 collects the estimated regression coefficients, and derived estimates for H and A_{sol}. Finally, Figure 5.35 visualises the retained co-heating test data points and the linear regression lines that we fit through them. This way of visualising co-heating test analysis was introduced in Section 3.6.3 of Chapter 3.

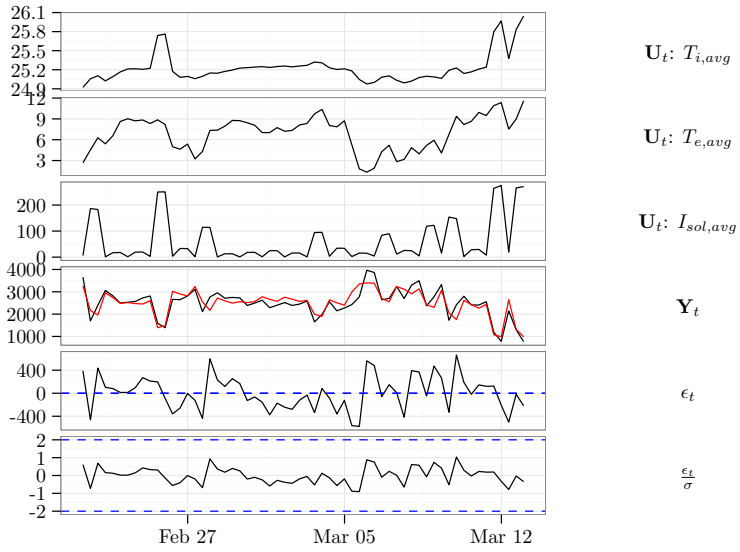

Figure 5.33: Time series plots of inputs $\mathbf{U}_t$: $T_{i,avg}$ and $T_{e,avg}$, in °C, and $I_{sol,avg}$, in $\mathrm{W\,m^{-2}}$; outputs $\mathbf{Y}_t$: measured output, Φ_h^h, and model output, $\hat{\Phi}_h^h$ (red), in W; residuals $\epsilon_t = \Phi_h^h - \hat{\Phi}_h^h$, and normalised residuals $\frac{\epsilon_t}{\sigma}$.

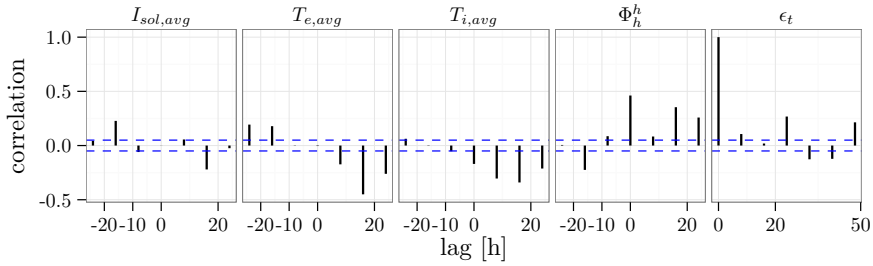

Figure 5.34: (All but right): Cross-correlations of candidate predictors $I_{sol,avg}$, $T_{e,avg}$, $T_{i,avg}$ and output Φ_h^h, with model generated residuals, ϵ_t. (Right): $ACF(\epsilon_t)$.

Table 5.6: Estimated regression coefficients, transmission heat loss coefficient H_{tr}, in $\mathrm{W\,K^{-1}}$, and global solar aperture A_{sol}, in $\mathrm{m^2}$, estimated by applying linear regression on aggregated co-heating test data.

	Estimate	σ
ω_i	145.9	4.8
ω_e	-127.5	17.2
ω_{sol}	-4.9	0.5
H_{tr}	145.9	4.8
A_{sol}	4.9	0.5

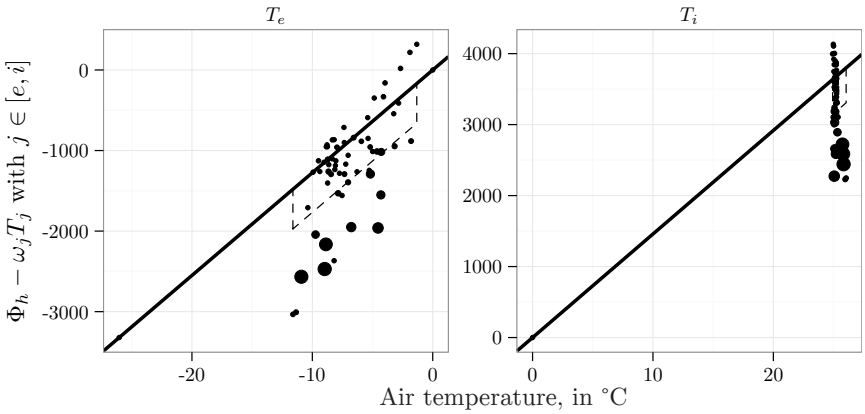

Figure 5.35: LR analysis of co-heating test data. The heating power Φ_h^h on the y-axis is corrected with respective $\omega_j T_j$'s.

5.3.4 Estimating H_{tr} using ARX models

The $ACF(\epsilon_t)$ in Figure 5.34 confirms that linear regression analysis generates residuals that are autocorrelated. We can resolve this by assuming an ARX model, as described by Eq. 3.34 (page 49 in Chapter 3). Similar to the linear regression analysis, we assume $\Phi_h^h - \Phi_v$ as model output and assume $\mu = 0$. The transmission heat loss H_{tr} is now estimated as $\frac{\omega_i(1)}{\omega_h(1)}$.

We start with a first-order model, $k = 1$. We then gradually increase k, until one or more of the autoregressive (AR) coefficients prove insignificant. In each step, lagged inputs and outputs that prove insignificant are skipped using backward elimination. As final model, we retain the highest order model that has k significant AR coefficients. We repeat this procedure, assuming data with varying sampling times t_s. Figure 5.36 collects the periodograms and cumulative periodograms, generated by the residuals that correspond to the respective final models.

The cumulative periodogram, generated by the ninth-order model, assuming a t_s of 10 min, reveals that its residuals are very well-behaved. The residual plot, in Figure 5.37, and the $ACF(\epsilon_t)$, in Figure 5.38, indeed confirm that ϵ_t is white noise. Table 5.7, on page 120, collects the estimated parameters.

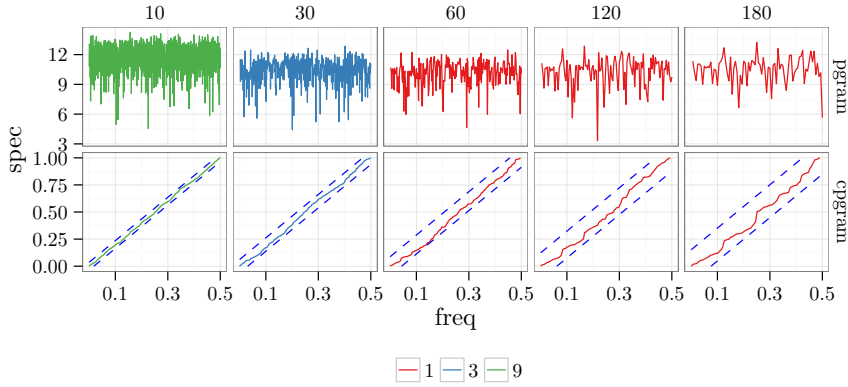

Figure 5.36: Log-periodogram (top) and cumulative periodogram (bottom) of residuals. Their colours reflect the retained model order k. For sampling times t_s of 10 min, a 9th order model is retained. For a t_s of 30 min, a 3rd order model suffices, and for higher t_s, a first-order model suffices.

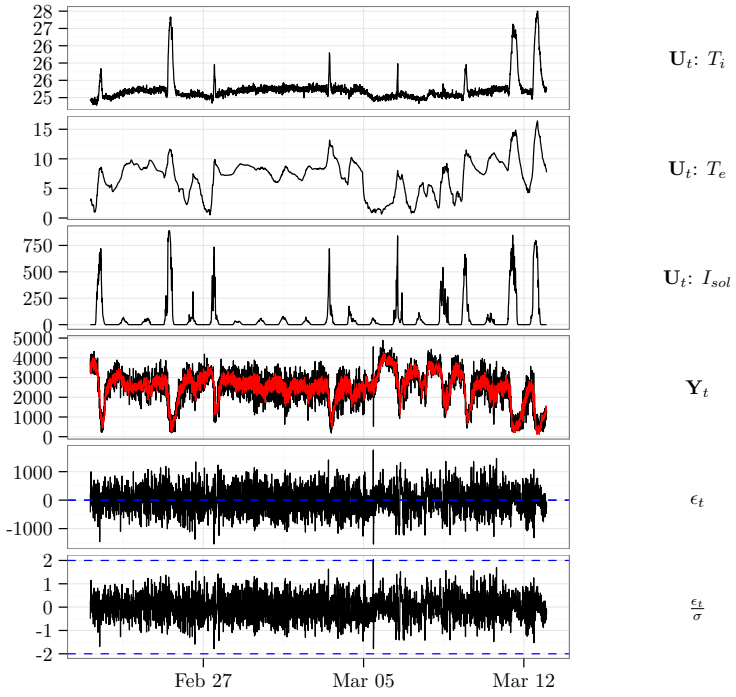

Figure 5.37: Time series plots of inputs $\mathbf{U}_t$: T_i and T_e, in °C, and I_{sol}, in $\mathrm{W\,m^{-2}}$; output $\mathbf{Y}_t$: measured output Φ_h^h, and model output $\hat{\Phi}_h^h$ (red); residuals ϵ_t, and normalised residuals $\frac{\epsilon_t}{\sigma}$.

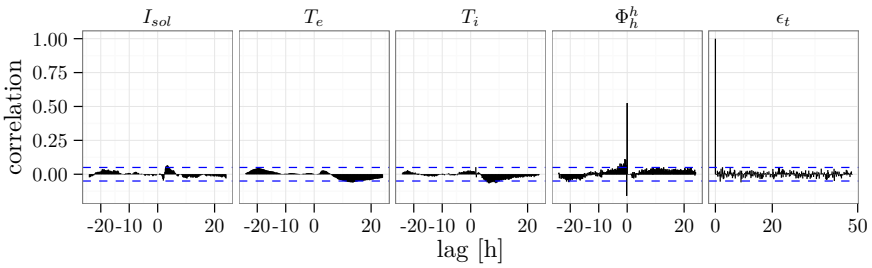

Figure 5.38: (All but right): Cross-correlation between ϵ_t and inputs I_{sol}, T_e, and T_i; and between ϵ_t and output Φ_h^h. (Right): Auto-correlation of residuals.

Table 5.7: Estimated parameters, assuming 9th order ARX model, with a sampling time, t_s, of 10 min. In this case, $\frac{\omega_i(1)}{\omega_h(1)}$ represents the overall transmission heat loss coefficient, H_{tr}. A_{sol} is estimated as $\frac{\omega_{sol}(1)}{\omega_h(1)}$. Time constants, τ, in h.

	Estimate	σ
μ	0.0000	0.0000
$\omega_{h,0}$	1.0000	0.0186
$\omega_{h,1}$	0.3007	0.0194
$\omega_{h,2}$	-0.0375	0.0193
$\omega_{h,3}$	-0.2578	0.0195
$\omega_{h,4}$	-0.2143	0.0191
$\omega_{h,5}$	-0.2929	0.0194
$\omega_{h,6}$	-0.1847	0.0188
$\omega_{h,7}$	-0.1150	0.0188
$\omega_{h,8}$	-0.0281	0.0182
$\omega_{h,9}$	0.0347	0.0000
$\omega_{i,1}$	360.1781	114.7233
$\omega_{i,2}$	-373.8872	125.7564
$\omega_{i,3}$	381.0862	130.7341
$\omega_{i,6}$	215.1169	120.2127
$\omega_{i,7}$	-552.1234	105.2397
$\omega_{e,3}$	-186.1498	95.4229
$\omega_{e,4}$	343.8036	166.2662
$\omega_{e,5}$	-184.9018	90.5791
$\omega_{sol,0}$	-0.6637	0.1573
$\omega_{sol,3}$	0.6572	0.3841
$\omega_{sol,4}$	-1.1094	0.3408
τ_1	0.0066	0.0000
τ_2	0.0726	0.0000
τ_3	0.1811	0.0000
$\frac{\omega_i(1)}{\omega_h(1)}$	148.1	19.8
$\frac{\omega_e(1)}{\omega_h(1)}$	132.9	24.0
$\frac{\omega_{sol}(1)}{\omega_h(1)}$	-5.4	0.7

5.3.5 Reliability plots

The reliability plots in Figures 5.39 and 5.40 show very consistent results for ω_i (LR) and $\frac{\omega_i(1)}{\omega_h(1)}$ (ARX). If we focus on their mean values, they both yield robust results, as of a duration of 2 weeks, or 14 days: regardless of the chosen sampling time, t_s, the estimates remain within 11.2 % (LR) and 11.3 % (ARX) of their mean. If we assume a t_s of 480 min for LR, and a t_s of 10 min for ARX, we obtain fairly robust results after only 7 days: results remain within 11.9 % (LR) and 12.2 % (ARX). As of 14 days, they remain within 1.4 % (LR) and 1.7 % (ARX). LR and ARX yield, for durations of 14 days and higher, estimates within 2.3 and 4.1 % of each other, with LR systematically lower. Nonetheless, the ARX method indicates confidence intervals that remain large, even for longer durations. For instance, for a t_s of 10 min and a duration of 20 days, the standard deviation $\sigma_{H_{tr}}$ amounts to 19.8 $\mathrm{W\,K^{-1}}$.

5.3.6 Comparison with expected values

Based on the norm (DIN 4701, 2003), building plans and material characteristics, researchers at the BBRI calculated that this detached test house needs a nominal power of 5540 W, to sustain a ΔT of 27.9 °C. The larger part of this nominal power, 4186 W, is due to transmission heat loss, the remaining 1354 W due to ventilation heat loss. These calculations were based on the building's initial specifications. Mid 1990's, the ordinary double glazing was replaced with improved double glazing, thereby reducing the glazing U-value from 2.9 $\mathrm{W\,m^{-2}\,K}$ to 1.3 $\mathrm{W\,m^{-2}\,K}$. Taken together, we expect the value for H_{tr} to lie around 143.8 $\mathrm{W\,K^{-1}}$. Table 5.8 collects the values for H_{tr}, assessed using LR and ARX modeling. They yield consistent, but slightly higher values than the expected one. This small discrepancy, however, remains well within the estimated H_{tr}'s confidence interval.

Table 5.8: Comparison between expected and assessed transmission heat loss coefficients, in $\mathrm{W\,K^{-1}}$. H_{tr} is estimated using both linear regression (*LR*) and *ARX* modeling.

	H_{tr}	$\sigma_{H_{tr}}$
Expected	143.8	-
LR	145.9	4.8
ARX	148.1	19.8

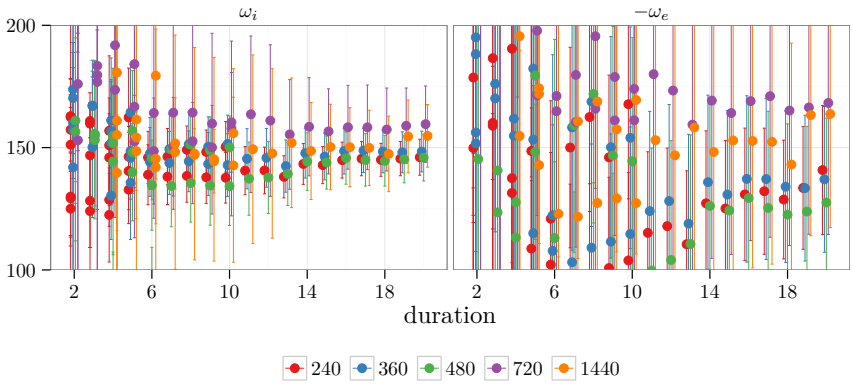

Figure 5.39: Estimates of H, in $\mathrm{W\,K^{-1}}$, that result from a linear regression analysis, assuming model $\Phi_h^h - \Phi_v = \omega_i T_{i,avg} + \omega_e T_{e,avg} + \omega_{sol} I_{sol,avg} + \epsilon$. The columns collect the results for ω_i and $-\omega_e$, and for this test case, $H = \omega_i$. Different sampling times t_s (dodged position and colour of points), and data subsets with varying duration (x-axis), are considered.

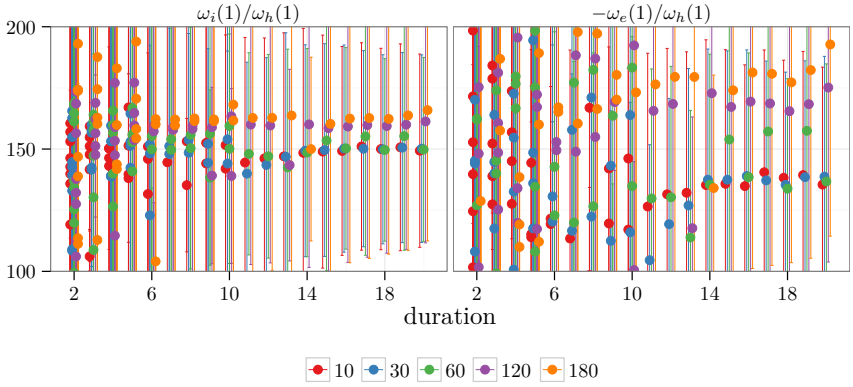

Figure 5.40: Estimates of H, in $\mathrm{W\,K^{-1}}$, that result from ARX modeling, assuming $\omega_h(B)(\Phi_h^h - \Phi_v) = \omega_i(B)T_i + \omega_e(B)T_e + \omega_{sol}(B)I_{sol} + \epsilon$. The columns collect the results for $\frac{\omega_i(1)}{\omega_h(1)}$ and $-\frac{\omega_e(1)}{\omega_h(1)}$. For this test case, H is estimated as the first. Different sampling times t_s (dodged position and colour of points), and data subsets with varying duration (x-axis), are considered.

5.3.7 Discussion

The investigated test house is a detached house, with a ventilated attic and a cellar that, although ventilated, exhibits an air temperature, T_c, that is very stable. We categorised these boundary conditions as *Scenario 2*: the cellar influences the building heat balance as if it were a soil mass, and the building fabric between T_i and T_c needs to be assessed as part of the building envelope. To obtain a physically relevant estimate for ω_i, and thus H, we were compelled to neglect μ, despite the relative importance of heat losses towards T_c (10.5%).

By investigating the cumulative periodogram, we find that, with regard to linear regression analysis, the sampling time t_s can be reduced to 8h, leaving us with more data points and a reduced uncertainty.

We showed that linear regression yields autocorrelated residuals, and that ARX models resolve this by explicitly modeling Φ_h^h's autoregressive features. Nevertheless, both methods estimate similar values for the transmission heat loss H_{tr}, and they lie very close to its design value. Reliability plots indicate that LR and ARX are equally robust. The ARX model thereby better assesses its uncertainty.

5.4 Test Case 3: Detached house in Verlaine

We found that we could categorise the previous test case in *Scenario 2*, as its floor above cellar effectively behaves as a floor on ground. Here, we analyse a detached house, that actually has a floor on ground, thus again illustrative for *Scenario 2*. Whereas in Test Case 2, we had detailed measurements at our disposal, of the actual air change rate during the experiment, here we have to rely on a pressurisation test. We again apply both LR and ARX models to analyse the data. We first estimate H, and in a second step, we split it into H_{tr} and H_v. Particularly interesting about this test case, is that the building was tested right after it was completed. We discuss the potential impact of latent heat, due to drying out of wet plaster during the heating experiment.

5.4.1 Description

The house of interest is situated in Verlaine, Belgium. Figure 5.42 shows images of street and garden facades. Figure 5.41 collects plans and sections. Its volumetric characteristics are summarised in Table 5.9. It is a *detached* house, only connected with its neighbour by a carport and an unheated storage space. The rectangular volume comprises two storeys. Windows turn towards all orientations, however primarily towards west and east. It has a light-weight attic floor, with a wooden structure, and in between 18 cm of mineral wool insulation. The pitched roof is not insulated. A hatch in the attic floor provides access to the attic space. The house does not have a basement, but a floor on ground, with a concrete structure, and a layer of screed that rests on 4 cm of rigid XPS insulation.

Table 5.9: House geometry.

Building volume (outer)	V_o	495.9 m^3
Building volume (inner)	V_i	380.2 m^3
Heat loss surface	A_T	379.5 m^2
Total window area	$A_{w,T}$	48.8 m^2

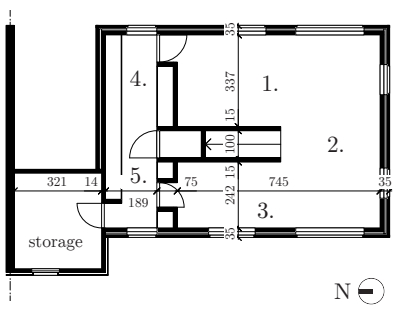

(a) Ground floor plan.

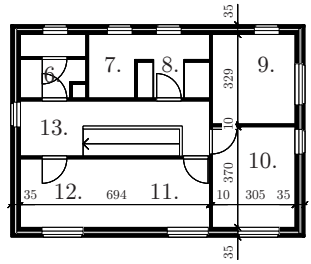

(b) Floor level 1 plan.

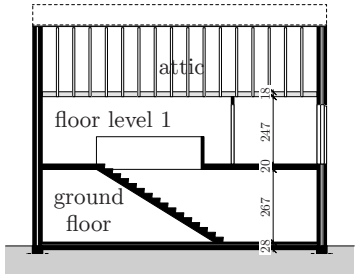

(c) Longitudinal section.

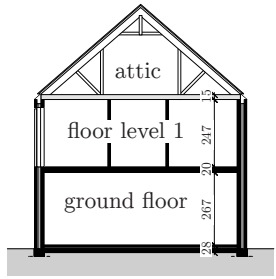

(d) Transverse Section.

Figure 5.41: Schematic plans and sections of the investigated house.



(a) Street facade.



(b) Garden facade.

Figure 5.42: Pictures of the investigated house.

5.4.2 Co-heating test

We performed a typical co-heating test (Figure 5.43) on the house from December 15, 2012, to January 4, 2013. It started right after the building was completed. Hence, brickwork, concrete slabs, and especially the wet plaster interior finishing were not fully dried out. The applied indoor sensors combine measurements of air temperatures and relative humidities, which allows us to quantify internal and external water vapour pressures, p_i and p_e, respectively. These quantities prove invaluable to assess the effect of a drying building fabric.



(a) (b)

Figure 5.43: Co-heating test setup.

Beginning of December 2012, a pressurisation test was performed on the dwelling. The estimated n_{50}-value amounts to 2.1 h^{-1}. We consider this value as valid throughout the co-heating test. At the onset of the heating experiment, measures were taken to reduce air leakages towards the unheated storage space outside of the main volume, and towards the attic. Openings were closed with wooden boards and their edges sealed airtight.

As a basis for analysis, we consider a 13 day period, that spans from December 22, 2012, to January 3, 2013. Figure 5.44 plots the collected measurement data. It shows a high-quality co-heating test: a very stable and elevated Φ_h^h; low values for I_{sol}, and thus no overheating of T_i; low values for T_e, and thus high ΔT's, ranging from 12 to 23 °C. Also in Figure 5.44, we plotted the difference between internal and external water vapour pressure, $p_i - p_e$. In a next section, we use this quantity to estimate the dry-out rate, G_{si}, of the building fabric.

Figure 5.45 plots the ACF of Φ_h^h, and the CCFs between Φ_h^h and all candidate predictors. Heating power Φ_h^h is significantly autocorrelated. Φ_h^h is also significantly cross-correlated with T_i, T_e, I_{sol}, and $p_i - p_e$.

Although we did not measure the air temperature of the storage space (Figure 5.41a), we can reasonably assume it is correlated with T_e. Hence, we do not distinguish any neighbouring zones.

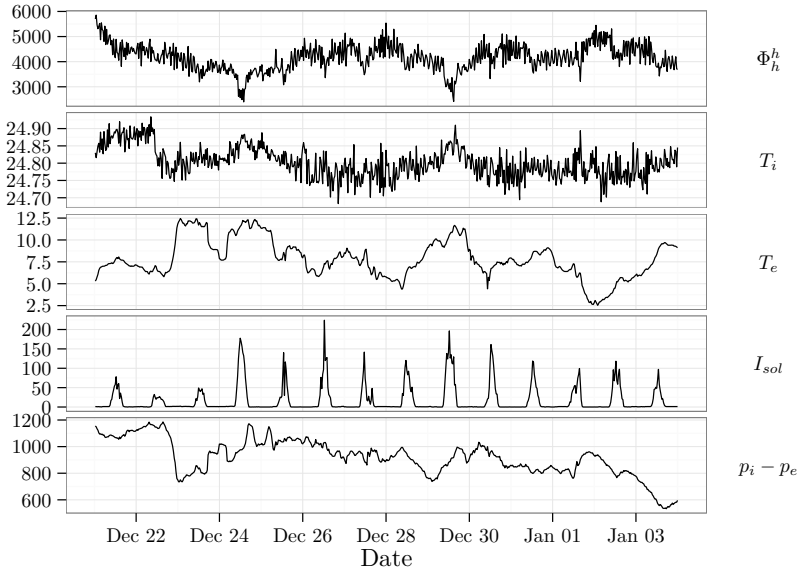

Figure 5.44: Time series plots, with $t_s = 30$ min, of co-heating test performed in a detached house in Verlaine, Belgium. Φ_h^h represents the total heating power delivered to the house, in W. A representative indoor air temperature T_i, in °C, is calculated as the first principal component of indoor air temperatures measured in the different rooms. T_e represents the outdoor air temperature, in °C, and I_{sol} the global horizontal solar radiation, in $\mathrm{W\,m^{-2}}$. Finally, p_i and p_e reflect internal and external water vapour pressure, in Pa.

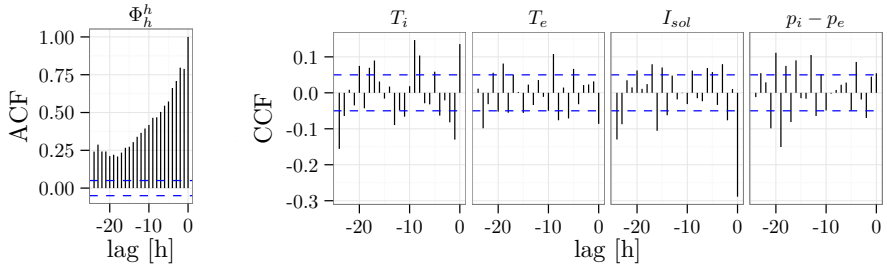

(a) (b)

Figure 5.45: (a): $ACF(\Phi_h^h)$; (b): CCFs between Φ_h^h and candidate predictors T_i, T_e, I_{sol}, and $p_i - p_e$. 60-min averaged values are assumed.

5.4.3 Estimating H using linear regression

The house has a floor on ground. And we do not distinguish a neighbouring zone. Hence, this test case is a clear example of *Scenario 2*, introduced in Chapter 3, Section 3.6, and we can estimate H as ω_i in Eq. 3.33. As suggested in 3.5.2, we assume $\mu = 0$. The ground floor is insulated, and $T_i - T_g$ is small compared to $T_i - T_e$. In Section 3.5.1, we estimated that the ground floor heat loss amounts to $\pm$ 205.8 W, or 5 % of Φ_h^h's mean value during the experiment. We thus ignore $\omega_g^{B_g} \frac{1-\phi_g}{1-\phi_g B} T_g$, in Eq. 3.27.

We tested the house shortly after it was built. Hence, given the materials used, the building fabric still has a high moisture content. This encapsulated moisture is efficiently dried out by the co-heating test. We now assume a stationary moisture balance towards the indoor air, to estimate the average dry-out rate of the building fabric, G_{si}, in $\mathrm{kg\,s^{-1}}$:

$$G_{si} = \frac{n_{actual} V}{3600 R T_i}(p_i - p_e) \approx 9.56 \times 10^{-5} \tag{5.3}$$

with T_i the indoor air temperature, in K; p_i the indoor air water vapour pressure, in Pa; p_e the external air water vapour pressure, in Pa; R the specific gas constant of water vapour, 461.52 $\mathrm{J\,kg^{-1}\,K^{-1}}$; and finally, V_i is the interior building volume, 380.2 $\mathrm{m^3}$. p_i and p_e are calculated from temperature and relative humidity measurements. For stationarity to hold, T_i, p_i and p_e are averaged over the duration of the experiment period.

We estimate the latent heating power needed to dry out moisture, at a rate G_{si}, by multiplying it with the latent heat of evaporation of water, h. With h approximately 2.26e+6 $\mathrm{J\,kg^{-1}}$, hG_{si} amounts to 216.1 W. We thereby underestimate the effect latent heat has on the equivalent transmission heat losses through the building envelope. This value corresponds to 5.2 % of the average heating power Φ_h^h, delivered during the experiment (Figure 5.44). We thus ignore $\omega_G G_{si}$ in Eq. 3.27 as well.

We estimate all parameters using linear regression. Coefficients that prove insignificant are removed using backward elimination. By appropriately sampling and averaging predictors, we try to filter out the auto-correlation of Φ_h^h and its cross-correlations with T_i and T_e. As suggested in Chapter 3, Section 3.5.2, we average predictors over current and previous time steps. To select an appropriate sampling time t_s, we vary it, and investigate the corresponding residuals. The cumulative periodograms in Figure 5.46 indicate that our models perform well when t_s is 480 min, or 8 h, and above. To retain as many data points as possible, we continue our analysis assuming a t_s of 8 h.

Figure 5.47 and Table 5.10 collect the co-heating test analysis result. The $ACF(\epsilon_t)$ in Figure 5.49 shows significant values, that regularly exceed confidence bounds. Again, linear regression proves unable to generate decorrelated residuals.

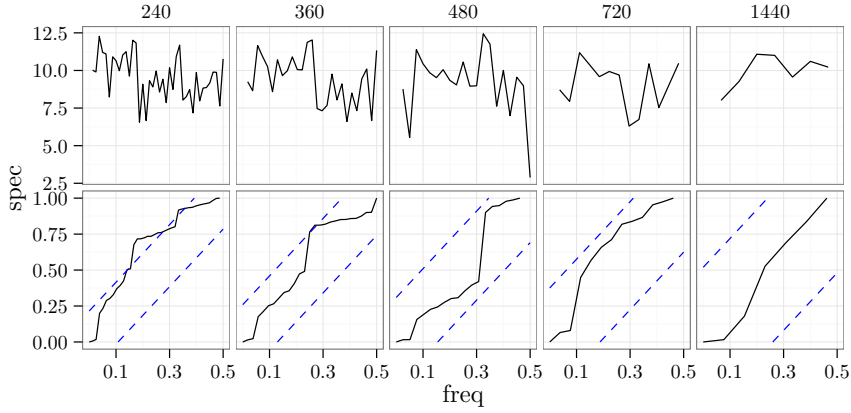

Figure 5.46: Log-periodogram (top) and cumulative periodogram (bottom) of residuals. Columns represent different sampling times t_s, in min.

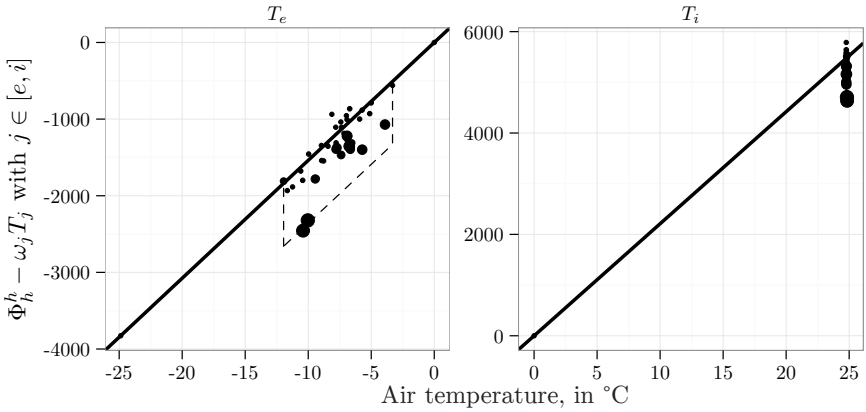

Figure 5.47: Linear regression analysis of co-heating test data. The heating power Φ_h^h on the y-axis is corrected with respective $\omega_j T_j$'s (Section 3.6.3).

Table 5.10: Overall heat loss coefficient H, in $\mathrm{W\,K^{-1}}$, and global solar aperture A_{sol}, in $\mathrm{m^2}$, estimated by applying linear regression on aggregated co-heating test data.

	Estimate	σ
ω_i	221.0	5.5
ω_e	-153.8	16.7
ω_{sol}	-8.2	2.2
H	221.0	5.5
A_{sol}	8.2	2.2

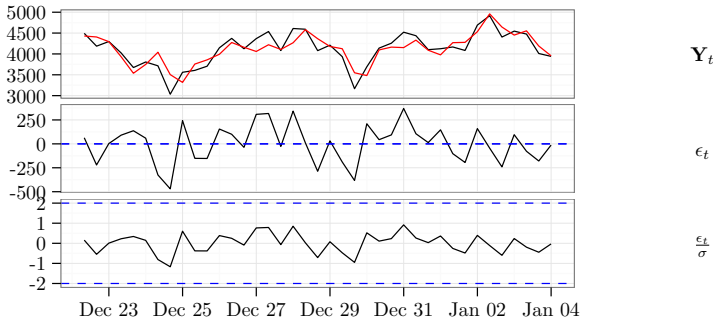

Figure 5.48: Output $\mathbf{Y}_t$: measured output Φ_h^h and model output $\hat{\Phi}_h^h$ (red); residuals ϵ_t and normalised residuals $\frac{\epsilon_t}{\sigma}$.

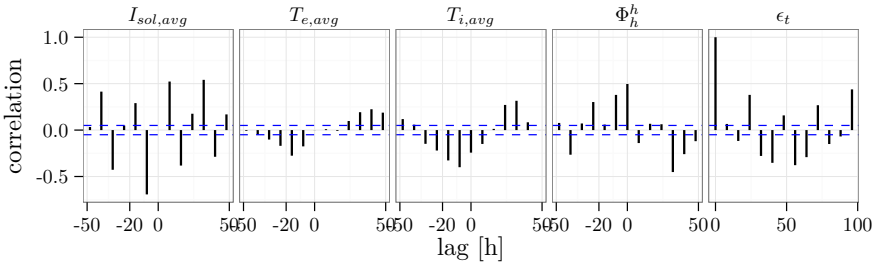

Figure 5.49: (All but right): Cross-correlation between ϵ_t and inputs $T_{i,avg}$, $T_{e,avg}$, and $I_{sol,avg}$, and between ϵ_t and output Φ_h^h. (Right): Auto-correlation of ϵ_t.

5.4.4 Estimating H using ARX modeling

Similar to Test Case 2, also here we apply ARX modeling on the co-heating test data. Figure 5.50 collects the periodograms and cumulative periodograms, generated by ARX models of order k, and assuming a sampling time t_s that ranges from 10 min to 180 min, or 3 h. For each t_s, we start from a first-order model, $k = 1$, and we increase k until at least one autoregressive (AR) coefficient, $\omega_{h,j}$, with $j \in [1, k]$, proves insignificant. As final model, we retain the highest order model that has k significant AR coefficients.

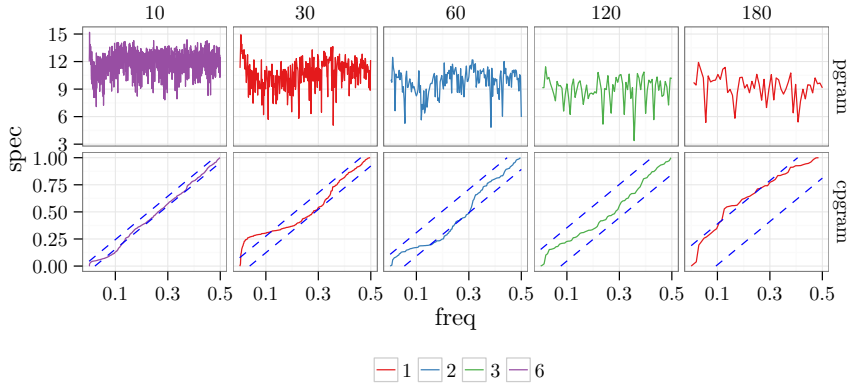

Figure 5.50: Log-periodogram (top) and cumulative periodogram (bottom) of residuals. Columns represent different sampling times t_s, in min. Colours represent the retained model order k.

A third-order model, $k = 3$, seems to perform well, given a sampling time t_s of 120 min. Figure 5.51 plots its residuals, and Figure 5.52 plots the $ACF(\epsilon_t)$ and the CCFs between ϵ_t and the candidate predictors. Although $ACF(\epsilon_t)$ shows values that exceed the confidence bounds, they are small and do not affect the first two lags.

5.4.5 Estimating H_v

A pressurisation test indicates that the building's n_{50}-value lies around 2.1 h^{-1}. From this value, using the rule of thumb introduced in Section 3.3, we crudely estimate the *actual* air change rate, that takes place as the test unfolds: $n_{actual} \approx 0.1$ h^{-1}. Applying Eq. 3.8, the ventilation heat loss coefficient H_v amounts to approximately 17.4 $\mathrm{W\,K}^{-1}$.

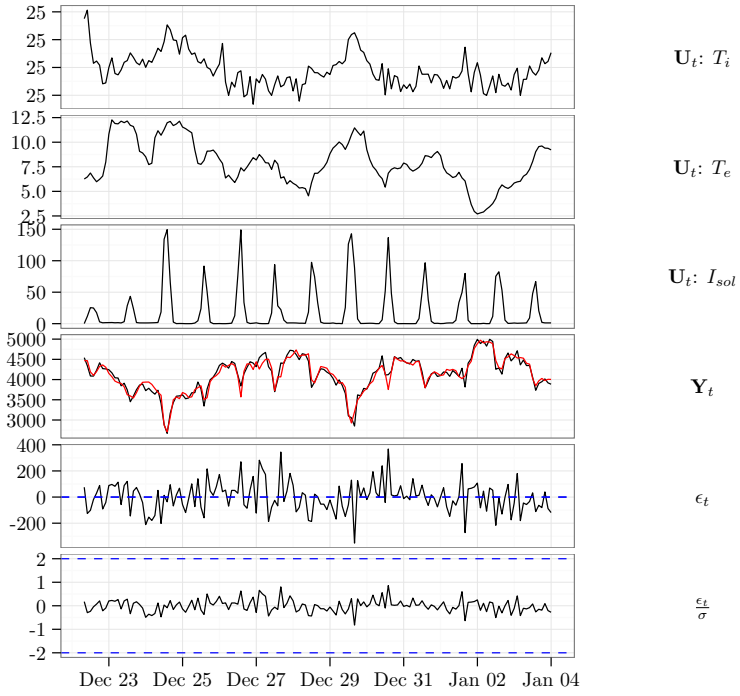

Figure 5.51: Time series plots of inputs $\mathbf{U}_t$: T_i and T_e, in °C, and I_{sol}, in $\mathrm{W\,m^{-2}}$; output $\mathbf{Y}_t$: measured output Φ_h^h, and model output $\hat{\Phi}_h^h$ (red); residuals ϵ_t, and normalised residuals $\frac{\epsilon_t}{\sigma}$

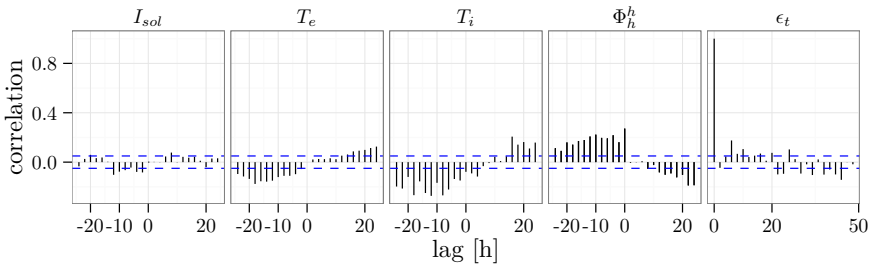

Figure 5.52: (All but right): Cross-correlation between ϵ_t and inputs T_i, T_e, and I_{sol}, and between ϵ_t and output Φ_h^h. (Right): Auto-correlation of residuals.

Table 5.11: Estimated parameters, assuming 3rd order ARX model, with t_s = 120 min. H is estimated as $\omega_i(1)/\omega_h(1)$. A_{sol} is estimated as $\omega_{sol}(1)/\omega_h(1)$. Time constants, τ, in h.

	Estimate	σ
μ	0.0000	0.0000
$\omega_{h,0}$	1.0000	0.0783
$\omega_{h,1}$	-0.5002	0.0792
$\omega_{h,2}$	-0.3069	0.0534
$\omega_{h,3}$	0.0941	0.0000
$\omega_{i,0}$	1867.1760	478.6152
$\omega_{i,1}$	-1803.2650	478.3962
$\omega_{e,0}$	-46.6256	7.4571
$\omega_{sol,0}$	-5.7818	0.4028
$\omega_{sol,1}$	2.3734	0.6653
$\omega_{sol,2}$	1.4377	0.5116
τ_1	0.5949	0.0000
τ_2	1.3968	0.0000
τ_3	2.7343	0.0000
$\frac{\omega_i(1)}{\omega_h(1)}$	222.6	52.9
$\frac{\omega_e(1)}{\omega_h(1)}$	162.4	39.1
$\frac{\omega_{sol}(1)}{\omega_h(1)}$	-6.9	2.3

5.4.6 Reliability plots

In Figures 5.53 and 5.54, we plot the estimates for H ($= H_{tr} + H_v$). H is estimated as ω_i (LR), and as $\frac{\omega_i(1)}{\omega_h(1)}$ (ARX). As in Test Case 2, the estimated values are consistent, both with regard to method used, LR or ARX, and with regard to sampling times t_s. Both LR and ARX yield very robust estimates, already after 7 days: regardless of the chosen sampling time, t_s, the estimates are within 8.1 % (LR) and 7.6 % (ARX) of their mean. If we assume a t_s of 480 min for LR, and a t_s of 120 min for ARX, the estimates remain within 2.5 % (LR) and 6.9 % (ARX). The reliability plots in Figure 5.54 show that, with a t_s of 10 min, ARX provides even more robust estimates for H: for durations as of 7 days, estimates remain within 2.2 %. LR and ARX (with $t_s = 10$) yield, for durations of 7 days and higher, estimates within 2.3 and 4.6 % of each other.

The confidence intervals (CIs) associated with the estimate of H, calculated on the basis of the ARX models, are however considerable. The most optimal CI is seen when t_s is 30 min; for a duration of 13 days, H amounts to 214.6 $\pm$ 12.8 W K^{-1}.

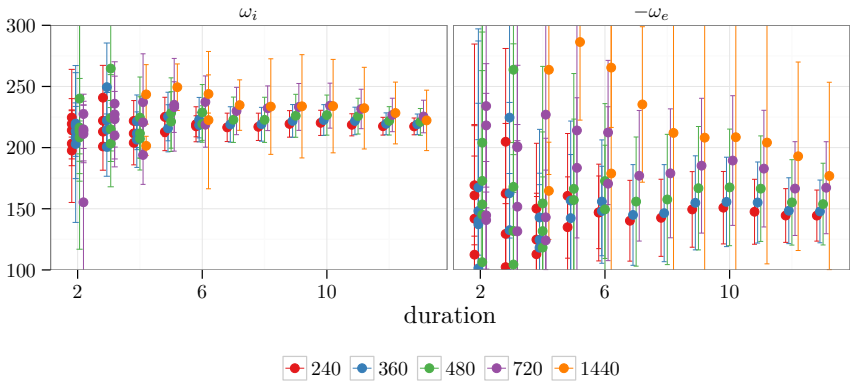

Figure 5.53: Estimates of H, in $\mathrm{W\,K^{-1}}$, that result from a linear regression analysis, assuming model $\Phi_h^h = \omega_i T_{i,avg} + \omega_e T_{e,avg} + \omega_{sol} I_{sol,avg} + \epsilon$. The columns collect the results for ω_i and $-\omega_e$, and for this test case, $H = \omega_i$. Different sampling times t_s (dodged position and colour of points), and data subsets with varying duration (x-axis), are considered.

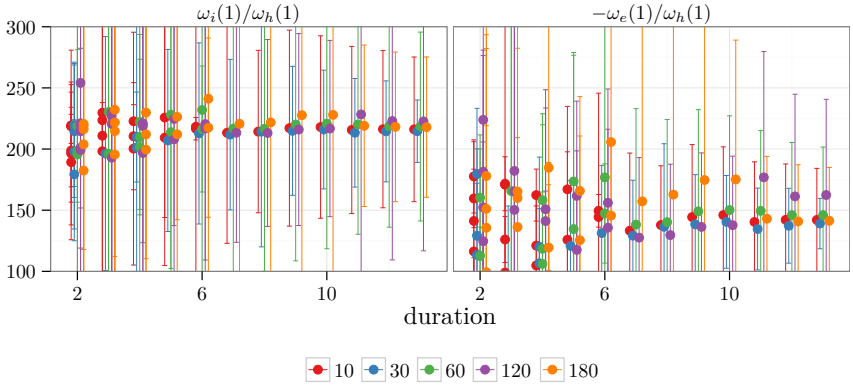

Figure 5.54: Estimates of H, in $\mathrm{W\,K^{-1}}$, that result from ARX modeling, assuming $\omega_h(B)(\Phi_h^h) = \omega_i(B)T_i + \omega_e(B)T_e + \omega_{sol}(B)I_{sol} + \epsilon$. The columns collect the results for $\frac{\omega_i(1)}{\omega_h(1)}$ and $-\frac{\omega_e(1)}{\omega_h(1)}$. For this test case, H is estimated as the first. Different sampling times t_s (dodged position and colour of points), and data subsets with varying duration (x-axis), are considered.

5.4.7 Comparison with expected values

The expected transmission and ventilation heat loss coefficients are calculated on the basis of standard (NBN B62-301, 1989). Only the main volume is considered as the heated volume. The storage space, outside the main volume, is excluded. Ground floor heat loss is calculated on the basis of standard (ISO 13370, 2007).

From Table 5.12, we conclude that the estimated values for H_{tr} lie very close to the expected value. However, the standard deviation, $\sigma_{H_{tr}}$, of the ARX model is considerable. In Section 5.4.6, we saw that a more optimal choice of t_s can reduce $\sigma_{H_{tr}}$ significantly, to 12.8 $\mathrm{W\,K^{-1}}$, for a t_s of 30 min.

Table 5.12: Comparison between expected and assessed transmission heat loss coefficients, in $\mathrm{W\,K^{-1}}$. $H_{tr} = H - H_v$ is estimated using both linear regression (LR), with $t_s = 480$ min, and ARX, with $t_s = 120$ min. $\sigma_{H_{tr}}$ ignores the uncertainty, associated with H_v.

	H_{tr}	$\sigma_{H_{tr}}$
Expected	207.2	-
LR	203.6	5.5
ARX	205.2	52.9

5.4.8 Discussion

Test Case 3 is a detached house, with floor on ground. We thus used the strategy laid out in *Scenario 2*: $H = \omega_i$. To obtain a physically relevant estimate for ω_i, we ignored μ. The expected heat losses through the ground floor, and the expected latent heat associated with a drying-out building fabric, combine to ± 10 % of the average heating power Φ_h^h, delivered to the house during the co-heating test. As in Test Case 2, by investigating the cumulative periodograms, generated by linear regression models, we were able to reduce t_s to 8h, leaving us with more data points and a reduced uncertainty.

Test Case 3 was the last in a series of three co-heating tests. The next three Test Cases cover the analysis of dynamic tests, where a dynamic heating power excites the building in a dynamic way. In Test Case 4, we start small, by investigating the thermal performance characteristics of a small scale model of a building, the IEA EBC Annex 58 Round Robin Test Box.

5.5 Test Case 4: IEA EBC Annex 58 Round Robin Experiment

In the framework of the IEA EBC Annex 58 project (Annex 58, 2015), a Round Robin Experiment was organised, to design, perform and compare different heating experiment designs and data analysis methods. To support this, KU Leuven designed and constructed a small scale model of a building, the Knauf Insulation (KI) Test Box. In fact, two copies of this Test Box were constructed. One travels around the world, where different institutes, participants of Annex 58, perform heating experiments on it using their own equipment. The other stayed in Leuven, Belgium.

In this Section, we focus on a dynamic test, performed in winter 2012-2013, during which we applied a PRBS-type heating power to the KI Test Box, as it was placed in the field, near the Vliet test building at KU Leuven's premises. We analyse the collected measurement data using discrete-time ARX models and continuous-time lumped state space models. Our aim is to estimate values for the box's overall heat loss coefficient, H, in $\mathrm{W\,K^{-1}}$, its global solar aperture, A_{sol}, in $\mathrm{W\,m^{-2}}$, and its time constants, τ, in h.

5.5.1 Description

Figure 5.55 illustrates the KI test box design. It is a cube, with exterior dimensions of 120^3 cm^3. Floor, roof and wall components are identical and 12 cm thick, leaving an inner volume of 96^3 cm^3. One wall contains an operable wooden window with dimensions 71x71 cm^2, of which 52x52 cm^2 is glazed. The double glazing (4-15-4) has a U-value of 1.1 W m^{-2} K^{-1}, in a vertical position and with a ΔT of 15 °C (EN 673, 2011), and a g-value of 0.63. The air gap (15 mm) between both glass layers (4 mm) is 90% argon-filled. The fixed window frame has the same thickness (12 cm) as the other facade elements.

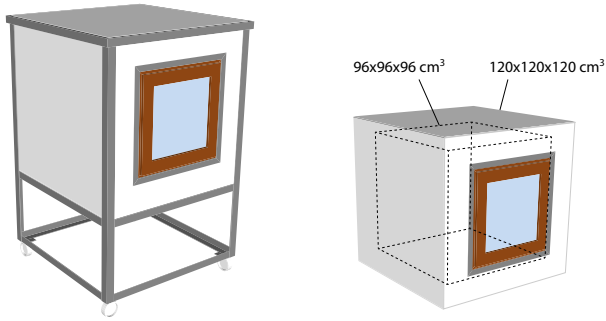

(a) (b)

Figure 5.55: KI Test Box design.

To limit the effect of thermal bridges and other local phenomena, the Test Box walls do not have an inner structure. Instead, they comprise, from inside to outside, two layers of fibre cement boards, a layer of insulation boards and again two layers of fibre cement boards. Figure 5.56 walks us through the construction process. The first layers are glued and screwed together to form an inner box. On this inner box, insulation boards are glued. A number of large screws make sure they are pulled tight to the inner box. The outer two layers are glued and screwed together to form an outer box. This outer box is again glued to the insulation boards. The outer fibre cement boards are white coloured facade cladding boards, selected because of their high emissivity with regard to both long-wave and short-wave radiation. The inner surface of the box is painted in a mat black paint, to emulate black box radiation at the indoor surfaces. We can safely assume that the box is very airtight. The fabric is glued together, and all the joints are sealed. The only opening in the box's fabric, where sensor wires and power supply pass, is completely filled with dense insulation material. Finally, the box is held up by a separate steel structure, such that it remains free from the thermal influence of the ground.

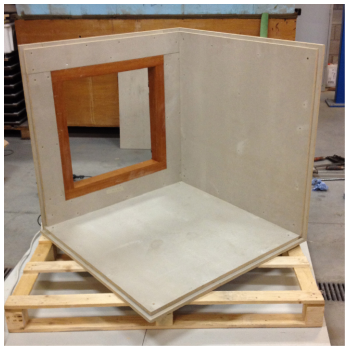

(a) Inner box, with two layers of fibre cement boards

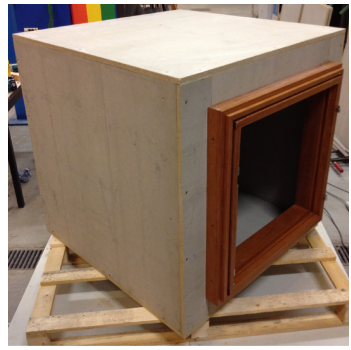

(b) Operable window in one facade part

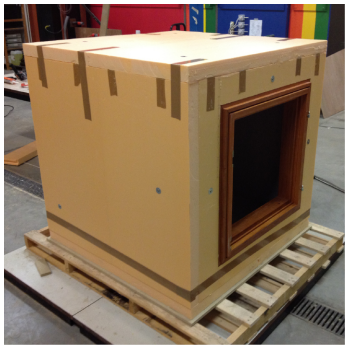

(c) Insulation glued, and locally screwed, to the inner box

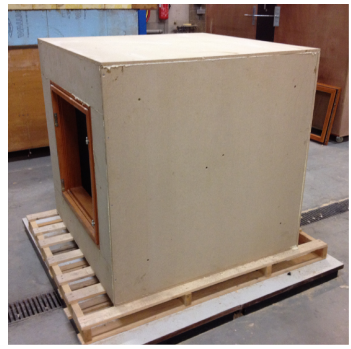

(d) Outer box of fibre cement board

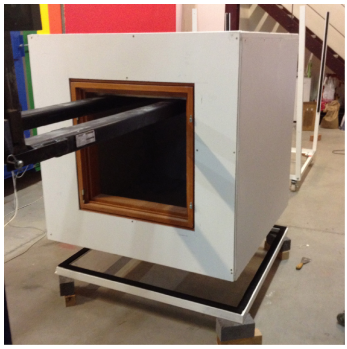

(e) White fibre cement cladding

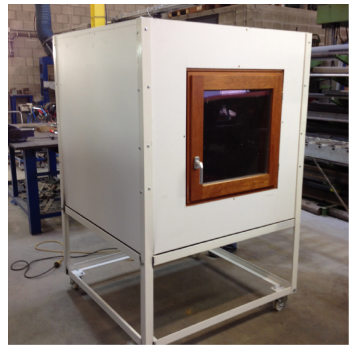

(f) Steel structure that supports the box

Figure 5.56: Construction of the KI Test Box.

5.5.2 Dynamic test using PRBS heating power

From January 2 to January 23, 2013, a dynamic heating experiment was performed on the KI Test Box. Figure 5.57 depicts the box, with its window oriented south, situated in the field at KU Leuven premises. The picture shows that there were some snowy days during the experiment. As of January 14, late evening, to January 17, around noon, there was a layer of snow about 5 cm thick on the Test Box roof.

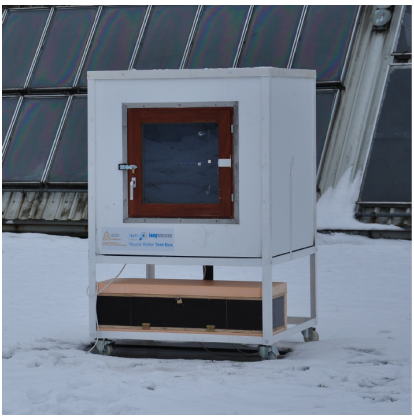

Figure 5.57: KI Test Box set up for testing. Picture taken on January 25, 2013, just after the measurement campaign considered here.

The applied heating power time series, plotted in Figure 5.58, toggles between two levels: 0 W and ± 117 W. As the heating power was switched on and off manually, we were not able to impose an ideal PRBS. The imposed signal, however, retains some of its characteristics. The shortest time span at one level is 6 hours. The longest 3 days, or 72 hours.

The data, collected in Figure 5.58, shows a very well-conditioned heating experiment: T_i varies significantly, over about 30 °C, in response to the imposed heating power, Φ_h^h, and external weather conditions. T_i is derived as the average of two air temperature measurements, performed at different heights, in the middle of the box. We have low values for both T_e and I_{sol}, but they vary over a respectable range. I_{sol} does not seem to significantly influence T_i, except for days when it exceeds 200 $\mathrm{W\,m^{-2}}$, and especially when its direct solar radiation part is high (exemplified by the smooth curve on January 16, 2013).

Figure 5.59 shows that T_i is significantly autocorrelated, and significantly cross-correlated with Φ_h^h, but also with T_e and I_{sol}.

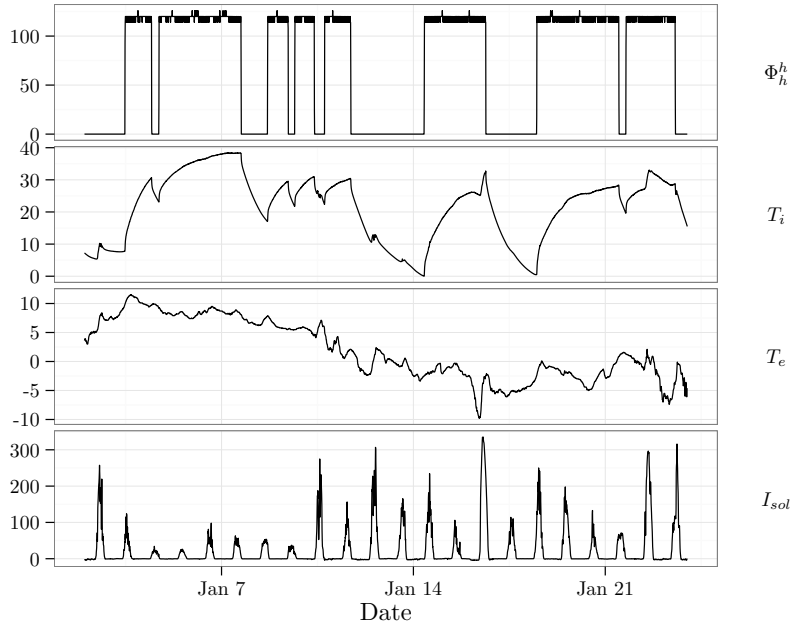

Figure 5.58: Measurement data collected during dynamic test, performed on the KI Test Box. From top to bottom: dynamic heating power, Φ_h^h, in W; averaged indoor air temperature, T_i, in °C; external air temperature, T_e, in °C; global horizontal solar radiation, I_{sol}, in $\mathrm{W\,m^{-2}}$.

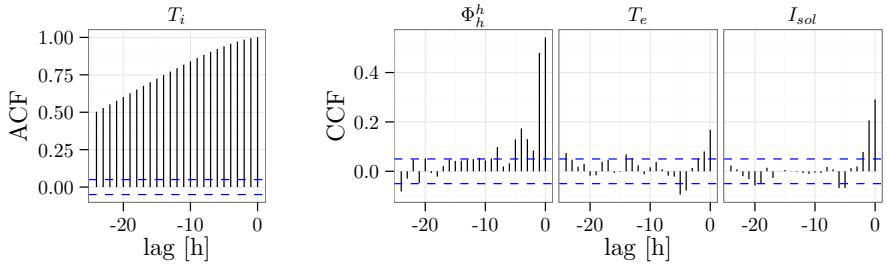

(a) (b)

Figure 5.59: (a): $ACF(T_i)$; (b): CCFs between T_i and candidate predictors Φ_h^h, T_e, and I_{sol}. 60-min averaged values are assumed.

5.5.3 Estimating H using ARX models

We assume the ARX models, that we defined in Eq. 4.23 on page 74, and we apply the model selection procedure proposed in (Bacher and Delff, 2013b; Bacher and Delff, 2013a; Madsen, Bacher, Bauwens, et al., 2015): we gradually increase the order, k, of polynomials $\omega_i(B)$, $\omega_e(B)$, $\omega_h(B)$, and $\omega_{sol}(B)$, until we obtain white noise residuals. We thereby make sure that all autoregressive coefficients ($\omega_{i,j}$ with $j \in [1, k]$) are significant, and that the model's time constants, τ, are well separated. Bacher and Delff (2013b), Bacher and Delff (2013a) and Madsen, Bacher, Bauwens, et al. (2015) suggest to select the highest order model that passes all these criteria. But as we are mainly interested in estimating H, we instead opt to combine the lowest order model and lowest sampling time that pass these criteria.

As the KI Test Box floats in free air, this Test Case is an ideal example of *Scenario 4*: we can estimate H as the minimum variance weighting of $\omega_i(1)/\omega_h(1)$ and $\omega_e(1)/\omega_h(1)$. Figure 5.61 shows that a sampling time, t_s, of 30 min, and a 2nd order ARX model, combine to yield white noise residuals. Such residuals are also obtained for higher model orders k, and higher t_s. But by combining the lowest k and t_s, we lower the risk of having too many parameters for too little data. Figure 5.60 illustrates this. Although the estimate for H seems to better approximate the expected value when we increase the model order k, the associated uncertainty also increases, and more so for higher t_s.

Table 5.13 collects the estimated parameters, Figure 5.62 plots the corresponding time series, and Figure 5.63 plots the autocorrelation of model residuals, and their cross-correlation with model inputs. The residuals show outliers when the heating power signal shifts from one level to the other, or when solar radiation shows higher values. This is confirmed by the autocorrelation and cross-correlation plots. The ARX models that we derived in Section 4.2.3 are *explicit*: to model their output, they only involve *previous* values of the inputs. In Test Case 5, we will apply *implicit* ARX models. Contrary to explicit ARX models, they also involve current values of the inputs, which allows them to much better adapt to abruptly changing inputs.

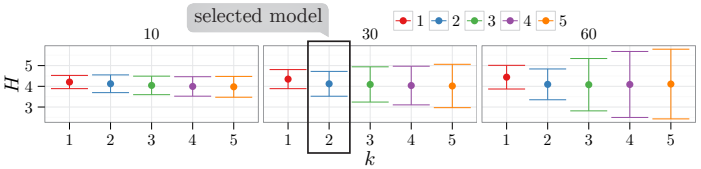

Figure 5.60: Selection of appropriate model order k and sampling time t_s. The plots depict the influence of k (1 to 5, coloured), and t_s (from left to right, 10 min, 30 min, 60 min).

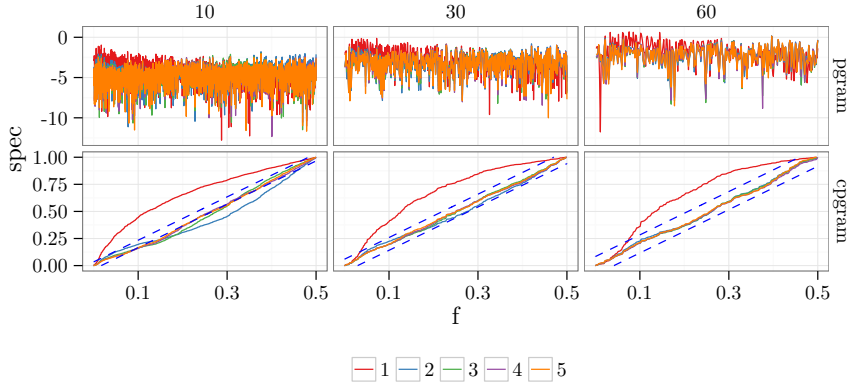

Figure 5.61: Periodogram and cumulative periodogram of residuals generated by ARX models of order k (1 to 5), that consider data with sampling times t_s, of 10, 30 and 60 minutes.

Table 5.13: Estimated parameters, assuming a 2nd order ARX model, with $t_s = 30$ min. The overall heat loss coefficient, H, in $\mathrm{W\,K^{-1}}$, is estimated as the minimum variance weighting of $\frac{\omega_i(1)}{\omega_h(1)}$, and $\frac{\omega_e(1)}{\omega_h(1)}$. A_{sol}, in $\mathrm{W\,m^{-2}}$, can be estimated as $\frac{\omega_{sol}(1)}{\omega_h(1)}$. The time constants, τ_1 and τ_2, in h, are well separated.

	Estimate	σ
$\omega_{h,1}$	0.0249	0.0013
$\omega_{h,2}$	-0.0179	0.0010
$\omega_{i,0}$	1.0000	0.0000
$\omega_{i,1}$	-0.8018	0.0469
$\omega_{i,2}$	-0.1690	0.0456
$\omega_{e,1}$	0.0524	0.0353
$\omega_{e,2}$	-0.0254	0.0354
$\omega_{sol,1}$	0.0068	0.0006
$\omega_{sol,2}$	-0.0051	0.0005
τ_1	0.0126	0.0000
τ_2	0.8763	0.0000
H	4.12	0.30
$\frac{\omega_i(1)}{\omega_h(1)}$	4.20	0.34
$\frac{\omega_e(1)}{\omega_h(1)}$	3.89	0.37
$\frac{\omega_{sol}(1)}{\omega_h(1)}$	0.24	0.03

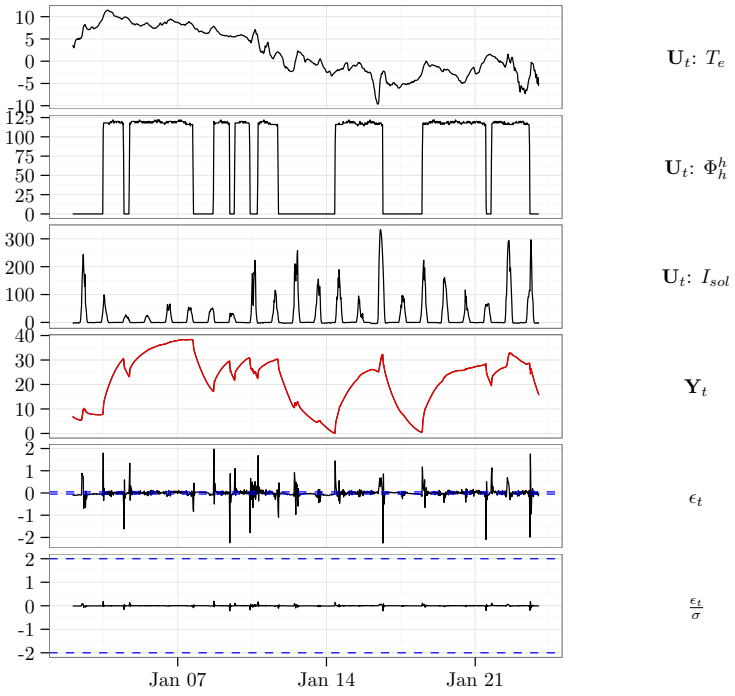

Figure 5.62: Time series plots of inputs $\mathbf{U}_t$: T_e, Φ_h^h, and I_{sol}; outputs $\mathbf{Y}_t$: measured output, T_i, and model output, $\hat{T}_i$ (red); residuals ϵ_t, and normalised residuals $\frac{\epsilon_t}{\sigma}$.

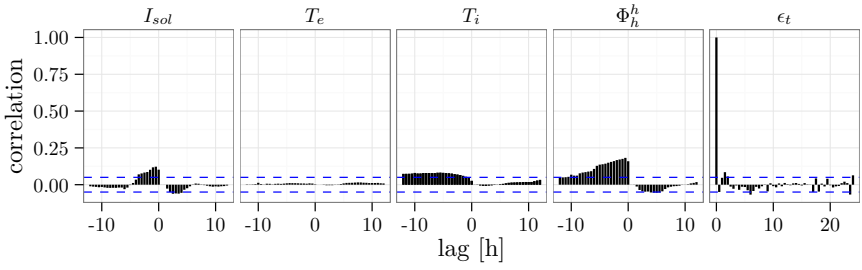

Figure 5.63: (All but right): Cross-correlation between ϵ_t and inputs T_e, Φ_h^h, and I_{sol}, and between ϵ_t and output T_i. (Right): Autocorrelation of residuals.

5.5.4 Estimating H using CTSM-R

The construction of the box, and the steel frame that makes it float in the air, allow us to assume simplified models that exclude thermal influence of ground and neighbouring zones. Figure 5.64 illustrate the minimal and maximal order candidate models that we might consider. Figure 5.73 in Section 5.5.9 collects the second and third order models that, in addition to first-order model T_i (Fig. 5.64a), we actually fitted to the data. As the box is airtight, we do not assume a direct ventilation heat loss between T_i and T_e. We take inspiration from the model selection procedure proposed by (Bacher and Madsen, 2011), briefly introduced near the end of Section 4.1. They increase the model complexity, until likelihood ratio tests show that further model extensions are no longer justified. Here, we want to stop earlier; we want to retain the lowest model order, k, and sampling times, t_s, that yield white noise residuals.

Figure 5.65 shows that a first-order model (red lines) does not yield white noise residuals, regardless of t_s. For a t_s of 10 min, the second-order model, $T_i + T_1$, and the third-order model, $T_i + T_1 + T_m$, both yield white noise residuals, with the latter behaving slightly better in the high frequency spectrum. Figure 5.66a investigates whether taking the step towards a third-order model makes sense. The arrows in the left plot show that, based on (Bacher and Madsen, 2011)'s model selection procedure, we can argue to take the step from model $T_i + T_1$ to $T_i + T_1 + T_m$ (likelihood ratio test p-value < 0.05). Figure 5.66b, however, shows that the uncertainty on the resulting estimate of H increases with 49.6 %. For our purposes, we thus stick to the second-order model: the log-likelihood is significantly increased and the standard deviation around the estimate for H remains small. Moreover, Table 5.15 shows that the estimated coefficients are not cross-correlated, apart from minor cross-correlations between C_i and the diffusion term in the SDE of T_1, $W_{2,t}$, and between $r_{i,1}$ and the measurement noise term, $\epsilon_{1,t}$.

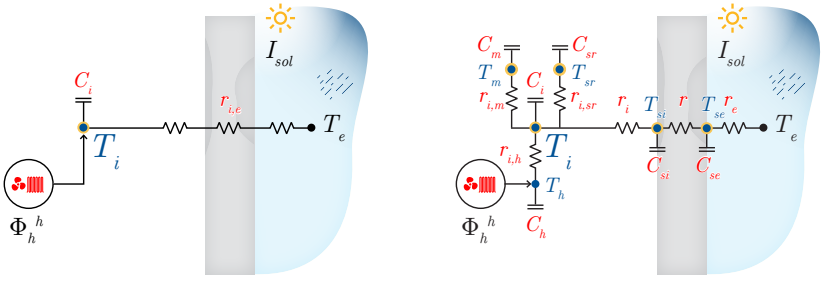

(a) First-order model, with T_i as sole state.

(b) Fifth-order model, with states T_i, T_1, T_k, T_m and T_{sr} (defined in Ch. 2)

Figure 5.64: Minimum and maximum order candidate models.

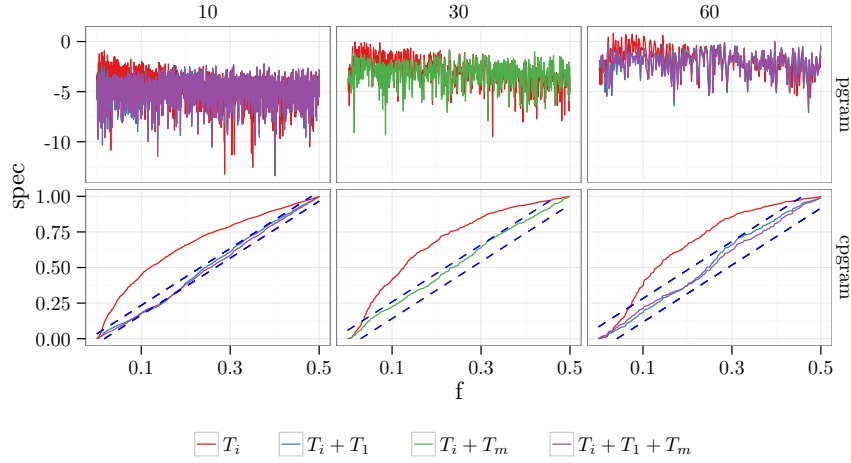

Figure 5.65: Periodograms and cumulative periodograms of residuals, generated by models selected from the model library in Section 5.5.9 (colours), that proved to maximise log-likelihood, for sampling times t_s of 10, 30, and 60 min.

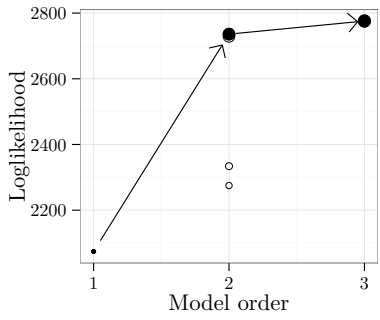

(a) Finding most optimal model, by maximising log-likelihood, while respecting likelihood ratio test. Arrows highlights those steps, from a smaller to a larger model, that are associated with a likelihood ratio test p-value < 0.05.

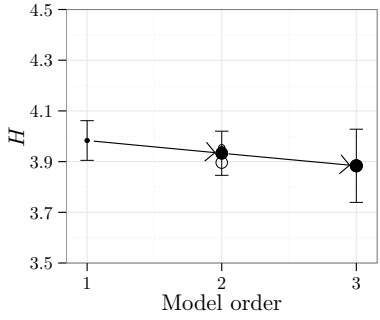

(b) Corresponding estimate for H

Figure 5.66: Selection of suitable model order. Model order 1: T_i; Model order 2: $T_i + T_1$; Model order 3: $T_i + T_1 + T_m$.

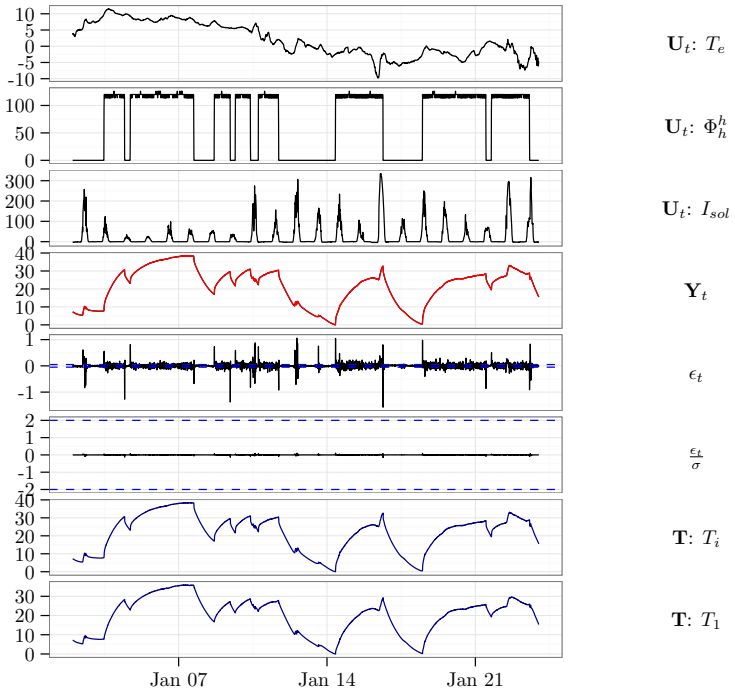

Figure 5.67: Time series plots of inputs $\mathbf{U}_t$: T_e, Φ_h^h, and I_{sol}; outputs $\mathbf{Y}_t$: measured output, T_i, and model output, $\hat{T}_i$ (red); residuals ϵ_t, and normalised residuals $\frac{\epsilon_t}{\sigma}$; and model states $\mathbf{T}$: T_i and T_1.

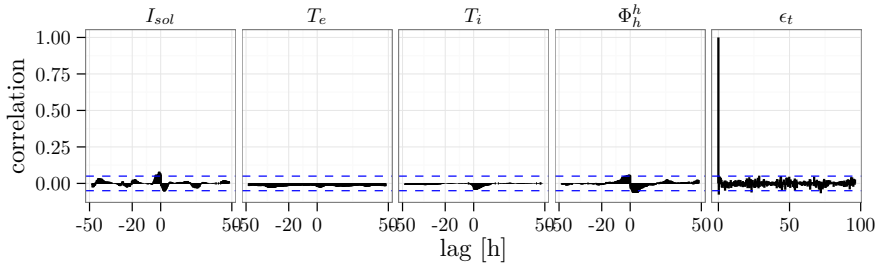

Figure 5.68: (All but right): Cross-correlation between ϵ_t and inputs T_e, Φ_h^h, and I_{sol}, and between ϵ_t and output T_i. (Right): Autocorrelation of residuals.

Table 5.14: Model $T_i + T_1$: estimated values for initial states, parameters and time constants, τ, in h. Derived parameters are collected at the bottom: Overall heat loss coefficient, H, in $\mathrm{W\,K^{-1}}$, global solar aperture, A_{sol}, in $\mathrm{m^2}$, and effective fabric heat capacity, C_f, in $\mathrm{J\,K^{-1}}$.

	Estimate	σ
$T_{i,0}$	7.2387	0.0639
$T_{1,0}$	7.1669	0.1511
$A_{sol,1}$	0.0235	0.0233
$A_{sol,i}$	0.2455	0.0136
C_1	0.0028	0.0001
C_i	0.0004	0.0000
$R_{1,e}$	233.2084	2.7499
$R_{i,1}$	21.0521	0.6085
$R_{i,e,v}$	2.0000	0.1221
τ_1	0.1870	0.0000
τ_2	20.4489	0.0000
H	3.93	0.04
A_{sol}	0.25	0.01
C_f	32017.20	1045.19

Table 5.15: Model $T_i + T_1$: correlation matrix of estimated coefficients. Only rows and columns with values > 0.5 are shown.

	C_i	$r_{i,1}$
$W_{2,t}$	0.63	-0.34
$\epsilon_{1,t}$	-0.33	0.52

5.5.5 Reliability plots

In Figures 5.69 and 5.70, we plot the estimates for H, based on explicit ARX models, and lumped state space models, respectively. With regard to the first, the estimates only become consistent after 15 days. As of this duration, regardless of sampling time t_s, they lie within 13.4 % of their mean. H is estimated as the minimum variance weighting of $\frac{\omega_i(1)}{\omega_h(1)}$ and $\frac{\omega_e(1)}{\omega_h(1)}$, and we see that it is mostly drawn towards the first, as it is associated with less uncertainty.

Continuous-time stochastic state space models, that aside from T_i, discern a capacitive state, T_1 or T_m, prove very effective. As of 4 days, they attain a

reliability that the explicit ARX models never attain: all results lie within 12.7 % of their mean. As of 7 days, this even becomes 6.5 %. Moreover, the confidence intervals seem to accurately grasp the uncertainty related to the estimates.

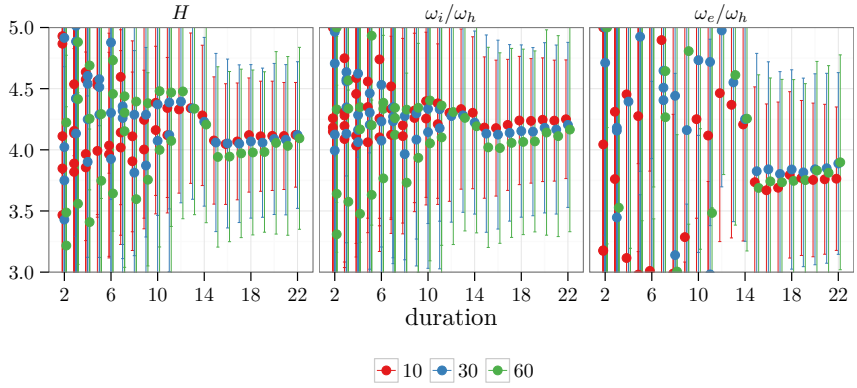

Figure 5.69: Estimates for H, $\frac{\omega_i(1)}{\omega_h(1)}$ and $\frac{\omega_e(1)}{\omega_h(1)}$, assuming an explicit ARX model, with output T_i, model order $k = 2$, and $t_s = 30$ min. Different sampling times t_s (dodged position and colour of points), and data subsets with varying duration (x-axis), are considered.

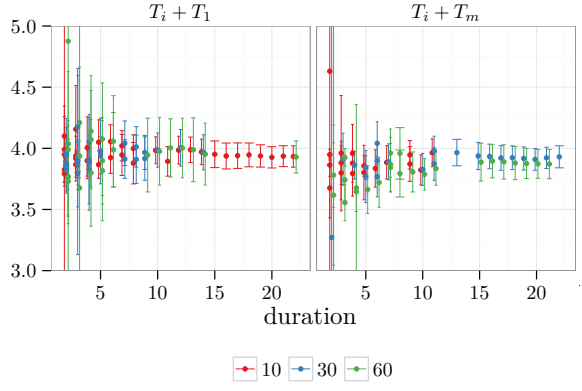

Figure 5.70: Estimates for H based on lumped state space modeling. The columns reflect second-order models, that are selected on the basis of likelihood ratio tests. Their title reflects that states that are discerned. Different sampling times t_s (dodged position and colour of points), and data subsets with varying duration (x-axis), are considered.

5.5.6 Comparison with expected values

Table 5.16 compares the estimates for H, obtained using ARX and grey-box modelling. As the box is very airtight, for this test case, H approximately equals the transmission heat loss H_{tr}. As discussed in a next Section, depending on the fabric's construction quality, the actual λ of the insulating layer, and indoor and outdoor surface transfer coefficients, h_i and h_e, the expected value for H might vary from 3.21 to 4.50 $\mathrm{W\,K^{-1}}$.

Both ARX and lumped state space modelling yield results that are close to H's design value. The latter's CI seems to indicate that the actual value is actually a bit lower, given the actual fabric and weather conditions during the heating experiment. The estimate based on the explicit ARX model is associated with a large confidence interval. As previously discussed, explicit ARX models have difficulties coping with abruptly changing heating power.

Table 5.16: Comparison between expected and assessed H (in this case $\approx H_{tr}$), in $\mathrm{W\,K^{-1}}$. It is estimated using ARX and grey-box modeling. The expected value for H assumes a fabric thermal resistance, R, of 1.93 $\mathrm{m^2\,K\,W^{-1}}$ (Section 5.5.8), indoor surface transfer coefficient $h_i = 8$ $\mathrm{W\,m^{-1}\,K^{-1}}$, and outdoor surface transfer coefficient $h_e = 23$ $\mathrm{W\,m^{-1}\,K^{-1}}$.

	H	σ_H
Expected	4.08	-
ARX	4.12	0.30
CTSM-R	3.93	0.04

5.5.7 Discussion

For this test case, we applied explicit ARX models, to estimate H. Such models do not cope well with abruptly changing inputs, e.g. a heating power that shifts between two levels, or suddenly changing solar gains. To better model such phenomena, in a next test case, we suggest implicit ARX models.

Both for ARX and CTSM-R, we do not necessarily consider the highest order model. For instance, Figure 5.66 justified taking the step from a second-order model to a third-order one. But the confidence interval around H increases as a result. Instead, we prefer a model with a lower order, that combined with a small sampling time t_s, still yields white noise residuals. This way, we limit the risk of over-fitting, and limit σ_H. Figure 5.70 indicates that a second-order lumped state space model, with aside from T_i an additional capacitive state, yields very robust estimates of H.

5.5.8 Appendix: Expected value for H

To quantify an expected value for H, we performed detailed simulations and laboratory measurements. The first allow to vary material characteristics, and boundary conditions. For instance, the outdoor heat transfer coefficient, h_e, shows higher values on a windy day, than it does on a calm day. The latter allows us to perform experiments under well-controlled laboratory conditions. Together, they provide a solid reference to compare assessment results with. To prepare ourselves, however, we first discuss the Test Box fabric characteristics.

Table 5.17 on page 152 collects the material properties of the different layers of the box. Based on these values the one-dimensional R-value of the Test Box fabric amounts to 1.93 $\mathrm{m^2\,K\,W^{-1}}$. Taking into account standard surface resistances (ISO 6946:2007), this corresponds to a U-value of 0.48 $\mathrm{W\,m^{-2}\,K^{-1}}$. These values disregard the dependence of the materials' λ-values on temperature and moisture content. For instance, the λ_{XPS} might rise to 0.038 $\mathrm{W\,m^{-1}\,K}$ at 40 °C, causing R to drop to 1.74 $\mathrm{m^2\,K\,W^{-1}}$. Above mentioned values also disregard the possible presence of thin layers, filled with air and glue, between the different material layers, that might slightly increase the fabric's actual thermal resistance. For instance, a thin air layer of 2.0 mm at each interface between two layers could raise the thermal resistance by 16.6 %, to 2.25 $\mathrm{m^2\,K\,W^{-1}}$.

On the basis of a detailed analysis of measured surface temperatures and heat fluxes during a co-heating campaign at the test site of the Belgian Building Research Institute (BBRI), Deconinck and Roels (2014) revealed that the actual R-value of the Test Box fabric is slightly higher than expected. They applied the averaging method (ISO 9869), but also linear regression and state space models, to find that it lies between 2.01 and 2.23 $\mathrm{m^2\,K\,W^{-1}}$, which is in line with our earlier remarks.

Aside from the uncertainty related to R, an additional uncertainty is introduced by surface heat transfer coefficients h_i and h_e, that vary over time and over the surface. At the outdoor surface, lower wind speeds decrease h_e compared to the standard value, while higher wind speeds increase it. At the inside surface, thermal stack effects and indoor surface temperatures deviate h_i from standard values. To quantify how these uncertainties affect H, we simulated the Test Box repeatedly, with different values for R, h_i and h_e. These simulations, performed in Physibel software Voltra 7.0w, assume the material characteristics in Table 5.17, a glazing U-value of 1.1 $\mathrm{W\,m^{-2}\,K}$, and consider a stationary heating experiment, with T_i at 25 °C and T_e at 0 °C. Table 5.18 collects the values for H that we can thus expect. Depending on R, h_i and h_e, H varies over a considerable range, from 3.21 $\mathrm{W\,K^{-1}}$ to 4.50 $\mathrm{W\,K^{-1}}$. Hence, depending on experiment conditions, different reference values for H are appropriate.

If we do combine a fabric R-value of 1.93 $\mathrm{m^2\,K\,W^{-1}}$, with standard surface heat transfer coefficients, $h_i = 8$ and $h_e = 23$ $\mathrm{W\,m^{-2}\,K^{-1}}$ (ISO 6946:2007), simulations show an overall heat loss coefficient H of 4.08 $\mathrm{W\,K^{-1}}$.

From December 14 to December 18, 2012, we tested the KI Test Box in the Building Physics Section laboratory, to determine H under laboratory conditions. During the test, the box is thermostatically heated to 25 °C, using a 60 W light bulb. The air temperature in the laboratory is also thermostatically controlled and hovers around 18.5 °C. Figure 5.71 shows the indoor air temperatures in laboratory and box, and the delivered heating power, from December 15 to noon of December 17, 2012. The air temperature in the laboratory, T_l, is seen to vary slightly on December 15, falling from slightly above to slightly below 19 °C, after which it stabilises. To estimate H, we select as appropriate reference period the morning of December 17, from 0:00 to 12:00. It is estimated as $\Phi_h^h/\Delta T$, with Φ_h and ΔT averaged over the full reference period. As such, we obtain a target value of 3.82 $\mathrm{W\,K^{-1}}$.

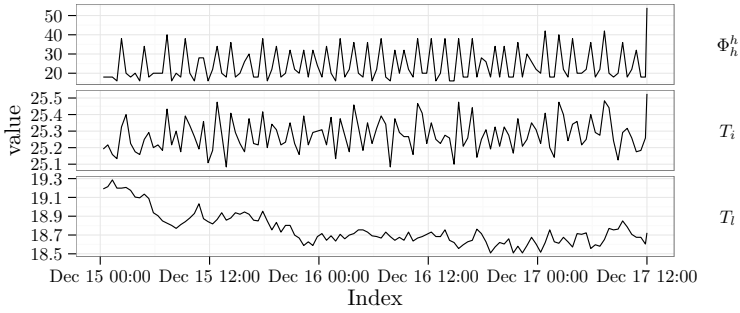

Figure 5.71: Measurement data collected during a stationary heating experiment, performed in the laboratory. Heating power, Φ_h^h, delivered to test box, in W; indoor air temperature, T_i, in °C; air temperature in laboratory hall, T_l, in °C.

For the KI Test Box, we can safely assume that the window determines solar gains. A target value for A_{sol} can thus be estimated on the basis of the window's g-value, 0.63 and the glass surface, 0.26 $\mathrm{m^2}$. We obtain a reference solar aperture value $A_{sol,ref}$ of 0.16 $\mathrm{m^2}$. This estimate does not account for shading, neither of the window frame nor of the environment. It assumes a constant g-value, but simulations by the manufacturer show that, for 2 significant numbers, this is indeed correct. Given the volume and specific heat capacity of the materials out of which the box was constructed (Table 5.17), the total heat capacity amounts to 3.52×10^5 $\mathrm{J\,K^{-1}}$. By combining expected values for H and C_f, and the fact that a dynamic test will only excite part of the box's heat capacity, we expect estimated time constants to not exceed 24 h.

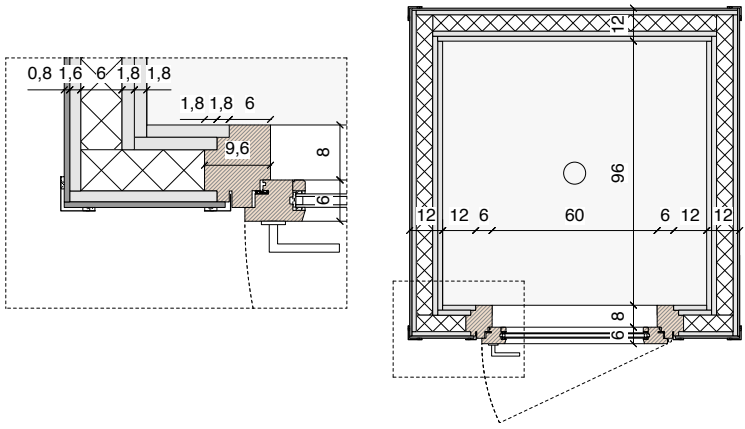

(a)

Figure 5.72: KI Test Box detailed plans.

Table 5.17: Test Box Composition. Thickness of boards, d, in mm, thermal conductivity, λ, in $\mathrm{W\,m^{-1}\,K}$, volumetric density, ρ, in $\mathrm{kg\,m^{-3}}$ and specific heat capacity, c, in $\mathrm{J\,kg^{-1}\,K}$.

Material	d	λ	ρ	c
Fibre cement boards	18 (2x)	0.350	1250	1470
Window frame (wood)	-	0.170	700	2070
XPS insulation	60	0.034	25	1450
Fibre cement boards	16	0.350	1250	1470
Fibre cement boards	8	0.600	1925	1018

Table 5.18: Simulated values for overall heat loss coefficient H ($\approx \mathrm{H}_{tr}$, as $H_v \approx 0$), in $\mathrm{W\,K^{-1}}$, that assume different values for R, h_i, and h_e. R is the thermal resistance of the Test Box wall component; We assume a standard value of 1.93 $\mathrm{m^2\,K\,W^{-1}}$, a 15% increased value of 2.22 $\mathrm{m^2\,K\,W^{-1}}$ to take into account thin layers of air and glue, and a value of 1.74 $\mathrm{m^2\,K\,W^{-1}}$ (with $\lambda_{XPS} = 0.038$ $\mathrm{W\,m^{-1}\,K}$). h_i and h_e are the indoor and outdoor surface transfer coefficients, in $\mathrm{W\,m^{-1}\,K^{-1}}$, that represent varying conditions at surfaces.

$\lambda_{XPS} = 0.038$		$\lambda_{XPS} = 0.034$		$\lambda_{XPS} = 0.034$ + thin air layer			
R	H	R	H	R	H	h_i	h_e
1.74	3.70	1.93	3.49	2.22	3.21	4.00	10.00
1.74	4.33	1.93	4.08	2.22	3.75	8.00	23.00
1.74	4.50	1.93	4.24	2.22	3.90	10.00	30.00

5.5.9 Appendix: Reduced-order models

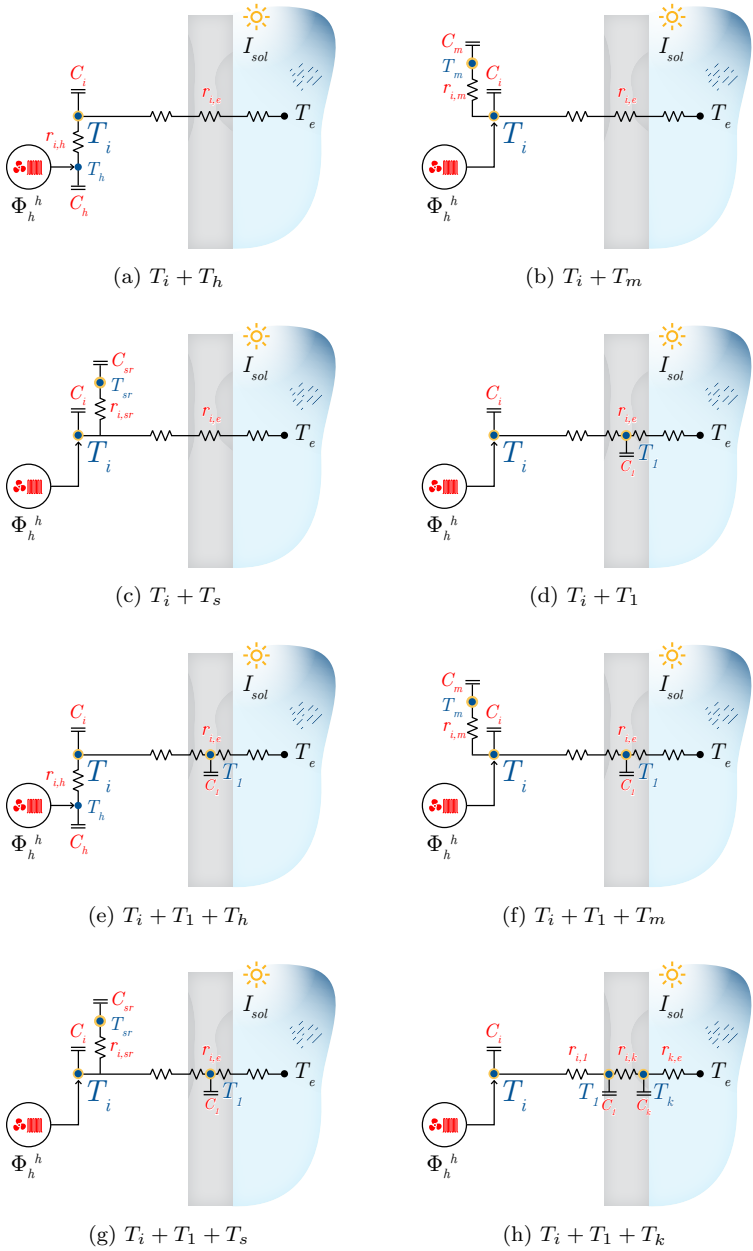

(a) $T_i + T_h$ (b) $T_i + T_m$

(c) $T_i + T_s$ (d) $T_i + T_1$

(e) $T_i + T_1 + T_h$ (f) $T_i + T_1 + T_m$

(g) $T_i + T_1 + T_s$ (h) $T_i + T_1 + T_k$

Figure 5.73: Second-order and third-order simplified thermal models.

5.6 Test Case 5: Twin Test House

In the framework of the IEA EBC Annex 58 project (Annex 58, 2015), to verify the goodness of fit between simulated and actual building response, heating experiments were performed on the identical *Twin Test Houses*, situated at the test site of Fraunhofer-IBP, Holzkirchen, Germany. They are comprehensively described in (Strachan, Heusler, et al., 2014). We consider one of these heating experiments, performed on Twin Test House *O5*, that was specifically designed such that the generated data might also serve as a basis for parameter estimation. It comprises a series of co-heating tests, and one dynamic test. Here, we focus on the latter.

5.6.1 Description

The Twin Test Houses (TTHs) comprise a ground floor, attic and cellar. In the framework of this experiment, the south rooms on the ground floor, numbered *4* to *7* in Figure 5.74a, are conditioned separately. Essentially, they have two boundary conditions: a thermostatically controlled neighbouring zone, T_n, and the ambient weather conditions. Here, we want to characterise the interface between T_i and the latter. The neighbouring zone comprises the three north rooms on ground floor, numbered *1* to *3* in Figure 5.74a, the cellar and the attic. The north rooms are sealed off from the south rooms to avoid ventilation heat exchange. Also the attic hatch is sealed. To limit solar gains in the attic and north rooms during the experiment, the blinds of the corresponding windows were closed. For the south rooms, blinds were left open. Twin Test House O5 is essentially unshaded, and has no neighbouring buildings towards the south.

Light-weight electric heaters deliver the heating power Φ_h^h. They are placed in rooms *4*, *6* and *7*. To maintain similar temperatures in the conditioned south zone, their individual powers are adapted such that they correspond to expected heat loads of these rooms. The researchers placed 1800W in the living room, and 500W in both bathroom and south bedroom. All doors between south rooms, as well as the corridor, are fully opened during the heating experiment. Hence, they can be modelled as a single zone.

Table 5.19: Geometry of heated volume (rooms 4 to 7)

Building volume (outer)	V_o	247.2 m^3
Building volume (inner)	V_i	150.7 m^3
Heat loss surface	A_T	72.2 m^2
Heat loss surface towards T_n	A_T^n	169.8 m^2
Total window area	$A_{w,T}$	26.3 m^2

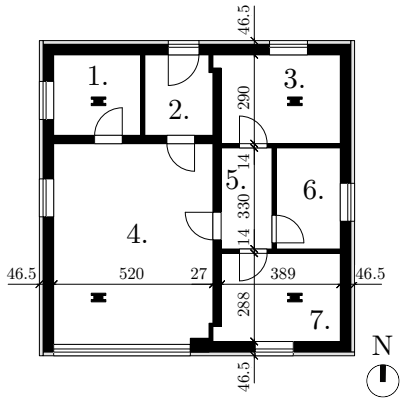

(a) Ground floor plan. (North rooms): 1. Kitchen, 2. doorway, 3. bedroom; (South rooms): 4. Living room, 5. corridor, 6. Bathroom, and 7. bedroom.

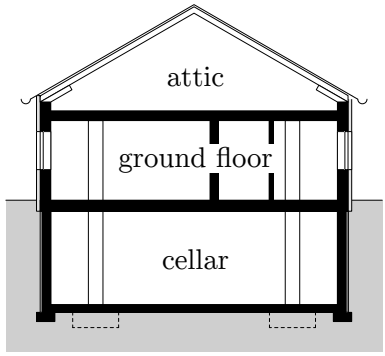

(b) Section along north-south axis.



(c) South facade of Twin Test House N2.



(d) North facade of Twin Test House O5.



(e) (Front right): Twin Test House O5; (Back left): Twin Test House N2.



(f) Living room (*4.*).

Figure 5.74: Building plans and pictures of the Twin Test Houses.

5.6.2 Dynamic test using ROLBS heating power

From April 30 to May 13, 2014, a dynamic heating experiment was performed on Twin Test House 05. Figure 5.75 plots the collected measurement data. Zone temperatures T_i and T_n are constructed as the principal component of a series of air temperatures measured in the different zone rooms. In some of these rooms, air temperatures are measured at different heights.

Heating power Φ_h^h switches between two levels, thereby obeying a ROLBS. To excite the building around its expected time constants, the duration between successive switches varies between 1h to 90 h.

Before the heating experiment, a pressurisation test was performed on the conditioned south rooms, with the doors towards the neighbouring zone sealed. This resulted in a n_{50}-value of 2.49 h^{-1}. After the heating experiment, a similar pressurisation test resulted in a n_{50}-value of 2.3 h^{-1}. Pressurisation tests were performed with the blower door located in the living room door. Leakages through this door are thus excluded from these estimates.

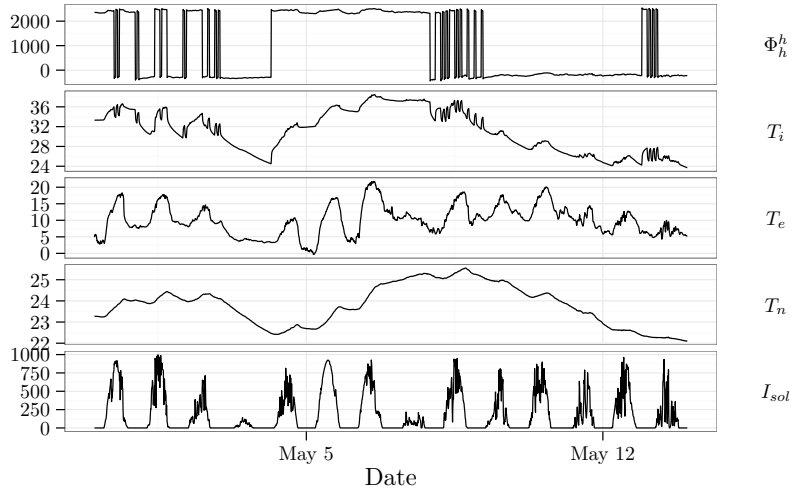

Figure 5.75: Plots of collected measurement data (t_s = 30min). Φ_h^h is the delivered heating power, in W. T_i is the first PC of the indoor air temperatures in the heated zone (rooms 4 to 7), in °C. T_e is the outdoor air temperature, in °C. T_n is the first PC temperature, in °C, of the neighbouring zone (rooms 1 to 3). Finally, I_{sol} is the global horizontal solar radiation, in $\mathrm{W\,m^{-2}}$.

During the heating experiment, the ventilation system was running continuously, at a nominal supply flow rate of 60 $m^3\,h^{-1}$ into the living room, and an extract flow rate of 30 $m^3\,h^{-1}$ in both bathroom and south bedroom. The associated heating power is calculated on the basis of the supply flow rate and the difference between T_i and the supply air temperature, T_{sa}, into the living room.

Figures 5.76a and 5.76b reveal that T_i is significantly autocorrelated, strongly cross-correlated with Φ_h^h, and moderately correlated with T_e, T_n, and I_{sol}. Figure 5.76c reveals that, on its turn, T_n is also slightly correlated with T_i, T_e and I_{sol}. Despite thermostatic control and lowered blinds, the neighbouring zone is visibly influenced by the heating experiment, and external weather conditions.

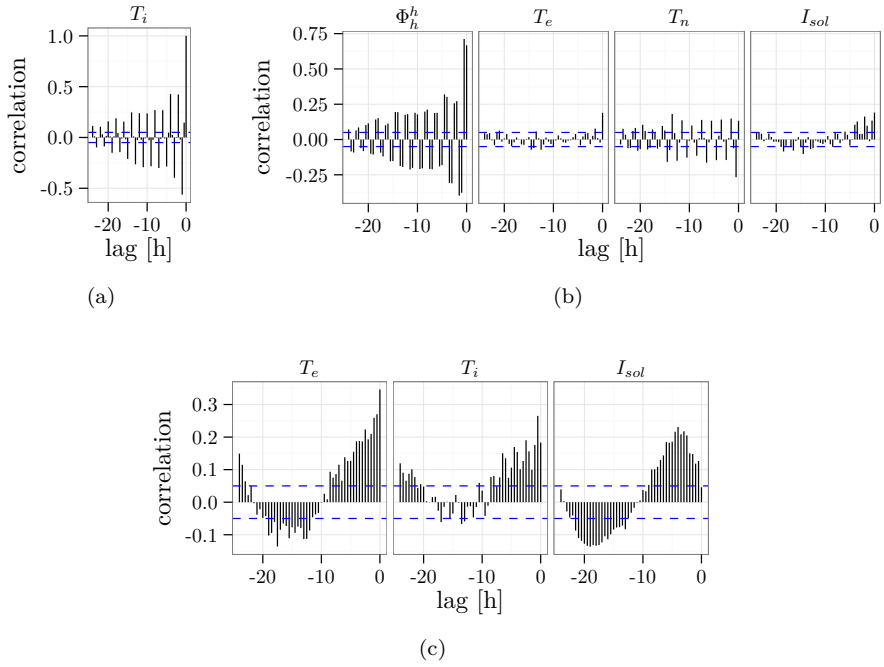

Figure 5.76: (a) $ACF(T_i)$; (b) CCFs between T_i and candidate predictors Φ_h^h, T_e, T_n and I_{sol}. (c) CCFs between T_n and T_e (left), T_n and T_i (middle), and T_n and I_{sol} (right). A sampling time of 60 min is assumed.

5.6.3 Estimating H using ARX models

In Section 4.2.3.2 of Chapter 4, we related a first-order continuous-time stochastic state space model to its discrete-time transfer function equivalent. We thus obtained an *explicit ARX model*: the state of the system at the current time is calculated from previous values of its state. The analysis of the Round Robin Test Box in Section 5.5 shows that such models can indeed deliver results that are consistent with the first. Nonetheless, we need to be cautious. When we analyse a stiff system, as for instance a building, the explicit method demands, to limit uncertainty, a very small sampling time t_s. If t_s is not small, the model output $\hat{T}_i$ tends to overshoot the actual output T_i, each time Φ_h^h switches. This is illustrated by the time series in the left-hand column of Figure 5.77. They are generated by a 3th order *explicit* ARX model, that respects Eq. 4.23 (page 74).

Significant peaks in the residuals result. Moreover, in subsequent time steps, $\hat{T}_i$ jumps more closely to T_i again, thereby disturbing $\hat{T}_i$'s heating curve and corrupting the estimates for H. These issues are exacerbated when Φ_h^h switches multiple times and in rapid succession.

To cope with these issues, we can assume *implicit ARX models*. They involve both current and previous system states, and are thus able to get much more intimate with T_i's actual response to Φ_h^h. For instance, the time series in the right-hand column of Figure 5.77 are generated by a 3th order *implicit* ARX model. Compared to Eq. 4.23, the inputs are shifted one time step forward, by multiplying them by B^{-1}:

$$\omega_i(B)T_{i,t} = \omega_e(B)B^{-1}T_{e,t} + \omega_h(B)B^{-1}\Phi_{h,t} + \omega_{sol}B^{-1}(B)I_{sol,t} + \epsilon_t \quad (5.4a)$$

Although it has the same number of parameters, the implicit method does not show large peaks in the residuals at times when Φ_h^h switches on and off; $\hat{T}_i$'s heating curve does not detach from T_i at regular intervals and we obtain a more accurate assessment of H. For this particular test case, we thus opt for an *implicit ARX model*.

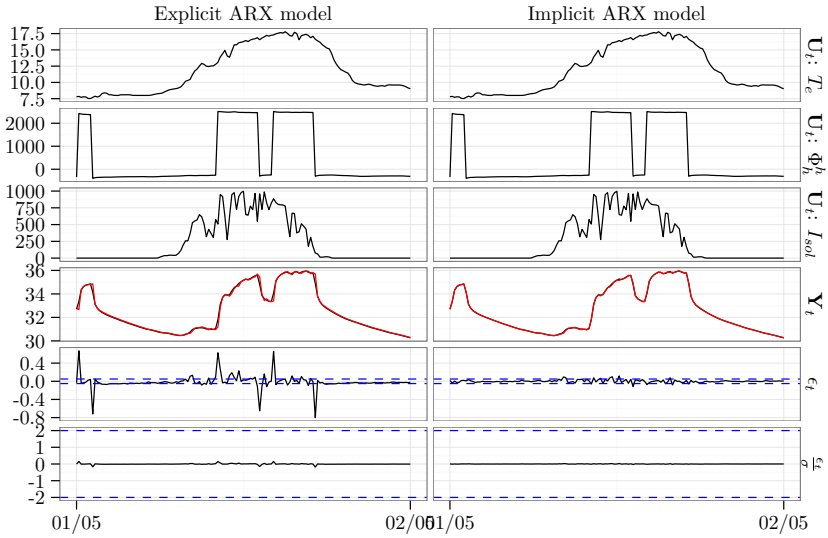

Figure 5.77: (Left): Explicit method; (Right): Implicit method. Time series plots of inputs $\mathbf{U}_t$, measured output and model output (red) $\mathbf{Y}_t$, residuals ϵ_t, and normalised residuals $\frac{\epsilon_t}{\sigma}$.

This test case is a peculiar case of *Scenario 3*. As already mentioned, T_i interfaces with both the external environment, and T_n. Moreover, considerable heat is exchanged between the latter and T_i. Parameter estimation shows that, for a first-order implicit ARX model, T_n indeed significantly influences T_i. Such a first-order model, however, does not yield white noise residuals. When we increase the model order, all ω_n's become insignificant, and taken together, they tend to cancel out the influence of T_n. This confirms the behaviour we see in $CCF(T_i, T_n)$, in Figure 5.76b. Moreover, if we take into account T_n as a predictor, the estimates for H are clearly corrupted. We thus estimate H as $\frac{\omega_e(1)}{\omega_h(1)}$. But as T_n is slightly correlated with T_e, its value remains highly uncertain.

On the basis of the cumulative periodograms in Figure 5.78, we retain a sampling time t_s of 30 min and a fifth order model. For a sampling time of 10 min, even for higher order models, a wavy pattern persists, and the lines slightly exceed the confidence bounds around a frequency f of 0.083, or a period of 6 h. For a t_s of 30 minutes, the fourth order model tends to underperform for higher frequencies. In any case, going from model order 4 to 5 does not change the estimate's uncertainty.

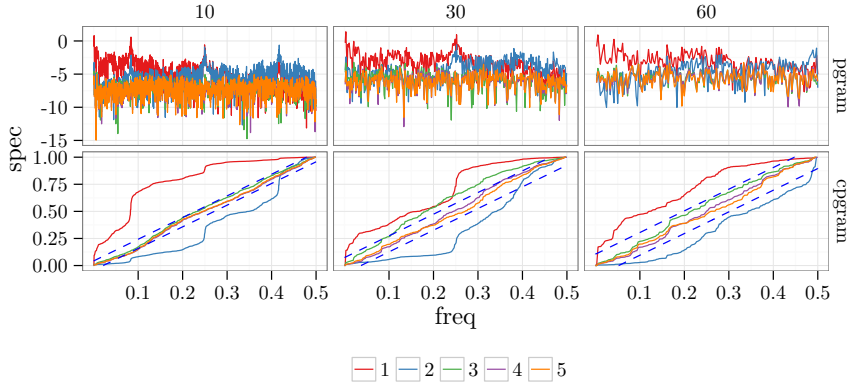

Figure 5.78: Periodogram and cumulative periodogram of residuals generated by ARX models of order 1 to 5 (colours) that consider data with sampling times of 10, 30 and 60 minutes (from left to right).

Table 5.20 collects the parameter estimates. As could be expected from the correlation functions in Figure 5.76, the standard deviation around the estimate of H is considerable. For our model of choice, the 95% confidence interval ranges from 6.1 to 56.1 $\mathrm{W\,K^{-1}}$, with a mean value of 31.1 $\mathrm{W\,K^{-1}}$.

Table 5.20: Estimated stationary gains, on the basis of an implicit ARX model, with T_i as output, a t_s of 30 min, and model order $k = 5$.

	Estimate	σ
$\frac{\omega_i(1)}{\omega_h(1)}$	178.2	23.6
$\frac{\omega_e(1)}{\omega_h(1)}$	31.1	12.5
$\frac{\omega_{sol}(1)}{\omega_h(1)}$	2.1	0.3

Figure 5.79 shows the time series associated with our model of choice. The $ACF(\epsilon_t)$ plot in Figure 5.80 confirms that the residuals behave as white noise. And ϵ_t's cross-correlation with the considered inputs indicates that we've taken them into account properly.

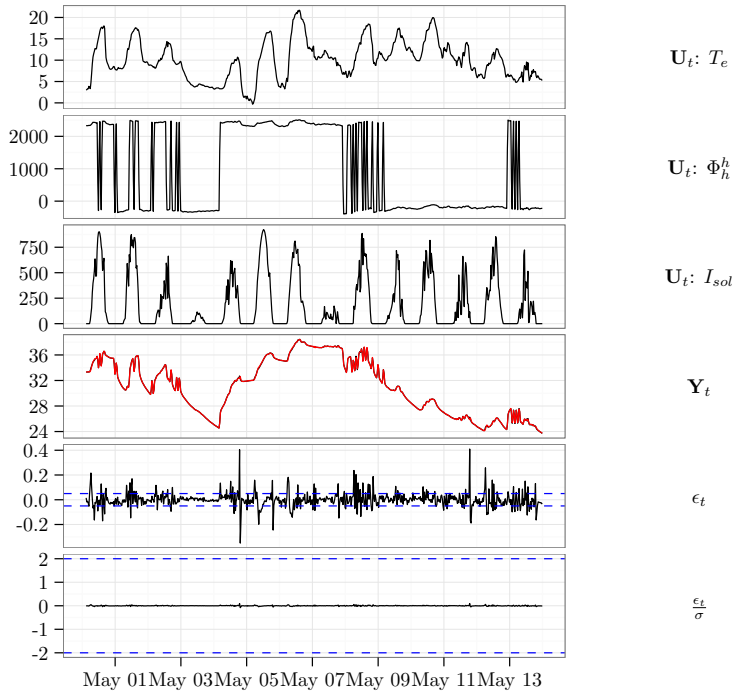

Figure 5.79: Time series plots of inputs $\mathbf{U}_t$: T_e, Φ_h^h, and I_{sol}; output $\mathbf{Y}_t$: measured output T_i, and model output $\hat{T}_i$ (red); residuals ϵ_t, and normalised residuals $\frac{\epsilon_t}{\sigma}$.

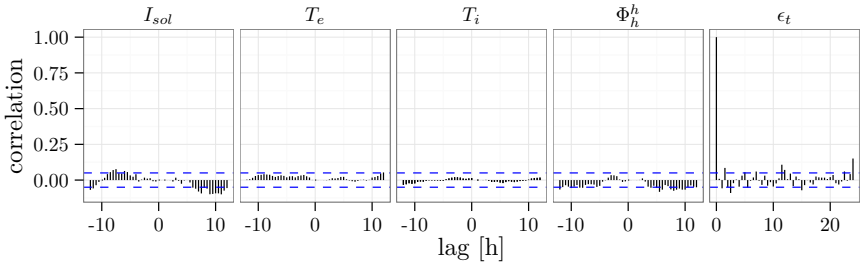

Figure 5.80: (All but right): Cross-correlation between ϵ_t and inputs T_e, Φ_h^h and I_{sol}, and between ϵ_t and output T_i. (Right): Auto-correlation of residuals.

5.6.4 Reliability plots

Figure 5.81 collects the estimates for H as a function of sampling time t_s (columns), data subset duration (x-axes), and model order k (colour and position of points). For durations of 9 to 14 days, assuming a t_s of 30 or 60 minutes and a model order of 5, the mean estimates for H vary consistently around 30 $\mathrm{W\,K^{-1}}$, and within 25.8 % (30 min) and 17.3 % (60 min) of their mean. For a t_s of 60 minutes, as of duration 12, results for model orders 3, 4 and 5 remain within 16.7 % of their mean, and seem to support our adopted strategy. For all combinations, however, the uncertainty around the estimates is high. Moreover, Figure 5.82 illustrates that these high uncertainties are there to stay. They drop significantly until a duration of 10 days, but after that they remain almost constant.

5.6.5 Comparison with expected values

Unfortunately, the heating experiment conditions did not promote an accurate assessment of H. Nonetheless, we compare our estimate with its expected values. From Table 5.21, we see that the expected value indeed lies within the 95% confidence interval. However, as this interval captures a large range, this does not come as a surprise.

Table 5.21: Comparison between calculated and assessed overall heat loss coefficients, in $\mathrm{W\,K^{-1}}$.

	H	σ_H
designed	38.4	-
assessed	31.1	12.5

5.6.6 Discussion

Test Case 5 is an outsider, and it is unlikely that we will encounter it in practice. As Table 5.19 indicates, its heated zone has a much larger interface with T_n (169.8 $\mathrm{m^2}$), than with the external environment (72.2 $\mathrm{m^2}$). Moreover, the indoor walls are not insulated, whereas the building envelope is well insulated. Hence, although $T_i - T_n$ is smaller than $T_i - T_e$, the heat exchanges between T_i and T_n, and T_i and the external environment, are of the same order of magnitude. During the dynamic test discussed here, T_n was also correlated with T_e, and as a result, the estimate for H, as $\frac{\omega_e(1)}{\omega_h(1)}$ is corrupted.

To remedy above issues, a future heating experiment should measure Φ^n_{tr}, and make sure that $\Phi^e_{tr} + \Phi^g_{tr}$ is considerable. Assume $\Phi^h_h - \Phi^n_{tr}$ as heating power input, and estimate H as the minimum variance weighting of $\frac{\omega_i(1)}{\omega_h(1)}$ and $\frac{\omega_e(1)}{\omega_h(1)}$. If possible, reduce Φ^n_{tr}, by simultaneously heating the neighbouring zone, thereby minimising $T_i - T_n$.

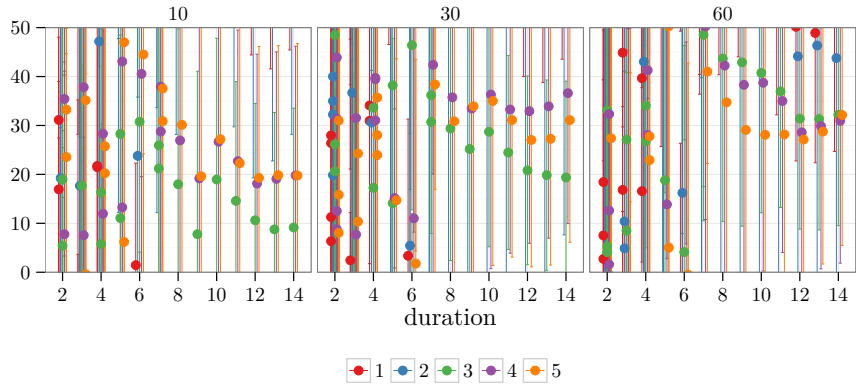

Figure 5.81: Estimates of $\frac{\omega_e(1)}{\omega_h(1)}$, that result from an implicit ARX model, of the form $\omega_i(B)T_i = \omega_e(B)T_e + \omega_h(B)T_h + \omega_{sol}(B)T_{sol} + \mu + \epsilon$. The columns collect the results for different t_s, in min. The colours reflect model orders k, from 1 to 5.

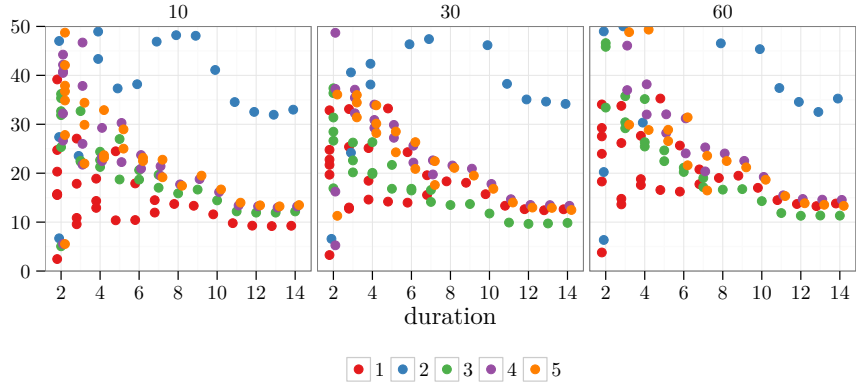

Figure 5.82: σ_H, corresponding to estimates for H, as $\frac{\omega_e(1)}{\omega_h(1)}$, in Figure 5.81.

5.7 Test Case 6: Detached house in Limelette, Belgium

In this last Test Case, we again analyse the detached house, that we considered in Test Case 2 (Section 5.3). This time, the house is excited using a dynamic heating experiment. For the reasons discussed in Test Case 5, we assume *implicit ARX models*. Furthermore, we apply second-order lumped stochastic state space models, and as discussed in Section 4.3, we take into account that ω_i^i, in system matrix $\mathbf{A_c}$ (Eq. 4.26c, page 76), is influenced by heat losses towards the cellar. This is especially relevant when these heat losses are not modelled explicitly.

5.7.1 Dynamic heating experiment

The dynamic heating experiment considered here is performed by researchers at BBRI. Lethe et al. (2014) describe details with regard to its experimental setup and experiment design. From several dynamic experiments that were performed in this campaign, we select 10 days, from February 8 to February 17, 2014, during which the house is excited with a heating power Φ_h^h, that follows a PRBS.

Figure 5.83 plots the time series that feed the analysis. Φ_h^h represents the total heating power that is delivered to the rooms of the ground floor zone. To ensure that the indoor air temperatures in the individual rooms remain homogeneous, for instance when Φ_h^h switches to a higher level, the total heating power is distributed sensibly among these rooms: the amount of heating power that each individual room j receives is controlled on the basis of its temperature, and the heating power it received in a previous time step (Lethe et al., 2014):

$$\Phi_{h,t+1}^j = \frac{\Phi_{h,t+1} \frac{\Phi_{h,t}^j}{T_{i,t}^j}}{\sum_j (\frac{\Phi_{h,t}^j}{T_{i,t}^j})} \tag{5.5}$$

Similar to Test Case 2, detailed measurements of n_{actual} are available, and by applying Eq. 2.20 on page 22, we calculate the actual natural ventilation heat losses, Φ_v, that occur as the heating experiment unfolds. Figure 5.84 plots the corresponding time series.

We only have available a volume-weighted indoor air temperature T_i. In any case, given the way Φ_h^h is distributed among the rooms, the indoor air temperatures in the individual rooms remain very similar. Hence, a plain average, a volume-weighted average or a principal component of the indoor air temperature time series are likely to result in similar representative signals.

Figure 5.85a shows that T_i is significantly autocorrelated, and the CCFs in Figure 5.85b show that T_i is cross-correlated with all candidate predictors Φ_h^h, T_e, I_{sol}, T_{attic}, and T_c. However, Figure 5.85c shows that T_{attic} varies together with T_e; it should thus not be included as a separate term in our models. Finally, T_c is only slightly correlated with T_e (Figure 5.85c).

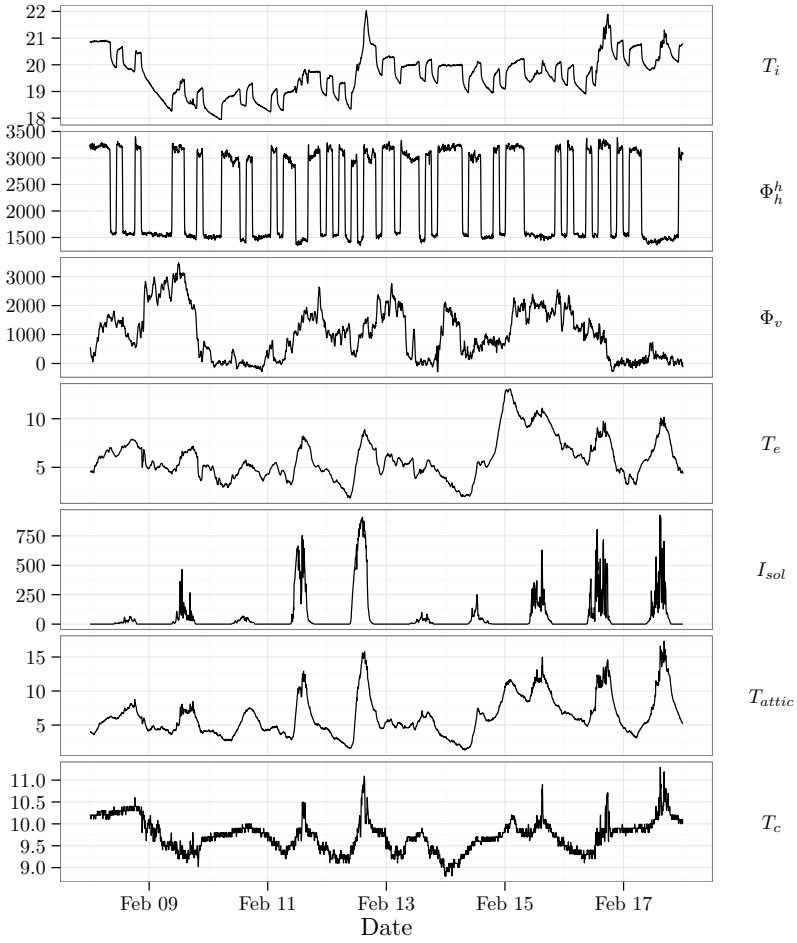

Figure 5.83: Measurement data, collected during dynamic heating experiment. T_i is the indoor air temperature, in °C; Φ_h^h the heating power, in W; Φ_v the ventilation heat loss, in W; T_e the external air temperature, in °C; I_{sol} the global solar radiation measured perpendicular to south oriented upright plane, in $\mathrm{W\,m^{-2}}$; T_{attic} the attic air temperature, in °C; and T_c the cellar air temperature, in °C.

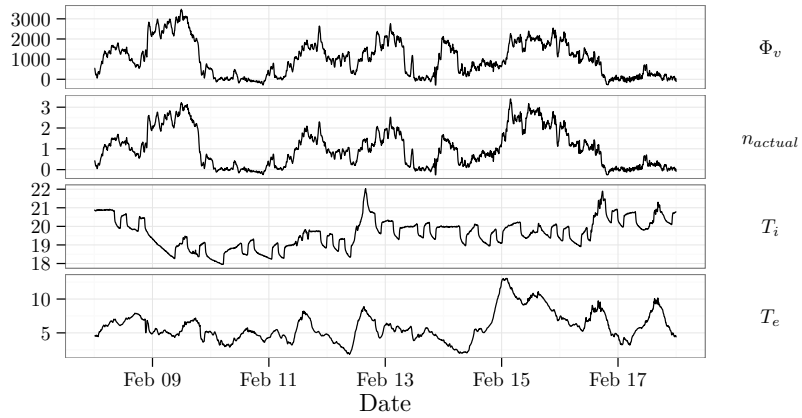

Figure 5.84: Calculated ventilation heat loss, Φ_v, in W; measured air change rate, n_{actual}, in h^{-1}; volume-weighted indoor air temperature T_i, in K; outdoor air temperature T_e, in K.

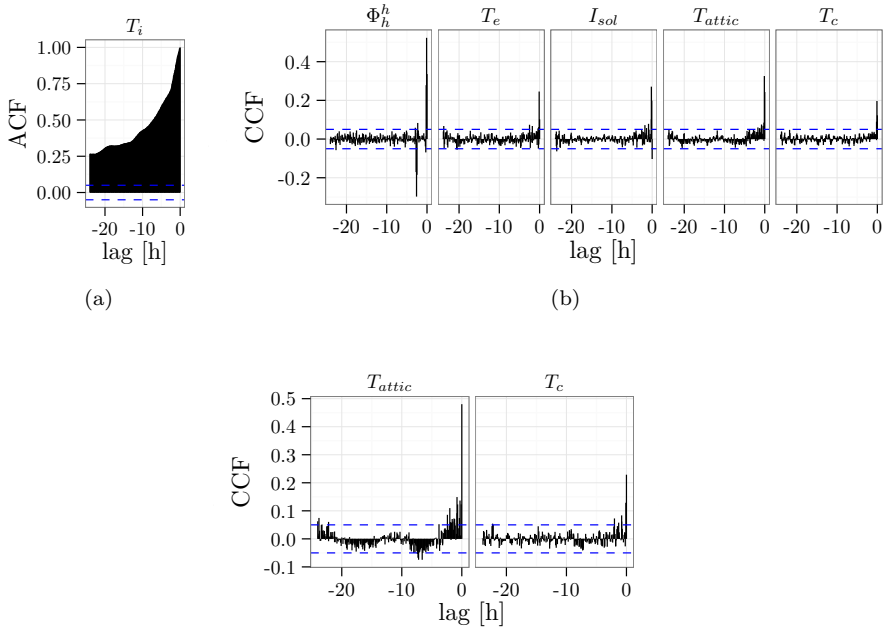

Figure 5.85: (a): $ACF(T_i)$; (b): CCFs between T_i and candidate predictors Φ_h^h, T_e, I_{sol}, T_{attic}, and T_c. (c) Cross-correlations of T_e with T_{attic} and T_c. A sampling time of 5 min is assumed.

5.7.2 Estimating H_{tr} using ARX modelling

Similar to Test Case 2, we categorise this case as a *Scenario 2*. We thus estimate H_{tr} as $\omega_i(1)/\omega_h(1)$, thereby assuming Eq. 3.34, with $\Phi_h^h - \Phi_v$ as model output. The $CCF(T_e, T_c)$ in Figure 5.85c shows that there is some correlation between T_e and T_c. We could thus argue for *Scenario 4*. But in any case, when following the corresponding strategy, H will be drawn much more towards $\omega_i(1)/\omega_h(1)$, than $\omega_e(1)/\omega_h(1)$.

The estimate for H_{tr} is corrupted when, similar to Test Case 2, we include T_c as a separate predictor, and when we do not ignore μ in Eq. 4.23. Figure 5.92 in Section 5.7.7 illustrates the latter. For some data subset durations and t_s, we obtain values for H_{tr} that are an order of magnitude higher than we would expect from the physics. In what follows, we thus ignore $\mu = 0$. Surely, heat losses towards the cellar should not be underestimated. But as T_e and T_c are slightly correlated, the coefficients $\omega_{e,j}$ can be expected to compensate for that. In any case, the influence of these heat losses remains embedded in $\omega_i(1)/\omega_h(1)$.

Figure 5.86 collects the periodograms and cumulated periodograms that are generated by implicit ARX models, as they are defined in Test Case 5 (Section 5.6.3). As in Test Case 2 and 3, for each sampling time t_s, we start with a first-order model, $k = 1$, and then gradually increase k until we find the highest order model that has k significant AR coefficients. In each step, lagged inputs and outputs that prove insignificant are skipped using backward elimination. Figure 5.86 illustrates that this procedure is not flawless. For some t_s, it seems to halt before we reach a model order that yields white noise residuals. Nonetheless, a fourth-order model and a t_s of 5 min proves suitable.

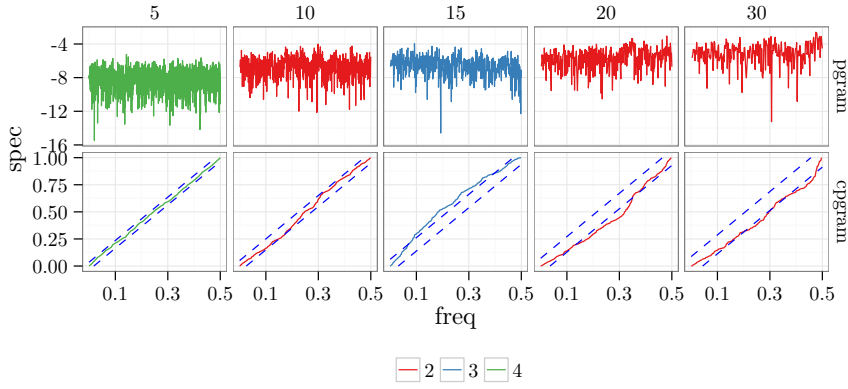

Figure 5.86: Log-periodogram (top) and cumulated periodogram (bottom) of residuals. Columns reflect different sampling times t_s. Colours reflect the retained model order, k.

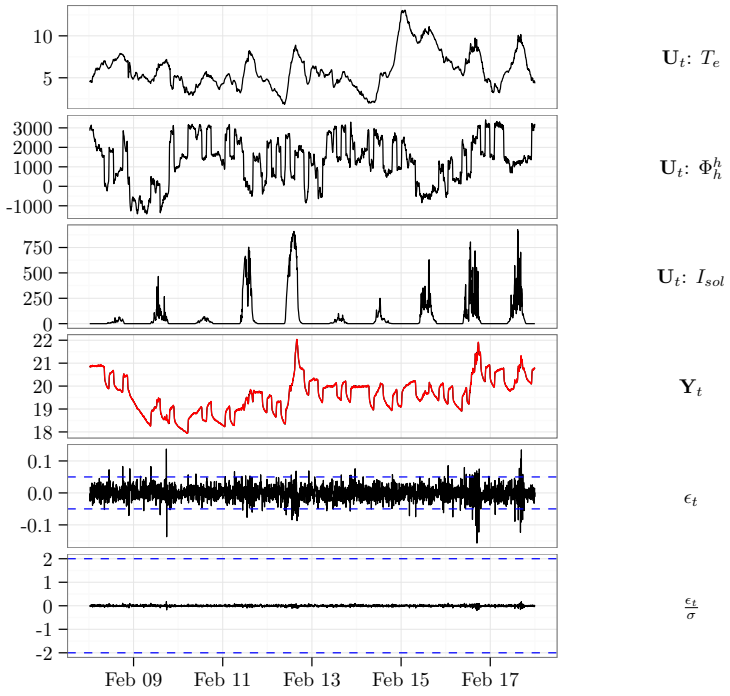

Figure 5.87: Time series plots of inputs $\mathbf{U}_t$: T_e, Φ_h^h, and I_{sol}; output $\mathbf{Y}_t$: measured output T_i, and model output $\hat{T}_i$ (red); residuals ϵ_t, and normalised residuals $\frac{\epsilon_t}{\sigma}$.

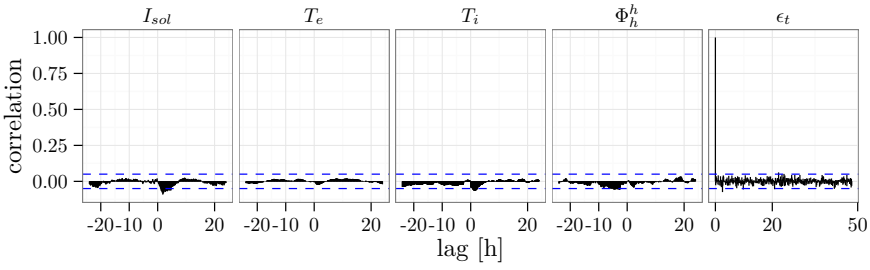

Figure 5.88: (All but right): Cross-correlation between ϵ_t and inputs T_e, Φ_h^h and I_{sol}, and between ϵ_t and output T_i. (Right): Autocorrelation of residuals.

5.7.3 Estimating H_{tr} using CTSM-R

In this section, we apply the second-order stochastic state space model, defined in Section 4.2.4 of Chapter 4. Particular aspects about this test case are that we have measured values for $-\Phi_v$, or $\frac{1}{r_v}(T_e - T_i)$ in Eq. 4.24, and that, instead of T_n and T_g, we consider the cellar temperature T_c as main boundary condition other than T_e. Figure 5.89 schematically illustrates this. By rewriting Eqs. 4.24 and 4.26 accordingly, we obtain following system of DEs:

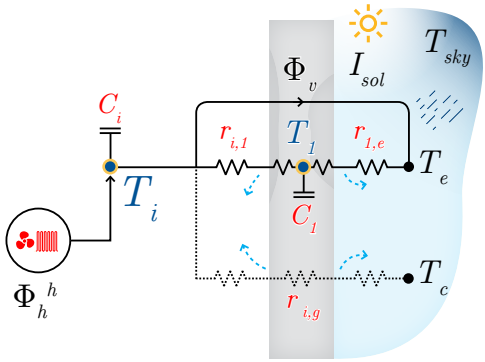

Figure 5.89: Second-order lumped state space model, with an indoor air temperature state T_i and building fabric state T_1. T_i is both *system state* and *measured output*.

$$
\begin{aligned}
C_i \frac{\partial T_i}{\partial t} = {} & (\Phi_h^h - \Phi_v) + A_{sol}(azel) I_{sol} + \\
& \frac{1}{r_{i,1}} \Big(T_1 - \big(T_{Ri} + r_i (A_{sol,si}(azel) I_{sol} + h G_{si}) \big) \Big) \\
& + \frac{1}{r_{i,c}} \Big(T_c - \big(T_{Ri} + r_i^c (A_{sol,si}^c(azel) I_{sol} + h G_{si}^c) \big) \Big)
\end{aligned} \tag{5.6}
$$

$$
\begin{aligned}
C_1 \frac{\partial T_1}{\partial t} = {} & \frac{1}{r_{i,1}} (T_{Ri} + r_i (A_{sol,si}(azel) I_{sol} + h G_{si}) - T_1) \\
& + \frac{1}{r_{1,e}} (T_e + r_e (A_{sol,se}(azel) I_{sol} + \frac{1}{r_{sky}} (T_{sky} - T_{se}) + h G_{se}) - T_1)
\end{aligned} \tag{5.7}
$$

The model parameters then reduce to:

$$\begin{aligned}
&\omega_i^i = -(\frac{1}{r_{i,1}} + \frac{1}{r_{i,c}}) && \omega_h^i = 1 && \omega_h^1 = 0 \\
&\omega_1^i = \frac{1}{r_{i,1}} && \omega_e^i = 0 && \omega_e^1 = \frac{1}{r_{1,e}} \\
&\omega_i^1 = \frac{1}{r_{i,1}} && \omega_c^i = \frac{1}{r_{i,c}} && \omega_c^1 = 0 \\
&\omega_1^1 = -(\frac{1}{r_{i,1}} + \frac{1}{r_{1,e}}) &&&&
\end{aligned} \tag{5.8}$$

When we model T_c explicitly, and T_c significantly influences T_i, we can estimate $r_{i,c}$ in Eq. 5.8. But the values for $CCF(T_e, T_c)$, in Figure 5.85c, do not support this, neither does our experience with T_c as a separate predictor in the ARX models. Instead, we do not model T_c explicitly. Hence, ω_i^i collapses into a single term: $-1/r_{i,1}^i$. We estimate $1/r_{i,1}^i$ and $1/r_{i,1}$ separately, and follow the strategy for *Scenario 2*, as introduced in Section 4.3.

5.7.4 Reliability plots

The reliability plots in Figures 5.90 and 5.91 collect the estimates for H_{tr}, generated by ARX models (Figure 5.90) and grey-box models (Figure 5.91).

ARX models yield results that are not very robust. As of 8 days, the estimates for $\omega_i(1)/\omega_h(1)$ remain within 31.1 % of their mean, regardless of sampling time t_s. If we only consider a t_s of 5 min, estimates remain within 21.6 %. Even for a duration of 10 days, there remains a deviation of 25.2 %, depending on chosen t_s. Also the confidence intervals (CIs) are considerable, as also confirmed in Table 5.22. Compared to the results we obtained in Test Case 2, where we analyse a co-heating test performed on the same property, using linear regression and ARX modelling, the estimates are less robust: In Test Case 2, results remain within 17.6 %, for linear regression, and 19.0 %, for ARX modelling, for a duration of 10 days and regardless of t_s.

Grey-box models yield much more reliable estimates for H_{tr} than the ARX models. Their estimates, based on a duration of 2 days, remain within 36.4 %, for a t_s of 5 min. Hence, they attain a reliability that the ARX models can only match after 10 days (21.6 %). Again assuming a t_s of 5 min, for durations of 3 days and higher, estimates remain within 15.7 %, and for durations of 5 days and higher, within 3.5 % of their mean.

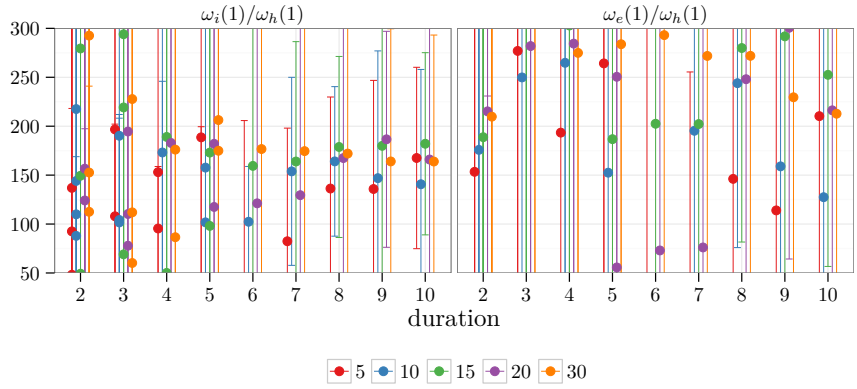

Figure 5.90: Estimates for $\frac{\omega_i(1)}{\omega_h(1)}$ (left), and $\frac{\omega_e(1)}{\omega_h(1)}$ (right), that result from an implicit ARX model, of the form $\omega_i(B)T_i = \omega_e(B)T_e + \omega_h(B)(\Phi_h^h - \Phi_v) + \omega_{sol}(B)T_{sol} + \epsilon$, fitted to data subsets of varying durations (x-axis). The colours reflect sampling times of 5 to 30 min.

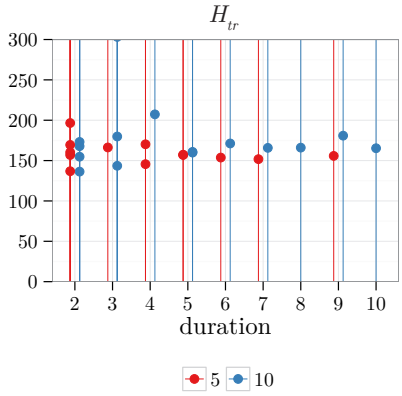

Figure 5.91: Estimates for H_{tr}, obtained by fitting a second-order lumped state space model, to data subsets of varying durations (x-axis). The colours reflect sampling times of 5 min (red), 10 min (blue).

5.7.5 Comparison with expected values

Table 5.22 compares the estimates, obtained using ARX models and grey-box models, with the expected value for H_{tr}. Grey-box models more closely approach the expected value for H_{tr}, but are associated with a large confidence interval, due to the added complexity of the model, and the way H_{tr} is derived from its parameters.

Table 5.22: Comparison between expected and assessed transmission heat loss coefficients, in $\mathrm{W\,K^{-1}}$. H_{tr} is estimated using both ARX and grey-box models.

	H_{tr}	$\sigma_{H_{tr}}$
Expected	142.4	-
ARX	167.5	46.3
CTSM-R	155.8	83.1

5.7.6 Discussion

For this test case, we pondered between Scenario 2 and Scenario 4. CCFs revealed a slight correlation between T_e and T_c, but we deemed it not strong enough to argue for Scenario 4.

The dynamic test, if analysed with ARX models, does not yield more robust results, than a co-heating test, analysed using linear regression or ARX models (Test Case 2). On the other hand, the combination of a dynamic test and grey-box modelling is promising. For this test case, it yields very reliable results after a limited duration of 3 to 4 days. Sensibly applying grey-box models, however, demands significant expertise from the practitioner.

5.7.7 Appendix: Reliability plots ARX model with $\mu \neq 0$

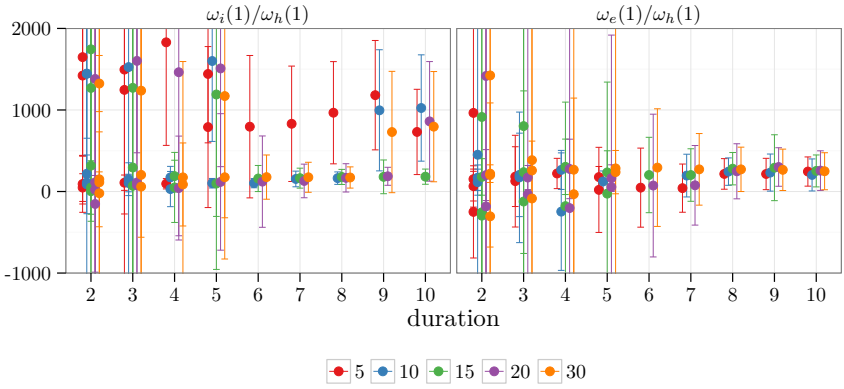

Figure 5.92: Estimates for $\frac{\omega_i(1)}{\omega_h(1)}$ (left), and $\frac{\omega_e(1)}{\omega_h(1)}$ (right), that result from an implicit ARX model, of the form $\omega_i(B)T_i = \omega_e(B)T_e + \omega_h(B)(\Phi_h^h - \Phi_v) + \omega_{sol}(B)T_{sol} + \mu + \epsilon$, fitted to data subsets of varying durations (x-axis). The colours reflect sampling times of 5 to 30 min.

5.8 Conclusions

Before we conclude this dissertation, we take a step back, and assemble the lessons we learned from the three quasi-stationary and three dynamic test cases, that we analysed in this chapter.

In *Test Case 1*, we investigated three co-heating test periods, that ran before and after two renovation steps. It involves a brick house with cavity walls, that is terraced, and has a ventilated cellar. We categorised it in *Scenario 3*, and estimated H as $-\omega_e$, using linear regression (LR). We found that, in a first period, the building fabric was still charging. Calculations however show that the associated heating power is limited to about 2 % of total heating power Φ_h^h. And for future test cases, it could be even further reduced by ensuring that the investigated house is pre-conditioned appropriately. The heat flux and surface temperature measurements indicate that buildings that are well-insulated are more easily heated to quasi-stationary conditions. We estimated H as 221.38 $\pm$ 58.71 $\mathrm{W\,K^{-1}}$, in period *Before*, 118.96 $\pm$ 22.67 $\mathrm{W\,K^{-1}}$, in period *After 1*, and 106.72 $\pm$ 8.73 $\mathrm{W\,K^{-1}}$, in period *After 2*. These estimates show large confidence intervals (CIs), especially considering LR tends to underestimate them. Moreover, reliability plots show that they are not robust: in period *Before*, estimates are very unstable, and deviate up to 51.4 % from their mean; in period *After 1*, up to 30 %, for durations of 11 days and higher; in period *After 2*, up to 32 %, for durations of 9 days and higher. They are also systematically lower than expected. Limited information about the envelope's actual characteristics prevented us from pinpointing specific reasons for this.
Test Case 2 is a co-heating test, performed on a detached house, with attic and ventilated cellar. The house has well-insulated brick cavity walls, an insulated wooden attic floor and an insulated floor above cellar. The first principal component of the indoor air temperatures was drawn towards the indoor air temperature of a smaller room, that was not heated separately. Instead, we selected the volume-weighted indoor air temperature, to better represent the heated zone. T_c is slowly varying and uncorrelated with T_e. Hence, following *Scenario 2*, H_{tr} is estimated as ω_i, using LR and ARX models. As a separate predictor, T_c proved to corrupt the estimates for H. Although heat losses towards the cellar are significant, to obtain a physically relevant estimate for ω_i, we ignored μ. Using LR, we estimate H as 145.9 $\pm$ 4.8 $\mathrm{W\,K^{-1}}$. Using ARX, we estimate H as 148.1 $\pm$ 19.8 $\mathrm{W\,K^{-1}}$. The expected value for H is 143.8 $\mathrm{W\,K^{-1}}$. Reliability plots show that the estimates are consistent, with regard to both analysis methods. They are, however, sensitive to the chosen sampling time, t_s. Given we assume a t_s of 480 min for LR, and a t_s of 10 min for ARX, we obtain fairly robust results after only 7 days: results remain within 11.9 % (LR) and 12.2 % (ARX). As of 14 days, they remain within 1.4 % (LR) and 1.7 % (ARX).

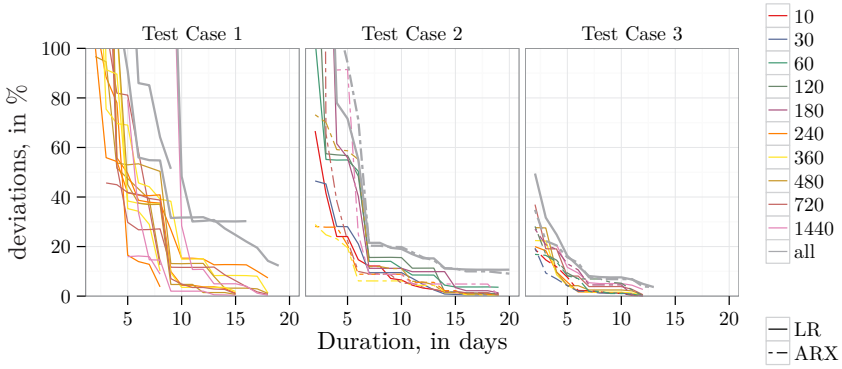

(a)

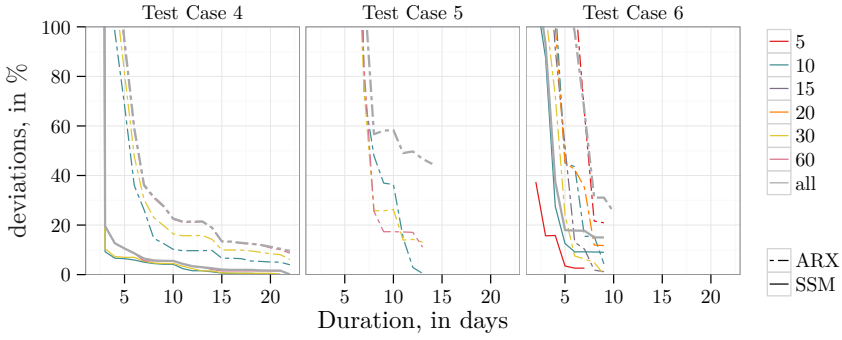

(b)

Figure 5.93: Deviation of estimates from their mean, in %, for test cases 1 to 6. Coloured lines indicate the deviations, when only one sampling time t_s is considered. Thick grey lines indicate the deviations, when all sampling times are taken together. Linetypes indicate the analysis methods: linear regression (LR), auto-regressive models with exogenous inputs (ARX), and lumped state space models (SSM).

Also *Test Case 3* analyses a co-heating test, performed on a detached house with a floor on ground, assuming *Scenario 2*: H is estimated as ω_i. Similar to Test Case 2, though slightly larger, the house is well-insulated and heavy-weight, with an insulated wooden attic floor. Compared to Test case 2, the heat loss towards the ground is limited, and around 5 % of Φ_h^h's mean value during the experiment. Specific to this Test Case, however, is that the experiment was performed shortly after the building was completed. Calculations show that

latent heat, to dry out moisture encapsulated in the building fabric, amounts to 5.2 % of Φ_h^h's mean value. The combined impact of ground floor heat loss and latent heat thus amounts to about 10 % of total heating power. Nevertheless, when we ignore these terms, by ignoring μ, we obtain results that closely approach the expected value of 207.2 $\mathrm{W\,K^{-1}}$. Using LR, we estimate H_{tr} as 203.6 ± 5.5 $\mathrm{W\,K^{-1}}$. Using ARX, we estimate H_{tr} as 205.2 ± 52.9 $\mathrm{W\,K^{-1}}$. The estimates are also very consistent, with respect to the analysis method used, and very robust, with respect to experiment duration and t_s. Already after 7 days, regardless of the chosen t_s, they lie within 8.1 % (LR) and 7.6 % (ARX) of their mean. If we assume a t_s of 480 min for LR, and a t_s of 10 min for ARX, the estimates remain within 2.5 % (LR) and 2.2 % (ARX). Nonetheless, the value for $\sigma_{H_{tr}}$, with regard to the ARX model is high. Reliability plots, however, reveal that a lower sampling time, e.g. 30 min, yields a consistent estimate, with a much smaller confidence interval.

With regard to the chosen sampling time, Test Case 3 seems to be much less sensitive than Test Case 2. This is likely due to the fact that, in Test Case 2, we ignored a term that amounts to ± 18.5 % of Φ_h^h's mean value, whereas in Test Case 3, the ignored term amounts to ± 10 % of Φ_h^h's mean value.

In *Test Case 4*, we performed a dynamic test on a small scale model of a house, the KI Test Box. As it is a solitary object that floats in the air, it is an ideal example of *Scenario 4*. We thus estimated H as the minimum variance weighted combination of $\omega_i(1)/\omega_h(1)$ and $\omega_e(1)/\omega_h(1)$. Using explicit ARX models, we estimate H_{tr} as 4.12 ± 0.30 $\mathrm{W\,K^{-1}}$. Using a second-order lumped state space model, with T_i and an additional state in the envelope, T_1, we estimate H_{tr} as 3.93 ± 0.04 $\mathrm{W\,K^{-1}}$. In Test Case 5, we illustrated that explicit ARX models are not suited to describe the dynamic thermal behaviour of buildings, on the basis of sampling times that typically lie in the range of several minutes. This explains the fact that above confidence intervals do not overlap. It also explains that the estimates, based on explicit ARX models are not robust. They only become consistent after 15 days. As of this duration, regardless of t_s, they lie within 13.4 % of their mean. On the other hand, the second-order lumped state space models, yield estimates that are within 12.7 % of their mean, as of 4 days, and within 6.5 %, as of 7 days.

Test Case 5 investigates a dynamic test, performed on a well-insulated, heavyweight test house. Particular about this case is that the heated zone has a large interface with a thermostatically controlled neighbouring zone. Clearly, it can be categorised as a *Scenario 3*. We estimate H as $\omega_e(1)/\omega_h(1)$. Although T_n significantly influences T_i, model fits are corrupted when we model the associated heat flow explicitly. Moreover, T_n is moderately correlated with T_e, which corrupts the estimate for $\omega_e(1)/\omega_h(1)$. Using implicit ARX models, we estimate H to be in the range from 6.1 to 56.1 $\mathrm{W\,K^{-1}}$, with a mean value of

31.09 $\mathrm{W\,K^{-1}}$. For durations of 9 to 14 days, assuming t_s of 30 or 60 minutes and a model order of 5, the mean estimates for H vary consistently around 30 $\mathrm{W\,K^{-1}}$, and within 25.8 % (30 min) and 17.3 % (60 min) of their mean. For a t_s of 60 minutes, as of duration 12, results for model orders 3, 4 and 5 remain within 16.7 % of their mean. As expected, we are unable to obtain a reliable estimate based on the performed heating experiment.

Test Case 6 illustrates that very reliable results can be obtained, by identifying, using maximum likelihood estimation, state space models that are tailored to *Scenario 2*. Assuming a t_s of 5 min, and durations of 3 days and higher, estimates remain within 15.7 % of their mean, and for durations of 5 days and higher, within 3.5 %. Also ARX models converge to a reasonable estimate for H, though they demand more measurement days to attain it. Moreover, the estimates, based on the latter, do not prove to be more reliable than the estimates on the basis of the co-heating test, discussed in Test Case 2. As of 8 days, the estimates for H remain within 31.1 % of their mean, regardless of sampling time t_s. If we only consider a t_s of 5 min, estimates remain within 21.6 %. Even for a duration of 10 days, there remains a deviation of 25.2 %, depending on chosen t_s.

Overlooking the different test cases, we see that the reliability of the estimate for H is very dependent on *experiment duration* and *weather conditions*. Their uncertainty is also very dependent on the *building characteristics*, the *heating experiment* and the chosen *analysis method*. Moreover, it is clear that the selection of an appropriate scenario is crucial to obtaining reliable and physically relevant estimates. Results are particularly promising, for scenarios where we can rely on ω_i (co-heating test), or $\omega_i(1)/\omega_h(1)$ (dynamic test analysed with ARX), to estimate H. Also in case of the minimum variance weighting, applied in Scenario 4, most weight is associated with ω_i, or $\omega_i(1)/\omega_h(1)$, as it shows a much smaller variance. In case of both LR and ARX, the success of these scenarios depends on whether we can safely ignore the physical phenomena that are not modelled explicitly, e.g. ground floor heat loss. This is certainly true for the co-heating test, as illustrated in Test Case 2 and Test Case 3, and elaborated in Section 3.5.2, but also for the dynamic test in Test Case 6. The test cases show that, in many practical cases, we can indeed ignore them to improve the estimate for H. For instance, for Test Case 3, for some combinations of sampling time and duration, the data lead us to estimate $\mu = 0$. And where we explicitly ignored μ, we obtained very consistent results. In Test Case 6, the reliability plots compelled us to set $\mu = 0$, as this yields more consistent results, and avoids that, for some durations and sampling times, H is corrupted. Finally, state space models were shown to yield very robust and reliable results, provided they are tailored to the respective scenarios and the physics involved.

Chapter 6

Conclusions

6.1 Concluding remarks

The aim of this work was to estimate the thermal performance of whole building envelopes, based on measurement data acquired during specific dedicated heating experiments. We thereby focused on the overall heat loss coefficient H, in $\mathrm{W\,K^{-1}}$. In this section, we collect our findings. The data to support these findings were summarised in the concluding section of Chapter 5.

We first set up an extensive *building physical framework*, that provides a complete description of a building's thermal behaviour, during such specific heating experiments. In practice, we can only collect a limited amount of data, and this data only reveals part of the building's actual behaviour. We thus distilled, from this framework, simplified thermal models, that directly apply to quasi-stationary and dynamic tests. Simplified models no longer explicitly describe the multitude of physical phenomena that inform a building's behaviour. Instead, they are lumped into a limited set of model parameters. The direct link, however, between the simplified models and the building physical framework allowed us to correctly interpret these parameters. Moreover, it uncovered guidelines for organising high quality heating experiments. At the same time, the building physical framework provides a blueprint, from which the practitioner can extract simplified thermal models.

In literature, often a trade-off is made between grey-box models, that contain lumped parameters that exhibit a direct link with the physics, and black-box models, that lack such direct link. By deriving, from a continuous-time first-order grey-box model, a discrete-time first-order black-box transfer

function model, we showed that the parameters, embedded in the latter, remain physically relevant. More specifically, we thus derived an *explicit* ARX model. In Test Case 4 and 5, however, we illustrated that *implicit* ARX models are much better apt to deal with dynamic heating experiments, with a heating power that switches between two discrete levels. Hence, on the basis of our findings, for the purpose of thermal performance characterisation, we suggest to use implicit ARX models.

In this work, we illustrated that we can analyse quasi-stationary and dynamic tests using very similar statistical techniques. We thus effectively embedded both in a single statistical framework. The adopted analysis strategies are tailored especially to the building typology, but also to the heating experiment, and the chosen analysis method. In fact, for a certain building typology, they are shown to be very similar, regardless of the test and analysis method considered.

With regard to the quasi-stationary co-heating test, by analysing the model residuals, we were able to consider data that are averaged over smaller sampling times, t_s, thereby retaining more informative data points, whilst retaining assumptions of quasi-stationarity. To support the analysis of co-heating test data using multiple linear regression, we proposed, as an alternative to a higher-dimensional scatter plot, a two-dimensional scatter plot, from which the overall heat loss coefficient and the global solar aperture can be read instantly. Furthermore, we suggest the use of reliability plots, to track the robustness of H's estimate.

We defined *four scenarios*, that collect tailored strategies to estimate H. Based on the investigated building, and the performed heating experiment, each test case can be categorised as one of them. The scenarios, and the analysis strategies suggested therein, illustrate that the analysis of both quasi-stationary and dynamic tests, as we find them in literature, can only rightfully be applied in a limited number of cases. We revealed that, for some test cases, we need to assume models that are more detailed than generally assumed in literature. For instance, co-heating tests are often analysed assuming stationary heat balance models that group T_i and T_e in a single predictor ΔT. We showed that, in most scenarios, this is not suitable. Instead, we suggest to assume, at all times, T_i and T_e as separate predictors. Also, in literature, often H is estimated as the stationary gain, with regard to the outdoor air temperature T_e. In this work, we showed that this is only correct in Scenario 3, i.e. when the building has neighbouring zones, and a ventilated and unheated attic and cellar. We showed that the resulting estimates are not very robust, and highly uncertain. We suggest to resolve this, by measuring the heat loss towards the neighbouring zones, in which case H can be estimated as the stationary gain with regard to the indoor air temperature.

In a last chapter, we applied the developed methodology to three quasi-stationary tests and three dynamic tests. We showed that the selection of an appropriate scenario underpins the reliability and physical relevance of the obtained estimates. The four scenarios merely serve to guide the mind, and should be verified based on the actual data. In Test Case 1, we combined strategies from Scenario 1 and Scenario 3, and in Test Case 2, we applied analysis strategies from Scenario 2, instead of Scenario 4.

Test Cases 1 and 5 showed that Scenario 3 yields unstable, and highly uncertain estimates for H. Test Cases 2, 3 and 6, that are categorised in Scenario 2, illustrate that values for H are very reliable, when they are estimated as the stationary gain with regard to T_i, in case of linear regression and ARX models, or from appropriate grey-box model parameters (Test Case 6). In Test Case 2, we disturbed the estimates for H, when we explicitly accounted for the slowly varying cellar temperature, in the linear regression model. Results became more reliable and robust when the corresponding term, and the linear regression intercept, μ, were ignored. We could thus estimate H as ω_i, which thereby still comprises the influence of heat losses towards the cellar. Also in Test Case 3, although latent heat and ground floor heat losses combined for about 10 % of total heating power, we ignored μ. We thereby obtained very reliable results for H, that approach the expected value very well. With regard to the co-heating tests in Test Case 2 and 3, we find that LR and ARX yield equally robust results. ARX has the added advantage that it more accurately estimates confidence intervals.

Both in Test Case 4 (Scenario 4) and Test Case 6 (Scenario 2), the combination of a dynamic heating experiment, and grey-box modelling, where we use maximum likelihood estimation to fit continuous-time lumped stochastic state space models to collected data, proved to yield reliable and very robust results, even for experiment durations of only 4 to 5 days. On the other hand, the results for Test Cases 2 and 6 indicate that a dynamic test, analysed with ARX modelling, is not more robust than a co-heating test, analysed with either linear regression or ARX modelling, nor does it yield reliable results for a shorter duration.

6.2 Flowchart to estimate H

On the basis of the developed methodology, and the application thereof on six test cases, we suggest following onset of a flowchart, that practitioners can consult when performing and analysing heating experiments, to characterise a building's overall heat loss coefficient, H, in $\mathrm{W\,K^{-1}}$.

1. **Based on its typology, categorise the investigated building in one of four scenarios**
   Four test case scenarios below are introduced in Figure 3.7, on page 51.

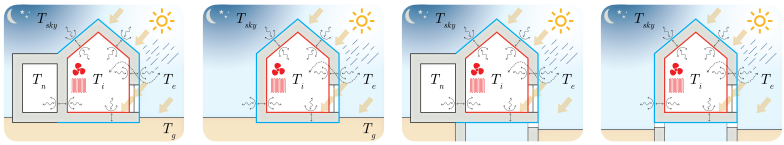

(a) Scenario 1 (b) Scenario 2 (c) Scenario 3 (d) Scenario 4

2. **Select an appropriate test**
   1. If limited experiment time is available, perform a *dynamic test* (Chapter 4), and consider step 8.1.a.
   2. Otherwise, perform a *quasi-stationary test* (Chapter 3).
3. **Consider additional tests/measurements**
   1. If the investigated building has neighbouring zones (*Scenario 1* or *Scenario 3*): consider measuring Φ_{tr}^{n}, to obtain estimates that are more reliable and robust.
   2. In case test is performed shortly after building is constructed, measure relative humidity indoor and outdoor, and verify step 6.2.
   3. To disaggregate transmission and ventilation heat loss, perform a pressurisation or tracer gas test.
4. **Perform measurement campaign**
   Basic guidelines are collected in Sections 3.3 and 3.4, for quasi-stationary tests, and in Sections 4.2.3 and 4.2.4, for dynamic tests. In case of a quasi-stationary test: pre-heat well-insulated buildings for 1 to 2 days; pre-heat poorly insulated, heavy-weight buildings for 3 to 4 days, and evaluate step 6.1.
5. **Prepare data for analysis**
   1. Collect, clean up and synchronise data
   2. Calculate representative temperature signals for the heated volume and its boundary conditions. Prefer their first principal component. If there are outlier signals, consider removing them, or assign lower weights to them. Alternatively, consider weighted (Test Case 2) or unweighted averaging.
   3. Investigate candidate inputs and assess how they inform the building's behaviour during the experiment, using time series plots, and plots of auto and cross-correlation functions.

6. **Verify particular aspects**

    1. In case of a co-heating test, verify whether thermal mass is indeed charged to an equilibrium level, using surface temperature and heat flow sensors. Test Case 1 (Section 5.2), however, shows that in most practical cases, this is not an issue.
    2. If the building is tested shortly after it is constructed, use relative humidity measurements, to assess potential impact of latent heat (Test Case 3, Section 5.4).

7. **Verify chosen scenario**
   Based on pre-processed data, verify whether the building is indeed behaving according to the scenario, chosen in step 1. If not, alter choice. Test Case 1 (Section 5.2) and Test Case 2 (Section 5.3) illustrate this.

8. **Estimate H using strategy, appropriate to verified scenario and performed test.**

    1. In case of a *dynamic test*, appropriate strategies for each scenario are introduced in Section 4.3.
        a. if possible, assume a second-order stochastic lumped state space model, and estimate its parameters using maximum likelihood estimation (Section 4.2.1). Follow model selection procedure illustrated in Test Case 4 (Section 5.5.4).
        b. otherwise, assume an ARX model, and estimate its parameters by minimising the sum of squared simulation errors (Section 4.2.2). Assume implicit ARX models, and determine model order following procedure illustrated in Test Case 6 (Section 5.7.2).
    2. In case of a *quasi-stationary test*, appropriate strategies for each scenario are introduced in Section 3.6.
       Assume linear regression models, and if possible, ARX models (improved estimate of confidence interval), and estimate their parameters by minimising the sum of squared simulation errors. Follow procedure illustrated in Test Case 2 (Sections 5.3.3 and 5.3.4).

9. **Optimise sampling time and model order**

    1. Select appropriate sampling time, t_s, and model order, k, by investigating residual plots, autocorrelation functions and cross-correlation functions, and periodograms and cumulative periodograms.
    2. Use reliability plots (Section 5.1.3) to verify robustness of estimates, and to further optimise choice of t_s and k (illustrated in Test Case 3, Section 5.4.6).

6.3 Further fine-tuning of methodology

We started by defining an extensive building physical framework, but inevitably, some aspects were ignored. For instance, we described all physical phenomena in a linear and time-invariant form. Non-linear and time-variant effects are thereby encapsulated in the simplified model parameters. Non-linear effects are introduced by solar gains, that depend on solar irradiation, sky cloudiness, and the position of the sun; by short-wave radiative heat exchange with the sky, that depends on the sky temperature to the fourth power; by latent heat, that depends on temperature and relative humidity; by air change rates, that depend on temperature differences, wind speed and direction. They might also be introduced by solar shading, phase-change materials, and hydraulic heating systems, among many others. Time-varying effects are, among others, introduced by the varying position of the sun.

In this work, ventilation heat loss and solar gains were simplified significantly. On one hand, we described the ventilation heat loss coefficient as the inverse of the specific thermal resistance r_v. Ideally, we would describe it as a non-linear function of its driving forces, e.g. wind speed and thermal stack. On the other hand, we limited ourselves to assuming a global solar aperture, A_{sol}, that is constant throughout the day. Ideally, however, it is a time-varying parameter, that varies as a function of the sun position and local shading effects. Future work could focus on modelling these phenomena in more detail, and extend the simplified models to explicitly described significant non-linear and time-varying aspects. But true to the aim of this work, we propose to only consider such model extensions, in case they improve the reliability of H's estimate, and reduce its uncertainty.

6.4 Towards on-board monitoring

The dedicated heating experiments, assumed in this work, are mostly performed on vacant buildings. They have the disadvantage that they are intrusive, costly, and take several days or weeks to complete. Dynamic tests are generally proposed as an alternative to quasi-stationary tests, because they hold the promise of rewarding shorter measurement campaigns with a more detailed and accurate assessment. But they nonetheless remain intrusive and costly, and the experimental setup potentially grows more complex. Moreover, in this work, we showed that a dynamic test is not guaranteed to yield more reliable results than a quasi-stationary test.

As an alternative, we consider on-board monitoring of in-use buildings. Our building stock is increasingly equipped with smart meters and other sensing devices, that monitor real buildings, as they are used and heated with building-own services.

We can distinguish between extensive and intensive on-board monitoring. The first comprises a limited set of data, e.g. total energy meter readings, climate data and surveys (Bacher, Madsen, et al. 2013). The latter comprises a complete set of sensors, spread throughout the building, that yield information about separate building zones and different energy vectors. On-board monitoring is commonly used to give users feedback on their energy use, by comparing data with earlier collected data or with data collected from similar neighbouring buildings. Little research work has been done on characterising the thermal performance of buildings on the basis of such on-board monitoring data. It is difficult to set up and run such a campaign, and the collected data reflects the intricate behaviour of the building fabric, its services, and its usage. Moreover, contrary to dedicated heating experiments, we are unable to persistently excite the building. We are indeed monitoring in-use buildings, that we can only excite within narrow comfort bounds, imposed by the users. But as on-board monitoring can be organised in a non-intrusive way, the 'heating experiment' can continue over longer measurement periods.
This work represents a valuable stepping stone, towards developing a methodology to characterise the thermal performance of building envelopes, based on on-board monitoring data. Moreover, dedicated heating experiments prove invaluable to validate the results, that are obtained on the basis of on-board monitoring data.

6.5 Applications

More than half of the final energy use of building is attributable to space heating demand. If Europe is serious about cutting its energy use and greenhouse gas emissions to the levels it committed to, it needs to be able to verify the actual energy performance of its buildings, disaggregated into contributions related to building envelope, its services and usage. Only then can policy makers intervene effectively.

Although more research is needed to bring the discussed methodology to a state where it can be applied in practice, significant steps have been taken in the right direction. The scenarios that we defined here, allow practical test cases to be analysed using tailored strategies. We focused on residential houses, but these strategies can inspire robust analyses of other building types. The current work can thus be used as an onset for a procedure, that characterises building on the basis of dedicated or on-board heating experiments.

On a longer term, data-generated energy labelling could be made complementary to the legislative requirements installed today. It would raise awareness about real performance of buildings and help policy makers take informed actions with regard to improving the energy efficiency of our building stock.

Appendix A

T_i and T_e together apart

In cases where both heat loss towards ground and towards neighbouring zones can be ignored, we can treat both ω_i and ω_e as estimates for H in their own right. Consider again the linear regression model in Eq. 3.31. For readability, we only consider T_i and T_e as separate independent variables. In matrix form:

$$\mathbf{Y}_t = \mathbf{U}_t\omega + \epsilon_t \tag{A.1}$$

with $\mathbf{Y}_t = \Phi_h$, $\mathbf{U}_t = \begin{bmatrix} T_i & T_e \end{bmatrix}$ and $\omega^T = \begin{bmatrix} \omega_i & \omega_e \end{bmatrix}$. To couple the estimated parameters ω^T to a physically relevant value for H, we need to add a restriction to above least-squares problem: in steady-state conditions, ω_i equals ω_e. We can reformulate Eq. A.1 to incorporate such linear constraint:

$$\begin{aligned} \mathbf{Y}_t &= \mathbf{U}_t\omega + \epsilon_t \\ \mathbf{A}\omega &= \mathbf{0} \end{aligned} \tag{A.2}$$

Assuming $\mathbf{A} = \begin{bmatrix} 1 & -1 \end{bmatrix}$. We can directly solve this by performing a constrained optimisation with Lagrange multipliers, which leads to following constrained least squares estimates (Norlen, 1993; Nelles, 2001; Soderstrom and Stoica, 2001).

$$\hat{\omega}_c = \hat{\omega} - \mathbf{U}_t^T\mathbf{U}_t\mathbf{A}^T(\mathbf{A}\mathbf{U}_t^T\mathbf{U}_t\mathbf{A}^T)^{-1}\mathbf{A}\hat{\omega} \tag{A.3}$$

with $\hat{\omega}_c$ the constrained least squares estimate.

Developing Eq. A.3, we can write $H = \omega_{i_c} = \omega_{e_c}$ as:

$$H = \frac{\sum_{k=1}^{N} T_{e_k}^2 - \sum_{k=1}^{N} T_{i_k} T_{a_k}}{\sum_{k=1}^{N} T_{i_k}^2 + \sum_{k=1}^{N} T_{a_k}^2 - 2\sum_{k=1}^{N} T_{i_k} T_{a_k}} \omega_i + \frac{\sum_{k=1}^{N} T_{i_k}^2 - \sum_{k=1}^{N} T_{i_k} T_{a_k}}{\sum_{k=1}^{N} T_{i_k}^2 + \sum_{k=1}^{N} T_{a_k}^2 - 2\sum_{k=1}^{N} T_{i_k} T_{a_k}} \omega_e \tag{A.4}$$

Multiplying nominators and denominators with the variance of the residuals (assuming they are white noise), we can rewrite H as follows:

$$H = \lambda\omega_i + (1 - \lambda)\omega_e \tag{A.5}$$

With

$$\lambda = \frac{\mathrm{Var}(\omega_e) - \mathrm{Cov}(\omega_i, \omega_e)}{\mathrm{Var}(\omega_i) + \mathrm{Var}(\omega_e) - 2\mathrm{Cov}(\omega_i, \omega_e)} \tag{A.6}$$

Bibliography

Andrews, J. (Aug. 1995). *Electric coheating as a means to test duct efficiency: a review and analysis of the literature*. Tech. rep.

Annex 58 (2015). *IEA EBC Annex 58: Reliable Building Energy Performance Characterisation Based on Full Scale Dynamic Measurements*. http://www.kuleuven.be/bwf/projects/annex58/index.htm.

Bacher, P. and P. Delff (Apr. 2013a). *IEA Common Exercise 3: ARX models for thermal performance characterization based on constant indoor temperature experiments*. Tech. rep.

— (Oct. 2013b). *IEA Common Exercise 4: ARX, ARMAX and grey-box models for thermal performance characterization of the test box*. Tech. rep.

Bacher, P. and H. Madsen (2011). "Identifying suitable models for the heat dynamics of buildings". In: 43, pp. 1511–1522.

Bacher, P., H. Madsen, H. Nielsen, and S. Mortensen (2013). *Modelling and evaluation of building thermal performance from smart meter readings*. Tech. rep.

Baker, P. and H. van Dijk (2008). "PASLINK and dynamic outdoor testing of building components". In: 43, pp. 143–151.

Bauwens, G. and S. Roels (June 2014). "Co-heating test: state-of-the-art and application challenges". In: *10th Nordic Symposium on Building Physics*. Building Physics in the Nordic Countries.

Bauwens, G., P. Standaert, F. Delcuve, and S. Roels (Sept. 2012). "Reliability of co-heating measurements". In: *First Building Simulation and Optimization Conference*. IBPSA.

Bell, M., J. Wingfield, and D. Miles-Shenton (2010). *Low carbon housing. Lessons from Elm Tree Mews*. Tech. rep. Joseph Rowntree Foundation.

Boogaerts, F. (Mar. 1987). *Syntheserapport energieaudits: een vergelijkende studie van vier woningtypes*. Tech. rep. Building Physics Section KU Leuven (Nationaal onderzoeks- en ontwikkelingsprogramma op het gebied van energie).

Carbon Independent (Jan. 2015). *Home energy sources*. URL: http://www.carbonindependent.org/sources_home_energy.htm#h7.

CTSM-R (2015). *Continuous Time Stochastic Modeling in R: User's Guide and Reference Manual*. Tech. rep.

Deconinck, A.-H. and K. Leunis (2012). "Co-heating: a critical evaluation of data analysis methods". MA thesis. KU Leuven.

Deconinck, A.-H. and S. Roels (Apr. 2014). *Estimation of the R-value of the opaque walls of the RR Test Box*. http://www.kuleuven.be/bwf/projects/annex58/index.htm.

Delff, P., M. Jimenez, H. Madsen, and R. Carsten (Apr. 2013). *Characterisation of heat dynamics of arctic low-energy house with floor heating*. Tech. rep.

DIN (2003). *Energy efficiency of heating and ventilation systems in buildings - Part 10: Heating, domestic hot water supply, ventilation*. DIN 4701-10:2003-08.

Economidou, M. (Oct. 2011). *Europe's buildings under the microscope: A country-by-country review of the energy performance of buildings*. Tech. rep. Buildings Performance Institute Europe (BPIE).

European Commission (Dec. 2011). *Energy Roadmap 2050*. URL: http://eur-lex.europa.eu/legal-content/EN/TXT/PDF/?uri=CELEX:52011DC0885&from=EN.

European Parliament (Dec. 2002). *Directive 2002/91/EU*. Brussels.

— (Oct. 2012). *Directive 2012/27/EU*. Brussels.

Eurostat (May 2015). *Consumption of energy*. Eurostat. URL: http://ec.europa.eu/eurostat/statistics-explained/index.php/Consumption_of_energy.

Everett, R. (Aug. 1985). *Rapid thermal calibration of houses*. Tech. rep. ERG 055. Open University Energy Research Group, Milton Keynes UK.

Everett, R., A. Horton, and J. Doggart (1985). *Linford Low Energy Houses*. Tech. rep. Open University Energy Research Group, Milton Keynes UK.

Fels, M. F. (1986). "PRISM: An Introduction". In: *Energy and Buildings* 9, pp. 5–18.

Fraisse, G., C. Viardot, O. Lafabrie, and G. Achard (2002). "Development of a simplified and accurate building model based on electrical analogy". In: 34, pp. 1017–1031.

Francisco, P. W., J. Siegel, L. Palmiter, and B. Davis (2006). "Measuring residential duct efficiency with the short-term coheat test methodology". In: *Energy and Buildings* 38, pp. 1076–1083.

Godfrey, K. (1980). "Correlation methods". In: *Automatica* 16, pp. 527–534.

Gutschker, O. (2008). "Parameter identification with the software package LORD". In: 43, pp. 163–169.

Hens, H., A. Janssens, W. Depraetere, J. Carmeliet, and L. Lecompte (2007). "Brick cavity walls: a performance analysis based on measurements and simulations." In: *Journal of Building Physics* 31.2, pp. 95–124.

Hens, H. (2008). *Building Physics - Heat, Air and Moisture: Fundamentals and Engineering Methods with Examples and Exercises*. John Wiley & Sons. ISBN: 9783433018415.

Houvenaghel, G. and H. Hens (2003). *Pitched roofs with a vapour permeable underlay*. Tech. rep. Building Physics Section, KU Leuven.

Howard, B. and D. Saunders (1989). *Building Performance Monitoring - The Thermal Envelope Perspective - Past, Present and Future*. Tech. rep.

ISO (1994). *Thermal insulation - Building elements - In-situ measurement of thermal resistance and thermal transmittance*. ISO 9869:1994. Geneva, Switzerland: International Organization for Standardization.

— (2007a). *Building materials and products – Hygrothermal properties – Tabulated design values and procedures for determining declared and design thermal values*. ISO 10456:2007. Geneva, Switzerland: International Organization for Standardization.

— (2007b). *Thermal performance of buildings – Heat transfer via the ground – Calculation methods*. ISO 13370:2007. Geneva, Switzerland: International Organization for Standardization.

— (2008). *Energy performance of buildings - Calculation of energy use for space heating and cooling*. ISO 13790:2008. Geneva, Switzerland: International Organization for Standardization.

Jimenez, M. and H. Madsen (2008). "Models for describing the thermal characteristics of building components". In: *Building and Environment* 43, pp. 152–162.

Jimenez, M., H. Madsen, and K. Andersen (2008). "Identification of the main thermal characteristics of building components using MATLAB". In: *Building and Environment* 43, pp. 170–180.

Johnston, D., D. Miles-Shenton, D. Farmer, and J. Wingfield (June 2013). *Whole House Heat Loss Test Method (Coheating)*. Tech. rep.

Juang, J.-N. (1994). *Applied system identification*. Prentice Hall, Englewood Cliffs.

Kemna, R. (Aug. 2014). *Average EU building heat load for HVAC equipment*. Tech. rep.

Kissock, J. K., J. S. Haberl, and D. E. Claridge (2003). "Inverse Modeling toolkit: Numerical Algorithms". In: *ASHRAE Transactions* 109, Part 2.

Kramer, R. and J. van Schijndel (Mar. 2012). *Inverse Modeling of climate responses of monumental buildings*. Tech. rep.

Kristensen, N., H. Madsen, and S. Jrgensen (2004). "Parameter estimation in stochastic grey-box models". In: 40, pp. 225–237.

Kronvall, J. (1978). "Testing of houses for air leakage using a pressure method". In: *ASHRAE Transactions* 84(1): 72-9.

Lethe, G., P. Steskens, G. Flamant, and B. Meurisse (Dec. 2014). "An adapted co-heating test and experimental infrastructure for thermal dynamic

response and performance identification of residential buildings." In: *9th SSB Conference*.

Lowe, R., J. Wingfield, M. Bell, and J. Bell (2007). "Evidence for significant heat losses through party wall cavities in load-bearing masonry construction". In: *building Services Engineering Research and Technology* 28 2, pp. 161–181.

Madsen, H. (2008). *Time Series Analysis*. Boca Raton, Florida: Chapman & Hall/CRC.

Madsen, H., P. Bacher, G. Bauwens, S. Roels, and G. Lethe (Mar. 2015). *Annex 58: Guidelines for ST3 Analysis*. Tech. rep.

Madsen, H., P. Bacher, and P. Delff (Oct. 2010). "Mathematical and Statistical Models and Methods for Describing the Thermal Characteristics of Buildings". In:

Madsen, H. and J. Holst (1995). "Estimation of continuous-time models for the heat dynamics of a building". In: *Energy and Buildings* 22, pp. 67–79.

Madsen, H. and J. Schultz (Nov. 1993). *Short time determination of the heat dynamics of buildings*. Tech. rep.

Mangematin, E., G. Pandraud, and D. Roux (2012). "Quick measurements of energy efficiency of buildings". In: *Comptes Rendus Physique* 13, pp. 383–390.

Martin, S., J. Demeester, and D. Ducarme (June 1997). *Oververhitting van gebouwen in zomervoorwaarden*. Tech. rep. Belgian Building Research Institute (BBRI).

Masy, G. (2004). "Modsation thermique d'un bment et de son systeme de chauffage". MA thesis. Universit Liege.

Melgaard, H. (1994). "Identification of physical models". Madsen, H. (supervisor). PhD thesis. Mathematical Statistics, Informatics and Mathematical Modelling, Technical University of Denmark, DTU. URL: `http://www2.imm.dtu.dk/pubdb/views/publication_details.php?id=2072`.

Melgaard, H. and H. Madsen (Oct. 1992). *An Investigation of CTLSM and MRQT Using Simulated Test Sequences*. Tech. rep.

Naveros, J. and C. Ghiaus (2015). "Order selection of thermal models by frequency analysis of measurements for building energy efficiency estimation". In: 139, pp. 230–244.

NBN (2011). *NBN EN 673. Glas voor gebouwen - Bepaling van de warmtedoorgangscoefficient (U-waarde) - Berekeningsmethode*. Tech. rep. Brussels.

Nelles, O. (2001). *Nonlinear System Identification: From Classical Approaches to Neural Networks and Fuzzy Models*. Springer.

Nielsen, A. and B. Nielsen (1983). *A dynamic test method for the thermal performance of small houses - Model Set-up, Test Design, Measurements, Parameter Estimation and Simulation*. Tech. rep.

Norlen, U. (Oct. 1993). "Determining the Thermal Resistance from In-Situ Measurements". In:

Ortega, J. K., J. V. Anderson, J. M. Connolly, and C. E. Bingham (July 1981). *An electric coheating experiment to determine the heat-loss coefficient of a double envelope house*. Tech. rep.

Palmer, J., G. Pane, M. Bell, and J. Wingfield (2011). *Comparing primary and secondary terms analysis and re-normalisation (PStar) test and co-heating test results*. Tech. rep. AECOM, Leeds Metropolitan University.

Palmiter, L., L. Hamilton, M. Holtz, S. E. R. Institute, and U. S. D. of Energy (1979). *Low Cost Performance Evaluation of Passive Solar Buildings*. SERI/RR. Department of Energy, Solar Energy Research Institute.

Rabl, A. (Feb. 1988). "Parameter estimation in Buildings: Methods for Dynamic Analysis of Measured Energy Use". In: 110.

Reynders, E. (2012). "System Identification Methods for (Operational) Modal Analysis: Review and Comparison". In: *Archives of Computational Methods in Engineering* 19.1, pp. 51–124.

Siviour, J. (1981). *Experimental Thermal Calibration of Houses*. Tech. rep. Electricity Council Research Centre, Chester, UK.

Soderstrom, T. and P. Stoica (2001). *System Identification*. Prentice Hall International.

Sonderegger, R. (1978). "Dynamic models of house heating based on equivalent thermal parameters". PhD thesis. Engineering, heat and thermodynamics, Princeton University.

— (1980). *In-situ measurements of residential energy performance using electric co-heating*. Tech. rep.

Sonderegger, R. and M. Modera (Mar. 1979). "Electric Co-heating: A method for Evaluating Seasonal Heating Efficiencies and Heat Loss Rates in Dwellings". In: *Second CIB Symposium on Energy Conservation in the Built Environment*. Lawrence Berkely National Laboratory.

Stamp, S. (2011). "The Error and Uncertainty in Coheating Tests". MA thesis. University College London Energy Institute.

STAT 510 (2015). *STAT 510 Applied Time Series Analysis*. URL: `https://onlinecourses.science.psu.edu/stat510/`.

Strachan, P. and A. Guy (Oct. 1992). *Normalisation of Parameters and Determination of Real Building Performance*. Tech. rep.

Strachan, P., I. Heusler, M. Kersken, and M. Jimenez (2014). *Empirical Whole Model Validation and Common Exercise for Identification: Modeling Specification*. Tech. rep.

Subbarao, K., J. Burch, C. Hancock, A. Lekov, and J. Balcomb (Sept. 1988). *Short-Term Energy Monitoring (STEM) - Application of the PSTAR Method to a Residence in Fredericksburg, Virginia*. Tech. rep. Prepared for

the U.S. Department of Energy, Contract No. DE-AC02-83CH10093. Solar Energy Research Institute.

van Dijk, D., G. van der Linden, and W. Bttger (Oct. 1992). *Parameter Identification Applied on PASSYS test at TNO: Light Weight Reference Wall*. Tech. rep.

VREG (2014). *Evolutie elektriciteits-en aardgasprijzen (incl. btw) voor huishoudelijke afnemers*. `http://www.vreg.be/sites/default/files/document/evolutie_prijzen_hh.pdf`.

Wingfield, J., D. Miles-Shenton, and M. Bell (2011). *Comparison of Measured versus Predicted Heat Loss for New Build UK Dwellings - Unpublished Data*. Tech. rep. Leeds Metropolitan University, Leeds, UK.

Curriculum

Geert Bauwens
Kasteelpark Arenberg 40, bus 2447
B-3001 Heverlee, Belgium

Education

2011-2015: PhD in Engineering Science: Civil Engineering: "In situ testing of a building's overall heat loss coefficient - Embedding quasi-stationary and dynamic tests in a building physical and statistical framework."

2004-2009: Master's degree of Applied Sciences and Engineering: Architecture

Bachelor's degree obtained with honours (73.75%)

Master's degree obtained with honours (1st master: 73.42%, 2nd master: 77,66%)

Major in 'Building technical design'

Master thesis: "Airtightness of the Intermediate Floor in Wooden-Frame Buildings", successfully completed (85%)

Exchange program with *Norwegian University of Science and Technology (NTNU)*, in Trondheim, Norway, during the autumn semester of academic year 2008-2009

1998-2004: Equivalent to 'A' Levels, option Science-Mathematics
Scheppers-instituut, Mechelen, Belgium

Graduation thesis: "Algorithmic Art", successfully completed.

Work Experience

2011-2015: PhD in Engineering Science: Civil Engineering: "In situ testing of a building's overall heat loss coefficient - Embedding quasi-stationary and dynamic tests in a building physical and statistical framework."

2011-2015: IEA EBC Annex 58-project: "Reliable building energy performance characterization based on full scale dynamic measurements". Secretary of project.

2009-2011: Project architect at BOB361 architectes (www.bob361.com), Brussels, Belgium.

Publications

Publications in international journals

Bauwens, G. and Roels, S. (2014). "Co-heating test: A state-of-the-art". In: Energy and Buildings 82, October 2014, pp. 163-172.

Publications at international conferences

Roels, S., G. Bauwens, H. Madsen, P. Bacher, and M.J. Jimènez (2015). "Characterising the actual thermal performance of buildings: current results of common exercises performed in the framework of the IEA EBC Annex 58-project". 6th International Building Physics Conference (IBPC), 2015.

Bauwens, G. and S. Roels (2014). "Co-heating test: state-of-the-art and application challenges". 10th Nordic Symposium on Building Physics, June 15-19 2014.

Bauwens, G. and S. Roels (2013). "Characterising thermal performance of buildings using dynamic model identification". Thermal Performance of Exterior Envelopes of Whole Buildings XII International conference, Oak Ridge, Tennessee, US, December 1-5 2013.

Bauwens, G., P. Standaert, F. Delcuve, and S. Roels (2012). Reliability of co-heating test methodology. BSO12 Building Simulation and optimisation, Loughborough, September 10-11 2012.

Presentations

Annex 58 6th Working meeting, April 13-15, 2015, Prague, Czech Republic: "Characterising the thermal performance of the Twin Test Houses using ARX models.".

Annex 58 5th Working meeting, September 17-19, 2014, Berkeley, California, US: "Subtask 3 - Common Exercise 5".

Annex 58 Seminar: Real building energy performance assessment, April 16, 2014, Ghent, Belgium. “Co-heating test: a state-of-the-art”.

Annex 58 3rd working meeting, October, 14-16, 2013, Hong-Kong, China: “Using subspace identification methods to characterise the thermal performance of buildings”.

Annex 58 1st working meeting, April 2-4, 2012, Bilbao, Spain: “Reliability of co-heating test methodology”.



FACULTY OF ENGINEERING SCIENCE
DEPARTMENT OF CIVIL ENGINEERING
BUILDING PHYSICS SECTION
Kasteelpark Arenberg 40, bus 2447
B-3001 Heverlee
geert.bauwens@bwk.kuleuven.be
http://www.bwk.kuleuven.be/bwf